

1990

An experimental and theoretical study of heat transfer effects during a laser-cutting process

Natarajan Rajendran
Iowa State University

Follow this and additional works at: <https://lib.dr.iastate.edu/rtd>

 Part of the [Mechanical Engineering Commons](#)

Recommended Citation

Rajendran, Natarajan, "An experimental and theoretical study of heat transfer effects during a laser-cutting process " (1990).
Retrospective Theses and Dissertations. 9407.
<https://lib.dr.iastate.edu/rtd/9407>

This Dissertation is brought to you for free and open access by the Iowa State University Capstones, Theses and Dissertations at Iowa State University Digital Repository. It has been accepted for inclusion in Retrospective Theses and Dissertations by an authorized administrator of Iowa State University Digital Repository. For more information, please contact digirep@iastate.edu.

3

91

00495

U·M·I

MICROFILMED 1990

INFORMATION TO USERS

The most advanced technology has been used to photograph and reproduce this manuscript from the microfilm master. UMI films the text directly from the original or copy submitted. Thus, some thesis and dissertation copies are in typewriter face, while others may be from any type of computer printer.

The quality of this reproduction is dependent upon the quality of the copy submitted. Broken or indistinct print, colored or poor quality illustrations and photographs, print bleedthrough, substandard margins, and improper alignment can adversely affect reproduction.

In the unlikely event that the author did not send UMI a complete manuscript and there are missing pages, these will be noted. Also, if unauthorized copyright material had to be removed, a note will indicate the deletion.

Oversize materials (e.g., maps, drawings, charts) are reproduced by sectioning the original, beginning at the upper left-hand corner and continuing from left to right in equal sections with small overlaps. Each original is also photographed in one exposure and is included in reduced form at the back of the book.

Photographs included in the original manuscript have been reproduced xerographically in this copy. Higher quality 6" x 9" black and white photographic prints are available for any photographs or illustrations appearing in this copy for an additional charge. Contact UMI directly to order.

U·M·I

University Microfilms International
A Bell & Howell Information Company
300 North Zeeb Road, Ann Arbor, MI 48106-1346 USA
313/761-4700 800/521-0600



Order Number 9100495

**An experimental and theoretical study of heat transfer effects
during a laser-cutting process**

Rajendran, Natarajan, Ph.D.

Iowa State University, 1990

U·M·I
300 N. Zeeb Rd.
Ann Arbor, MI 48106



**An experimental and theoretical study of
heat transfer effects during a laser-cutting process**

by

Natarajan Rajendran

A Dissertation Submitted to the
Graduate Faculty in Partial Fulfillment of the
Requirements for the Degree of
DOCTOR OF PHILOSOPHY

Major: Mechanical Engineering

Approved:

Signature was redacted for privacy.

In Charge of Major Work

Signature was redacted for privacy.

For the Major Department

Signature was redacted for privacy.

For the Graduate College

**Iowa State University
Ames, Iowa
1990**

TABLE OF CONTENTS

ACKNOWLEDGMENTS	xvii
CHAPTER 1. INTRODUCTION	1
Background	1
Scope and Objectives	6
Phase I - Literature review	6
Phase II - Experimental investigation	7
Phase III - Modelling of the process	7
CHAPTER 2. REVIEW OF THE LASER CUTTING PROCESS .	9
Introduction	9
Thermal Processes in Laser Cutting	10
Types of Laser Cutting Processes	11
Oxygen Assisted Laser Cutting Process	12
Laser Cut Quality	13
Kerf width	13
Heat affected zone (HAZ)	15
Edge striations	16
Dross attachment	16

Process Variables Affecting Quality	17
CHAPTER 3. LITERATURE REVIEW	19
Experimental Research	19
Studies on the feasibility of laser cutting	20
Reports on cut-quality improvement	25
Reports on monitoring laser process quality	26
Analytical and Computational Research	28
Summary	32
CHAPTER 4. EXPERIMENTAL EQUIPMENT AND PROCES-	
 DURES	34
Experimental Equipment	34
CO ₂ laser system	34
Data acquisition system	39
Measurement of HAZ	52
Experimental Variables	55
Summary	57
CHAPTER 5. MEASUREMENTS AND UNCERTAINTIES	58
Temperature Measurement	58
Process Quality Measurement	67
Summary	68
CHAPTER 6. RESULTS FOR KERF WIDTH	69
Kerf Width Variation with Position	69
Effect of Laser Beam Velocity	77

Kerf width	80
Surface temperature	80
Effect of Oxygen Gas Pressure	90
Mass flow rate	91
Convective heat loss	93
Oxidation reaction	98
Kerf width	103
Surface temperature	105
Kerf width prediction	107
Effect of Laser Power	111
Kerf width	111
Surface temperature	113
Kerf width prediction	116
Summary	119
CHAPTER 7. RESULTS FOR HEAT-AFFECTED ZONE	122
Oxidation and Heat-Treated Regions	124
HAZ Variation with Position	130
Effect of Laser Beam Velocity	138
Heat affected zone	138
Surface temperature	139
Effect of Oxygen Gas Pressure	149
Heat affected zone	149
Surface temperature	150

Effect of Laser Power	156
Heat affected zone	156
Surface temperature	156
Summary	166
CHAPTER 8. MODELS OF THE LASER CUTTING PROCESS .	168
Thermodynamic Model	169
Mass and energy balance	169
Simplification of the model	173
Results of the thermodynamic model	179
Finite Element Model	183
Problem formulation	184
Finite element mesh	184
Solution procedure	185
Results	187
Summary	193
CHAPTER 9. CONCLUSIONS AND RECOMMENDATIONS . .	195
Conclusions	195
Kerf width	196
Heat affected zone (HAZ)	197
Process Models	198
Recommendations for Future Research	199
BIBLIOGRAPHY	202

APPENDIX A: COMPUTER PROGRAMS	208
Data Acquisition Program	208
Program Used in Thermodynamic Model	220
ADINAT Input Data File	224
APPENDIX B: SUBSURFACE FLAW DETECTION	233
Test Conditions	234
Results	235
Summary	240

LIST OF FIGURES

Figure 1.1:	Basic structure of the transverse-flow CO ₂ laser	3
Figure 1.2:	Energy level diagram for a four-level laser system	4
Figure 2.1:	Emissivity of 1018 steel at 10.6 μ radiation	11
Figure 2.2:	Photograph of the oxygen gas-jet assisted laser cutting of mild steel	14
Figure 2.3:	Schematic of a typical laser-cut sample	15
Figure 4.1:	CO ₂ laser system with power delivery and work table compo- nents	36
Figure 4.2:	The nozzle and beam focussing system	37
Figure 4.3:	Programming sequence for laser process operation	38
Figure 4.4:	Computerized data acquisition with the IEEE 488 card	40
Figure 4.5:	Computerized data acquisition with the A/D boards	41
Figure 4.6:	Two methods to obtain a reference for the location of the beam on the work piece	43
Figure 4.7:	Photograph of the different components of the Vanzetti in- frared sensor system	47
Figure 4.8:	Test piece with thermocouples mounted in the intrinsic fashion	48

Figure 4.9:	Photograph of the capacitor discharge type of thermocouple welder used to install intrinsic thermocouples	50
Figure 4.10:	Aluminum fixture for mounting the infrared sensor	51
Figure 4.11:	Focussed spot location and size for the infrared sensor relative to laser beam	53
Figure 4.12:	Photograph of the heat treated region adjacent to the cut with hardness test indentations	54
Figure 5.1:	Example of the use of the Savitzky Golay smoothing technique	60
Figure 5.2:	Comparison of the manufacturer's curve-fit equation and the iteration method used, to the NBS table values	62
Figure 5.3:	Manufacturer's calibration curve for the infrared sensor in the low temperature range	63
Figure 5.4:	Manufacturer's calibration curve for the infrared sensor in the high temperature range	63
Figure 5.5:	Calibration curve for the type-K thermocouple wire	64
Figure 5.6:	Results of the calibration procedure for the infrared sensor .	65
Figure 6.1:	Upper surface kerf width variation with position at different beam velocities	71
Figure 6.2:	Variation of lower to upper surface kerf ratio with beam velocity	73
Figure 6.3:	Variation of lower to upper surface kerf ratio with upper surface kerf width	74
Figure 6.4:	Variation of lower to upper surface kerf ratio with beam velocity at the edges	75

Figure 6.5:	Variation of lower to upper surface kerf ratio with upper surface kerf at the edges	75
Figure 6.6:	Variation of edge to center kerf ratio with kerf at the center of the upper surface	76
Figure 6.7:	Energy input per unit length at different laser beam velocities for constant laser power	78
Figure 6.8:	Percentage of energy input used in the melting process at laser beam velocities	79
Figure 6.9:	The variation of kerf width with laser beam velocity	81
Figure 6.10:	Surface temperature at 4.8 mm from the cut line for different kerf width values	82
Figure 6.11:	Ratio of surface temperature to the kerf width for different surface temperature values	84
Figure 6.12:	Comparison of measured kerf with values predicted from Figure 6.11	84
Figure 6.13:	Schematic of the relative areas of the sensor and the kerf for purposes of radiant energy calculations	85
Figure 6.14:	Temperature to kerf ratio at different laser beam velocities and different locations of the sensor	88
Figure 6.15:	Temperature output of the sensor for different laser beam velocities and different locations	88
Figure 6.16:	Temperature to kerf ratio and surface temperature for the sensor ahead and behind the beam	89

Figure 6.17: Temperature to kerf ratio and surface temperature for the sensor around the beam	89
Figure 6.18: Schematic of the gas nozzle showing the inlet and exit conditions of the oxygen gas	91
Figure 6.19: Mass flow rate through the nozzle at different oxygen gas pressures	94
Figure 6.20: Convective heat loss due to the gas jet at different gas pressures	97
Figure 6.21: Convective heat loss due to the gas jet as a percentage of the input laser power at different gas pressures	97
Figure 6.22: Rate of energy produced due to the oxidation reaction	102
Figure 6.23: Energy produced by oxidation reaction as a percentage of the input laser power	102
Figure 6.24: Kerf width on the upper surface and at the center of the sample at different oxygen gas pressures	104
Figure 6.25: Temperature to kerf width ratio at different oxygen gas pressures	105
Figure 6.26: Temperature recorded by the sensor at different oxygen gas pressures and at different locations	106
Figure 6.27: Temperature to kerf width ratio at different temperature values with the sensor spot ahead and behind the beam	108
Figure 6.28: Temperature to kerf width ratio at different temperatures with the sensor spot surrounding the cutting zone	108
Figure 6.29: Comparison of measured kerf and kerf predicted from variable velocity data	110

Figure 6.30: Comparison of measured kerf and kerf predicted from data at a velocity of 33.8 mm/s	110
Figure 6.31: Kerf width dependence on incident laser beam power	112
Figure 6.32: Surface temperature dependence on incident laser beam power	113
Figure 6.33: Surface temperature to kerf width ratio at different incident laser beam power	115
Figure 6.34: Temperature to kerf ratio and surface temperature for the sensor ahead and behind the beam	117
Figure 6.35: Temperature to kerf ratio and surface temperature for the sensor around the beam	117
Figure 6.36: Predicted and measured values of kerf width for the case of varying beam power	118
Figure 7.1: The visible oxidation heat-affected zone adjacent to the cut .	123
Figure 7.2: The heat-treated metal beneath the visible oxidation region .	123
Figure 7.3: Photograph of the hardened region with the diamond-point indentation marks of the hardness testing process	125
Figure 7.4: Hardness profile for the upper surface perpendicular to the edge of the cut	126
Figure 7.5: Hardness profile for the lower surface perpendicular to the edge of the cut	126
Figure 7.6: DPH hardness values at a distance of 0.15 mm from the edge of the cut	127

Figure 7.7:	Heat-treated HAZ for the upper and lower surfaces at different beam velocities	129
Figure 7.8:	Oxidation HAZ for the upper and lower surfaces at different beam velocities	129
Figure 7.9:	Comparison of oxidation and heat-treated HAZ for the two surfaces	130
Figure 7.10:	Hardness profile at different sections of the cut sample for a beam velocity of 16.93 mm/s	131
Figure 7.11:	Hardness profile at different sections of the cut sample for a beam velocity of 42.33 mm/s	131
Figure 7.12:	Heat-treated depth at different sections of the cut sample for two different beam velocities	132
Figure 7.13:	HAZ and kerf width variation with position along the cut . .	133
Figure 7.14:	Lower to upper surface HAZ ratio variation with upper surface HAZ at the sample center	134
Figure 7.15:	Lower to upper surface HAZ ratio variation with sample thickness	135
Figure 7.16:	Lower to upper surface HAZ ratio variation with upper surface HAZ at the sample edges	136
Figure 7.17:	Center to edge HAZ ratio variation for the upper surface . .	137
Figure 7.18:	Effect of laser beam velocity on the HAZ at the center of the cut for the upper surface	139

Figure 7.19: HAZ and surface temperature variation at the center of the cut for the upper surface	141
Figure 7.20: Ratio of the surface temperature and HAZ at center of the cut for the upper surface	143
Figure 7.21: Ratio of predicted to measured HAZ at the center of the cut for the upper surface	143
Figure 7.22: Schematic of the relative areas of the sensor and the HAZ for purposes of radiant energy calculations	145
Figure 7.23: Ratio of the infrared sensor temperature to the HAZ for three different locations at different beam velocities	146
Figure 7.24: Temperature output of the infrared sensor for three different locations at different beam velocities	147
Figure 7.25: Infrared temperature to HAZ ratio for different infrared sensor temperature output ahead and behind the beam	148
Figure 7.26: Infrared temperature to HAZ ratio for different infrared sensor temperature output around the beam	148
Figure 7.27: Heat affected zone at different oxygen gas pressures	150
Figure 7.28: Ratio of the surface temperature to heat affected zone at different oxygen gas pressures	152
Figure 7.29: T_{sensor}/HAZ at different surface temperatures for the sensor located ahead and behind the beam	153
Figure 7.30: T_{sensor}/HAZ at different surface temperatures for the sensor located around the beam	153

Figure 7.31: Comparison of predicted and measured heat affected zones predicted from the data in velocity experiments	155
Figure 7.32: Error in predicting heat affected zone from the data in velocity experiments	155
Figure 7.33: Comparison of predicted and measured heat affected zones predicted by the second method	157
Figure 7.34: Error in predicting heat affected zone by the second method	157
Figure 7.35: Heat affected zone at different values of laser beam power . .	158
Figure 7.36: Surface temperature at different values of laser beam power .	160
Figure 7.37: Temperature-HAZ ratio at different values of laser beam power	160
Figure 7.38: Temperature-HAZ ratio and surface temperature variation for the cases of the sensor spot ahead and behind the beam . . .	162
Figure 7.39: Temperature-HAZ ratio and surface temperature variation for the case of the sensor spot around the beam	162
Figure 7.40: Predicted and measured values of heat affected zone for the case of varying beam power	165
Figure 7.41: Error between the predicted and measured heat affected zone at different values of laser beam power	165
Figure 8.1: Schematic of the metal being cut by the laser beam and the control volume showing the inlet and exit for the oxygen and metal	171
Figure 8.2: Schematic of the cutting front for the case of metal cutting showing the fraction of beam incident on the metal	175

Figure 8.3: Schematic of the cutting front for the case of thick-metal cutting showing the fraction of beam incident on the cutting front 176

Figure 8.4: The calculated radiation heat loss at different laser beam velocities for the case of AISI 1018 steel 178

Figure 8.5: Fraction of the laser beam actually striking the surface for the case of 302 stainless steel and 1018 steel used in the model verification 179

Figure 8.6: Kerf width predicted by the thermodynamic model and the experimental measured values for type 302 stainless steel . . 182

Figure 8.7: Kerf width predicted by the thermodynamic model and the experimental measured values for AISI 1018 steel 182

Figure 8.8: Finite element discretization of the flat plate 186

Figure 8.9: Temperature calculated by the finite element model compared with the exact solution 188

Figure 8.10: Maximum temperature at locations along the line of cut with and without phase change effects 189

Figure 8.11: Maximum temperature at locations along the line of cut from the leading to the trailing edge of the piece 190

Figure 8.12: Temperature at locations perpendicular to the line of cut at $x=2.0$ mm from the leading edge 192

Figure 8.13: Temperature at different y and $x=2.0$ mm with time taken as zero when the source crosses $x=2.0$ mm 192

Figure 8.14: Comparison of kerf width calculated by the finite element model and the experimental values for 0.05 mm thick type 302 stainless steel	193
Figure 8.15: Comparison of kerf width calculated by the finite element model and the experimental values for 3.2 mm thick AISI 1018 steel	194
Figure B.1: Schematic of the test sample with location of thermocouples	236
Figure B.2: Typical temperature record in the vicinity of a flaw	237
Figure B.3: Typical temperature record in regions with and without a flaw	237
Figure B.4: Surface temperature record for different flaw depths	239
Figure B.5: Peak surface temperature near regions with and without a flaw	239
Figure B.6: Surface temperature variation over the flaw for different beam velocities	241
Figure B.7: Peak surface temperature variation over the flaw for different beam velocities	241
Figure B.8: Surface temperature variation with increasing heat source distance	242
Figure B.9: Peak surface temperature variation with increasing heat source distance	242

ACKNOWLEDGMENTS

I would like to begin by thanking the Mechanical Engineering Department for supporting me and my research over the past four years. Professor William W. Bathie always had the confidence in me to give me the responsibility of teaching ME 330, Introduction to Thermodynamics, and ME 336, Heat Transfer. I thank him for the teaching experience that has proven to be extremely useful to me. I also owe thanks to Drs. William J. Cook, Gregory M. Maxwell, and Howard N. Shapiro for the support and encouragement they offered for my teaching efforts. To Dr. Howard N. Shapiro, I owe special thanks for introducing me to the Iowa State community in 1983, and for all his friendly advice and suggestions over the years.

I thank all the technicians in the Mechanical Engineering Department for their patience and timely assistance with material and time - Mr. Robert D. Steed, Mr. Gaylord N. Scandrett, Mr. James J. Dautremont, and Mr. Brian T. Espeland. This project would have been impossible if it hadn't been for Mr. Robert Steed's generosity with equipment and technical advice. The data acquisition system in this project had to be constantly upgraded, and each time I needed a better computer or a better A/D board, Mr. Robert Steed was always willing to loan me one. As a graduate student working on an unfunded research project, I was fortunate to have this fine team of technicians willing to lend their assistance.

My colleagues in the Building Energy Utilization Laboratory and the Heat Transfer Laboratory, both of the past and the present, have also been extremely helpful and supportive throughout my years at Iowa State. I made many good friends both in the laboratory and outside of it who have all immensely enriched my life in Ames. In particular, I would like to thank Mr. Richard Rusk, and his wife Mrs. Edith Rusk (and Thomas, too!) for their friendship during my time in Ames.

I thank the members of my doctoral committee for their efforts in my graduate education. I am grateful to Drs. Richard H. Pletcher, Ron M. Nelson, Thomas J. Rudolphi, and David M. Hsu for their time and interest in my work. Dr. Ron M. Nelson was gracious enough to step into an unexpected void in the committee in the middle of my graduate program, and I thank him for that. I also thank Dr. P. A. Molian for the use of the Laser Laboratory. Thanks go also to Ms. Shannon Breon for her assistance with the infrared sensor.

I am not sure I know where to begin to express my gratitude and appreciation of all the things that my major professor, Dr. Michael B. Pate, has done for me. He was always there, as a professor, and more importantly, as a friend, whenever I needed his guidance. I have learnt much from him, most importantly, to look at the "Big Pitcher" for any problem! It is therefore with the deepest gratitude that I thank Dr. Michael B. Pate for all his guidance of my work, and for the friendship over the past seven years.

Lastly, I wish to thank my family, my parents - my mother, and my late father, who would have been very proud and happy to see me graduate with a doctorate degree. They gave all their children a desire to pursue higher education and succeed;

they did not mind even when we wanted to go halfway around the world to do that. I thank my parents-in-law Mr. R. Natarajan and Mrs. S. Natarajan, for their encouragement, support, and confidence in me that I would succeed in everything I wanted to do. And my wife, Kunthavi - who is always so sure that I'll succeed and has much more confidence in my abilities than I myself do; and who was patiently supportive even when she had to work on her thesis - I thank her for all that and more.

CHAPTER 1. INTRODUCTION

The use of lasers by manufacturing industries has rapidly increased over the past few years. Today, lasers are routinely used for such processes as cutting, heat-treating, welding, cladding, and drilling of metals and nonmetals. Newer types of lasers and new applications are also being rapidly developed. One of the more important advantages of the device is the ease with which it lends itself to automation. As a consequence of automation and developments in Computer Integrated Manufacturing (CIM), computer-controlled laser materials processing now appears feasible in utilizing lasers for manufacturing. Therefore, the use of lasers in the manufacturing industry will undoubtedly increase in the coming years.

Background

The concept of the amplification of light by stimulated emission of radiation (LASER), was first proposed by Albert Einstein in 1917. The first device, called the "maser" was developed by Charles Townes and his co-workers in 1954. The first actual laser was not developed until 1960, when Theodore Maiman built the pulsed ruby laser which emitted radiation at a wavelength of 0.6943μ . Following this, the development of other types of lasers proceeded quite rapidly, and in 1961, the first gas laser was built.

In 1961 a helium-neon gas laser operating at a wavelength of 1.15μ was built by Ali Javan at the Bell Telephone Laboratories. Later, in 1962, a helium-neon laser that emitted radiation in the visible wavelength of 0.6238μ was built. This is the type of helium-neon laser that is most commonly used today. A year later, in 1963, the successful operation of a carbon dioxide gas laser was reported by Patel, also at the Bell Telephone Laboratories. The CO_2 gas laser, with several modifications over the original construction, is now regarded as the work-horse of the laser materials-processing industry.

Several new types of lasers that are more powerful and reliable in their operation have recently been developed and marketed. The result is that today's lasers are used in such diverse fields as medicine, engineering, instrumentation, etc., and their applications and use continues to grow. Towards the end of 1989, several new companies in the United States, Europe, and Japan, entered the CO_2 laser market, thus signifying an increasing market for the product. This competition has led to a lower per-watt cost of the product, which in turn, makes it increasingly viable to use the laser on the shop floor [10]. Carbon dioxide lasers from 250 W to 30 kW are readily available today.

Figure 1.1 shows a simple structure of a transverse-flow gas laser, of the type used in the experiments in this research. A typical CO_2 laser consists of a cavity with a circulating gas mixture of 10% carbon dioxide, 10% nitrogen, and 80% helium.

The operation of the laser can be explained with reference to Figure 1.2, which shows a schematic diagram of the energy levels for a four-level laser system, such as the CO_2 laser.

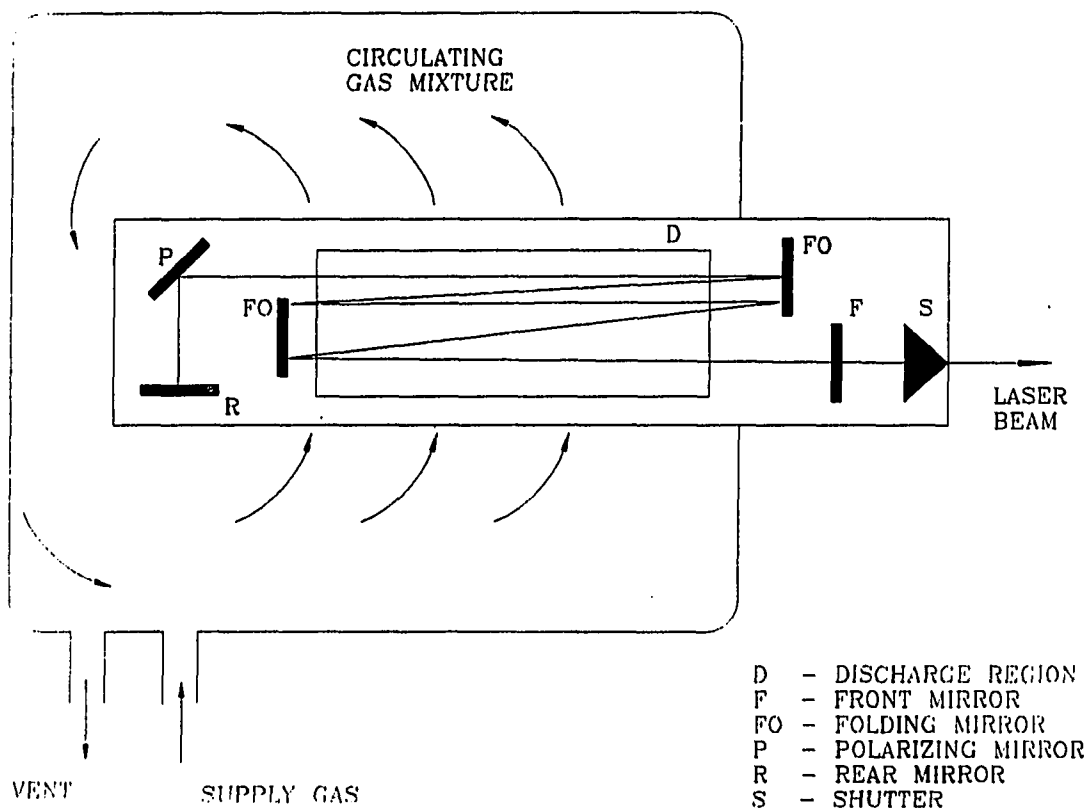


Figure 1.1: Basic structure of the transverse-flow CO₂ laser

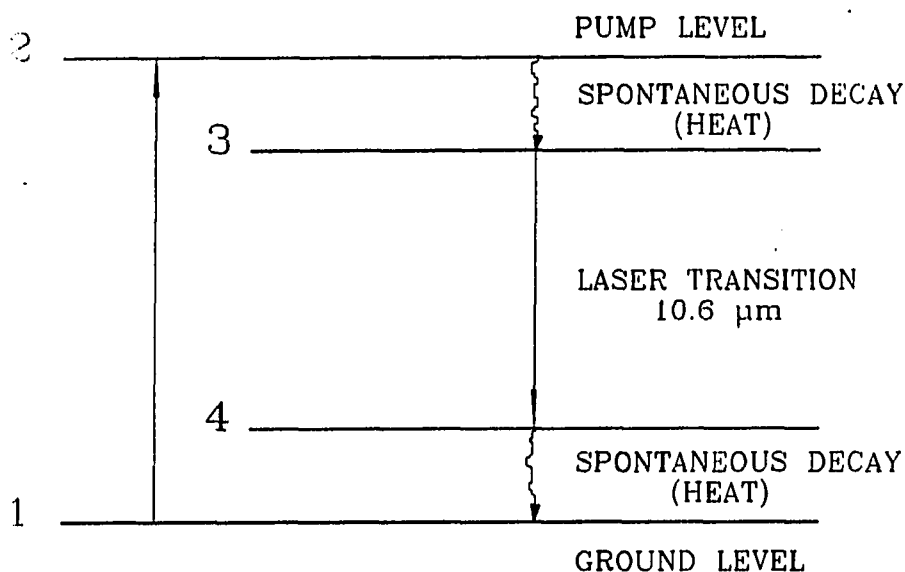


Figure 1.2: Energy level diagram for a four-level laser system

The discharge between the cathode and the anode excites the nitrogen molecules to a higher energy band, shown as level 2 in the figure. The carbon dioxide molecules originally at level 1, absorb energy through collisions with the nitrogen molecules and make the transition from the level 1 to the higher energy level. With increasing population at the high energy level, a population inversion is created for the carbon dioxide molecules. The carbon dioxide molecules make the transition from the unstable energy level 3 to a stable lower energy level 4. The difference in energy between these two levels is emitted as radiation with a wavelength of 10.6μ . The helium atoms present in the mixture serve to keep the mixture cool. They also reduce the carbon dioxide molecules from energy level 4 to energy level 1, thus maintaining a low population at energy level 4.

The radiation emitted in the energy-level transition is amplified by repeated

reflections between two mirrors on either sides of the cavity and stimulated emissions. The laser beam emerges through one of the mirrors which is only partially reflective. The laser radiation emerging from the cavity is monochromatic (of narrow spectral bandwidth), has a small beam divergence angle, and is coherent. The beam also has the required spatial and temporal characteristics, all of which make it ideally suited for its many applications in several fields.

These unique properties of laser radiation, coupled with availability of high values of output power, have made lasers a very useful tool in engineering. Some of the common lasers and their uses are [37]:

Carbon dioxide laser:

- Continuous-wave operation
- Used for welding, drilling, marking, cutting, heat-treating, cladding, and alloying
- Used with metals such as steels, copper, aluminum, and brass
- Used with nonmetals such as ceramic, plastic, paper, wood, and glass

Nd:YAG laser:

- Pulsed operation
- Used for drilling, balancing, resistor trimming, and trimming of electronic circuits
- Used with materials such as steels, titanium, copper, aluminum, ceramic, and plastic

Excimer laser:

- Pulsed operation
- Used for chemical vapor deposition and electronic material processing

Scope and Objectives

The objective of this research was to study, both experimentally and theoretically, the heat transfer effects in a laser cutting process. The experimental investigations consisted of monitoring surface temperature variations with process-quality in a laser-cutting process. The goal was then to show that it was feasible to determine the process-quality based on the temperature data alone.

The research effort consisted of three phases, namely, literature review, experimental investigation, and theoretical modelling of the process. A brief discussion of each of these phases is presented in the sections below. A detailed discussion of the laser-cutting process including the evaluation of process-quality is presented in Chapter 2.

Phase I - Literature review

The literature review consisted of three parts:

1. experimental investigations on the feasibility of cutting different materials,
2. theoretical and computational models of the laser processing of materials, including the cutting process, and,

3. laser-process monitoring and control in real-time with particular attention to reports on thermal techniques.

The results of the literature review are discussed in Chapter 3.

Phase II - Experimental investigation

A feasibility study was initially performed to test the hypothesis that surface temperatures correlated with cut-quality. Once this was established, a series of cutting experiments were performed using thermocouples mounted on the surface of samples. Another series of experiments were then performed with an infrared sensor mounted to read the surface temperature in the vicinity of the laser beam. The details of the experiments and the equipment used are discussed in Chapter 4. The procedure for data reduction and analysis are presented in Chapter 5, and the results of the experimental study are presented in Chapters 6 and 7.

A set of experiments were also performed to test the feasibility of detecting subsurface flaws (such as those formed during laser welding) by using surface temperature measurements. The details of these experiments and the results are discussed in Appendix B.

Phase III - Modelling of the process

The theoretical investigation of this research consisted of two parts. The first part was the development of a thermodynamic model to better understand the different aspects of the cutting process. The second part of this theoretical effort was to develop a two-dimensional model of the laser-processing of a sample with finite dimensions,

using a commercial finite element code. The details of the two models and the results are discussed and presented in Chapter 8.

CHAPTER 2. REVIEW OF THE LASER CUTTING PROCESS

Introduction

The laser-cutting process is accepted by the manufacturing industry as a viable method for cutting metals and nonmetals. This acceptance is mainly due to the advantages that the method has over conventional machining operations [56]. Some advantages of the laser-cutting process are:

- The cut width is very narrow leading to savings in material
- There is only a very narrow region that is heat-affected by the cutting process
- Work-holding requirements are minor
- There is no tool wear
- The cut can be started anywhere
- Cutting speeds are usually faster than in other conventional methods
- The process lends itself easily to automation

Thermal Processes in Laser Cutting

The laser cutting process is fundamentally a thermal process. Therefore, the thermal characteristics of the material play a very important role in determining both the ability of the laser to cut and the quality of the process.

The laser radiation that strikes an opaque surface is partly absorbed and partly reflected. The amount of laser radiation that is absorbed is determined by the reflectivity of the surface. Surface reflectivity is a function of the wavelength of the radiation, the surface temperature, the surface conditions, and the direction of the radiation. Figure 2.1 shows the emissivity in vacuum of AISI 1018 steel at 10.6μ radiation calculated by the following equation [13],

$$\varepsilon_{\lambda} = 0.365 \left(\frac{\rho(T)}{\lambda} \right)^{0.5} - 0.0667 \left(\frac{\rho(T)}{\lambda} \right) + 0.006 \left(\frac{\rho(T)}{\lambda} \right)^{1.5} \quad (2.1)$$

for $\lambda \geq 5\mu$, where, ρ is the electrical resistivity of the material [39].

The maximum value of the calculated emissivity in vacuum is 0.12. However, in the presence of atmospheric air or oxygen, oxidation of the surface occurs, especially at elevated temperatures. This can significantly increase the absorptivity of the surface to laser radiation. In addition, after a cut has been started, the cut acts as a "black body" and almost all of the incident radiation is absorbed.

The energy absorbed by the material raises the energy level of the electrons in the conduction band (in metals), and heat transfer by classical conduction occurs in the material. Rapid local heating is then produced which causes the material to first, melt and subsequently, to evaporate. Since thermal diffusivity determines the rate at which energy is dissipated in the material by conduction, materials with

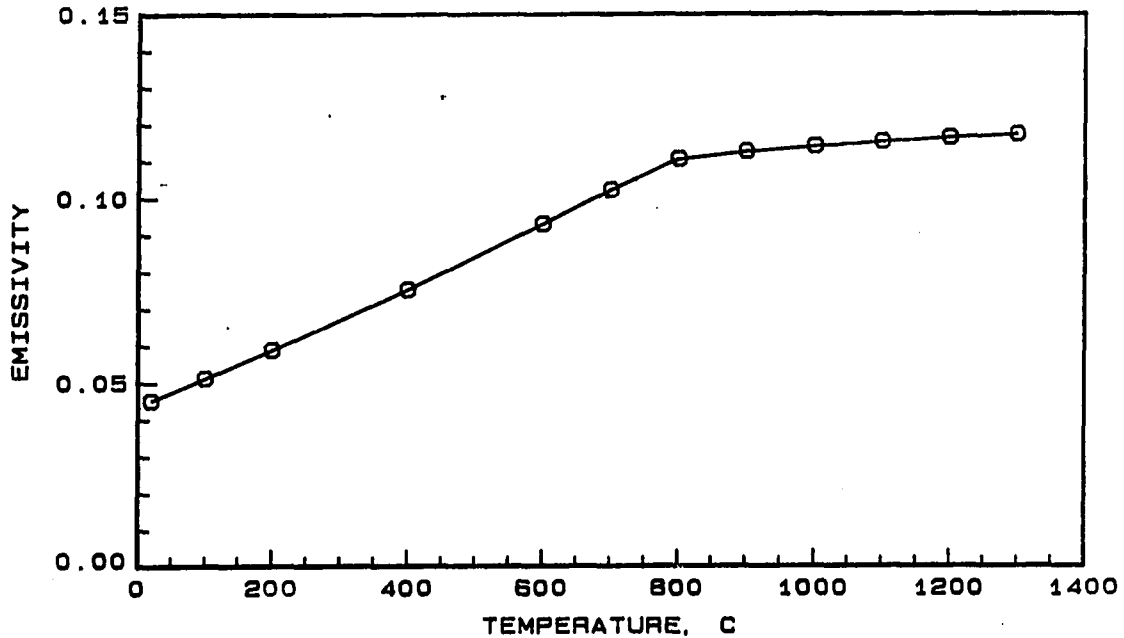


Figure 2.1: Emissivity of 1018 steel at 10.6μ radiation

low thermal diffusivities can be cut more readily than materials with high values of thermal diffusivity. It is a consequence of this that copper and aluminum are two of the most difficult materials to cut with the laser.

Types of Laser Cutting Processes

Laser-cutting can be classified into four types of processes [56]. The four types of processes are:

1. *Vaporization cutting*: In this type of process the material is heated beyond its melting temperature and eventually evaporated. Material removal is primarily by vaporization; the energy requirements depend upon the thermal properties of the material, but are usually quite high.

2. *Non-reactive assist-gas cutting*: This type of cutting process uses an inert gas such as argon as an assist-gas to blow away the material once it has melted. The energy requirements are lower than in the previous method, and the assist-gas also helps to protect the laser optics.
3. *Reactive assist-gas cutting*: This method, first proposed by Sullivan and Houldcroft [57], uses a reactive gas such as oxygen or methane as the assist gas. The gas not only blows away the molten metal, but also provides additional heat for the cutting process by some exothermic reaction. By this method, thicker metals can be cut at faster rates and with lower laser power requirements.
4. *Controlled fracture cutting*: The method is only suited for brittle materials, such as glass, where a crack is initiated by inducing thermal stresses in the material.

Of the four methods described above, the method of reactive gas cutting was used to perform the experiments in this research. This cutting process is discussed in greater detail in the following section.

Oxygen Assisted Laser Cutting Process

This is the most commonly used method of cutting steel thicker than 2.0 mm. Figure 2.2 shows a photograph of the oxygen gas-jet assisted cutting of mild steel. A nozzle delivers the oxygen gas-jet coaxial to the laser beam above the workpiece. The absorbed laser radiation initially creates a hole, known as the "keyhole". The keyhole then acts as a black-body and causes most of the radiation to be absorbed. The absorbed radiation increases the temperature locally, thus resulting in more melting

of the metal. The molten metal is rapidly blown away from the cut region by the impinging gas-jet.

In using oxygen as the assist-gas, an additional source of energy is obtained from the exothermic reaction of the oxidation of steel. The rate of oxidation increases with increasing temperature [28], thus, rendering the process almost self-sustaining. Typically, the oxidation reaction front and the laser beam travel at different velocities. However, a good cut is obtained only when the two are travelling at the same velocity [5]. The quality of a laser-cut is determined by several parameters. The definition of laser-cut quality and its evaluation are discussed in the following section.

Laser Cut Quality

A schematic of a typical cut made by an oxygen-assisted laser process (referred to, as the laser process), is shown in Figure 2.3. The quality of the cut is primarily determined by the amounts of material removed and material affected by the cutting process. A brief description of the terms used in evaluating the process-quality is presented below.

Kerf width

Kerf width is defined as the width of the cut produced by the laser-cutting process. This represents the material removed either by melting and blowing, or, by evaporation. Since this is material wasted, it is desirable to minimize kerf width at all times.

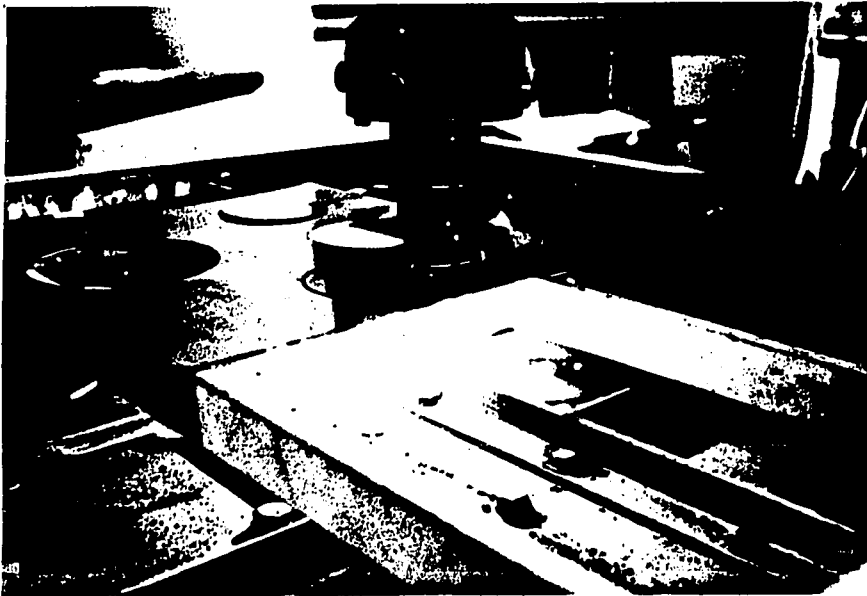


Figure 2.2: Photograph of the oxygen gas-jet assisted laser cutting of mild steel

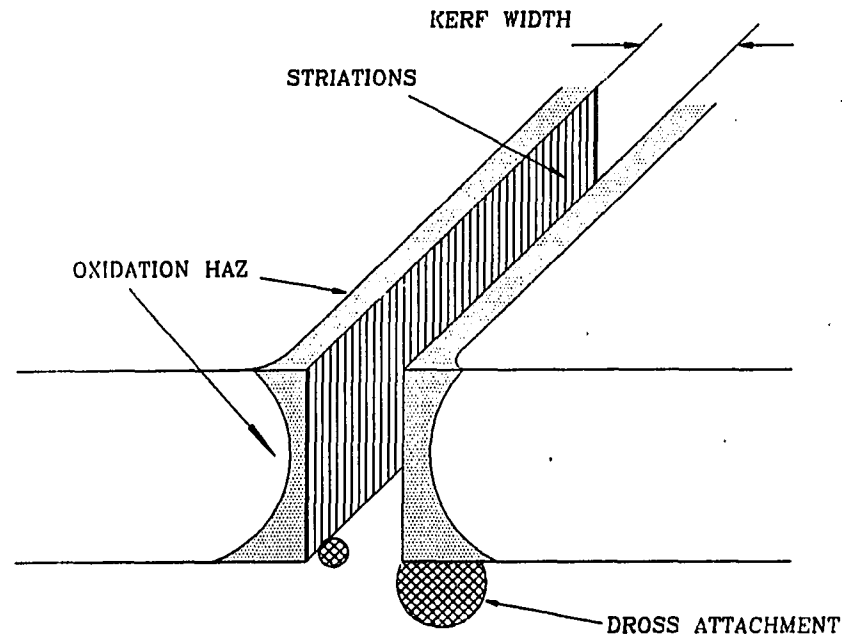


Figure 2.3: Schematic of a typical laser-cut sample

Heat affected zone (HAZ)

Heat affected zone (HAZ), is the region adjacent to the kerf that has been thermally affected by the laser-cutting process. This region is affected by the cutting process in two ways. One is the surface discoloration produced due to the oxidation reaction. This surface oxidation is not permanent and can be removed by as simple a process as sanding the affected region. This region can also be easily measured by optical instruments such as the tool-maker's microscope. The second form of HAZ is the heat-treated zone adjacent to the cut-edge. This region is narrower than the surface oxidation region, and can only be measured through a micro-hardness test. Because of the difficulty associated with making hardness measurements, it is standard practice to report only the surface oxidation HAZ [56].

A study was made to test the ability of oxidation HAZ to predict the heat-treated

HAZ. The experimental details and the results of this investigation are presented in Chapter 7. The results of the study showed that the oxidation HAZ correlated fairly well with the heat-treated HAZ. It was possible to estimate the permanent damage to the sides of the cut by a measurement of oxidation HAZ alone. In this research, therefore, only the oxidation HAZ is presented, with the understanding that this is a measure of the permanent damage to the metal. In the subsequent references to HAZ, the heat affected zone referred to is the oxidation HAZ.

Edge striations

The height and the spacing of the ridge-like striations determine the smoothness of the edges of the cut. This cut-edge quality is determined based on two measurements. One is the frequency or spacing of the striations, and the other is the height of striations as measured by a roughness indicator. The height of the striations is given by the roughness number, R_a . Several theories have been proposed for the presence of the striations. Based on high-speed photographs of the cut region, Arata et al. [5] suggest that the striations are due to the intermittent flowing of the molten metal. However, these theories have not been verified nor confirmed by others.

Dross attachment

Dross is the molten metal that does not get blown away rapidly enough by the oxygen jet and, therefore, attaches itself to the cut-edge by re-solidification. Dross attachment is undesirable as it causes the release of energy back to the metal leading to increased HAZ. Dross attachment can occur if the oxygen gas-jet is not powerful

enough to blow away the molten metal. This could be due to several reasons such as, low gas pressure, too great a distance between the nozzle and the plate, too high a velocity for cutting, or the viscosity of the molten metal being too high.

In this study, the quality of the cut was based on the measurements of the kerf width and the HAZ. In all the cases where a kerf width is reported, care was taken to ensure that there was no dross attachment. Where dross attachment was present, either on the upper or lower surfaces, it is treated as evidence of a poor cut and the data are presented as such.

Process Variables Affecting Quality

The laser-cutting process is affected by several variables, and not all the effects of all the variables have been clearly understood yet. There is much debate and research being performed to increase the understanding of the process which leads to improvements in the cutting process. Some of the more important variables that affect the process are:

- Laser beam power
- Laser beam velocity
- Laser beam quality
- Characteristics of focal optics
- Plane of focus of the beam
- Type of assist-gas used

- Assist-gas pressure
- Gas nozzle design
- Distance between nozzle and material being cut
- Type of material being cut
- Thermal properties of the material
- Surface characteristics of the material

Of the above variables only a few were varied during the course of the experiments. The variables that were varied are the laser beam power and velocity and, the oxygen gas pressure. The range of values of these variables are given in Chapter 4.

CHAPTER 3. LITERATURE REVIEW

This chapter discusses the research reported in the literature that pertain to the laser cutting process. Little information was found along the lines of the present research. The literature review is divided into two main categories, namely, (1) experimental research, and (2) analytical and computational research. Each of these is in turn subdivided into sections to discuss the results of the review. In the sections to follow, some reports on laser welding and heat-treating are also included when they were found to be relevant.

Experimental Research

The discussion on the review of the literature on experimental investigations is subdivided into three sections. The first section deals with the research on the feasibility of performing a cut on different materials. The second section discusses the studies reported on methods to improve the laser cutting process. The third, and final section, discusses the research into monitoring the cut quality. In this section, due to their relevance to the present study, some reports on monitoring other laser processes are also included.

Studies on the feasibility of laser cutting

An assist-gas was always used in the laser-cutting process to protect the lens assembly from debris from the cutting zone. In addition, the assist-gas aided the cutting process by blowing away the molten metal from the cutting zone. An inert gas such as argon was usually used in the cutting of metals and nonmetals. Sullivan and Houldcroft [57] were the first to show that by using oxygen as the assist-gas, steel sections greater than 0.3 mm in thickness could be cut with the laser. They were able to cut high carbon and stainless steels up to 0.3 mm in thickness at speeds of 16.9 mm/s. The cut width decreased with increasing laser beam velocity and there was an optimum velocity at which the oxygen reaction front did not propagate beyond the laser-heated area. At low velocities the cutting was intermittent and large kerf widths were obtained. This considerable increase in the speed of the process and the applicability of the process to thicker materials.

Several reports soon followed that documented the cutting of different materials using oxygen as the assist-gas. Arata and Miyamoto [2, 3, 4] published three reports on the laser as a source of energy for cutting, drilling and welding operations. They report that the laser beam tended to be "self-focussed" in a laser-drilled hole by the sides of the hole. This phenomenon, they conclude, permitted cutting thick sections of metals. They also found that the absorptance of the surface to laser radiation increased with increasing beam velocity. Coating the surface with an agent that had a boiling point lower than the base metal did not enhance the cutting process significantly. When the coating surface had a higher boiling point than the metal, the surface absorptance was increased.

Arata et al. [5], then followed with report on a close look at the cutting front in oxygen-assisted laser cutting of a 3 mm thick piece of stainless steel. They filmed the cutting front at a speed of 1000 frames per second to observe that the cutting was periodic at velocities below 2 m/min. This behavior was also independent of the laser beam power. The oxidation reaction front travelled at a higher velocity than the beam which gave rise to the periodicity due to the reaction stopping when the temperature was too low to sustain the reaction. At laser beam velocities higher than 2 m/min, the cutting was more uniform leading them to conclude that the reaction front was travelling at the velocity of the beam. They also report that the path of the melting metal was more inclined at higher than at lower beam velocities. This was also seen in the inclination of the striations on the cut-edge.

Temperature measurements were also made by Arata et al. [5] with a calibrated radiation pyrometer to read the temperature in the cutting zone. In cutting 2 mm-thick stainless steel (SS41), with a laser power of 1 kW and an oxygen gas pressure of 1.5 kg/cm², the temperature at a depth of 1.0 mm increased from 1700°C at a velocity of 1 m/min, to a value of 2000°C at a velocity of 4 m/min. The temperature also increased with depth in the cutting zone. They do not discuss the reason for this increasing temperature; however, they speculate that the temperature is likely to reach the evaporation temperature as the laser beam velocity is increased steadily. A reason for the increasing temperature with increasing beam velocity could be the increasing angle of the cutting front as discussed in greater detail in Chapter 6 and 7. This could also account for the increasing temperature with increasing depth in the cutting zone that was observed by Arata et al.

The development of lasers with continuous power output of over 10 kW lead to research in cutting steel thicker than 5 mm that had been possible until then. Sepold and Rothe [54] carried out experiments on mild steel and Cr-Ni-steel with a 5 kW laser. They showed that, with an oxygen-gas assist, steel samples up to 35 mm could be cut with the laser. The kerf width obtained in cutting a 35 mm sample of mild steel was 2.5 mm when cut at 8 mm/s. The velocity of cutting decreased with increasing sample thickness, and the kerf width increased with increasing sample thickness. One problem that they encountered was the failure of the molten slag to clear the lower edge of the cut at a sufficiently fast rate. This was solved by using high pressures of the oxygen gas jet.

It wasn't long after, that other metals besides steel were cut with the laser. Dillio et al. [18] attempted to cut aluminum alloy sheets with a 2 kW laser. Aluminum alloy sheets up to 2 mm in thickness were cut with the laser with both oxygen and helium as the assist-gas. Mechanical tests performed on the cut samples indicated that there were no significant morphological differences between the two shielding gases used. However, the optimum cutting speed was higher when oxygen was used as the assist-gas. The kerf width was similar for the two gases used, and varied between 0.25 and 0.35 mm.

The high thermal diffusivity of metals such as aluminum rendered them difficult to cut with the laser. Copper was one of the last metals to be successfully cut with the laser. Daurelio et al. [17] cut copper sheets ranging from 0.2 to 4 mm in thickness with a 2 kW laser. They accomplished this by causing cuprous and cupric oxide formation on the surface to enhance the absorption of the laser beam. The oxides formed at

increasingly rapid rates at the high temperatures, and the laser beam was able to enhance the oxide formation. By carefully adjusting the oxide formation ahead of the cutting beam, they were able to cut copper sheets up to 4 mm in thickness at speed of 2 mm/s which produced a kerf width of 0.8 mm. They do not specifically mention the type of gas used in the cutting, but, considering that surface oxidation is important for the process, it can be assumed that oxygen gas was used as the assist-gas.

Sharp [55] reports cutting aluminum and copper up to 6 mm in thickness by using a beam focussed to less than 0.1 mm in diameter without the use of any absorption coatings. For example, copper sheets of 2.5 mm thickness were cut with a laser power of 1200 W at speeds of 6 mm/s. They were able to do this by obtaining a perfectly gaussian beam focussed to a very small area which resulted in a high power density at the focal spot.

The cutting of fiber-reinforced polyesters was also attempted. Tagliaferri et al. [58] cut composites made of aramid, graphite and glass cloth-reinforced polyesters with a 400 W laser and helium as the assist-gas. They were successful in cutting these composites up to a thickness of 4.5 mm at speeds ranging from 8 to 58 mm/s. At low velocities excess loss of resin was observed along the cut-edge with the result that the fibers were exposed. This effect was less pronounced at the higher beam velocities employed. However, the thermal properties of the composite greatly influenced the maximum speeds possible. Similar attempts at cutting fiber-reinforced plastics have also been reported by Moriyasu et al. [41]. They also found that the plastic matrix along the cut-edge suffered damage, but, they were able to reduce the damage by using pulsed lasers with very short pulse duration for performing the cut.

Several review articles have also appeared in the literature that have detailed the state-of-the-art research in the laser cutting of metals. An early review of the field was done by Babenko and Tychinskii [7] which looked at work in the Soviet Union and elsewhere. They also presented a physical model of the cutting process which resulted in a set of nomograms which gave the cutting velocity and power for any material. They also presented results on the cutting of metals and other nonmetals. Besides cutting, the review article also considered other application of the laser, such as welding, engraving, and doping.

Steen and Kamalu [56] were the first to compile in great detail all of the results available on the laser-cutting process. Their report presents a comprehensive account of the effect of different variables on the cut-quality. Cut-quality was defined by the kerf width and the oxidation heat affected zone. Different types of laser cutting, such as vaporization cutting, fusion cutting, reactive fusion cutting, controlled fracture, and scribing are discussed. Practical performance results on the effect of laser power, the optical system, the nozzle design and gas flow effects, on the cut quality are also presented. The results are discussed in greater detail in Chapters 6 and 7, where appropriate.

A second review article by Schuocker [53] discusses a typical laser cutting system followed by the physical process involved. They then provide a detailed table of different materials and the laser power and velocity suitable for cutting these materials. The materials covered range from metals such as aluminum and steel to other materials such as asbestos, ceramics, plastics, wood, glass, paper, cloth, rubber, and corrugated cardboard. They conclude with a discussion on the criteria to select a

laser system, such as the laser, optics, computer control, and environmental factors.

A third and final review article by Mazumder [37] is more general in nature and discusses the state-of-the-art of laser materials processing. After recounting the advantages of the laser over conventional materials processing techniques, the author discusses the different laser processes. The laser processes discussed are, laser heat-treating, laser chemical vapor deposition, laser surface alloying, laser welding, and laser cutting.

Reports on cut-quality improvement

Much attention has been paid to improving the quality of the laser cut. A few of the important reports that appear in the literature are discussed in this section. One of the measures of the cut-quality is the striations that are present along the edge of the cut. Arata et al. [5] proposed a theory that these striations were due to the starting and stopping of the oxidation reaction when the oxidation rate is higher than the beam velocity. To reduce the edge roughness produced by the striations, Powell et al. [47] used a pulsed laser instead of a continuous-wave laser. Mild steel 1.25 mm in thickness was cut with a laser power of 350 W with an oxygen gas jet of 30 psi. The laser beam was pulsed at frequencies ranging from 100 to 1000 Hz. The roughness of the cut edge was measured and it was found that the striation roughness was a minimum at a laser pulsing frequency of 500 Hz. The authors report a decrease in the edge roughness by a factor of three or more. They conclude that the laser pulsing caused the laser-material interaction to be less dependent on the material characteristics. Too high a pulsing frequency caused little or no improvement in the

cut-edge quality, while, too low a frequency resulted in a rougher finish due to the drilling-like action in the process.

O'Neill and Steen [44] observed that when copper and aluminum samples were cut with a carbon dioxide laser, while simultaneously treated with an excimer laser operating at 248 nm, the absorptivity of the surface was enhanced. The ultraviolet excimer radiation caused surface damage and oxidation which resulted in the increased absorption of the CO₂ laser. The excimer laser was overlapped with the CO₂ laser while cutting which resulted in over 50% of the incident CO₂ laser being absorbed when the excimer was pulsed on the surface at a rate of 100 Hz.

Gabzdyl et al. [20] have shown that the nozzle and beam alignment can also have significant impact on the quality of the cut produced. They found that kerf width and the roughness of the cut edge increased with increasing misalignment of the laser beam. They tried five different beam centering methods and found all of them to be lacking in accuracy and reproducibility. In conclusion, they suggest that some method of self-centering of the beam has to be developed that does not rely on visual testing by the operator.

Reports on monitoring laser process quality

Efforts to monitor the laser process quality are relatively recent. Very few reports exist on process monitoring, and fewer still on monitoring with the use of temperature. Only one report is known on correlating the cut-quality with the temperature measured by an infrared sensor. Hence, in this section, reports on monitoring process quality is first discussed in brief, followed by a discussion on reports on the monitoring

of cut-quality.

Li et al. [35] report a study on the application of artificial intelligence in controlling a laser cladding process. Without providing details, they mention that non-contact sensors are being developed to detect the clad thickness, level of dilution, surface roughness and bead profile, the extent of surface oxidation, and substrate temperature. The software development, however, has been discussed by them in great detail in this report.

Webber [63] reports one of the few studies of surface temperature measurement during a laser welding process. The experimental procedure consisted of first recording the temperature trace of an acceptable weld to establish the criterion for acceptability for other welds. Reduced power during a welding operation, the presence of a contamination in the weld, and a gap in the weld seam all produced temperature traces that were less than the acceptable limit, thus causing the welds to be rejected. The study, however, did not provide any details on the equipment or the experiment.

A similar study by Auric et al. [6] used two infrared cameras that were connected to a microcomputer that collected images at the rate of 6.25 Hz from an area 14 mm by 38 mm. The infrared cameras were used to measure temperatures on a metal sample that was being heat-treated by a laser beam. The authors report that the temperature measurements were accurate to within 20°C, but errors in measurement were present due to surface preparation. The authors report that the measurement system is to be used to monitor laser materials processing. No follow-up report on the use of the equipment to monitor process quality is known to exist.

Tal and Lenz [59] report the only known work on using the surface temperature

for monitoring the cut-quality. An infrared sensor was used to measure the temperature at the cutting front while performing the cutting operation. The experiments were carried out on samples of AISI 304 stainless steel that were 3 mm thick. Laser power was varied from 500 to 1200 W and the laser beam velocity was varied from 8 to 33 mm/s.

When cutting at constant power of 1200 W, Tal and Lenz found that the temperature decreased from 860°C at a velocity of 8 mm/s to a value of 770°C at a velocity of 24 mm/s. The kerf width also decreased from 0.6 to 0.2 mm. The surface temperature and the kerf width increased with increasing laser power when the cutting was performed at a constant velocity. As a result of their study, the authors recommend an adaptive control system that would vary the laser beam velocity and the power based on the requirement of a preset temperature output from the infrared sensor. The study is not clear on the type of gas or the pressure used in the experiments; since stainless steel was cut at power values of 500 to 1200 W, helium could have been the assist gas.

Analytical and Computational Research

Many attempts have been made to model the laser processing of materials. Both analytical and numerical models have been developed that have been quite successful in predicting the heat-treated depth, the width of the weld, or the width of the cut. A few of the important models are discussed in this section

An early analytical model was that of Gonsalves and Duley [25] that used the exact solution for the steady-state temperature distribution around a moving point

source on the surface of a thin sheet of metal. Their model did not consider the variation of properties with temperature or the effect of the enthalpy of fusion. To account for the fraction of the laser energy that is lost through the kerf produced in the metal, the authors developed a model to predict the fraction of energy incident on the metal. The success of this model is verified by the close agreement between the experimental and model results that were obtained. But the model was restricted to thin sheets of metals only.

A second analytical model was developed by Cline and Anthony [16] to predict the temperature distribution around a moving source of heat. The model was applicable to thin and thick metals, and the beam was assumed to be gaussian instead of a point source. The model also assumed constant thermal properties and negligible effect of the latent heat of melting. The model fared well when it was used to predict the melt profile in laser scanning of a sample of titanium alloys [46].

Mazumder and Steen [38] developed a three-dimensional finite difference model of the heating of the surface of a sample with a laser beam. Their model also predicted only the steady temperature distribution around the heat source. The heat source was modelled as a gaussian source and material properties were functions of temperature. The model also accounted for the latent heat of melting and heat loss by convection from the sample surface. When the model was used to predict the weld depth in welding titanium alloys, the results compared well with the experimental data [46].

A finite difference model was also developed by Rajaram and Coyle [48] to study the laser welding operation of thin sections at low laser power levels. They assumed a gaussian power moving on a three-dimensional body resulting in a steady temper-

ature distribution around the heat source. They included radiation and convection losses from the surface, but neglected the effect of the latent heat of melting. Their model predicted fusion zone width and depth in welding, which was compared with experimental data. The results of their model were in fairly good agreement with the experimental observation, with predicted depths smaller than observed values. They attribute the errors in their results to the fact that material properties are functions of temperature, and the uncertainty in the estimation of the surface absorptance of the material.

Models were also developed to study the laser heat-treatment process. Sandven [52] presents a model for the prediction of the case depth in laser surface transformation hardening. The model is based on closed-form solutions to the problem of three-dimensional heat flow in plates of finite and infinite thickness. The author also presents a simple approximation to the three-dimensional heat flow in a semi-infinite body. The model assumed constant thermal properties and the closed-form solutions obtained were then solved on the computer. The model was tested for four different steels. The model predicted case depths that were within 20% of the experimental values over the entire range of processing speeds.

Gnanamuthu and Shankar [23] present a more complete model for the estimation of case depth in laser heat-treatment process. A finite difference model was developed that solved the time dependent three-dimensional heat conduction equation. Their model, which could be used to predict case-depth in finite and infinite bodies, did not include the effect of latent heat of melting and the temperature dependence of thermal properties. The model was also capable of modelling the effects of laser beams with

arbitrary shapes and intensity profiles. The authors compared their model results with experimental data obtained in heat-treating iron-base alloys with the laser, and found good agreement. The advantage of this model over all of the previous models discussed so far, is that this model can be used to predict the effects on a finite work-piece where the edge effects could be important.

Modest and Abakians [40] developed an early model for the laser cutting operation. The cutting operation is assumed to occur by the evaporation of material at the surface. The thermal properties of the material are assumed constant and the latent heat of melting is neglected with the added assumption that the change of phase from solid to vapor occurs in one single step. Heat loss to the environment by convection and radiation are accounted in a single constant heat transfer coefficient. The resulting differential equation is solved by using a simple integral method. The resulting equations were then solved numerically for the temperature distribution, the groove depth, width and shape. The authors present their results for a wide variety of laser powers and material properties; no comparison with experimental data are presented.

Glass et al. [22] modelled the laser cutting operation by developing a finite difference model similar to the welding model developed by Mazumder and Steen [38]. The authors included the effect of the material removal by the cutting process by removing nodes from the solution domain once they had reached the melting temperature. The model did not apply to thick materials, as material removal was possible only if the entire thickness of the material was above the melt temperature. As in most models, the model did not consider the variation of thermal properties

with temperature and the effect of the latent heat of melting. In addition, the model is capable of predicting only the quasi-steady temperature distribution around the moving heat source. The model was tested with experimental data obtained in cutting thin sheets of glass. The model was able to predict the relative effects of the laser power and velocity on the cutting process fairly well but produced results of kerf width and heat-affected zone that did not agree very well with the experimental data.

Summary

In this section, the reports in the literature that pertain to the laser processing problem have been reviewed. Abundant work has been reported in experimentally determining the feasibility of performing laser-cutting operations on different types of materials. Several useful review articles have appeared that provide important information to the researcher in this field. Some attention has also been paid to improving the quality of the cut by various means. These reports are also experimental and empirical in nature and they are successful to some extent. Only one known attempt has been made to monitor the cutting process by measuring temperature with an infrared sensor. This study does not look at all the effects of the different variables and presents a simple solution to the problem. Their study was directed at obtaining a temperature trace for the desired quality of cut and either speeding up or slowing down the beam when the temperature sensed did not agree with the reference temperature. Their goal was to control the process in as simple a way as possible, and the method was quite successful.

In the area of modelling the laser cutting process, only two models are known

to exist. One is a unverified model that uses the simple integral method to solve the differential equation. The second model is a finite difference model that does not predict results that are in agreement with experimentally observed values. Several good models exist for the laser welding and heat-treating processes which have been verified with experimental data.

It can be concluded that there is a definite need for a closer and in-depth study of using temperature as a tool to not only monitor the cutting process, but also predict the cut-quality. In addition, there is no good verified model of the cutting process.

CHAPTER 4. EXPERIMENTAL EQUIPMENT AND PROCEDURES

All the experiments were conducted in the Laser Laboratory in the Mechanical Engineering Department. In this chapter, the details of the equipment used are presented, followed by a discussion of a few experimental procedures. The chapter concludes with a discussion of the experimental variables and their ranges that were used in this study.

Experimental Equipment

The equipment for the experiments consisted of a CO₂ laser and the data acquisition systems. The selection of the data acquisition system was very important to this study since rapidly changing temperatures close to the cut had to be measured. The details of the equipment are discussed below.

CO₂ laser system

The laser system consisted of the laser, which generated the laser beam, the beam delivery and focussing system, the programmable controller, and the work-table for the work-piece. Each of these parts of the laser system is discussed below.

Laser and beam delivery system The energy source for the experiments was a carbon dioxide gas laser that emitted radiation in the continuous mode. This was a Model 820 unit manufactured by Spectra-Physics Corporation, with a output power range of 200-2000 W. The power fluctuation for the unit was a maximum of $\pm 1\%$. The output of the laser is a gaussian beam that is 25.4 mm in diameter.

Figure 4.1 shows a photograph of the CO₂ laser system with the work-table and the controller. The beam emerging from the laser cavity passes out of the output window and the shutter mechanism, and is reflected by three folding mirrors. The beam leaving the laser cavity is linearly polarized and, as such, is suitable for cutting in one direction only. The second folding mirror, which is also a quarter-wave plate, converts this linearly polarized beam into a circularly polarized beam. This makes it possible to cut in all directions equally well.

The circularly polarized beam is then focussed by a 25.4 mm- diameter coated Zn-Se lens with a focal length of 127 mm. The focussed diameter of the beam is calculated to be 0.2 mm. The beam focussing assembly is shown in Figure 4.2. To protect the lens and also to assist in the laser process, an assist gas-jet is provided. The nozzle used in all the experiments was a standard nozzle with a 2.0 mm diameter hole and made of copper. A 2 mW helium-neon laser is used to align the mirrors and the nozzle so that the beam emerges through the nozzle hole without striking the sides of nozzle.

Programmable controller and work-table The opening and closing of the shutter, the delivery of the gas-jet, and the motion of the work-table upon which the work-piece is placed are all controlled by a programmable Allen-Bradley controller.

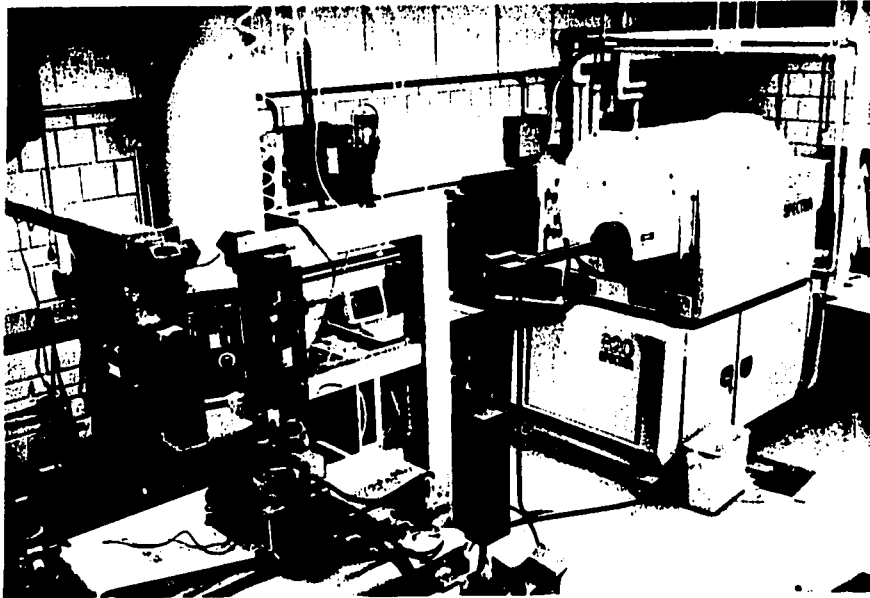


Figure 4.1: CO₂ laser system with power delivery and work table components

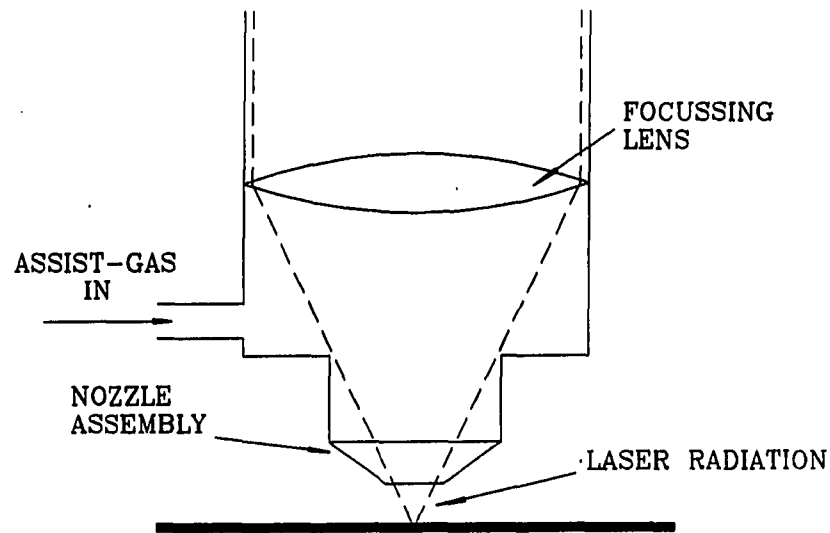


Figure 4.2: The nozzle and beam focussing system

The controller is operated in the manual mode for positioning the workpiece and focussing the laser beam on the sample. Normal execution of the laser-cutting process is carried out in the programmable mode of the controller. The sequence of operations in the program used to execute the cutting-process are shown in Figure 4.3. It is important to start the gas delivery before opening the shutter. Otherwise, the lens is likely to get damaged by the molten or vaporized particles produced by the beam striking the metal surface.

The work-piece is positioned on a table whose motion is controlled by the Allen-Bradley controller. The work-table had a travel of $0.6 \text{ m} \times 0.6 \text{ m} \times 0.15 \text{ m}$ along the x, y, and z axes and a maximum speed of 0.42 m/s (1000 inch/min) along the x and y axes. The table fixture is made of aluminum which can absorb the laser beam and dissipate the energy rapidly due to its high thermal diffusivity. This prevents the

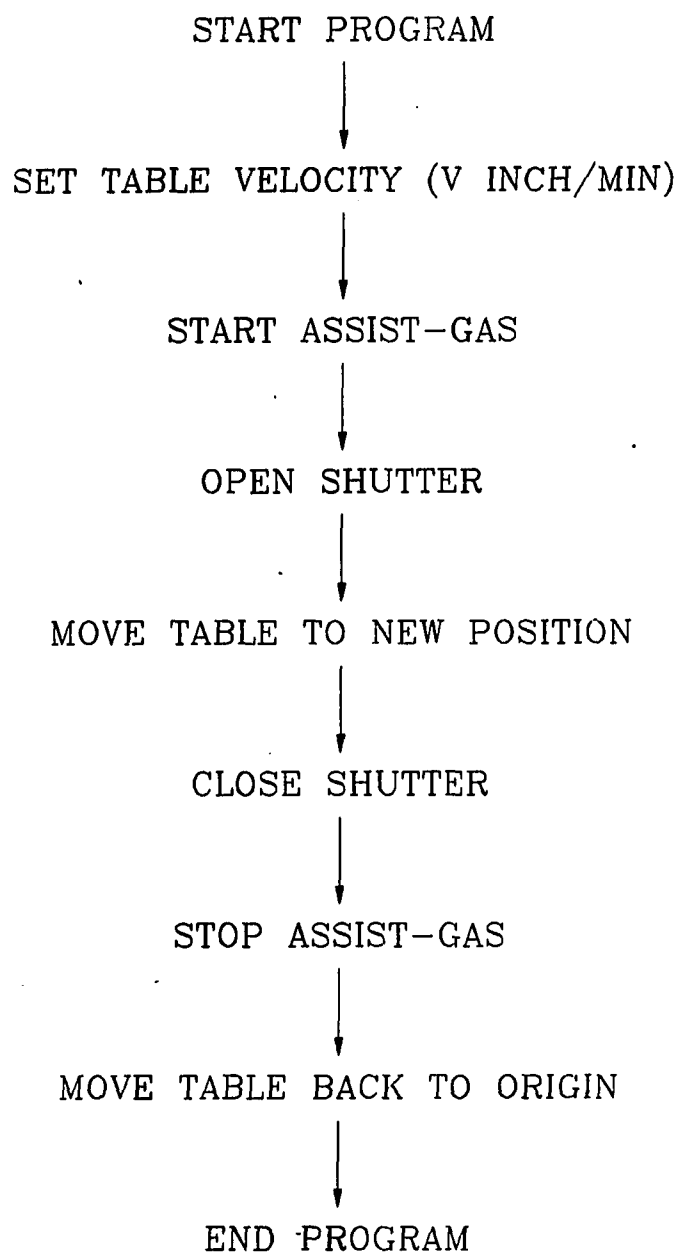


Figure 4.3: Programming sequence for laser process operation

table from damage due to laser radiation striking it.

Data acquisition system

To record the output of the temperature transducers and store the data in a file for later use, a computerized data acquisition system was used. Over the course of the experiments the data acquisition had to be updated four times, with each improvement leading to a system that was capable of collecting data at a faster rate.

Figure 4.4 shows the features of the system used in early experiments. The system consisted of a computer (DEC PRO 380) with a IEEE-488 card, an HP-3495A high-speed scanner capable of switching 1000 channels per second, and an HP-3456 digital voltmeter. A FORTRAN program was written to scan a sequence of channels, read the output, and place the data in a file. However, the DEC PRO 380 was capable of reading only 35 channels per second. This speed was reduced further as more channels were added to the scanning sequence. Temperature data could be collected only at locations where there were no rapid transients.

To be able to read at a faster rate, a Hewlett-Packard HP-85 computer was substituted for the DEC Pro 380. The HP-85 computer did not need a separate IEEE-488 card and was considerably faster at 175 readings per second. This permitted monitoring temperatures at locations closer to the line of cut than was previously possible.

Temperatures read more than 5 mm away from the line of cut did not accurately reflect the process at the line of cut due to the dissipation of heat in the metal. It was therefore necessary to read temperatures close to the line of cut, either with

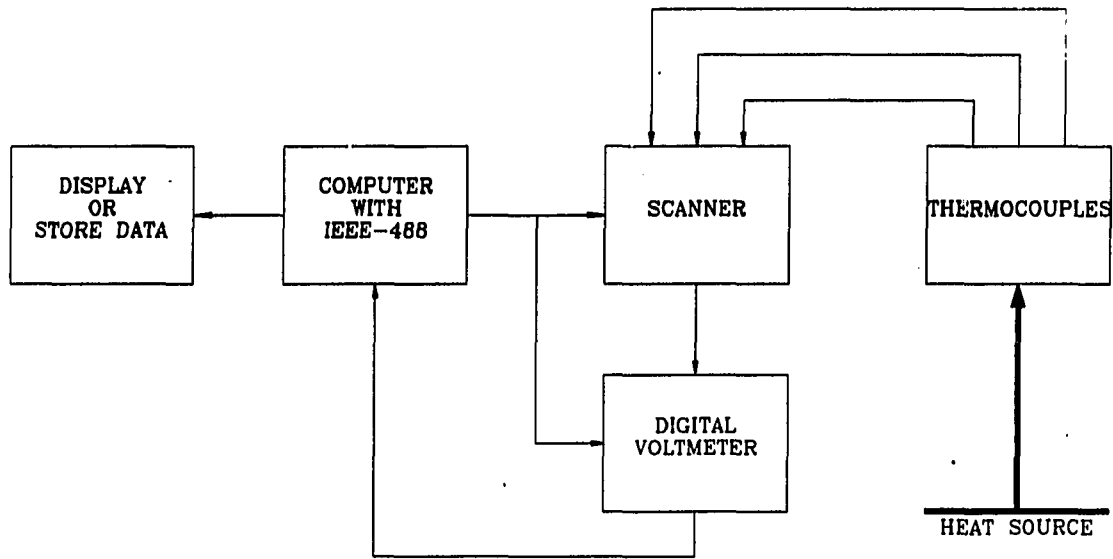


Figure 4.4: Computerized data acquisition with the IEEE 488 card

thermocouples or with the use of an infrared sensor. This necessitated data collection at rates beyond the capability of the systems that were available at that time in the Mechanical Engineering Department. Therefore, it was decided to use an IBM PC-XT with a plug-in type of D/A board. Figure 4.5 shows the resulting data acquisition system that uses Metrabyte Corporation's DAS-16 A/D card. This system could read data up to speeds of 35,000 readings per second on a single channel or up to 5000 readings/second on a scan of channels. The DAS-16 had eight double-ended channels for input. One of the channels was connected to a EXP-16 submultiplexer board which amplified the signal coming from the transducer. The EXP-16 also permitted 16 transducers to be connected at the same time, and it included a resistance temperature device that was used to read the temperature at the "cold" junction of the thermocouples for compensation to be included. The DAS-16 could either output

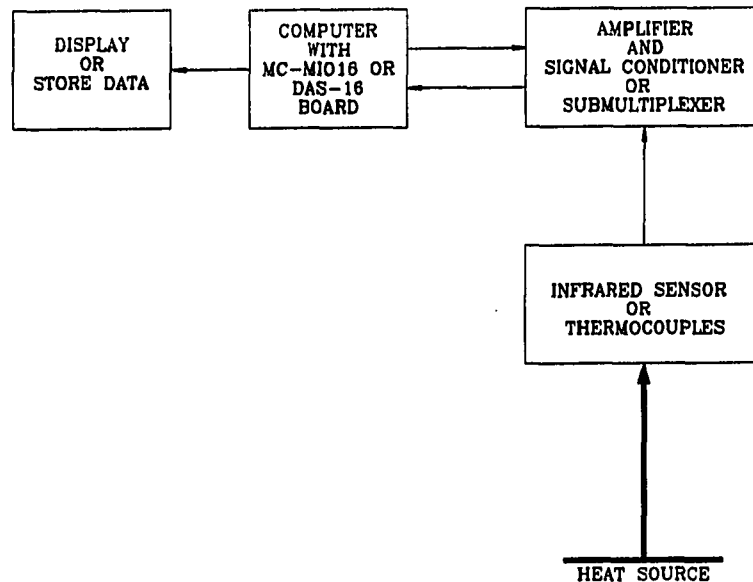


Figure 4.5: Computerized data acquisition with the A/D boards

the data to an array, or, in the direct memory access (DMA) mode, place the data directly into memory at a prespecified location. Direct access memory was the fastest mode since it did not involve the CPU of the computer directly.

This data acquisition was satisfactory for most experiments conducted during the study. However, the move to use the infrared sensor required data collection for a period of up to 6 seconds at speeds of 5000 readings/second or more. The IBM PC-XT had only a maximum of 64 kbytes of memory which limited the amount of data that could be collected. To overcome the above obstacles, a fourth and final data acquisition system was developed from an IBM PS/2 50-Z computer with a National Instruments' MC-MIO16 D/A board installed. This board was similar in operation to the DAS-16, but far superior in its capabilities. It could sample at rates of 50,000 readings/second, and also had the added capability of rotating DMA. In the rotating

DMA mode, the memory allocated was first split into two half buffers. The board output the collected data into the first half of the buffer by DMA transfer. As soon as the first half of the buffer was filled, the computer transferred the data to a file on the hard disk. With the filling up of the second half of the buffer, the board rotated back to the first half and continued filling the buffer. Hence, the board and the computer worked to fill and transfer a half-buffer at a time for as long as there was room on the hard disk or a stop signal was issued. This data acquisition system operated satisfactorily, and therefore it was used to collect all of the data with the infrared sensor.

Beam location methods To be able to track the temperature as a function of position on the material being cut, the data acquisition had to be started exactly when the beam struck the metal piece at the leading edge. Two methods were adopted to correlate a reference time in the data acquisition process and the beam location. These two methods are schematically shown in Figure 4.6.

The first of the two methods was used in performing experiments with the thermocouples. A thermocouple wire with the insulation removed was twisted together to create a thermocouple "junction" about 10 mm in length. This was then placed in the path of the laser beam at a specific distance from the edge of the workpiece. When the beam struck the wire, a sudden jump in the output of the thermocouple was registered. This provided the required information to locate the beam at a specific location during the data acquisition process.

The second method was used with the MC-MIO16 board which had the capability of stopping a continuous data collecting process with a 5 V signal applied to the

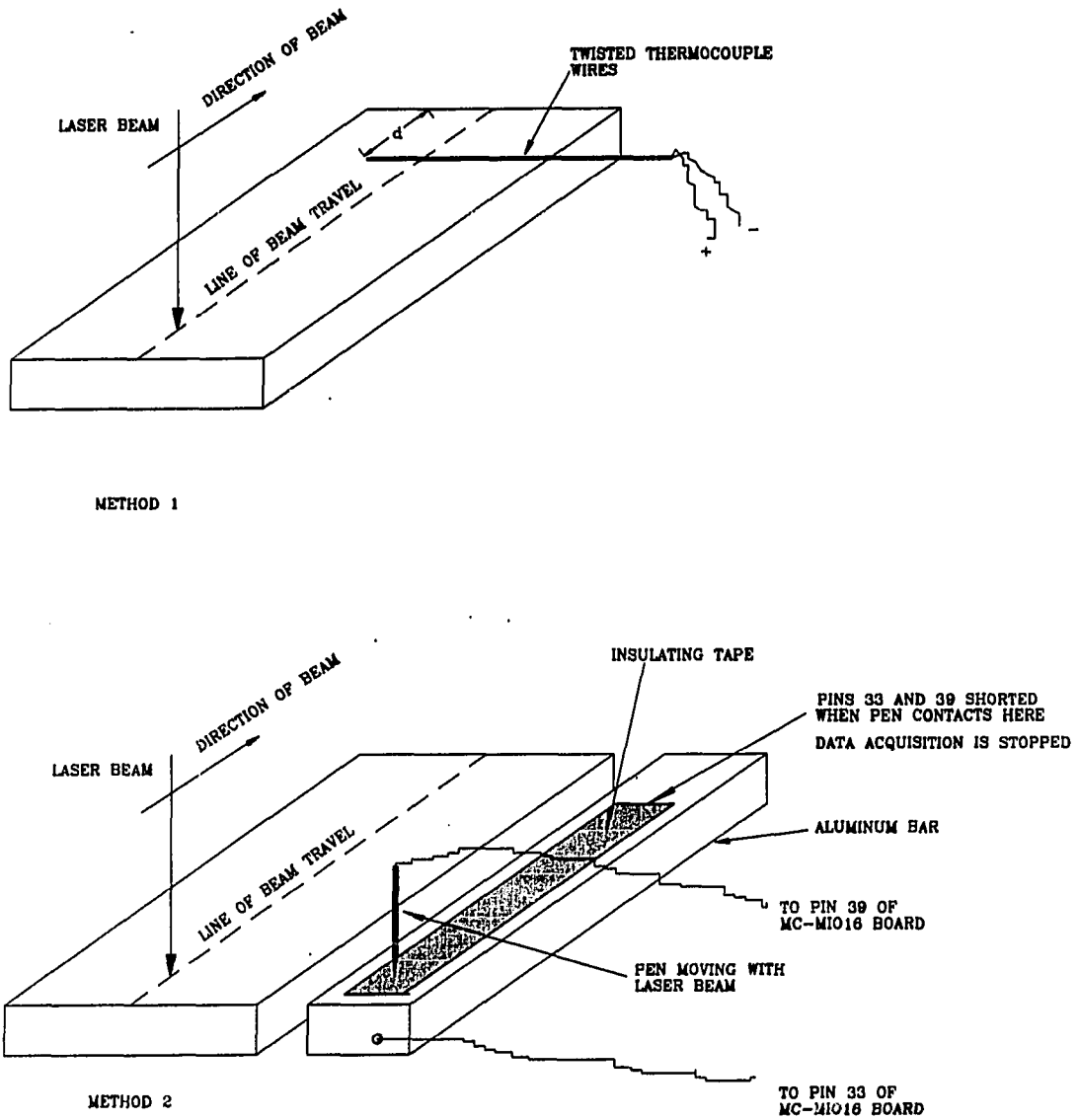


Figure 4.6: Two methods to obtain a reference for the location of the beam on the work piece

board. This was done by shorting pins 33 and 39 on the MC-MIO16 board as shown in Figure 4.6. Pin 33 of the board was connected to a flat bar of aluminum upon which was placed an insulating tape of a specific length. A sharp metal pen attached to a fixture rode on the tape as shown in the Figure 4.6. Pin 39 of the board was connected to this pen, with the result that when the pen reached the end of the tape and struck the metal bar, the 5 V signal was applied and the data acquisition was stopped. The length of the tape on the flat bar, the pen, and the work-piece were positioned such that the data acquisition was stopped when the beam was at a known position on the work-piece. Both the methods provided fairly accurate results, but the second was easier to implement and read.

Temperature transducers Two types of transducers were used to make temperature measurements. The first was the thermocouple and the second was an infrared sensor. The specifications of the two temperature measuring devices are now discussed.

Thermocouples were used to measure temperatures away from the line of cut. The thermocouple wire that was used was a 30 gage, type-K chromel-alumel wire. The wires were insulated with glass braiding which could withstand temperatures up to 500°C [43]. To protect the wires from stray electromagnetic radiation, they were braided and covered with a grounded conducting sheath. The output of the thermocouples was a voltage signal that was then converted to a temperature. The data conversion and analysis is discussed in Chapter 5.

The second type of transducer used was an infrared sensor manufactured by Vanzetti Systems Inc [62]. The infrared sensor consisted of a OH-15G lead sulfide

detector cell with a germanium filter. The detector cell was sensitive to radiation in the range 1.8μ to 3.0μ . This narrow range minimized the effects of fluorescent light and stray daylight, and completely eliminated any possible effects of the laser beam which had a wavelength of 10.2μ . The response time of the sensor was 1.0 millisecond, and it had an operating range of $175-1500^{\circ}\text{C}$, with an accuracy of 1% of the reading and repeatability of 0.5%. The 1 millisecond response time was made possible by the use of a 1000 Hz chopper assembly within the detector head. The radiation from the target area was focussed on the cell by a crown-glass lens assembly. This provided a target area of 0.38 mm at a distance of 76 mm.

Two lens tube assemblies were provided, one for the range of temperatures from $175-500^{\circ}\text{C}$ and another for the range $400-1500^{\circ}\text{C}$. To protect the lens tube assembly from particles of molten steel, a sheath was constructed which was then supplied with pressurized air which acted as an air-purge.

The output of the detector head was an alternating current at a frequency of 1000 Hz, which then was converted to a direct current voltage and amplified by a demodulating and amplifying board supplied by the manufacturer. The result was a nonlinear output from 0-10 V. A fiber-optic light source that connected to the detector head provided a means of locating the focal point of the detector head on the sample. A calibration source was provided by the manufacturer to calibrate the output of the detector head depending upon which of the two lens-tube assemblies was used.

Figure 4.7 shows a photograph of the detector head assembly consisting of the high temperature range lens-tube covered with the protective sheath, the fiber-optic

light source connecting to the back of the detector head, the calibration light source, the low-temperature range lens-tube, and the demodulating and amplifying board.

Installation of thermocouples The thermocouples had to be installed based on the criteria of quick response times and repeatability. The standard method of installing thermocouples is to first form a bead out of the two dissimilar materials of the thermocouple and then to attach the bead to the location at which the temperature is desired. The size of the bead and the environment properties then determine the response time and accuracy of the thermocouple [12]. However, since the laser cutting process involved rapidly changing temperatures, this method of installing thermocouples was found to be inadequate due to its slow response time. Instead, the thermocouples were installed in the intrinsic configuration which provided faster response times.

In the intrinsic type of thermocouple, the two wires of the thermocouple are spot welded onto the surface of the sample at the location where the temperature is desired. Figure 4.8 shows a typical case of thermocouples mounted on a test-piece. The intrinsic thermocouple has a faster response time than the beaded type, and the time necessary for an intrinsic thermocouple junction to reach 95% of the steady-state emf can be calculated from [30],

$$t_{0.95} = \frac{25D^2}{\pi\alpha} \left(\frac{k_T}{k} \right) \quad (4.1)$$

where, D is the diameter of the thermocouple wire in meters, α is the thermal diffusivity of the substrate in m^2/s , and k_T and k are the thermal conductivities of the thermocouple wire and the substrate, respectively, in $\text{W}/\text{m}\cdot\text{K}$.

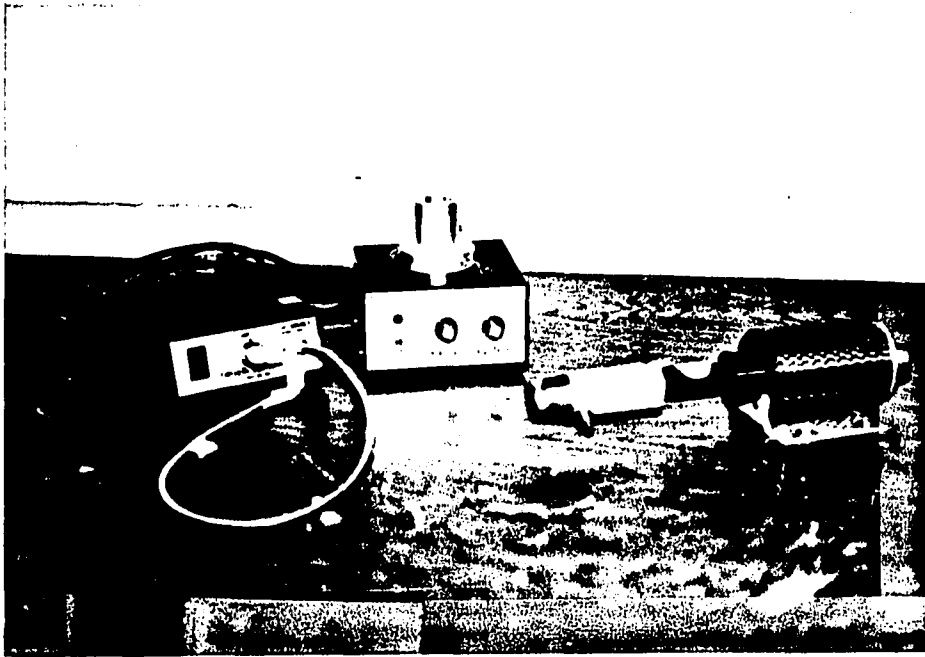


Figure 4.7: Photograph of the different components of the Vanzetti infrared sensor system

L - Length of sample
 W - Width of sample
 t - Thickness of sample
 a = 4.8 mm
 b = 3.2 mm

FIGURE NOT TO SCALE

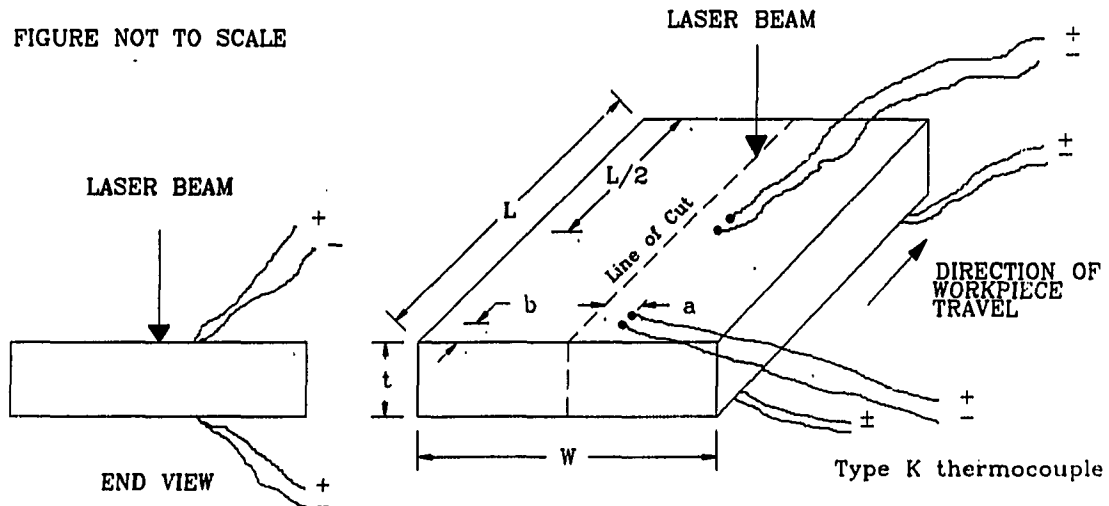


Figure 4.8: Test piece with thermocouples mounted in the intrinsic fashion

For example, based on the properties of the material used in the experiments (AISI 1018 steel), the response time of the 30-gage, type-K thermocouple is calculated to be 0.07 seconds.

In this study, the intrinsic thermocouple was formed by spot-welding a wire 0.2 mm in diameter onto a metal plate. Since there was no readily available method in the department to perform this type of operation, a capacitor discharge type of spot welder was designed and fabricated with the aid of the Research Equipment Assistance Program (REAP) at Iowa State University. A photograph of the capacitor discharge thermocouple welder is shown in Figure 4.9. The maximum voltage across the capacitors that produced a good weld was determined by method of trial-and-error. The usual procedure for welding a thermocouple involved connecting one plate of the capacitor to the test-piece and the second was brought into contact with the

thermocouple wire held close to the plate. The discharge between the thermocouple wire and the plate caused the end of the wire to melt and fuse to the plate.

Installation of infrared sensor The infrared sensor had to be mounted in a position fixed relative to the beam at a focal distance of 76 mm. For this purpose, a fixture was designed and fabricated out of aluminum. The fixture allowed the sensor to be moved up or down or tilted at any angle. The sensor could also be moved in and out to adjust the focal length. A sketch of the fixture is shown in Figure 4.10. The infrared sensor was typically inclined at an angle of 15° to the test-piece. This was done to obtain minimum interference of the sensor with the nozzle tip, and at the same time, to enable the sensor to record temperatures at the point of cutting.

Focussing the infrared sensor The infrared sensor averages the temperature over the region of the focal spot diameter. At 76 mm from the focussing lens in the lens-tube, which is the focal length of the lens, the spot diameter was 0.4 mm. However, due to the fact that the sensor was kept inclined at an angle to the plate, this spot diameter was considerably larger and was no longer a circle. Yet another factor that came into consideration was the clearance between the test-piece and the end of the lens-tube assembly. It was important to have a clearance of at least 2 mm, since during the cutting process, a tiny ball of molten metal can form on the top surface particularly when the cut was not executed properly. Therefore, if clearance was not provided, the lens-tube assembly could strike the solidifying metal ball and be pushed completely out of alignment. Taking all these factors into consideration,

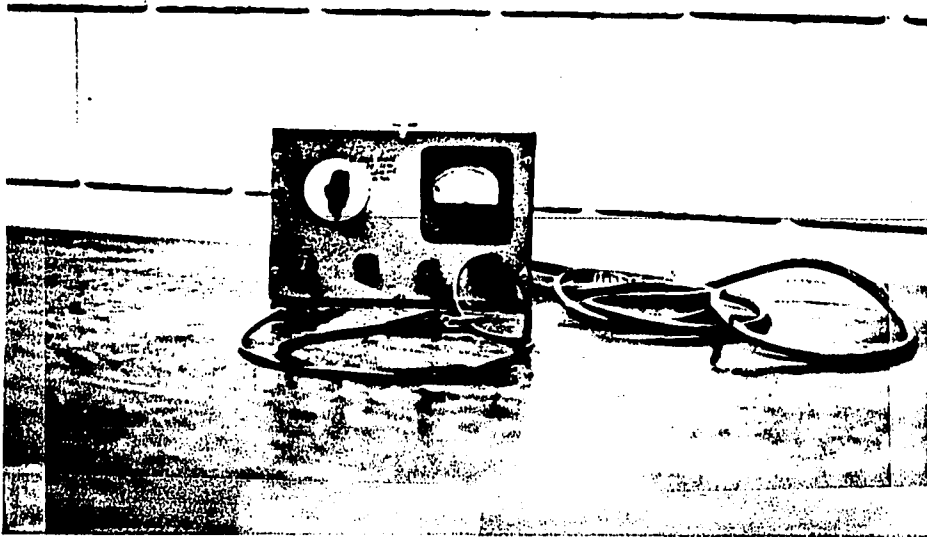


Figure 4.9: Photograph of the capacitor discharge type of thermocouple welder used to install intrinsic thermocouples

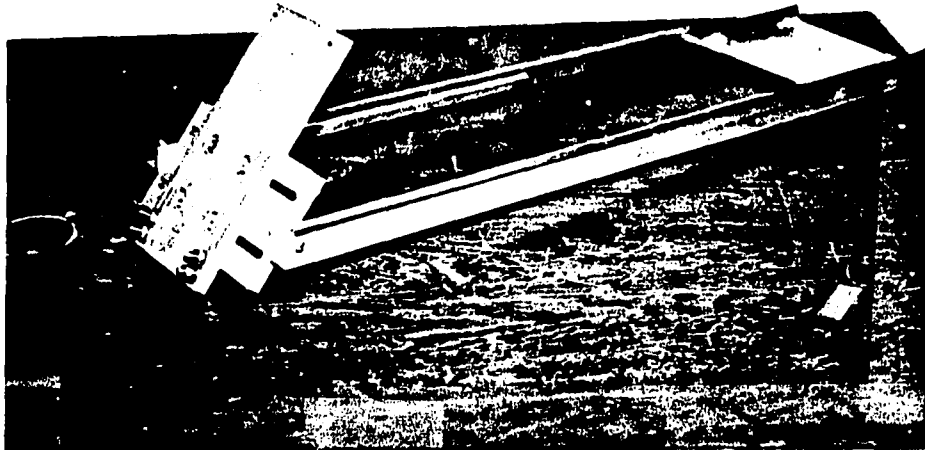


Figure 4.10: Aluminum fixture for mounting the infrared sensor

the final spot that was obtained was typically ellipse-shaped with a major diameter of 3 mm and a minor diameter of 1.5 mm.

Experiments were conducted with the temperature sensor mounted behind the beam. Two types of focal spots for the sensor were used in this study and are shown in Figure 4.11. The first focal spot was the standard ellipse-shaped spot, with the point of cutting (i.e., the point at which the laser beam strikes the surface) at the center of the sensor's focal spot. However, part of the nozzle fell within the field of view of the sensor because of the relative positions of the sensor, the test-piece, and the nozzle. Since the nozzle is usually at room temperature, the nozzle surface did not contribute to the radiation reaching the detector cell. But, the nozzle prevents the region of the test-piece ahead of the beam from radiating to the sensor. The result is that the detector cell "sees" only the part of the test-piece where the beam

strikes the metal and the region behind it.

The second focal spot for the sensor was in the form of a thin line 1.6 mm (1/16") in length and 0.8 mm (1/32") wide. The slit was obtained by placing a tape over the pin-hole in the lens-tube that permitted radiation to pass to the detector cell. The infrared sensor was not calibrated for this configuration.

Aligning the sensor spot and the laser beam There are two methods that were used to align the focal spot relative to the laser beam. One method consisted of first using the helium-neon beam for locating the point where the laser beam would strike the metal. The fiber-optic back-lighting source was then used for the sensor, to align the sensor's spot directly on or behind the laser beam, as required.

The second method consisted of first using the CO₂ laser beam in the pulse mode to mark the point on the metal where the beam strikes it. A short pulse of 0.3 second duration vaporizes a small amount of metal and creates a hole in the metal surface which is slightly larger in diameter than the beam diameter. The back-lighting source is then used with the sensor to align the center of the sensor light spot directly on the mark on the metal. Of the two methods used, the second method was found to be more accurate, and repeatable.

Measurement of HAZ

The oxidation HAZ is characterized by a dark black region, followed by a lighter brown region. In this research, the oxidation HAZ was measured as the width of the darker black region immediately adjacent to the cut-edge. This discoloration was measured with a tool-makers' microscope that had a resolution of 0.00254 mm

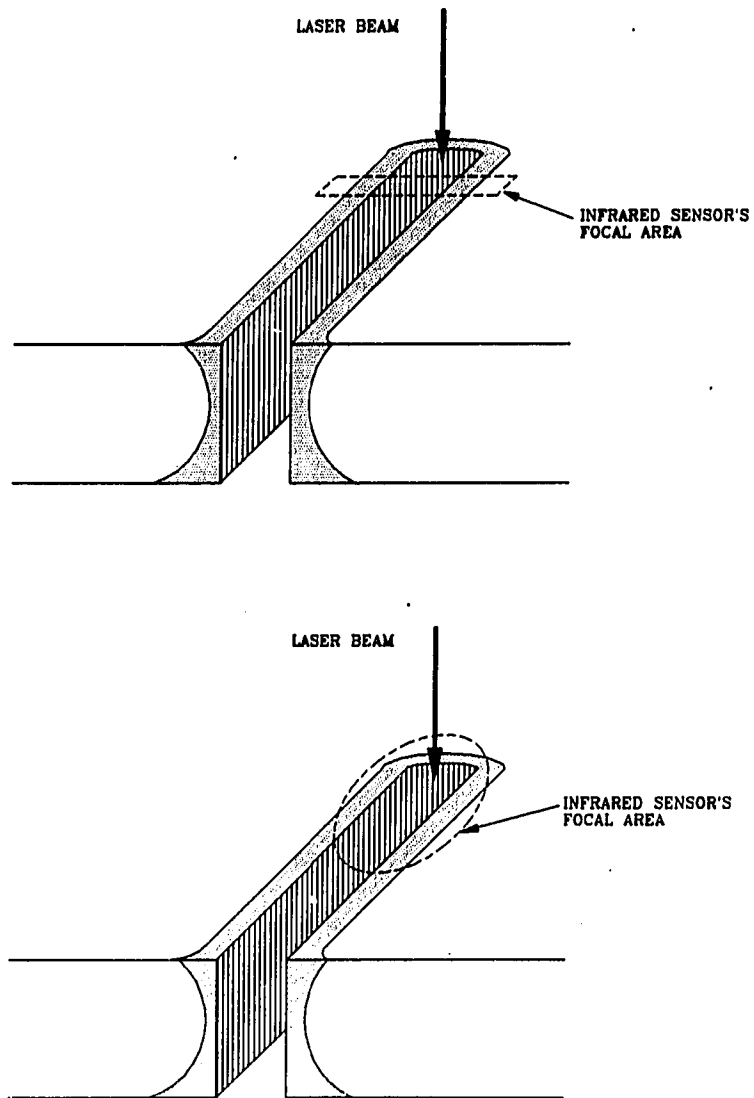


Figure 4.11: Focussed spot location and size for the infrared sensor relative to laser beam

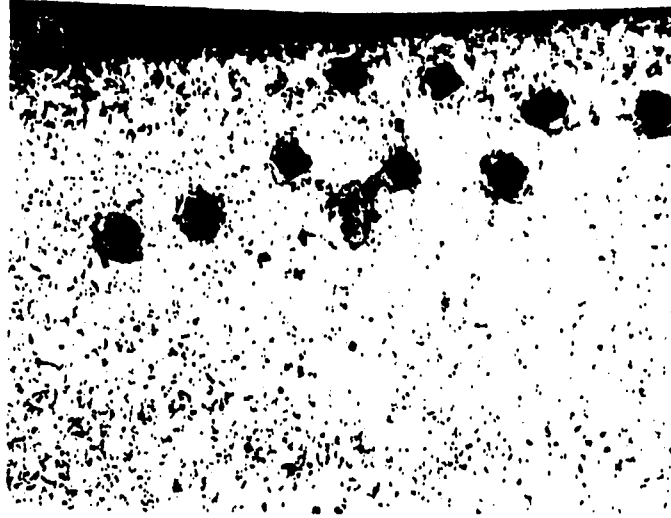


Figure 4.12: Photograph of the heat treated region adjacent to the cut with hardness test indentations

(1/10,000") and the measurements were made to an accuracy of ± 0.03 mm.

To perform the hardness measurements, rectangular pieces, approximately 1 cm long and 1 cm wide, taken from the cut edge of the test-pieces. These small samples were then mounted in Bakelite. The samples were then polished, and etched with a 10% solution of Nital which made visible the microstructure of the heat affected zone.

Hardness measurements were made with a Tukon DPH microhardness tester. The diamond-shaped indentations were made beginning as close to the cut edge as possible, and moving gradually perpendicular to the cut edge, as seen in Figure 4.12. Successive data points were approximately 0.0254 mm (0.001") apart, and continued well into the material beyond the visible microstructure of the heat-affected zone.

The average diagonal of each diamond indentation was measured, and the Dia-

mond Point Hardness number was calculated from,

$$DPH = \frac{2L \sin(68)}{d^2} \quad (4.2)$$

where, d is the average value of the indentation diagonal and L is the load applied in kilograms. The hardness profile was then obtained by measuring the distance between successive indentation marks.

Experimental Variables

The laser-cutting process is governed by several variables which were described in detail in Chapter 2. Some of these variables are the material being cut (size and thermal properties), the laser power output, beam velocity, the assist-gas type and pressure, and the characteristics of the beam and the focussing optics. Only a few of these were varied for this study, and the range of values of these variables are presented below.

Test-piece: The material selected for the cutting experiments was AISI-SAE 1018 steel, which is commonly available in the form of cold-rolled flat plates. The thickness of the plates used in the majority of the experiments was 3.2 mm (1/8 inch), while a few experiments were performed with thicknesses of 4.8 mm and 6.4 mm. The test-pieces were all uniformly cut into squares of 101.6×101.6 mm (4×4 inch). The surfaces were all ground to the same finish so that absorptivity of the surface to laser radiation would be uniform for all the samples.

Laser beam power: The CO₂ laser used in the experiments was rated for a laser power of 200 to 2000 W of continuous output. Because of the numerous variables that affect the laser-cutting process, it was difficult to choose a range of power values

from the published literature. Therefore, by a procedure of trial-and-error, a range of laser power values that could produce a reasonable cut was chosen. In spite of this approach, there were occasions when the cut was not properly executed. For all the experiments performed, the laser beam power was varied from 800 to 1200 W in steps of 100 W.

Laser beam velocity: The laser beam itself was fixed and could not be moved, but the table upon which the test-piece was placed could be translated along three axes. Moving the table at a fixed velocity had the same effect as keeping the test-piece fixed and moving the laser beam. Hence, in the discussions presented here, the table velocity is always referred to as the laser beam velocity.

The motion of the table was controlled by a programmable controller. The usual procedure was to program the table to move at a velocity of 42.33 mm/s (100 inch/min), and obtain different velocities by manually setting a velocity controller for different values from 0 to 200% of the program setting. By this method, the velocities used in the experiments ranged from 16.9 to 50.8 mm/s in step increments of 8.5 mm/s.

Focal length of lens: The focal length of the lens used determines the focal spot diameter. Since a smaller focal diameter gives a larger flux, it is desirable to choose a lens of small focal length for the cutting operation. All of the experiments were performed with a 25.4 mm-diameter, ZnSe lens with a focal distance of 127 mm. This resulted in a focal spot diameter of 0.2 mm.

TEM of the laser: The transverse electromagnetic mode (TEM) of the laser determines the ability of the laser to perform different operations. For the cutting

operation, the TEM₀₀ is the preferred mode, and this was used for all of the experiments.

Oxygen gas pressure: Oxygen gas was used as the assist gas to perform the cutting operation. The nozzle that was used in the experiments was a standard nozzle and is described in detail in Chapter 4. The oxygen supply could be turned on or off by the controlling program. The gage pressure of the gas was measured at the exit of the cylinder, and it was varied from 0.07 MPa to 0.2 MPa in increments of 0.035 MPa.

Summary

The preceding sections detailed and discussed the equipment used in the experiments including the laser and the data acquisition system, a few experimental procedures, and the values of the variables used in the study. A few comments about the precautions taken in using and performing these systems are made below.

While using the laser, care was exercised and all the necessary safety steps were taken. The CO₂ laser beam has a wavelength of 10.6 μ , which is outside the visible spectrum of radiation. However, when the beam strikes the metal, intense visible light is produced which can be harmful to the eye. Therefore, protective eyeglasses were worn while performing the experiments.

The laser, infrared sensor, and the data acquisition system required a minimum of one-half hour of operation to warm-up and reach normal operating conditions. In particular, the laser's output will stabilize only after at least one-half hour of operation. The infrared sensor also needs to be operating for a minimum of 15 minutes before its output reaches its rated values.

CHAPTER 5. MEASUREMENTS AND UNCERTAINTIES

Two types of data were important to this study; one was the measurement of surface temperature, and the other was the measurement of process quality. In this chapter, the data collected and the subsequent analysis performed to present the data in a suitable form are discussed. Also discussed are the errors associated with each type of measurement.

Temperature Measurement

As discussed in Chapter 4, surface temperatures were measured with thermocouples and an infrared sensor. In both cases, the transducer converts the analog input (temperature, in the case of the thermocouple, and, thermal radiation for the infrared sensor) to a voltage. In the following sections, the process of recording and interpreting the temperature data are presented.

Conversion from analog to digital output: The two data acquisition boards, the DAS-16 and the MC-MIO16 boards, were capable of accepting inputs in the following ranges: 0 to ± 10 V or -5 to $+5$ V. The two boards had a 12-bit A/D converter, which converted the input range to a digital output that ranged from either 0 to 4096 bits

or -2048 to +2047 bits. The smallest analog signal that could be resolved is given by,

$$Q = \frac{\text{Full scale range}}{\text{Total bits}} \quad (5.1)$$

For example, in the case of the infrared sensor, the MC-MIO16 board was configured to accept inputs in the range of 0 to 10 V, with the result that the minimum input voltage that could be resolved was,

$$\frac{10V}{4096 \text{ bits}} = 0.002441406 \text{ V/bit} \quad (5.2)$$

Usually the signal coming from the transducer is amplified before input to the A/D converter. The minimum input voltage that can be resolved is now obtained by dividing Equation 5.2 by the amplification introduced.

Smoothing of data: The data read by the data acquisition system will usually have some amount of "noise" present in it. This is due to the stray electromagnetic radiation that the lead wires pick up [15], in spite of efforts to eliminate or minimize this effect. In a standard digital voltmeter, filters are provided which eliminate this type of noise. Also, digital voltmeters tend to average the input signal over a period of time, thus smoothing out any noise present in the output. Data acquisition boards, of the type used in this study, do not have filters, nor can they "average" the reading over any period of time. This is the reason why the A/D converter boards are faster than the traditional digital voltmeters. However, the noise present in the output is undesirable and has to be removed by some means.

Standard practice to accomplish this is to include some type of hardware filtering mechanism or to perform the filtering process through software. The second of the two methods was used in this study to eliminate noise when necessary. This was done by

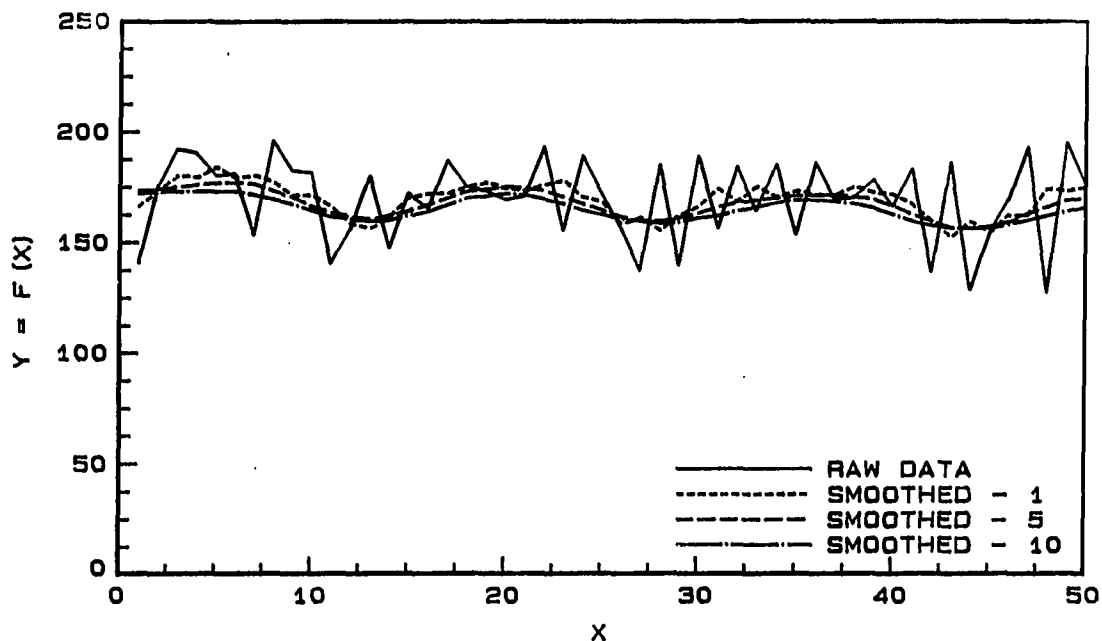


Figure 5.1: Example of the use of the Savitzky Golay smoothing technique

post-processing the digital output data and performing a smoothing operation. The smoothing technique used was one known as the Savitzky-Golay technique [21] which was both simple to use and effective. In this technique, four data points on either side of a data point appropriately weighted, are used to obtain a smoothed value for the data point. Depending upon the degree of smoothness required, the operation can be performed several times. Figure 5.1 shows an example of raw data with noise present in it, smoothed to different levels using the Savitzky-Golay technique. The digital output is then converted to a voltage signal.

Conversion to temperature: The data read by the A/D converter in the form of bits is first converted to a voltage as explained in the previous sections. This voltage has to then be converted to a temperature based on the calibration data for the device.

The conversion from a voltage to a temperature for a standard type-K thermocouple can be obtained from the manufacturer's catalog [43]. The equation provided by the manufacturer is usually in the form of a polynomial and has a standard conversion (curve-fit) error when compared to the National Bureau of Standards Thermocouple Tables [60]. In the case of the type-K thermocouple that was used, the conversion error in the polynomial provided by the manufacturer was found to have an error of $\pm 0.7^{\circ}\text{C}$. Since this error was found to be unacceptable for some experiments, an alternative method of conversion was found which considerably reduced the conversion errors. The alternative equation was a power series curve fit for the NBS tables that included exponential terms which provided voltage as a function of temperature [36]. The temperature was found from this equation by a process of iteration since this equation did not provide the temperature as an explicit function of the voltage. The error in temperature values obtained by this method and the conventional method of using the manufacturer's curve-fit are shown in Figure 5.2. It is seen that the iteration method is far more accurate than the standard method.

The conversion from voltage to a temperature for the infrared sensor was based on the calibration curve supplied by the manufacturer. Two calibration curves were provided, one for the range $175^{\circ}\text{-}500^{\circ}\text{C}$, and the other for the range $400^{\circ}\text{-}1500^{\circ}\text{C}$. The two calibration curves are shown in Figure 5.3 and Figure 5.4 respectively. In this study, since the absolute values of the temperature were not important as only relative differences in temperature were significant, the sensor was not calibrated for the cutting application, nor was it possible to perform such a calibration.

Calibration of transducers: Calibration of the thermocouples and the infrared

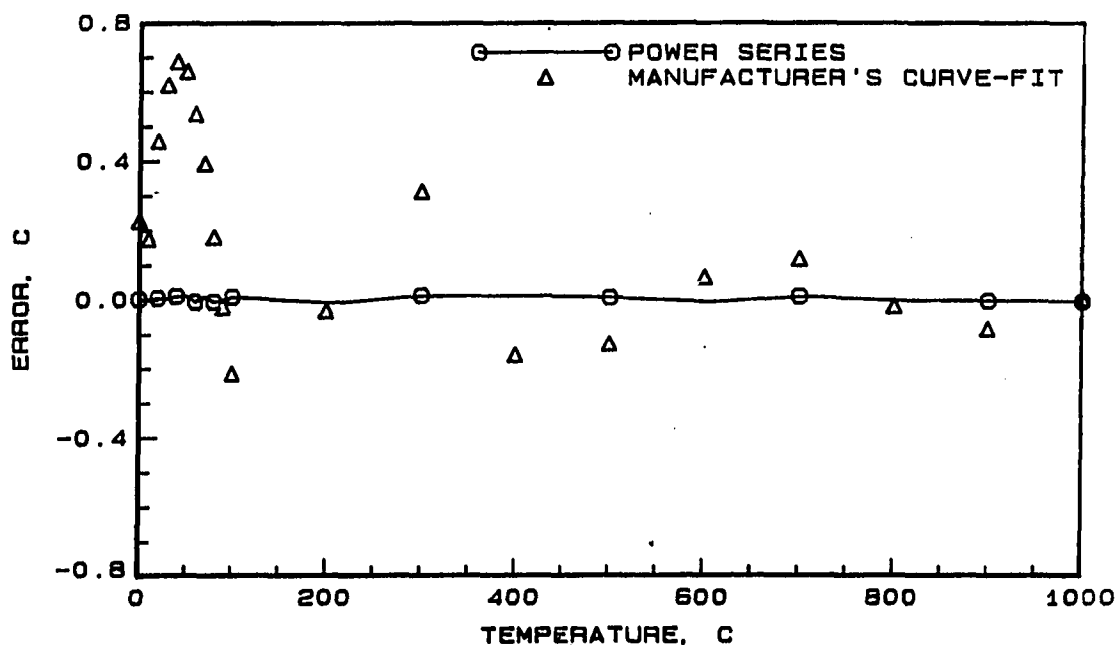


Figure 5.2: Comparison of the manufacturer's curve-fit equation and the iteration method used, to the NBS table values

sensor was done to minimize the errors in the output. Before calibrating the transducers, the DAS-16 and the EXP-16, or the MC-MIO16 boards had to be calibrated. The calibration procedures are usually well documented by the board manufacturers. A precision voltage source was used to apply all voltage signals required in the calibration procedure. Care was taken to ensure that the voltage source was connected in the same manner in which the transducers would be later connected. Once the boards were calibrated, then the thermocouples and the infrared sensor were calibrated.

To calibrate the thermocouples, a constant temperature water bath was used along with a set of precision thermometers. It was not possible to calibrate the thermocouples beyond 100°C since no accepted standards were available at Iowa State University. Figure 5.5 shows a typical calibration curve for the type-K thermocouple

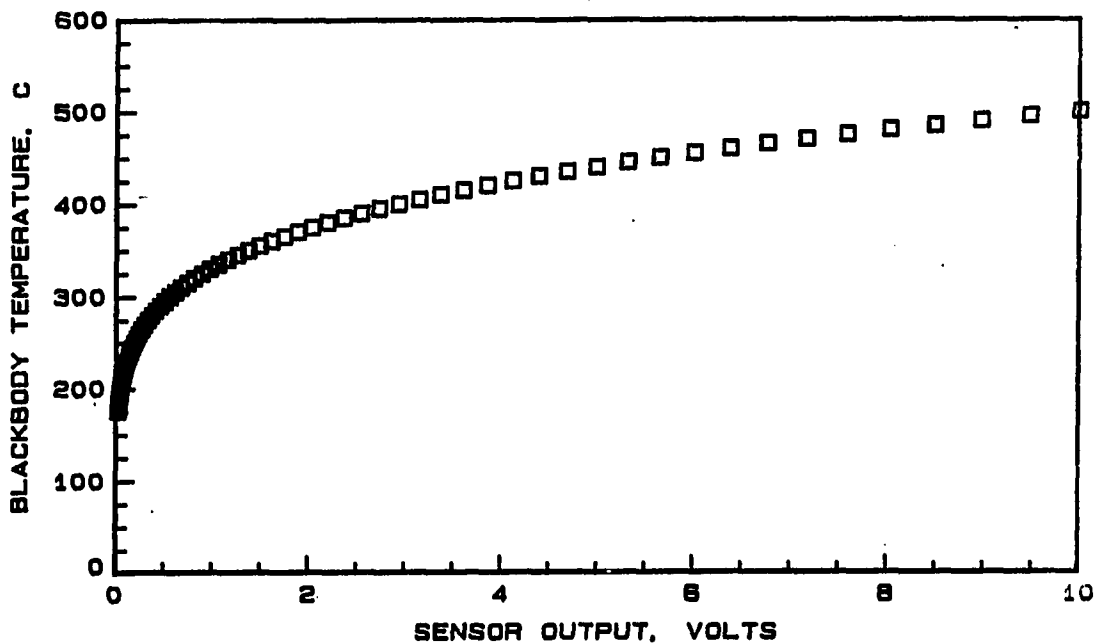


Figure 5.3: Manufacturer's calibration curve for the infrared sensor in the low temperature range

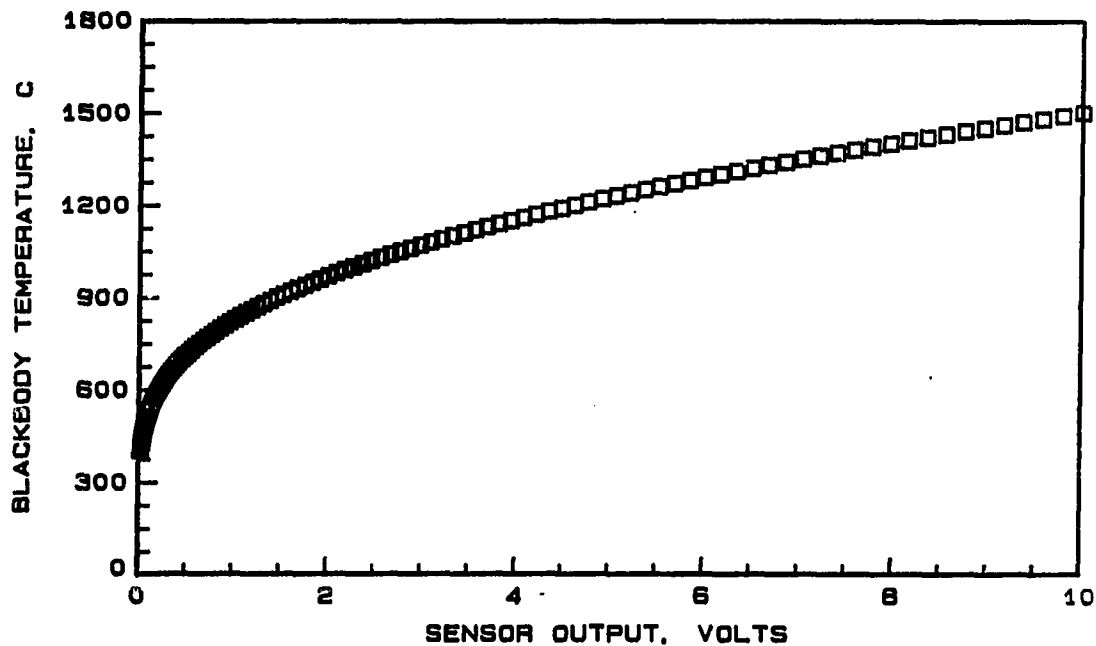


Figure 5.4: Manufacturer's calibration curve for the infrared sensor in the high temperature range

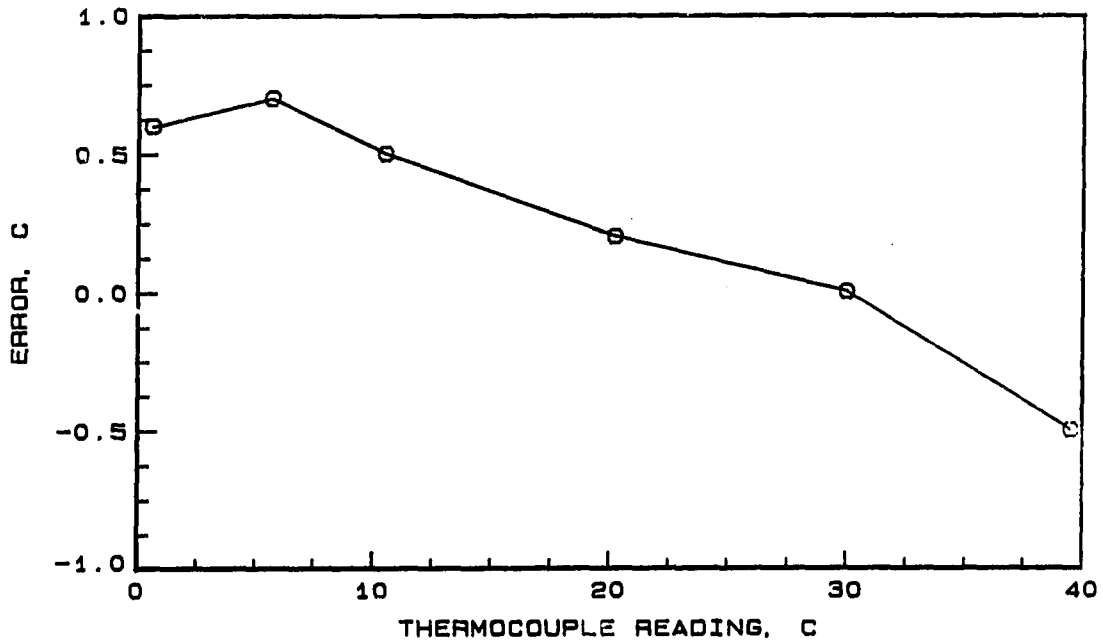


Figure 5.5: Calibration curve for the type-K thermocouple wire

upto 40°C . It is seen that the error was only a maximum of 0.4°C .

Calibration of the infrared sensor was considerably more involved. The manufacturer supplied the black body calibration curves which were seen earlier in Figure 5.3 and Figure 5.4. Ideally, the infrared sensor had to be calibrated for the surface on which it was to be used. The infrared sensor was typically used over the cutting region where the kerf and the oxidation HAZ greatly affected the surface conditions. Since this distortion of surface properties could not be predicted, the infrared sensor could not be calibrated for the actual use.

During the cutting process, if the infrared sensor is located behind the laser beam, the sensor receives thermal radiation from a surface that is mostly oxidized. Such an oxidized surface has an emissivity close to one. Therefore, the infrared sensor was calibrated for a flat piece of AISI 1018 steel that was coated with a commercially

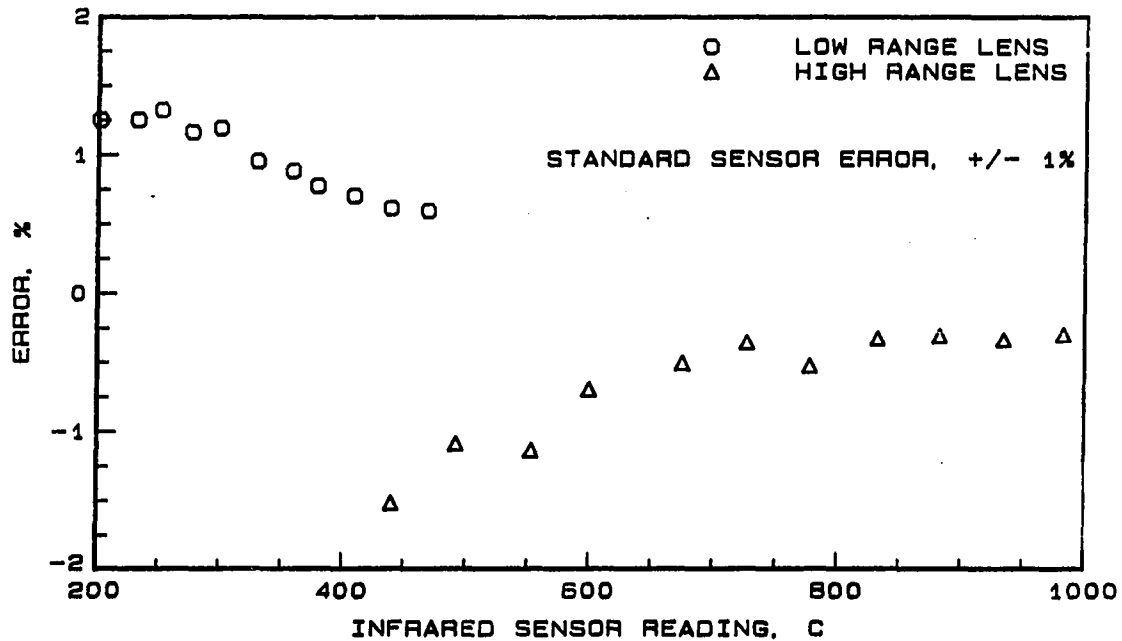


Figure 5.6: Results of the calibration procedure for the infrared sensor

available black paint. The sample was placed inside a large industrial-type furnace with three thermocouples mounted on its surface. The infrared sensor was placed in front of the furnace and a shutter on the furnace door could be operated to enable the sensor to read the surface temperature of the sample. The three thermocouples were constantly monitored to ensure temporal and spatial uniformity of temperatures. Figure 5.6 shows the results of this calibration process, where the error in the sensor output is plotted against the temperature as read by the type-K thermocouples. It can be seen that the percentage error was usually less than 1% which is the standard error in the infrared sensor's output as specified by the manufacturer [61]. It should be noted that the thermocouples were not calibrated which also results in a certain amount of uncertainty in the thermocouple output. These errors are discussed in the section that follows.

Uncertainties in temperature measurement: Temperature measurement errors are associated with the transducer and the data acquisition system. The important errors are:

- Standard transducer error
- A/D conversion error
- Voltage to temperature conversion error

Besides these errors, there are other errors such as the reference junction error for the thermocouple and errors caused by the continuous heating of the circuitry in the A/D conversion. These errors are not as significant as the ones that have been itemized, and therefore are not included.

The standard transducer error for the thermocouples is the error associated with the deviation between the actual thermocouple output voltage and the voltage predicted by the tables in NBS Monograph 125 [43]. This error arises due to impurities and inhomogeneity in the thermocouple material produced by the manufacturing process. This can be eliminated by performing a calibration on the wire. However, calibration was possible only up to 100°C. The standard wire error was therefore assumed to be $\pm 1.1^\circ\text{C}$ or 0.4% of the reading, whichever is higher. The infrared sensor had a manufacturer-specified standard uncertainty in the output of $\pm 1\%$ of the reading.

A/D conversion errors are the errors associated with accuracy of the A/D conversion system. For a constant analog input to the A/D board, the digital output is never a constant, but rather fluctuates by ± 1 bit. Depending upon the input voltage

range selected and the amplification introduced in the circuit, this error is,

$$\pm 1bit = \pm \frac{\text{Input voltage range}}{(\text{Gain})(4096 \text{ or } 2048bits)} \quad (5.3)$$

The error in the voltage read can then be converted to a temperature. For the type-K thermocouples, this error was about $12 \mu\text{V}$, which when divided by the sensitivity of the type-K material, $40 \mu\text{V per } ^\circ\text{C}$, gives an error estimate of $\pm 0.3^\circ\text{C}$. The A/D conversion uncertainty for the infrared sensor was $\pm 0.0025 \text{ V}$. For the low-range lens, this translated to errors between $\pm 3^\circ\text{C}$ at 175°C and $\pm 0.02^\circ\text{C}$ at 500°C . The error for the high-range lens was between $\pm 6^\circ\text{C}$ at 400°C and $\pm 0.1^\circ\text{C}$ at 1500°C . It should be pointed out that the infrared sensor was calibrated only for a black-body. The values of the temperature as presented in the results of this research are, therefore, not absolute temperatures. The differences in the temperatures, however, reflect the differences in the cutting process such as the heat input and the cut quality.

Process Quality Measurement

Process quality as defined by the kerf width and the heat affected zone were measured with a tool-makers' microscope. The oxidation HAZ was characterized by a dark region adjacent to the cut followed by a lighter brown region. The HAZ was taken to be the dark region only, since the lighter region could be easily be rubbed away with the hand. The tool-makers' microscope had a resolution of 0.003 mm and all measurements were made to an estimated accuracy of $\pm 0.015 \text{ mm}$.

The error in the measurement of hardness was estimated by the propagation of error method [12]. The equation that is used for the calculation of hardness is Equation 4.2. Assuming no uncertainty in the value of the load, L , and the angle of

the diamond point. the uncertainty in the hardness arises only due to the uncertainty in the measurement of the diagonal, d . The uncertainty in the hardness number is given by,

$$\frac{u_{DPH}}{DPH} = \frac{2u_d}{d} \quad (5.4)$$

Based on repeated measurements, the uncertainty in the measurement of the diagonal, u_d , was found to be equal to ± 0.003 mm. Equation 5.4 can now be written as,

$$\frac{u_{hardness}}{HardnessNumber} = \frac{0.006}{d} \quad (5.5)$$

The maximum uncertainty in the hardness number was calculated to be less than $\pm 5\%$.

Summary

The uncertainties and errors associated with the measurement of temperature and process quality were discussed in this chapter. In connection with temperature measurement, the collection and smoothing of data, the errors associated with conversion from analog to digital signals, the errors in the voltage to temperature conversion, and the calibration of the thermocouple wire and the infrared sensor were detailed. In addition, the errors associated with the measurement of oxidation and heat-treated heat affected zone and kerf width, were also presented.

CHAPTER 6. RESULTS FOR KERF WIDTH

The quality of the laser cut is measured by several factors, which were discussed earlier in Chapter 2, and one of the most important measures is the kerf width. The kerf width represents the amount of material removed by the cutting process. Since this is wasted material, it is desirable to keep the kerf width to a minimum. It is, therefore, important to choose the right combination of the process variables that would produce a uniform and narrow kerf.

In this chapter, the variation of kerf width between the upper and lower surfaces, and at different positions along the cut, are discussed. This discussion is then followed by a presentation of the experimental results which show the effect of process variables upon the kerf width and the surface temperature. These process variables are, the laser beam velocity, oxygen gas pressure, and the laser power.

Kerf Width Variation with Position

The kerf width varied depending upon whether it was at the leading edge, the center, or the trailing edge of the cut. The variation was also different for the top and bottom surfaces. These results are presented and compared with data from the literature whenever possible. In particular, at the leading edges and trailing edges of the cut, no data were found to exist in the literature; hence, no comparison with past

work in the literature is made for these cases.

Figure 6.1 shows the kerf width on the upper surface at different positions along the cut for several sets of experimental conditions. The kerf width is seen to be fairly constant, increasing only slightly along the bulk of the cut. Close to the leading and trailing edges, however, the kerf width is different from the value for the major portion of the cut. At the start of the cut, the kerf is narrow, usually about 80% of the value at the center of the sample. The kerf width increases very rapidly to the value at the center of the cut. This rapid increase in the kerf takes place within about 5 mm from the start of the cut. Close to the trailing edge of the cut, the kerf shows a rapidly increasing trend over the final 5 mm of the cut. The kerf at the trailing edge was usually about twice that at the center of the sample. These effects were more obvious at the lower laser beam velocities.

Kerf width variation with beam velocity, as described above, has not been documented elsewhere in the literature. A possible reason for this variation is that the experiments were performed on samples of steel that were square, measuring 102 mm by 102 mm. The finite dimensions of the sample could have resulted in the edges of the sample acting as adiabatic boundaries. The presence of the adiabatic boundaries would result in a greater temperature rise which in turn leads to a larger kerf width. The fact that the sample is continuously being heated could also have resulted in less heat being dissipated away from the cutting region which, in turn, could have led to the increase in kerf width with position.

In the remainder of this section, the kerf width at the center of the sample on the upper surface is compared with the kerf at different positions to establish a

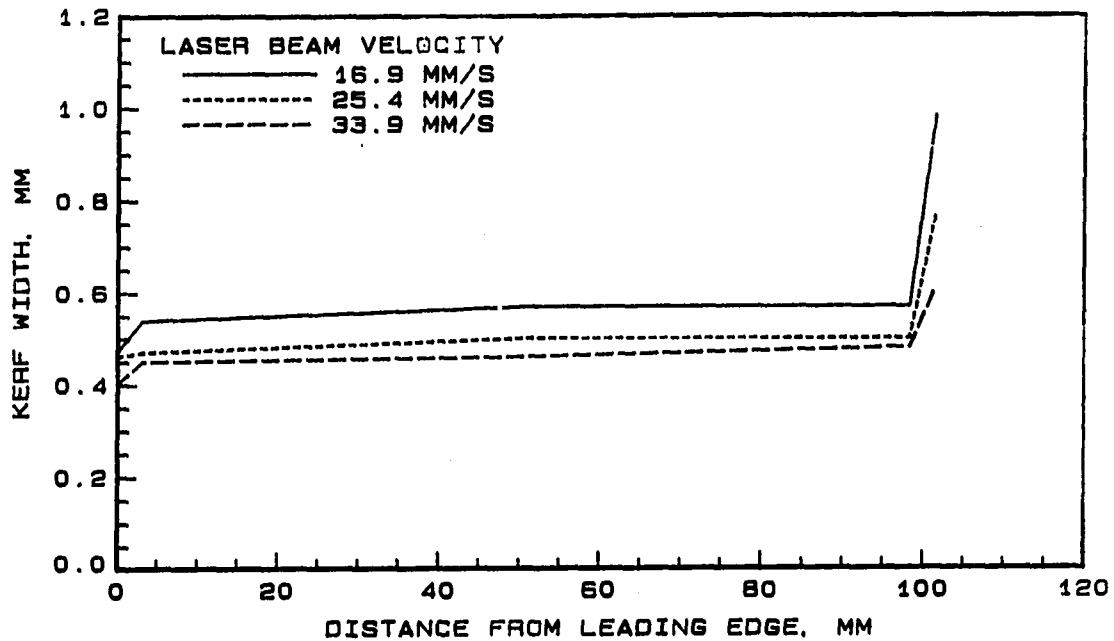


Figure 6.1: Upper surface kerf width variation with position at different beam velocities

functional relation between them. If the kerf at different positions along the cut could be expressed in terms of the kerf on the upper surface at the center of the cut, then only the kerf at the center need be known, at least for this size of sample.

The ratio of the lower to upper surface kerf width did not exceed a value of 1.0 for the bulk of the cut. In all the cases, the lower surface had a smaller kerf value than the upper surface. A possible reason for this behavior is presented below.

The intensity profile of the laser beam can be approximated by a gaussian function. When the laser beam is focussed by a lens of focal length, f , the peak intensity of the gaussian beam is a function of the distance from the focal point of the lens. This intensity is a maximum at the focal plane and decreases with increasing distance from the focal plane. The distance, d , on either side of the focal plane at which the

peak intensity has decreased by a factor of $\frac{1}{g^2}$ of its maximum value, is given by [51],

$$d = \pm \frac{\pi w^2}{\lambda} (g^2 - 1)^{1/2} \quad (6.1)$$

where, λ is the wavelength of the laser beam, and, w is the radius of the beam at the focal plane. The minimum spot radius can be calculated from,

$$w \simeq \frac{f\theta}{2} \quad (6.2)$$

Substituting for the focal length, f (127 mm), and the beam divergence, θ (1.4 milliradians), the minimum spot radius can be calculated to be ~ 0.1 mm. In all the experiments that were performed, the laser beam was focussed on the upper surface of the sample being cut. The reduction in the peak intensity of the beam at the lower surface of the sample, at a distance of 3.2 mm, can now be calculated from Equation 6.1. For the wavelength of the CO₂ laser beam, 10.6 μm , the peak intensity at the lower surface is calculated to have decreased to 36% of the value at the focal plane ($1/g^2 = 0.36$). Thus, even though the total energy input to the material at the lower surface is still the same as at the upper surface, the peak intensity decreases by 66%. This could account for the decreased kerf width at the lower surface.

Figure 6.2 shows the ratio of the lower to upper surface kerf width at the center of the sample for different laser beam velocities. The ratio is fairly constant at approximately 0.6 for beam velocities less than 30 mm/s. When the beam velocity is increased beyond 30 mm/s, the ratio increases suddenly to about 0.8, an increase of over 30%. It will be shown in the next section that for the set of conditions used in these experiments, the maximum recommended beam velocity is 33.9 mm/s. When the beam velocity is increased beyond this value, the molten metal fails to clear the

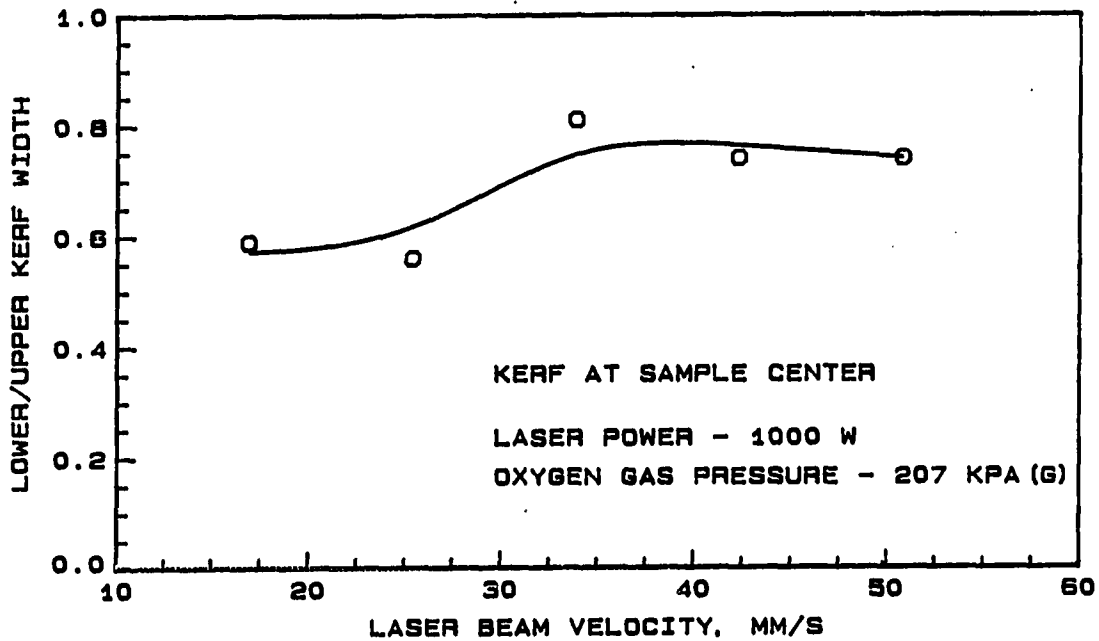


Figure 6.2: Variation of lower to upper surface kerf ratio with beam velocity

lower surface rapidly enough, thus leading to an increase in the kerf on the lower surface.

The effect of the maximum recommended velocity is also seen in Figure 6.3 which shows the kerf ratio dependence on the upper surface kerf width. It is seen that a ratio of 0.8 corresponds to low values of the kerf width, while the ratio of 0.6 corresponds to high values of the kerf. Upper surface kerfs of less than 0.5 mm were obtained when cutting at velocities greater than 30 mm/s. The higher values of kerf were obtained while cutting at velocities less than 30 mm/s.

Figure 6.4 shows the variation of the ratio of the lower and upper surface kerf at the edges of the sample. The plotted data are the average values of the ratio obtained in several tests. At the leading edge, at each beam velocity, the ratio varied by as much as 100%. The average values of the ratio show a tendency to decrease

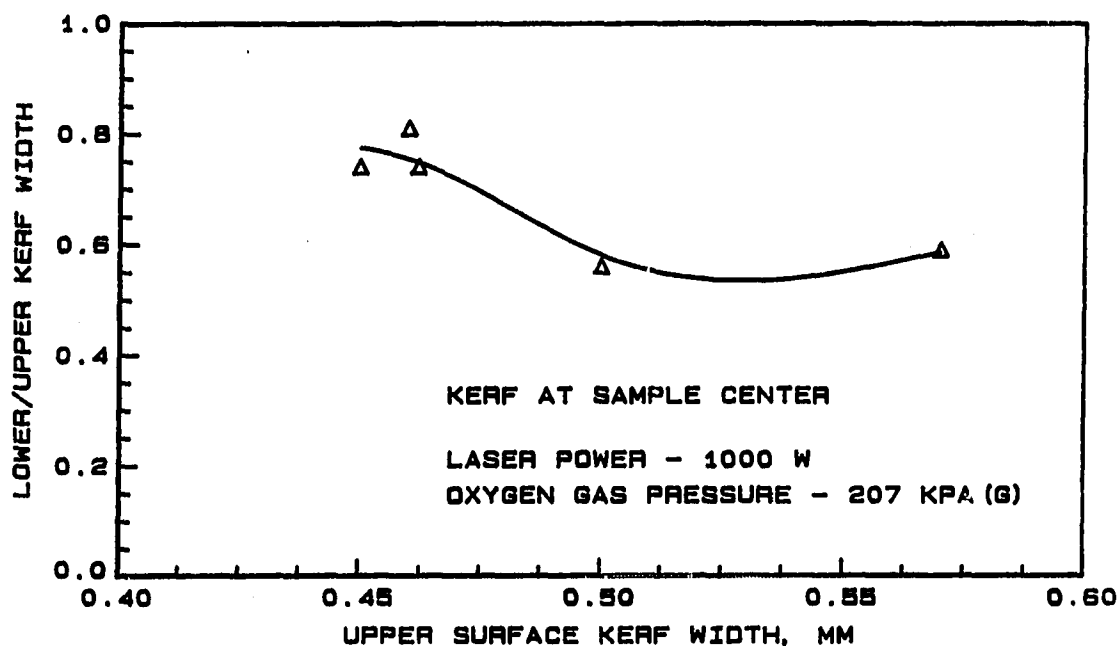


Figure 6.3: Variation of lower to upper surface kerf ratio with upper surface kerf width

steadily beyond a beam velocity of about 30 mm/s. Figure 6.5 shows the kerf ratio obtained for different upper surface kerf width values. It is seen that, at the leading edge, the variation of the value of the ratio of kerf widths on the two surfaces, was quite random. The kerf width on the two surfaces at the leading edge depended very strongly on the laser beam velocity, and the initiation of a clean cut.

At the trailing edge of the sample, the variation of the ratio with laser beam velocity is not random. With increasing beam velocity from 16.9 to 50.8 mm/s, the ratio decreases from 1.4 to 0.6, respectively. Comparing Figure 6.2 and Figure 6.4, it is seen that to obtain the same ratio of kerf width of approximately 0.6 for the sample center and the trailing edge, the velocity has to be increased from 30 mm/s at the center to 50 mm/s at the trailing edge of the sample. Unlike at the center of the

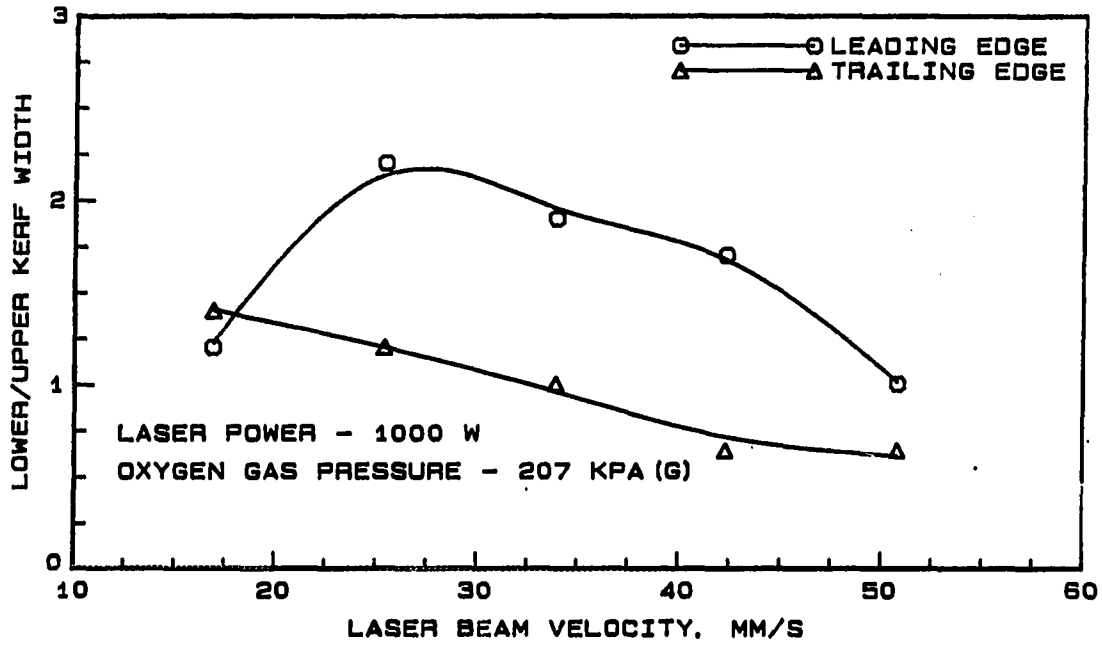


Figure 6.4: Variation of lower to upper surface kerf ratio with beam velocity at the edges

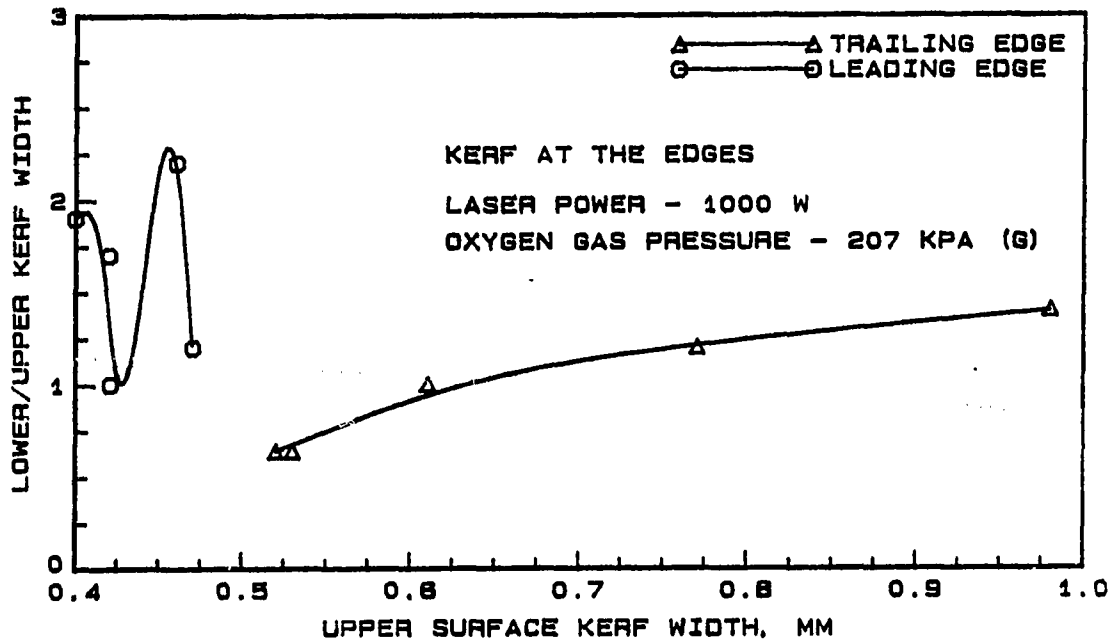


Figure 6.5: Variation of lower to upper surface kerf ratio with upper surface kerf at the edges

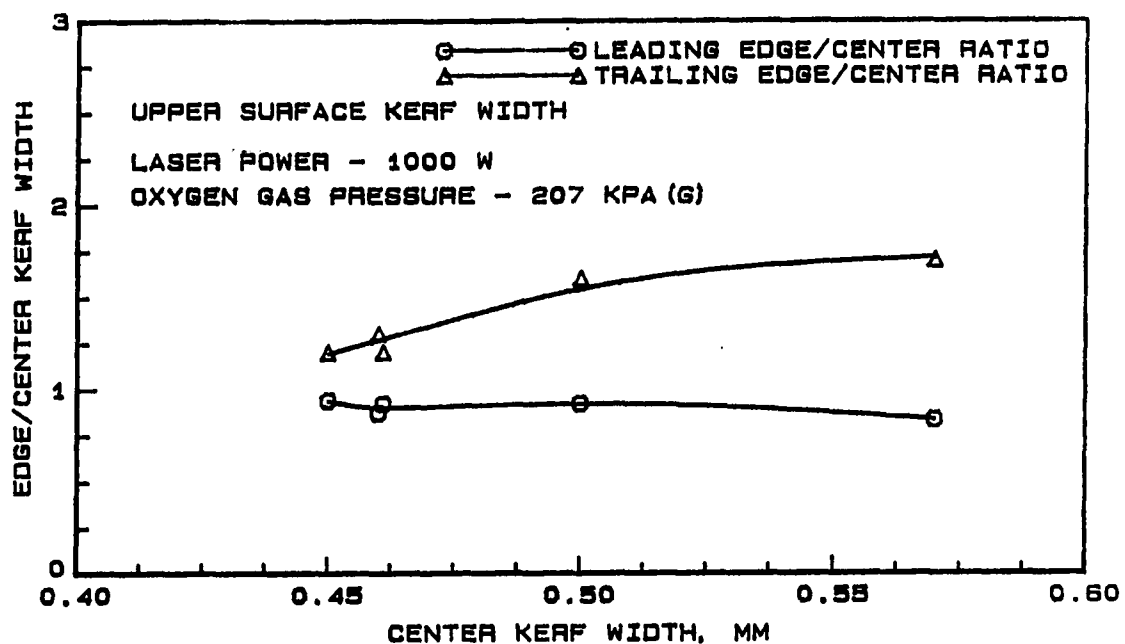


Figure 6.6: Variation of edge to center kerf ratio with kerf at the center of the upper surface

sample, no single value for the ratio can be used for the leading and trailing edges.

Figure 6.6 shows the ratio of the kerf width at the edges to the kerf at the center of the cut, for the upper surface. At the leading edge, the ratio is approximately equal to 0.9 over all values of the kerf width. At the trailing edge, however, the ratio is not a constant and varies with the kerf width measured at the center. The ratio increases from approximately 1.1 to about 1.7, with an average value of 1.4. This average value of 1.4 results in a maximum error of 18% over the whole range.

Effect of Laser Beam Velocity

The laser beam velocity, V , determines the total amount of energy, Q_{in} , input to a sample of length l , as seen in the following equation,

$$Q_{in} = \frac{\dot{Q}l}{V} \quad (6.3)$$

where \dot{Q} is the laser beam power. Since beam velocity directly affects the energy input to the metal, it can be expected to play an important role in determining the kerf width and the surface temperature.

The energy input to a sample per unit length ($\frac{Q_{in}}{l}$) at different beam velocities is shown in Figure 6.7. Increasing the beam velocity decreases the amount of energy input to the metal. An increase of beam velocity from 16.9 to 50.8 mm/s decreases the energy input from 59.2 to 19.7 J, a decrease of $\sim 65\%$. In the cutting process, only a fraction of the energy incident upon the sample is actually absorbed by the surface. The emissivity of the surface was calculated in Chapter 2 to be about 0.12 at the melting temperature of the steel. However, the kerf acts as a keyhole and causes more of the laser radiation to be absorbed [56]. At low laser beam velocities, a part of the beam passes through the kerf without striking any metal resulting in less energy being incident on the sample [56, 5, 25]. The actual energy input to the sample and the actual energy absorbed by the sample will be considerably less than the values shown in Figure 6.7. Because of the factors mentioned above, it is difficult to calculate the values of these energies. The effect of increasing the beam velocity is to increase the coupling efficiency of the beam and the metal which will result in an increase in the energy absorbed.

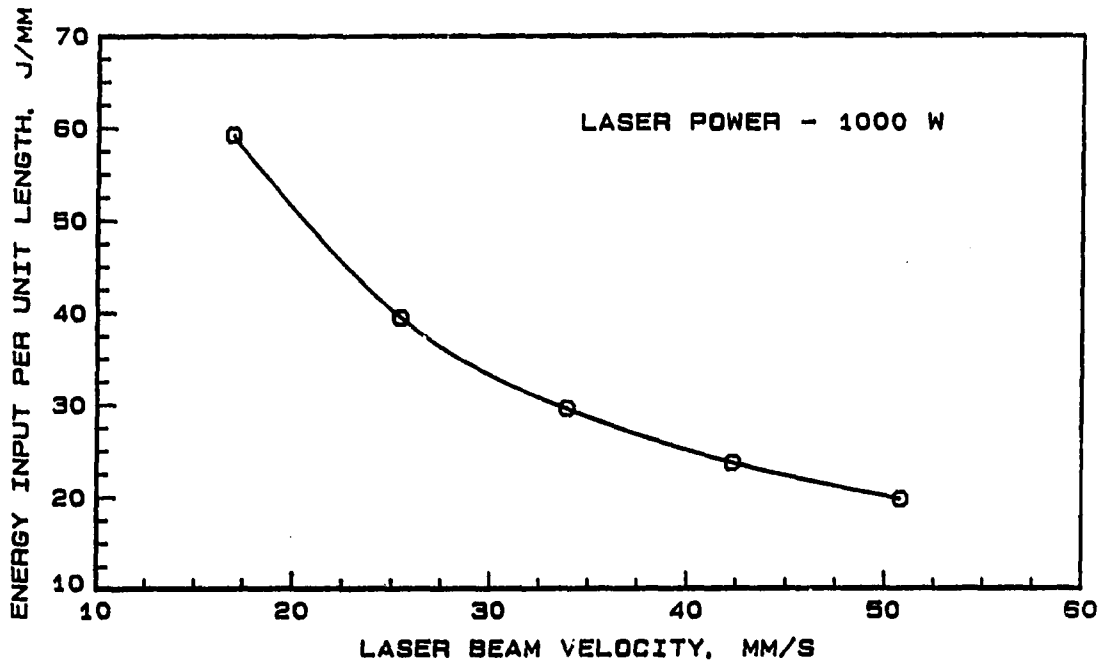


Figure 6.7: Energy input per unit length at different laser beam velocities for constant laser power

The approximate percentage of energy absorbed by the sample at different beam velocities can be calculated by using the procedure described below. The actual energy absorbed by the sample is contributed by the incident laser beam and the exothermic reaction. Three assumptions are made in the following analysis:

1. All the incident laser energy is absorbed due to the aforementioned keyhole effect.
2. The contribution of the exothermic oxidation reaction is assumed to be negligible. The effect of oxidation is considered later in this chapter.
3. The energy lost in the heating of the uncut metal is a small fraction of the energy consumed in the melting process.

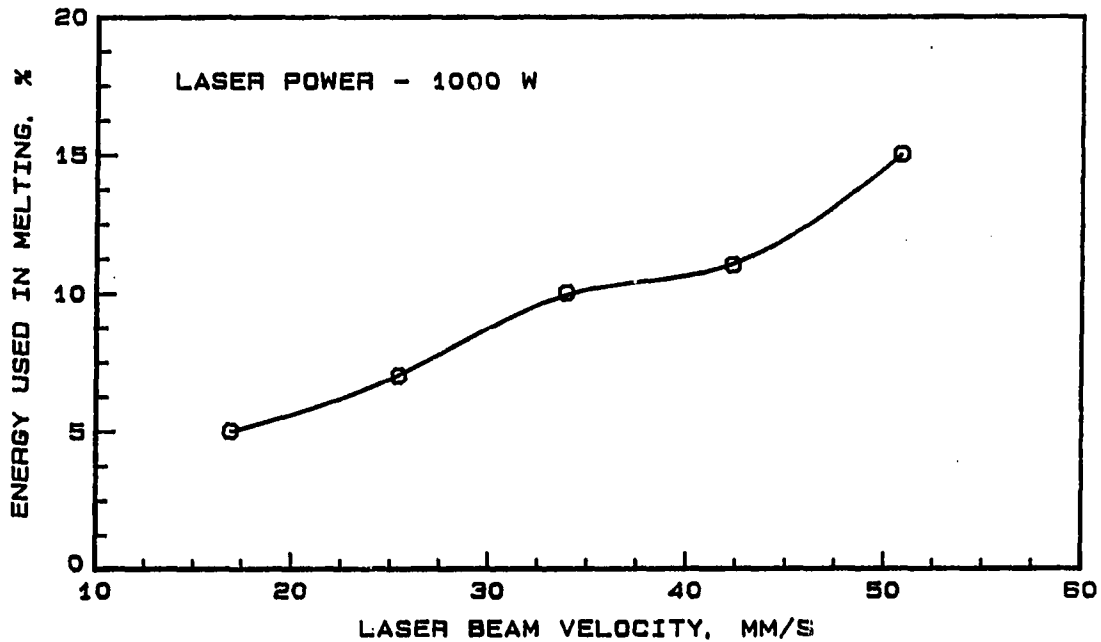


Figure 6.8: Percentage of energy input used in the melting process at laser beam velocities

The percentage of the energy input to the metal that is actually used in the melting of the metal is calculated knowing the kerf width, the length and thickness of the sample, the density of the material, and the latent heat melting of the material. Figure 6.8 shows the percentage of the energy input that is actually used in the melting process for different laser beam velocities. This value is extremely small, ranging from 5% at a velocity of 16.9 mm/s to 15% at 50.8 mm/s. The increase in the percentage of the energy used in melting is due to the decrease in the input energy when beam velocity increases. The remainder of the input energy is used either to heat the metal or else it passes through the kerf.

Kerf width

It was shown earlier that the amount of energy input to the metal decreased with increasing beam velocity. In that context, it was also pointed out that the coupling efficiency between the beam and the sample increased with laser beam velocity. Due to these effects, it is inevitable that the kerf width be a function of the laser beam velocity.

The kerf width for three sets of experiments at different beam velocities is shown in Figure 6.9. The figure shows that the kerf width is larger at the lower laser beam velocities due to the increased energy input at these velocities. The kerf decreases from a value of ~ 0.44 mm at a beam velocity of 16.9 mm/s to a value of ~ 0.35 mm between 30 and 40 mm/s. Subsequent increases in the beam velocity do not appear to produce any further decreases in the kerf. The maximum laser beam velocity at which a predictably minimum kerf width could be obtained, therefore, lies between 30 and 40 mm/s. The existence of the optimum maximum beam velocity for a set of experimental conditions have also been confirmed by other investigators [56, 5].

Surface temperature

Temperature measurements for the case of varying laser beam velocity were made with both thermocouples and the infrared sensor. The minimum temperature in the kerf width is equal to the melting temperature of the steel, $\sim 1530^{\circ}\text{C}$. The temperature at a specific location on the sample close to the cutting line will, therefore, be dependent on the kerf width; temperature should be higher for higher values of the kerf. To determine the relationship between temperature and kerf width, tempera-

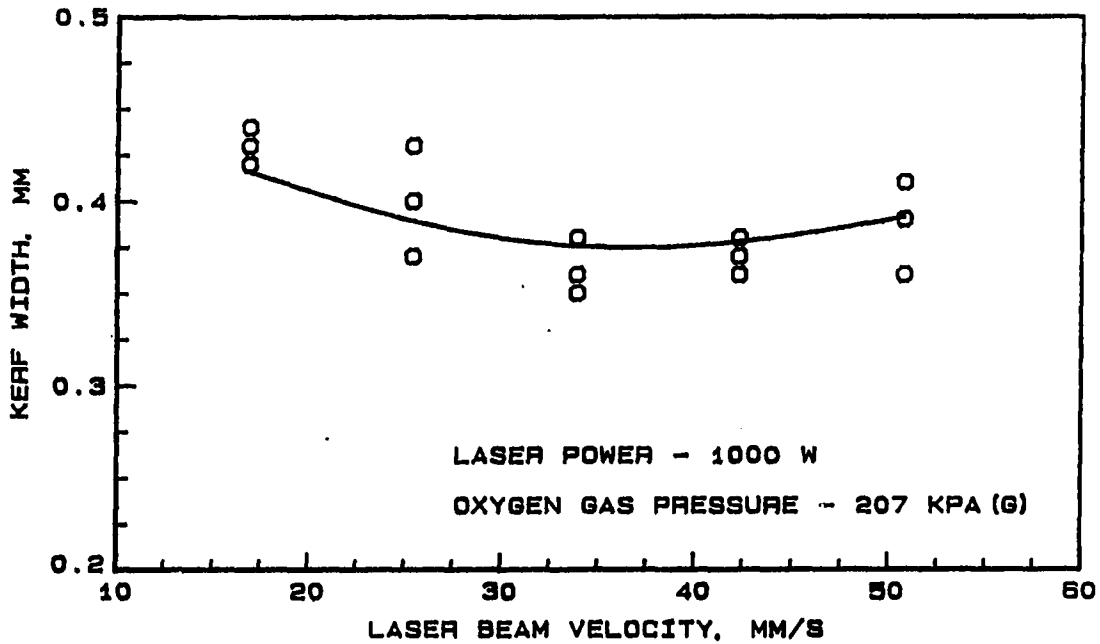


Figure 6.9: The variation of kerf width with laser beam velocity

tures were measured with thermocouples located 4.8 mm from the cutting line, as well as with the infrared sensor.

In addition to presenting the results of the temperature measurements, the kerf width is predicted from temperature measurements made with the thermocouples and compared to the measured kerf values. In the case of the infrared sensor, the results of temperature measurement at three different locations are presented, and a recommendation is made as to the best focal spot and location for the sensor.

Thermocouple measurements As seen earlier in this chapter, the laser beam velocity influences the energy input to the sample which, in turn, affects the kerf width. The temperature at a location some distance away from the cutting zone is also dependent on the energy input to the metal. In addition, the larger the kerf

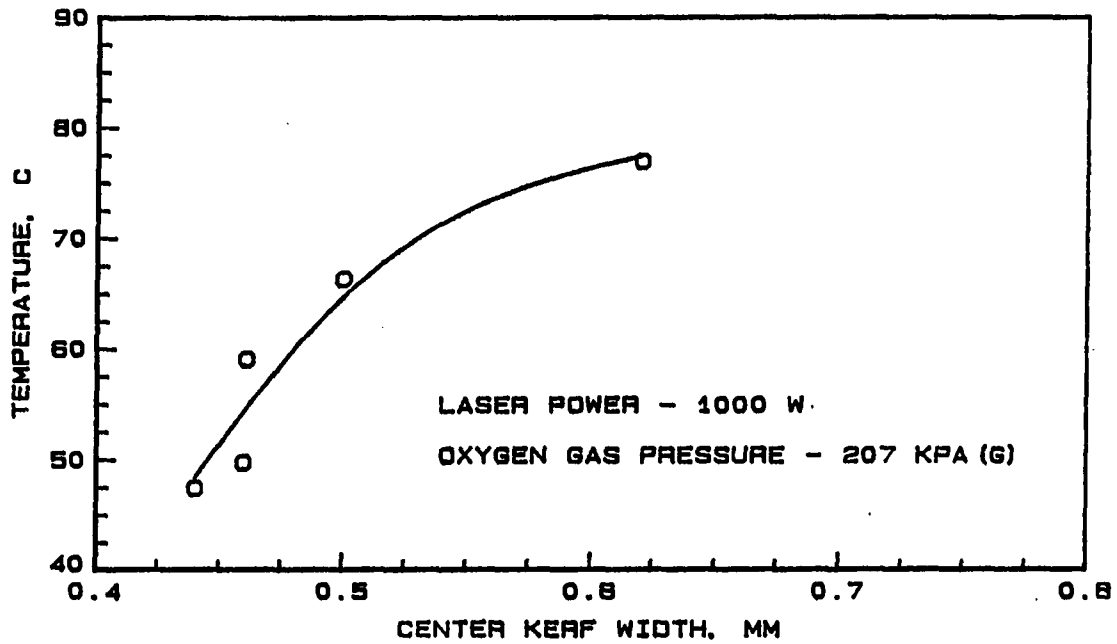


Figure 6.10: Surface temperature at 4.8 mm from the cut line for different kerf width values

width, then the closer will be the melt isotherm to the thermocouple location. Hence, the temperature at a fixed location should be dependent on both the energy input to the metal and the kerf width.

It was seen in the previous section that the kerf width and the energy input to the sample were higher at low beam velocities. Hence, the surface temperature measured by the thermocouple at a distance of 4.8 mm from the cutting region should be higher at the higher kerf widths. As shown in Figure 6.10 the general trend is as expected; higher temperatures were recorded at higher kerf values. Even at a distance of 4.8 mm, a relatively small increase in the kerf width produces a large increase in the surface temperature. All of the above tests were carried out at a fixed laser beam power of 1000 W and an oxygen gas pressure of 207 kPa (gage).

The surface temperature and kerf width both increase with decreasing laser beam velocity. Hence, the ratio of surface temperature to the kerf width should show a definite trend with increasing surface temperature. Figure 6.11 shows this ratio for different surface temperature values. As expected, there exists a definite functional dependence of the ratio on the temperature measured. Based on this figure, once the surface temperature is known, the ratio of the temperature to the kerf width can be found and then the kerf width can be calculated. Figure 6.12 shows the predicted and the measured kerf width values for a second set of experiments based on the results in Figure 6.11. The predicted results, for the most part, agreed with the measured values within 5%. The maximum error for all but one case was $\pm 2\%$; for the one case, the error was 6%, the reason for which is not known. These results show that the temperature measured at a distance of 4.8 mm was indicative of the process at the cutting zone.

Infrared sensor measurements Temperatures measured with the infrared sensor, besides depending on the process parameters, also depend on the focal spot area, shape, and location. Three different locations and two different focal spot shapes (and areas) were used in the experiments. The three focal spot locations were, respectively, one each, ahead and behind the beam, and one around the beam. The two focal shapes were the ellipse-shaped spot and the thin-line spot. The details of the location and focal spots were discussed in Chapter 2. The data for the temperature measurements made with the infrared sensor are presented as a ratio of the temperature and the kerf width. The reason for using this ratio is given below.

The output of the sensor T_s is proportional to the radiation energy received in

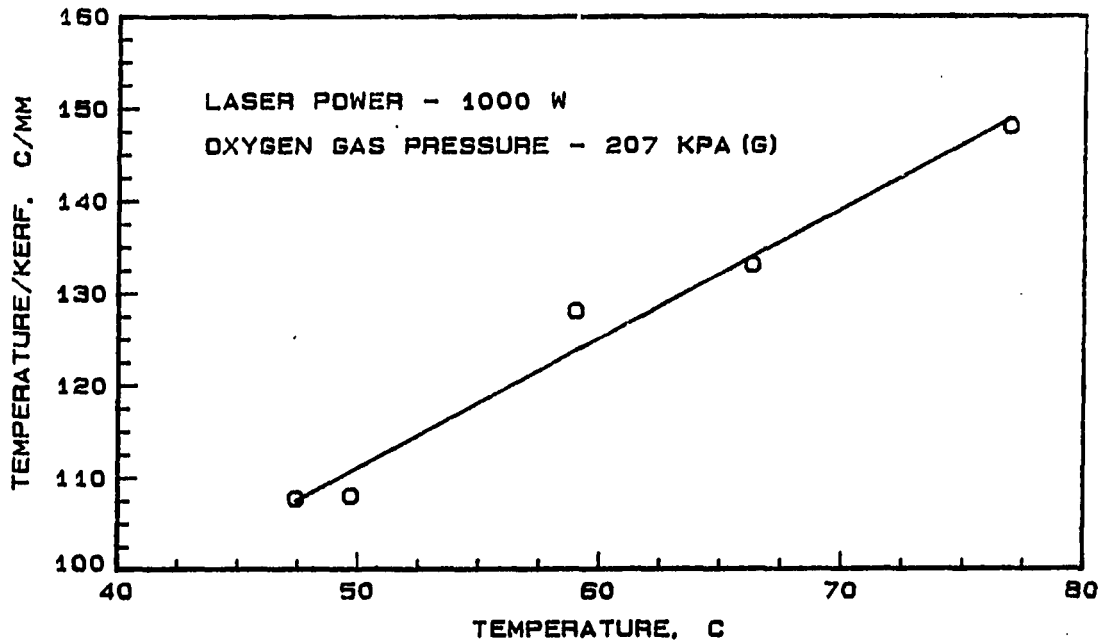


Figure 6.11: Ratio of surface temperature to the kerf width for different surface temperature values

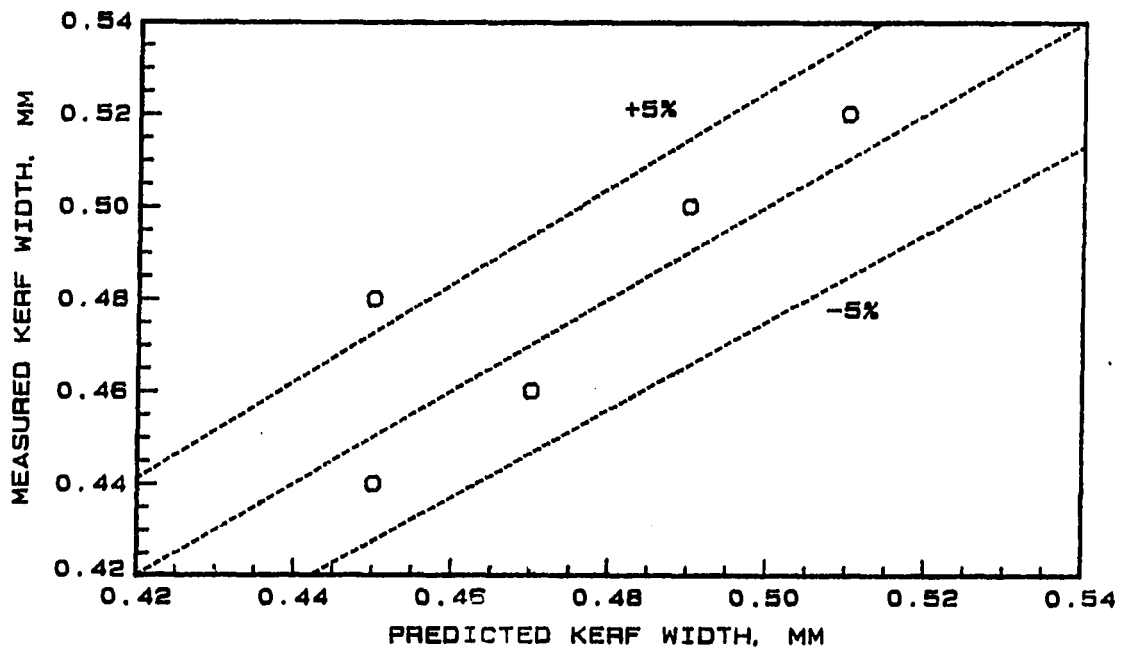


Figure 6.12: Comparison of measured kerf with values predicted from Figure 6.11

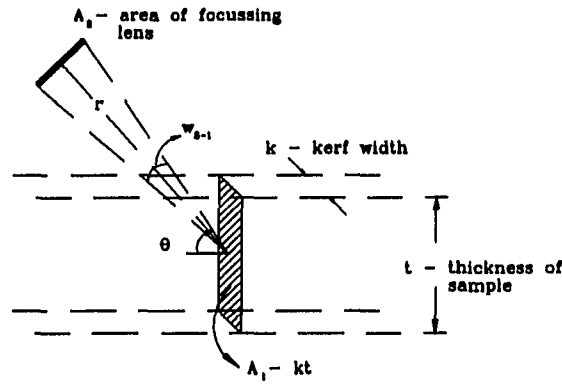


Figure 6.13: Schematic of the relative areas of the sensor and the kerf for purposes of radiant energy calculations

the wavelength band to which the sensor is sensitive, i.e., 1.8 to 3 μm . Figure 6.13 shows a schematic of the sensor's focussing lens and the focal spot around the kerf. Approximating the areas as differential areas, the rate at which radiation is intercepted by the focussing lens is,

$$q_{1-2} \simeq I(A_1 \cos\theta)\omega_{2-1} \quad (6.4)$$

where, I is the intensity of radiation in the bandwidth of the sensor, θ is the angle of inclination of the sensor and, A_1 is the area of the melt zone within the focal spot of the sensor. ω_{2-1} is the solid angle subtended by the lens at the surface of the sample.

The radiation intercepted by the sensor can also be written as,

$$q_{1-2} \simeq Ik(t \cos\theta \omega_{2-1}) \quad (6.5)$$

where all the terms in the parenthesis are constant. The angle θ is actually a function of the laser beam velocity, and decreases with increasing beam velocity [5] as evidenced by the inclination of the striation patterns on the sides of the cut edge. The intensity of radiation, I , is a function of the actual temperature, T_a , of the kerf and is given by the Planck's distribution of radiation; I increases with increasing temperature, T_a . Hence the output of the sensor, T_s , is proportional to the actual temperature, T_a , and the width of the kerf, k .

$$T_s \propto T_a k \quad (6.6)$$

and,

$$\frac{T_s}{k} \propto T_a \quad (6.7)$$

Since the actual temperature of the kerf width is a function of the velocity of the laser beam, a plot of the ratio of the temperature sensed by the infrared sensor to the kerf width should show dependence on the laser beam velocity.

Figure 6.14 shows the temperature-to-kerf width ratio for different laser beam velocities for the three sensor spot location cases. Locating the sensor spot around the beam produced the most change in the ratio with increasing beam velocity. When the sensor spot was located behind the beam, the ratio shows a tendency to increase initially and after a beam velocity of approximately 30 mm/s, starts to decrease again. The data for the sensor spot located ahead of the beam, shows a general tendency to increase with increasing beam velocity. This was also the case for the sensor spot located around the beam. The increase in this instance, however, is much greater. When the beam velocity increased from 16.9 to 50.8 mm/s, the ratio increased from 2598 to 4036 °C/mm, an increase of over 50%.

The increase in the ratio is primarily due to the increase in the temperature detected by the sensor. Figure 6.15 shows the temperature recorded by the sensor at different beam velocities. In the case of the sensor spot behind the beam, the temperature shows an increase with increasing beam velocity. This could be due to the location of the peak temperature for a moving source of heat, shifting behind the location of the beam with increasing beam velocity. This effect is further addressed in Chapter 8. In the case of the sensor spot located in front of the beam, there was inconsistency in the values of the temperature recorded.

When the spot was located such that it covered the entire region where the beam interacted with the metal, the result was an increase in the temperature with increasing beam velocity. This could be due to two reasons, one of which is the shifting of the peak temperature location behind the beam as discussed earlier. The second reason could be related to the fact that the striations on the lower half of the cut tend to become less vertical as the beam velocity increases. This, in turn, decreases the angle θ , which was referred to earlier in this section. Since the area "seen" by the sensor is proportional to $Cos\theta$, decreasing the angle increases the area, and therefore, the temperature sensed.

The temperature-to-kerf ratio dependence on the temperature output of the sensor is shown for the three locations of the sensor, in Figures 6.16 and 6.17. In the case of the sensor spot located ahead of the beam, it is seen that the ratio decreases with increasing temperature, indicating that the kerf width increases. However, at the optimum maximum beam velocity, the kerf width is a minimum even as the temperature increases, resulting in an increase in the ratio.

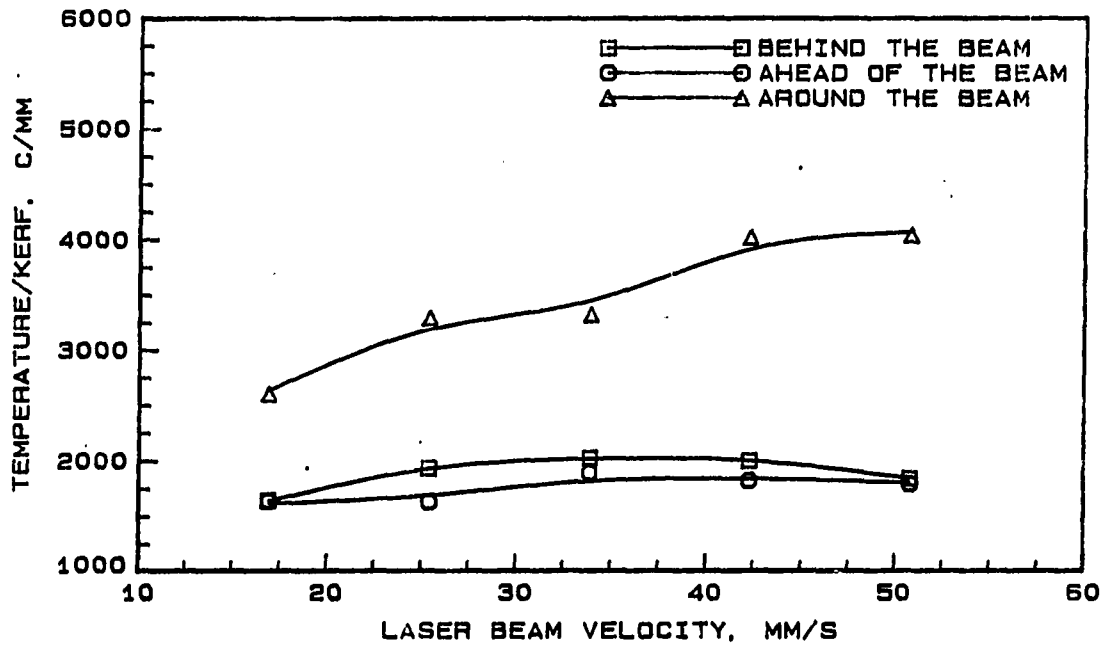


Figure 6.14: Temperature to kerf ratio at different laser beam velocities and different locations of the sensor

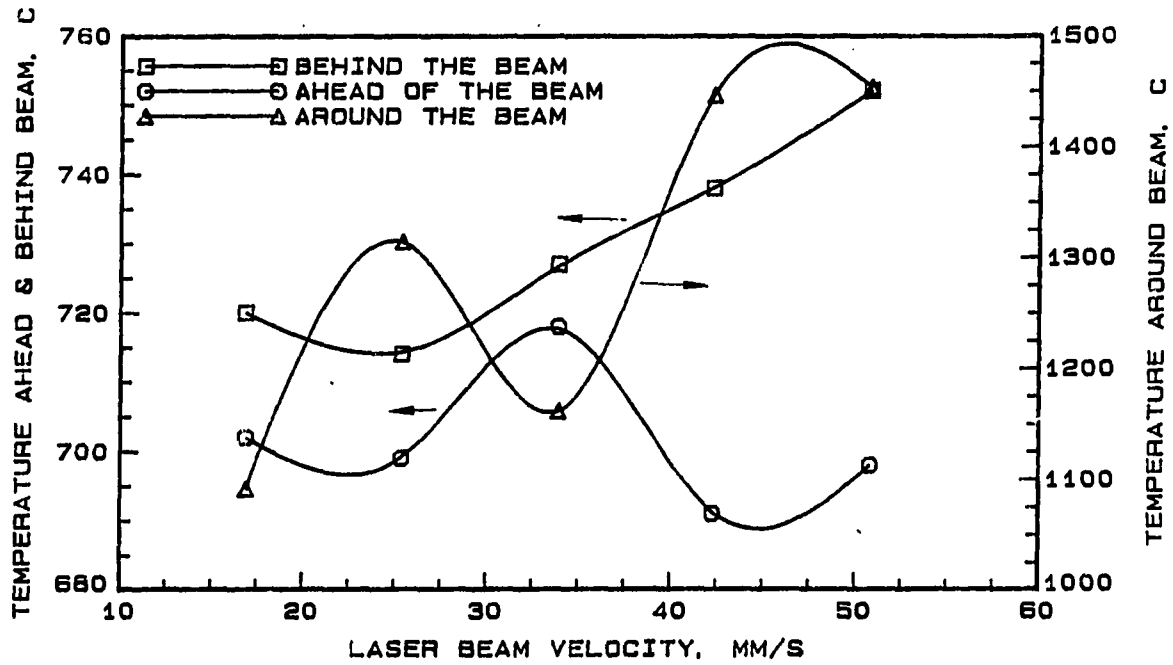


Figure 6.15: Temperature output of the sensor for different laser beam velocities and different locations

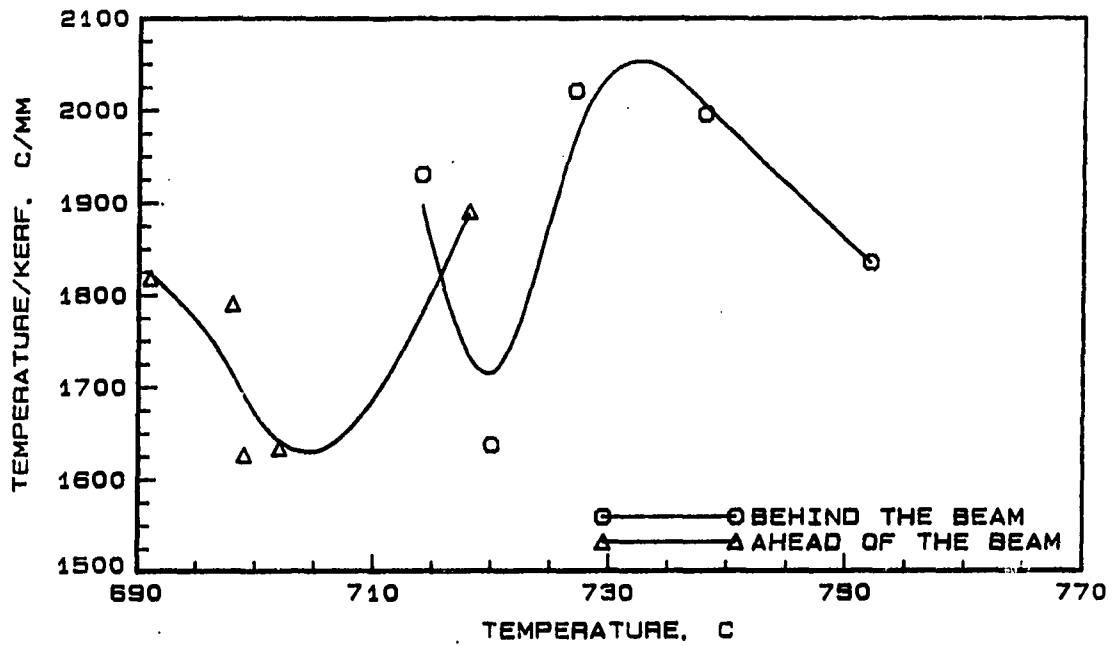


Figure 6.16: Temperature to kerf ratio and surface temperature for the sensor ahead and behind the beam

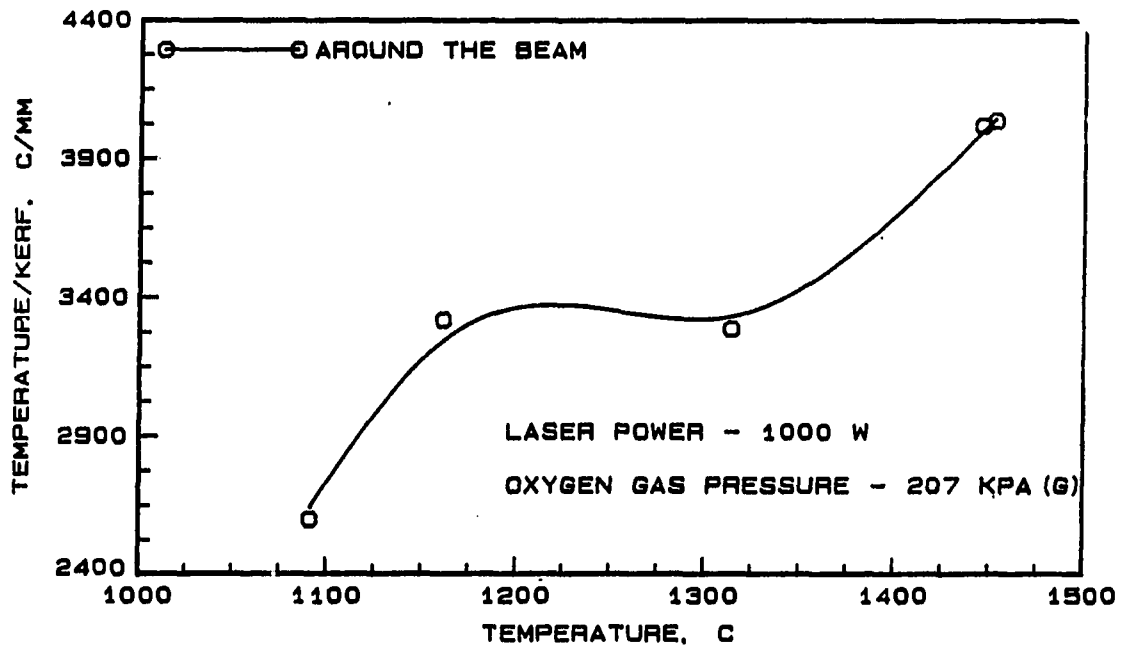


Figure 6.17: Temperature to kerf ratio and surface temperature for the sensor around the beam

When the sensor was located behind the beam, the general tendency of the temperature was to increase with increasing beam velocity. Also, the kerf width is a minimum at the optimum maximum beam velocity. Therefore, the temperature-to-kerf ratio goes through a maxima at the temperature value corresponding to the maximum velocity. An exception is the low value of the ratio at a temperature of $\sim 720^{\circ}\text{C}$, which is due to the higher value of the temperature detected in this case. The trend in the ratio for the case of the sensor located around the beam is also to increase with increasing temperature. The increasing trend deviates from the linear at a surface temperature of $\sim 1100^{\circ}\text{C}$, which corresponds to the optimum maximum beam velocity.

Effect of Oxygen Gas Pressure

Oxygen plays a very important role in the cutting process, since, as the assist-gas, oxygen acts to blow away the molten metal from the cutting zone. In addition, the oxygen gas reacts exothermically with the metal and the additional energy produced assists in the cutting process. The gas also acts as a purging mechanism to protect the laser optics from any stray particle from the cutting region. Finally, the cooling action of the gas jet acts to reduce the heat affected zone in the uncut metal.

In this section the role of oxygen in the cutting process is discussed. The effect of the oxygen gas pressure on the cooling action and the exothermic energy generated are also discussed. The results of the experiments on the effect of the gas pressure on the kerf width and the surface temperature are presented. Finally, the relationship between the temperature and the kerf are presented.

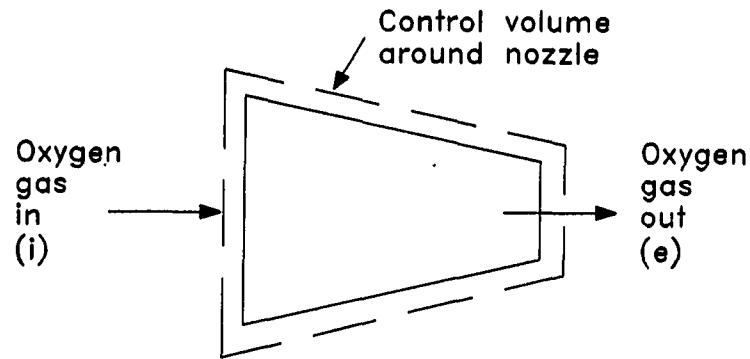


Figure 6.18: Schematic of the gas nozzle showing the inlet and exit conditions of the oxygen gas

Mass flow rate

The flow through the nozzle is treated as a reversible and adiabatic flow through a convergent nozzle. A schematic of a convergent nozzle is shown in Figure 6.18 along with the relevant data for the gas flow at the inlet and the exit. The exit back-pressure is assumed to be atmospheric and equal to 101.3 kPa. The inlet stagnation pressure is assumed to be the pressure at the exit of the gas cylinder, and the inlet velocity is assumed to be negligible.

Pressures were varied from a gage pressure of 69 kPa to 207 kPa. For this range of inlet pressures and the exit back pressure, the flow through the nozzle is choked at all the values of the inlet pressure except at 69 kPa. When the flow is choked, the maximum velocity at the nozzle throat (in this case, the exit) is equal to the

velocity of sound at the throat conditions. With the velocity, the density, and the throat area known, the mass flow rate can be calculated [61]. A sample calculation for a stagnation gage pressure of 103 kPa is presented below.

Sample calculation A simple mass balance on the nozzle treated as a control-volume yields,

$$\dot{m}_i = \dot{m}_e = \dot{m}_{cv} \quad (6.8)$$

At the inlet to the nozzle, the stagnation pressure and temperature are, respectively, 204.3 kPa and 300 K (27°C). Assuming a specific heat ratio (k) of 1.4 for oxygen, the critical pressure and temperature ratio, are, respectively [61],

$$\frac{p^*}{p_o} = \left(\frac{2}{k+1} \right)^{\frac{k}{k-1}} = 0.53 \quad (6.9)$$

$$\frac{T^*}{T_o} = \frac{2}{k+1} = 0.84 \quad (6.10)$$

Since the critical pressure calculated from Equation 6.9 is 108.2 kPa which is greater than the back-pressure of 101.3 kPa, the flow is choked at the nozzle throat (or, exit). The pressure at the exit of the nozzle is equal to the critical pressure, 108.2 kPa. The temperature, equal to the critical temperature, is calculated from Equation 6.10 is 250.7 K.

Since the flow is choked, the Mach number at the throat (or, exit) of the nozzle is 1.0. The velocity of the gas at the exit of the nozzle is,

$$V_e = c = (kRT_e)^{1/2} = 302m/s \quad (6.11)$$

where, c is the velocity of sound through the gas at the exit conditions.

The density of the oxygen gas at the exit can now be calculated from the pressure and the temperature as,

$$\rho_e = \frac{p_e}{RT_e} = 1.66 \text{ kg/m}^3 \quad (6.12)$$

With the density known, the mass flow rate through the nozzle can be calculated as,

$$\dot{m}_{cv} = \rho_e A_e V_e = 1575.5 \times 10^{-6} \text{ kg/s} \quad (6.13)$$

where, A_e is the throat area for a converging-diverging type of nozzle, which in this case, is the area at the exit.

Figure 6.19 shows the mass flow rate out of the nozzle at different pressures of the gas upstream of the nozzle. The mass flow rate increases with increasing stagnation pressure, from a value of 1321.6×10^{-6} to 2377.5×10^{-6} kg/s. This increased mass flow rate, in turn, will lead to an increase in the cooling produced by the jet and the energy produced by the exothermic reaction. These are discussed in detail below. In addition, the increase in mass flow rate increases the momentum available for the gas to blow away the molten metal in the kerf. Hence, with increased mass flow rate, there should be a greater probability for the molten metal to be cleared from the kerf as soon as it forms. This effect is discussed later in this section in the discussion on kerf width.

Convective heat loss

Typically, the nozzle is placed at a distance of ~ 1.0 mm from the plate that is being cut. The gas jet that exits the nozzle, therefore, produces a cooling effect on the plate that is heated by the laser beam. In this part of this section, the cooling

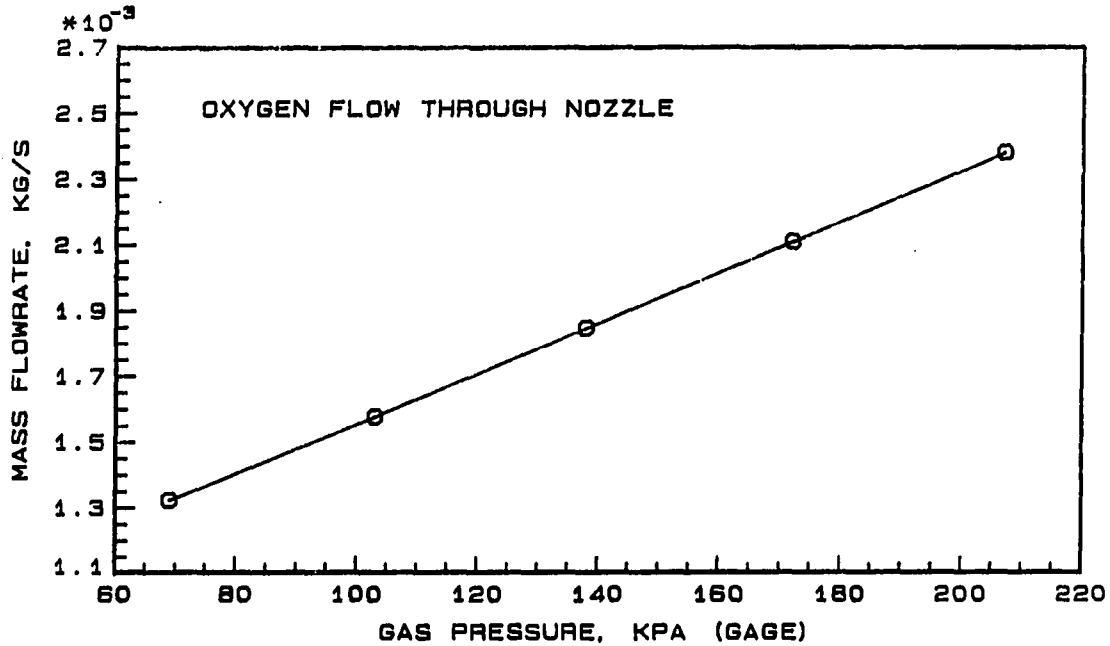


Figure 6.19: Mass flow rate through the nozzle at different oxygen gas pressures

effect of the gas jet are calculated for different stagnation pressures upstream of the nozzle.

The heat loss due to the jet is calculated from an experimental correlation developed by Goldstein et al. [24], from experiments on heat loss due to a normal jet impinging on a flat plate. The local Nusselt number is presented in the form,

$$Nu = \frac{hD}{k_j} \quad (6.14)$$

where, D is the diameter of the jet, k_j is the thermal conductivity of the gas. The local heat transfer coefficient, h , is given by,

$$h = \frac{q}{T_w - T_{aw}} \quad (6.15)$$

where, T_w is the temperature of the plate, and, T_{aw} is the adiabatic wall temperature.

The adiabatic wall temperature, T_{aw} is calculated from the recovery factor,

$$r = \frac{T_{aw} - T_j}{V_j^2 / 2C_p} \quad (6.16)$$

where, T_j is the static jet temperature, V_j is the velocity of the jet, and, C_p is the specific heat of the gas.

The recovery factor is a function of L/D , the nozzle-plate spacing to nozzle diameter ratio, R/D , the radial distance to nozzle diameter ratio [24]. The recovery factor was also shown to be independent of the Reynolds number of the jet. The recovery factor for an L/D of 0.5 (= 1.0 mm/2.0 mm) varies from 1.0 at an R/D of 0.0, to 0.7 at a R/D of 2.0. In performing experiments in this research, it was found that at a distance of 5 mm from the beam, the temperature measured was less than 100°C. Hence, heat loss due to the gas jet was assumed insignificant beyond 5 mm or an R/D of 2.0. Assuming an average value of the recovery factor of 0.85 for the region between R/D of 2.0 and 0.0, the adiabatic wall temperature can therefore be found.

Goldstein et al. [24] also showed that for the region between R/D of 2.0 and 0.0, the local Nusselt number can be correlated by,

$$\frac{Nu}{Re^{0.76}} = 0.04 \quad (6.17)$$

where, Re is the Reynolds number of the jet. The average Nusselt number, therefore, can also be calculated from the Equation 6.17. A sample calculation of the convective heat loss due to the jet is given below.

Sample calculation Assuming that the jet velocity, density, and static temperature are the same as at the exit of the nozzle in the sample calculation of the

previous section, the Reynolds number of the jet can be calculated to be,

$$Re_j = \frac{V_j D}{\nu_j} = 62820 \quad (6.18)$$

where, ν_j is the kinematic viscosity of the gas.

The Nusselt number can now be calculated from Equation 6.17 as,

$$Nu = 177.3 \quad (6.19)$$

Based on a recovery factor of 0.85, the adiabatic wall temperature is now calculated from Equation 6.16 as,

$$T_{aw} = 287 K \quad (6.20)$$

where, a value of 302 m/s is used for the jet velocity.

An average heat transfer coefficient is calculated as,

$$h = 1976.5 W/m^2 - C' \quad (6.21)$$

from which the heat loss rate can be calculated as,

$$\dot{Q}_l = hA(T_w - T_{aw}) = 122.0 W \quad (6.22)$$

where, A is assumed to be an area of radius 5.0 mm, and T_w is calculated as an average value between the temperatures of $\sim 50^\circ C$ at 5.0 mm (from thermocouple measurements in experiment) and $1535^\circ C$, the melting temperature at the cutting zone.

The heat loss from the plate at different stagnation pressures is shown in Figure 6.20. It is seen that the heat loss increases with increasing gas pressure, from a value of 106 W at 69 kPa to 166 W at 207 kPa, gage. The heat loss as a percentage of the laser beam power for different gas pressures is shown in Figure 6.21 for a laser beam power of 1000 W.

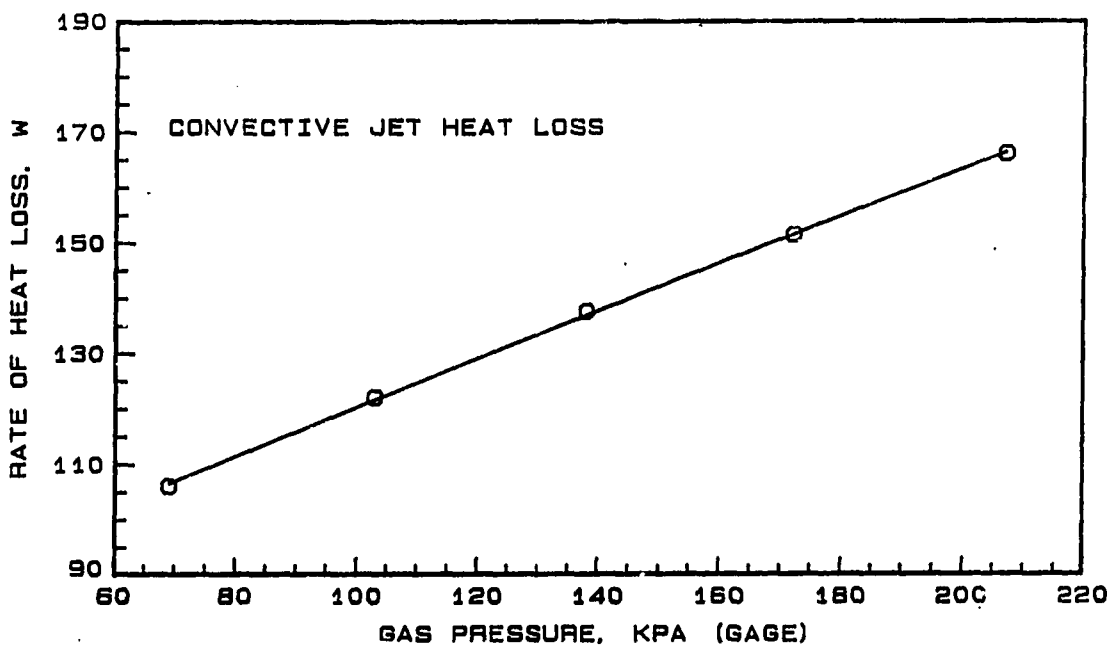


Figure 6.20: Convective heat loss due to the gas jet at different gas pressures

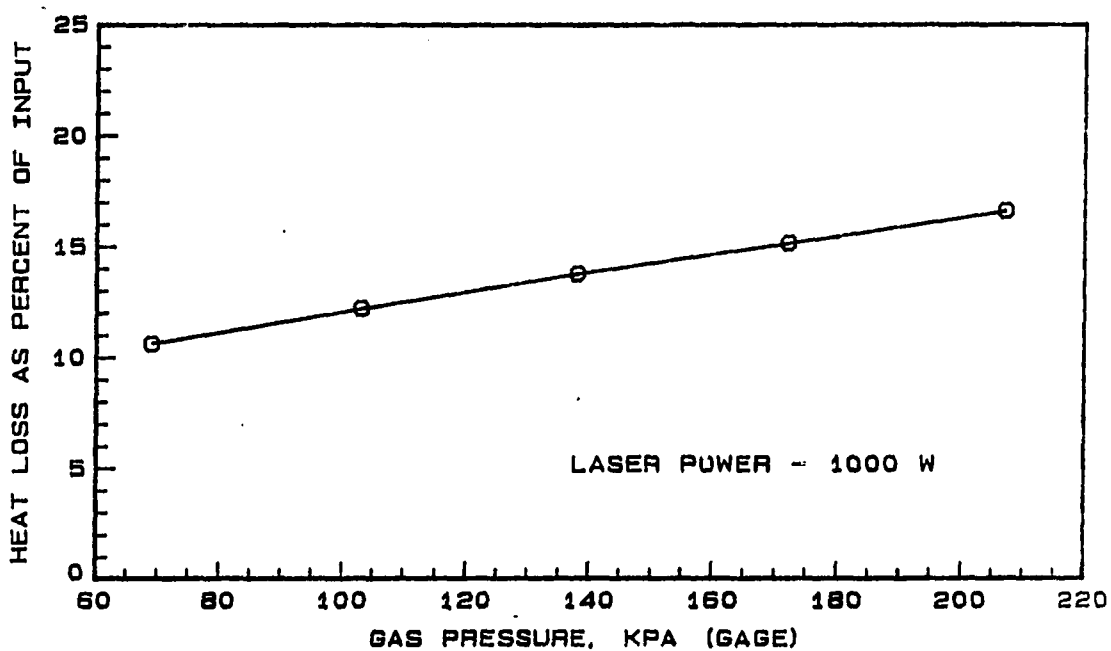


Figure 6.21: Convective heat loss due to the gas jet as a percentage of the input laser power at different gas pressures

Oxidation reaction

The oxidation reaction of iron produces three stable oxides: wustite, FeO , magnetite, Fe_3O_4 , and hematite, Fe_2O_3 [34]. The ratio of the three oxides formed, $FeO/Fe_3O_4/Fe_2O_3$ is, about 100/10/1, and is independent of temperature [45]. However, Kirschfeld [32] has shown that in the presence of excess oxygen, at temperatures close to the melting point of the iron, wustite reacts with the oxygen to form the higher oxides. In his analysis, the oxide formed is 58.5% Fe_3O_4 , and 41.5% Fe_2O_3 which is used in this study.

The oxidation reaction is exothermic and the enthalpy of formation of the iron oxide is assumed to be an average value of [26],

$$\Delta H_R = -18.062 \times 10^3 J/gm - of metal \quad (6.23)$$

Once the oxidation rate of the metal known, the rate of energy produced by the reaction can then be determined.

Several relationships have been suggested in the literature for the rate of metal oxidation [34]. The experimental data are usually correlated in terms of the weight per unit area of oxide, Δm , produced as a function of the time, t . The simplest of all the relationships is linear as follows,

$$\Delta m = k_l \times t \quad (6.24)$$

Other relationships such as the, parabolic, cubic, and logarithmic relationships have also been extensively used to correlate the experimental data.

In the usual oxidation process, which has been studied extensively in the literature, the oxide scale that forms on the surface increases in thickness with time. The

oxidation reaction rate is usually slow and is diffusion-controlled, governed by the diffusion of oxygen through the oxide layer. Since the oxide layer grows continuously, the reaction rate decreases with increasing time.

However, if the oxide layer that is formed is porous, or if it should be removed as it forms, then in the presence of sufficient oxygen, the reaction is rate-controlled and the oxide growth is governed by the linear rate law, Equation 6.24. In the present case, the oxide that is formed on the metal surface melts and is continuously removed by the oxygen gas-jet. This exposes fresh metal to oxidation continuously, thus leading to the rate-controlled reaction.

The linear reaction rate constant k_l is a function of both the temperature and the pressure of the oxygen gas [34]. The temperature dependence of the rate constant is given by the Arrhenius equation, as,

$$k_l = Ae^{-E/RT} \quad (6.25)$$

where, A is the frequency factor, E is the activation energy, R is the universal gas constant, and T is the temperature of the oxidation reaction. The frequency factor and the activation energy have to be determined experimentally to obtain the temperature dependence of the rate constant. There exists an abundance of experimental data in the literature for the temperature dependence of the parabolic, cubic, and logarithmic rate constants [34, 33]. Unfortunately, no information on the linear rate constant was found in the literature.

However, studies on the burning of metals in an oxygen atmosphere have been reported in the literature [27, 32]. In these studies, iron wires of different diameters were burnt in oxygen atmospheres and the burning rate of the metal was obtained

by filming the process. The metal formed magnetite and hematite and the energy released in the exothermic reaction contributed to the melting of the metal and the oxide. The molten metal and oxide dropped off from the end of the wire as the oxidation process proceeded. Since these studies closely resembled the oxidation process and the subsequent melting of the metal and the oxide in the laser cutting process, the results of these studies were used in this research to determine the oxidation rate.

The rate of molten metal and oxide formed in an oxygen environment at atmospheric pressure was measured to be in the range, 0.04–0.05 gm/s [27, 32] at the melting temperature of iron, 1535°C. An average value of the rate of burning was chosen as 0.045 gm/s at an oxygen gas pressure of one atmosphere. Since only 28.5% of the melt was oxide [32], the rate of metal oxidation is calculated to be 0.0013 gm/s. This oxidation rate is also dependent on the gas pressure. Pressure values from a quarter to one atmosphere were tested and it was found that the reaction rate was proportional to the square root of the oxygen pressure [27, 32]. This type of pressure dependence was also found in the case of the parabolic reaction rate that was discussed earlier [34].

Based on the above results, the equation for the oxidation reaction rate can now be written as,

$$\dot{X} = 0.0013\sqrt{P_{O_2}} \quad (6.26)$$

where, P_{O_2} is the absolute gas pressure in kilo-Pascals (kPa), and \dot{X} is the rate of metal oxidized in gm/s. Once the rate of oxidation is found, the rate at which energy is released by the exothermic reaction is calculated from knowing the heat of reaction

of the formation of the oxides. The rate of energy released is,

$$\dot{Q} = -(\Delta H_R)\dot{X} \quad (6.27)$$

where, ΔH_R is the heat of reaction of formation of the oxides and was given earlier in Equation 6.23.

The rate of energy released by the reaction is calculated at different gas pressures, and is shown in Figure 6.22. The rate of heat produced increases as the square root of the gas pressure from a value of 300 W at a gas pressure of 69 kPa(gage), to 400 W at a gas pressure of 207 kPa(gage). The overall increase in the heat produced by the oxidation increased by about 35% when the gas pressure increased by 200%. Assuming a constant input laser power of 1000 W, the heat of oxidation as a percentage of the input power is shown in Figure 6.23. The heat of reaction is approximately 30% at a gas pressure of 69 kPa(gage), and increases to 40% at a pressure of 207 kPa(gage). Thus, it is seen that increasing the gas pressure increases the heat lost by convection while increasing the heat produced by oxidation. In addition increasing the gas pressure increases the momentum of the jet and, hence, its ability to blow away the molten metal.

It would, therefore, appear that increasing the gas pressure produces desirable effects. However, it has been shown that at pressures of 207 kPa(gage), a density gradient field is produced over the plate being cut [56]. The presence of this density gradient defocusses the beam on the metal, thus reducing the peak intensity of the beam on the sample being cut. This, in turn, reduces the cutting efficiency and quality [56].

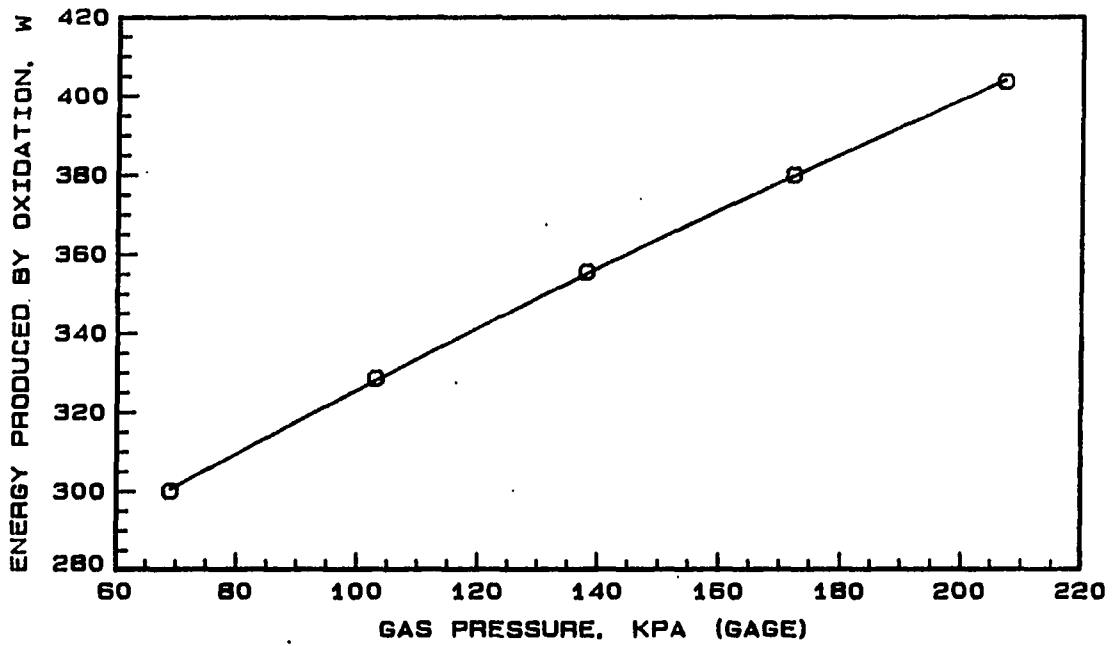


Figure 6.22: Rate of energy produced due to the oxidation reaction

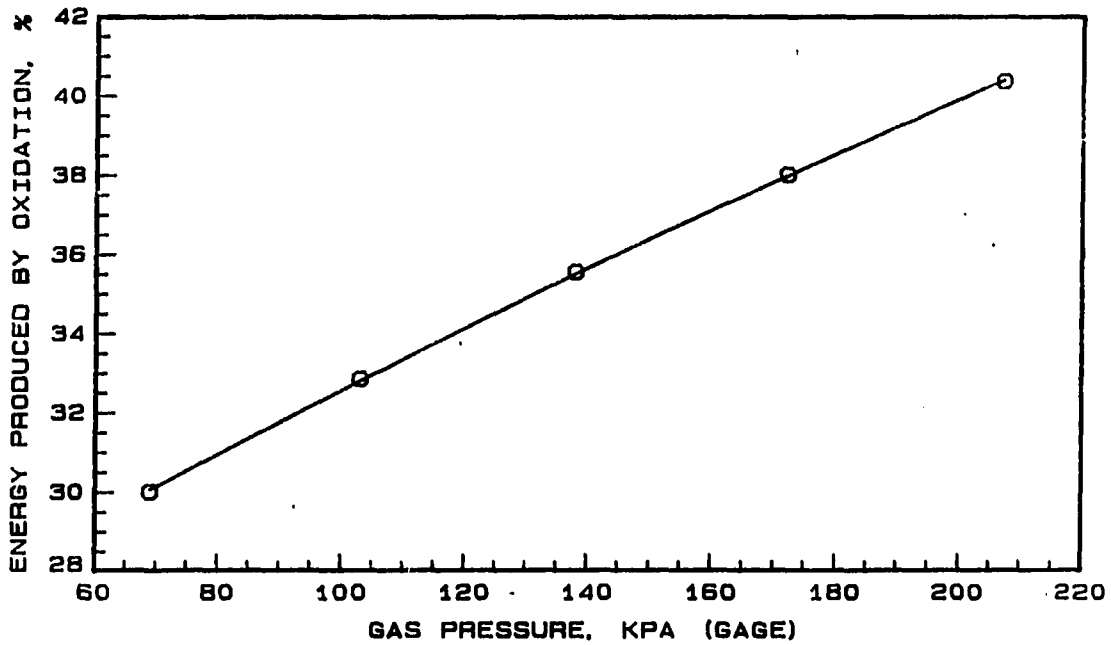


Figure 6.23: Energy produced by oxidation reaction as a percentage of the input laser power

Kerf width

It was seen earlier that the laser beam velocity had a significant effect on the kerf width. Increasing the beam velocity from 16.9 to 50.8 mm/s was found to produce a decrease of over 20% in the kerf width. Even though an increase in the gas pressure was associated with an increase in the convective heat loss and exothermic heat generation, the gas pressure did not have a significant effect upon the kerf width.

Figure 6.24 shows the kerf width values for several experiments at different gas pressures. An increase of 200% in the gas pressure produces only a 10% decrease in the kerf width. In general, for all the values of the gas pressure, the kerf width on the upper surface lies between 0.3 and 0.4 mm. Na et al. [42] also observed that oxygen gas pressure did not have a significant effect upon the kerf width in the cutting of mild steel. As seen in Figure 6.24, at the lower gas pressures, the kerf is wider. There is a minimum gas pressure below which it was not possible to cut. In the case of cutting at 33.8 mm/s, this minimum gas pressure was found to be 103 kPa(gage).

A possible reason for the higher kerf values at the lower gas pressures could be as follows. In the experiments performed in this research, since the laser power used was 1000 W, a minimum gas pressure of 103 kPa was essential to perform the cut. When the criterion of minimum kerf is chosen to determine the optimum maximum velocity and gas pressure combination, it was found that at a beam velocity of 33.8 mm/s, the optimum value of the gas pressure was 207 kPa. At values of the gas pressure below this value, the velocity of 33.8 mm/s that was used is lower than the optimum maximum for this gas pressure. Hence, there is more energy available for cutting and the kerf width is wider.

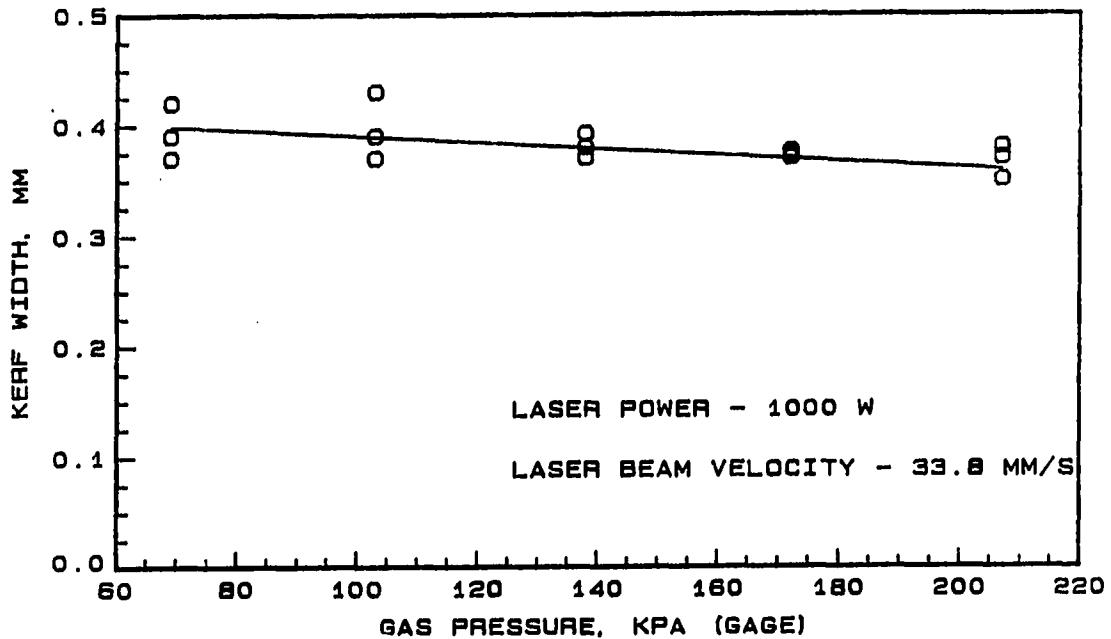


Figure 6.24: Kerf width on the upper surface and at the center of the sample at different oxygen gas pressures

The maximum velocity at which a cut can be performed has been found to depend on the gas pressure [56]. In cutting 3 mm thick mild steel at 1500 W, increasing the gas pressure increased the maximum velocity up to about 45 mm/s at a gas pressure of 70 kPa. Increasing the gas pressure beyond this value produced a decrease in the maximum velocity possible. It was also shown that for all values of the laser power, increasing the gas pressure beyond 100 kPa produced a decrease in the maximum possible velocity of the beam. One possible explanation for this behavior could be the presence of the density gradient field that was mentioned in an earlier section. The presence of the density gradient field could result in defocussing of the beam thus reducing the peak intensity of the beam available for cutting. The net result is that the velocity has to be decreased in order to produce a cut.

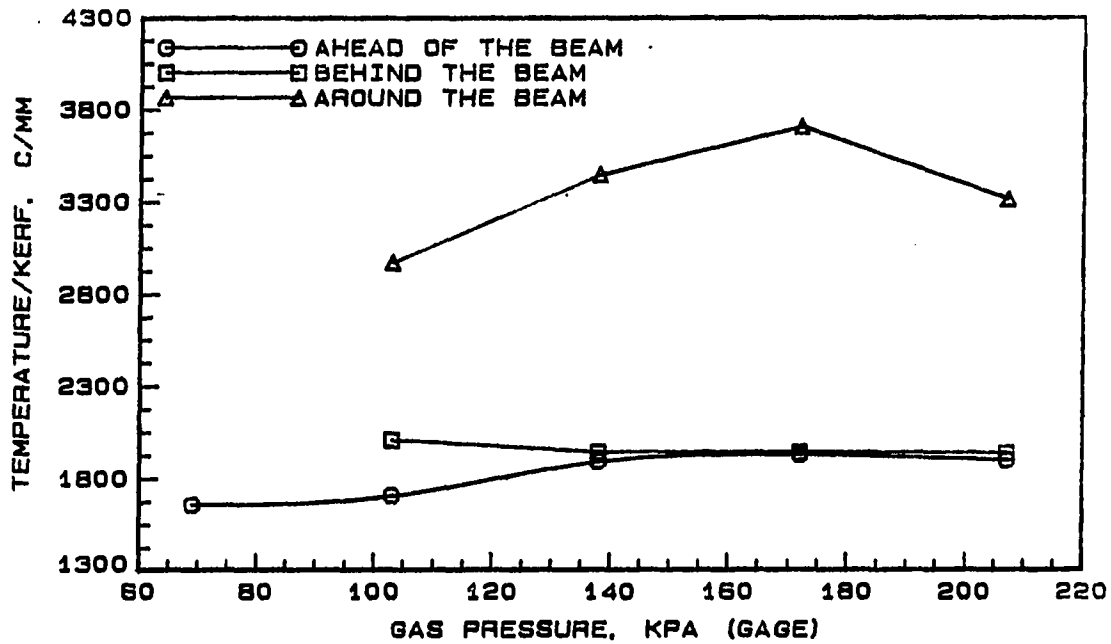


Figure 6.25: Temperature to kerf width ratio at different oxygen gas pressures

Surface temperature

Surface temperatures were made with the infrared sensor mounted ahead, behind, and around the beam and the cutting zone. For reasons discussed in an earlier section, the data for the temperature measurements and the kerf are presented as a ratio of the temperature and the kerf values. This enables observation of the relative increases in the temperature and kerf with increasing gas pressure.

Figure 6.25 shows the ratio of the temperature to the kerf for the three locations of the sensor. In the case of the sensor located ahead and behind the beam, the ratio is seen to increase with increasing gas pressure. Beyond a pressure of 140 kPa(gage), the ratio is fairly constant at a value of ~ 1920 °C/mm.

Locating the sensor such that the spot covered the cutting zone resulted in higher temperatures being recorded. From Figure 6.25, it is seen that the relative increase

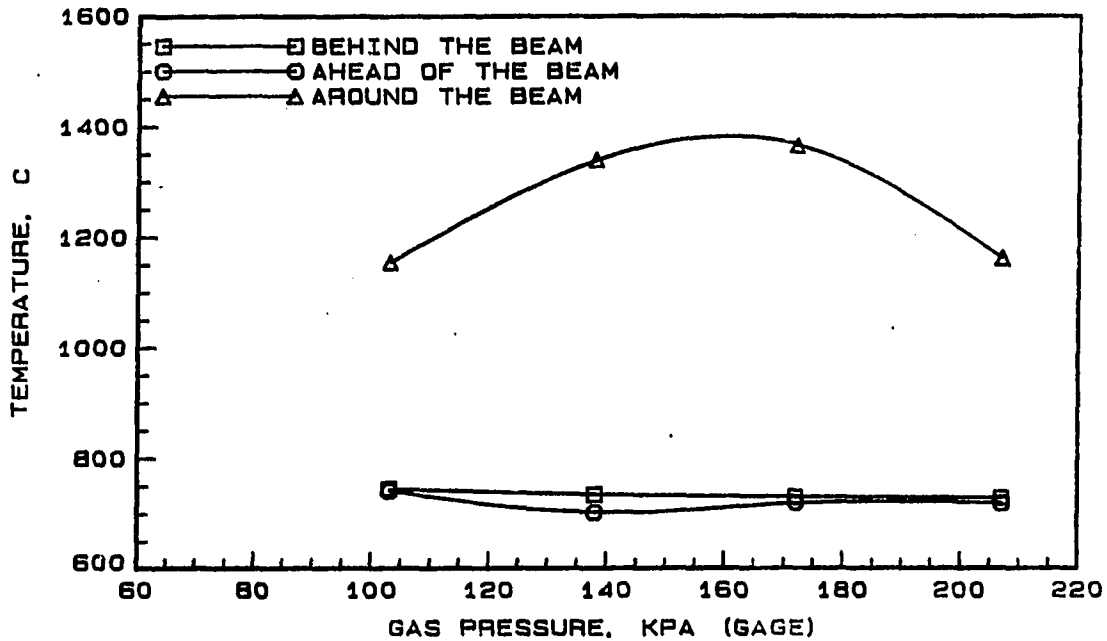


Figure 6.26: Temperature recorded by the sensor at different oxygen gas pressures and at different locations

of temperature and kerf with increasing gas pressure was such that the ratio of the temperature and kerf increased with pressure. This is primarily due to the fact that the temperature sensed by the sensor increases with increasing pressure. The temperature sensed by the infrared sensor at different gas pressures is shown in Figure 6.26. The temperatures recorded ahead and behind the beam remained fairly constant with increasing gas pressure. The temperature recorded with the sensor spot surrounding the cutting zone, however, increased with increasing gas pressure.

It was seen in the section on the effect of velocity that the temperature recorded by the sensor also depended upon the width of the kerf. At a gas pressure of 207 kPa, the kerf width obtained was a minimum with the result that the temperature recorded was also very low. Because of the decrease in kerf width coupled with the

decrease in temperature, the ratio of the temperature to kerf width in Figure 6.25 also shows a decrease. These results show that locating the sensor spot around the cutting zone produced the best results in terms of the resolution.

The ratio of the temperature to kerf dependence on the temperature is shown in Figure 6.27 for the case of the sensor spot located ahead and behind the beam, and in Figure 6.28 for the case of the spot surrounding the cutting zone. In the cases of the spot ahead and behind the beam, the ratio remains fairly constant with an average value of 1950 over a wide range of temperature from 700 to 740 °C. The exceptions were at temperatures below 700 and above 740 °C, where the kerf width obtained was high enough to cause an overall decrease in the ratio. When the spot was located surrounding the cutting zone, the general tendency was for the ratio to increase with increasing temperature. Again, the exception was at 1160 °C, where an unusually low temperature was obtained due to the kerf width being a minimum for this case.

Kerf width prediction

In this section, the feasibility of predicting the kerf width from the temperatures measured while varying oxygen gas pressure is discussed. Due to the fact that the kerf width was not strongly dependent on the gas pressure, the data from the velocity experiments are used, as described below. The procedure adopted is to use the temperature recorded to obtain the temperature to kerf ratio from the velocity experiments. From the knowledge of the temperature and the temperature-to-kerf ratio, the kerf width can then be determined.

Comparing Figures 6.16 and 6.27, it is seen that the trends in the results are

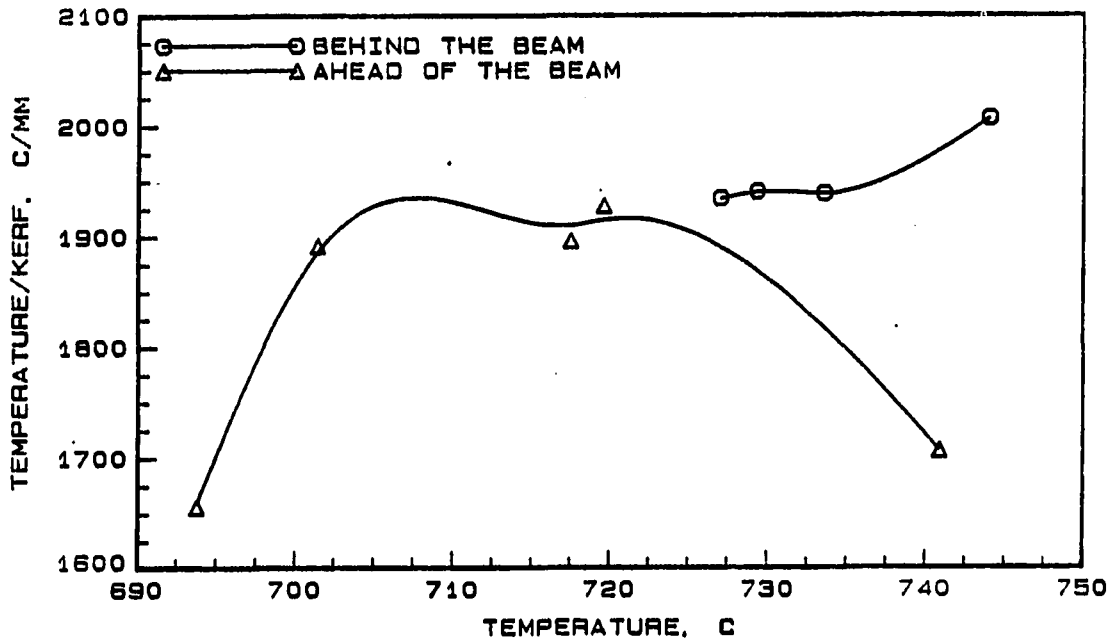


Figure 6.27: Temperature to kerf width ratio at different temperature values with the sensor spot ahead and behind the beam

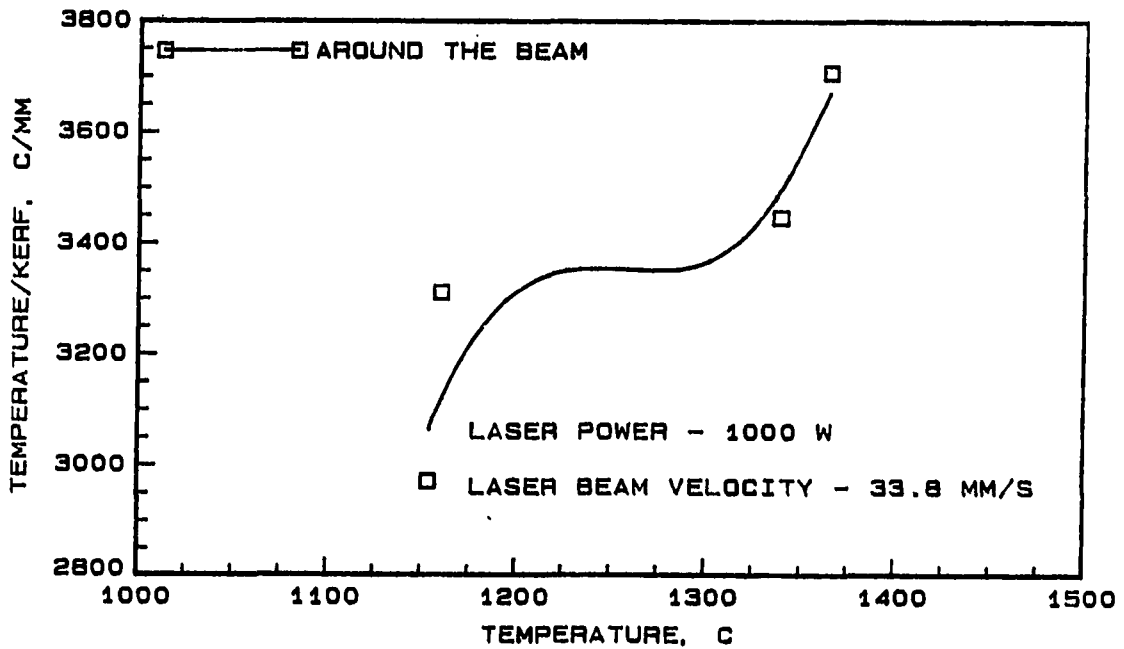


Figure 6.28: Temperature to kerf width ratio at different temperatures with the sensor spot surrounding the cutting zone

quite opposite while varying velocity and oxygen gas pressure. For this reason, the location of the sensor spot ahead and behind the beam is not a desirable location for purposes of predicting kerf width. Therefore, only the data collected with the sensor spot surrounding the beam is used for kerf width prediction.

The kerf width can be predicted by two different methods from the temperature data obtained while varying the gas pressure. The first method is to use the data in Figure 6.17, in conjunction with the temperature data, to obtain values of the temperature-to-kerf ratio. The second method is based on the observation that varying the oxygen gas pressure had less effect on the kerf width than varying the beam velocity. Since the experiments on varying the gas pressure were performed at a constant beam velocity of 33.8 mm/s, Figure 6.14 is used to obtain a single value of the temperature-to-kerf ratio. From the temperature-to-kerf ratio and the measured temperature, the kerf width can be determined.

The results of the two methods of prediction are shown in Figure 6.29 and 6.30. It is seen that the error in the first method was less than 5% in nearly all of the cases. In the case of using a single value of the ratio at all the temperatures, there was greater discrepancy between the predicted and the measured values of the kerf width. It can therefore be concluded that it is possible to predict the kerf width from the velocity data, but the first method of prediction, namely, that of using Figure 6.17 and the temperature data, is preferable.

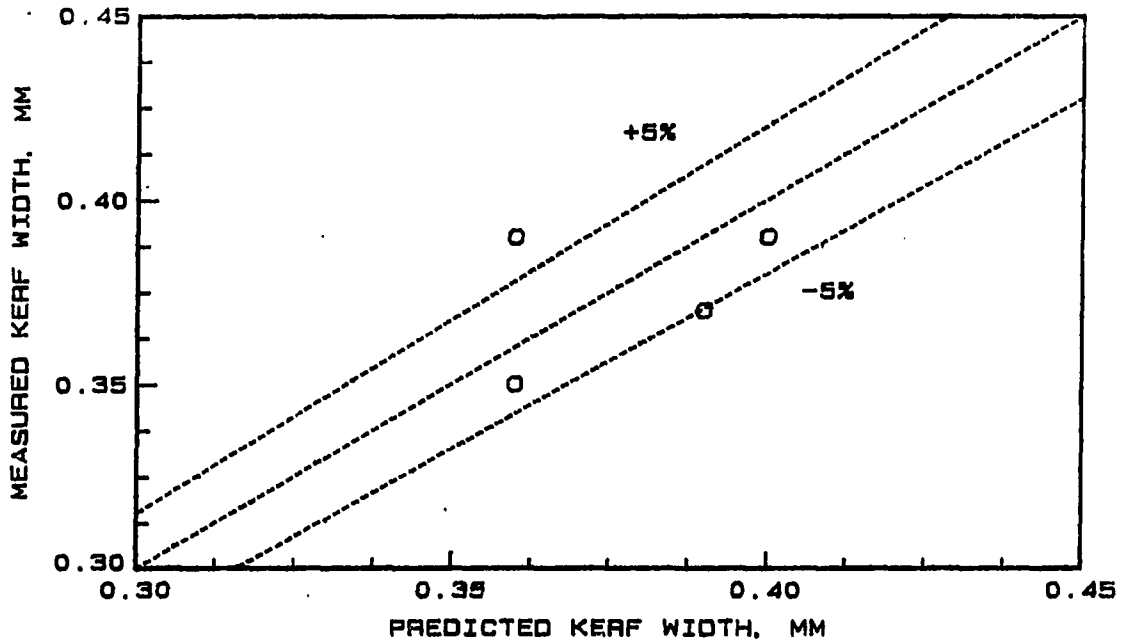


Figure 6.29: Comparison of measured kerf and kerf predicted from variable velocity data

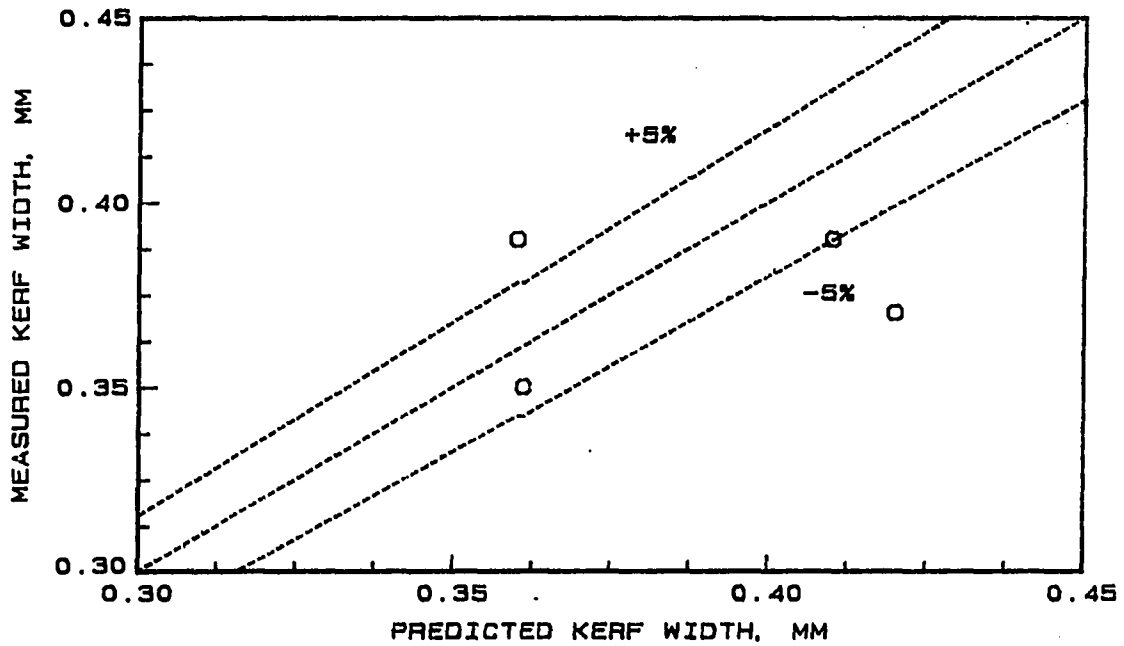


Figure 6.30: Comparison of measured kerf and kerf predicted from data at a velocity of 33.8 mm/s

Effect of Laser Power

In this section, the effect of the laser power on the kerf width and the temperature are discussed. The laser power was varied from 800 to 1200 W, in steps of 100 W. The laser beam velocity was maintained at a constant value of 33.8 mm/s, and the gas pressure was also kept constant at 207 kPa(gage). The convective heat loss and the heat produced by oxidation will, therefore, remain nearly constant for all values of the laser power. Increasing the laser power increases the energy input to the sample, and therefore it should affect the kerf width and the temperature.

Kerf width

Figure 6.31 shows the effect of the incident laser power on the kerf width of the cut sample. At the low and high ends of the range of power tested, i.e., around 800 and 1200 W, there was scatter observed in the kerf width data. The scatter in the data is observed to be a minimum at around 1000 W. This could be attributed to the observation made earlier that there exists an optimum maximum velocity for a set of experimental conditions at which the sample could be cut. The oxygen gas pressure used was 207 kPa, and the laser beam velocity was 33.8 mm/s. For these values of the gas pressure and beam velocity, the optimum value of the laser power is 1000 W. It was seen earlier, in the section on the effect of the beam velocity, that cutting at too low or too high a velocity produces high values of the kerf. At laser power values other than 1000 W, when the sample is being cut at a velocity of 33.8 mm/s, a velocity that is not the optimum value, is being used. The result is that the kerf width is wider.

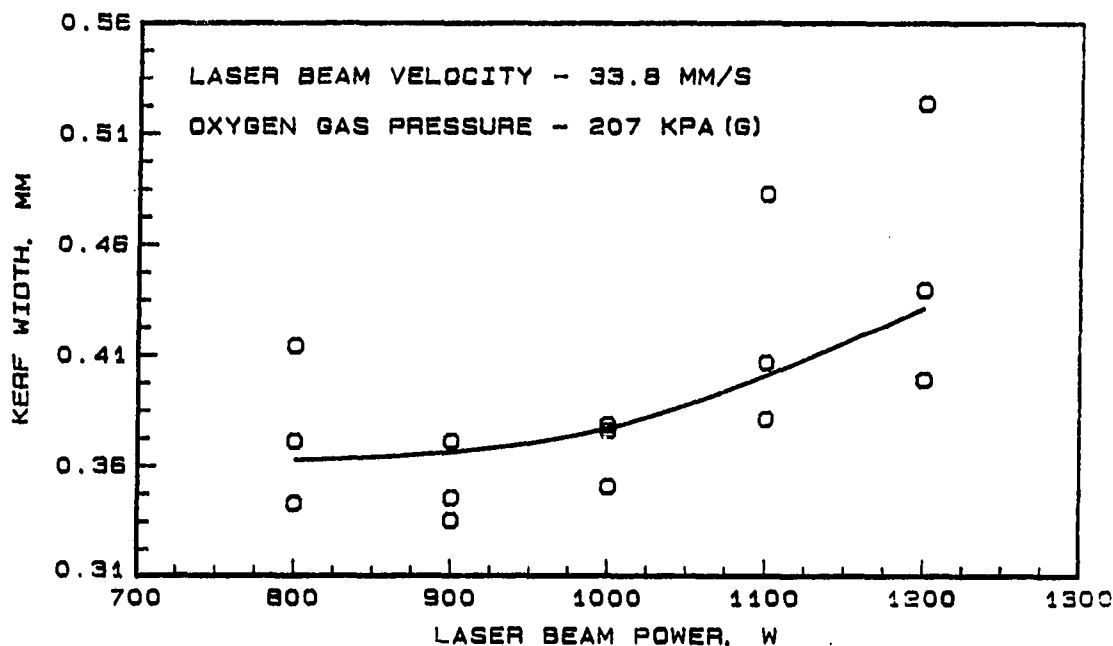


Figure 6.31: Kerf width dependence on incident laser beam power

The general tendency, as seen in Figure 6.31, is for the kerf width to increase with increasing laser power. The average increase in the kerf width was 20% for an increase of 50% in the laser power from 800 to 1200 W. Similar trends have been reported in the literature. Specifically, increases in kerf width values of 9% have been observed when the laser power increased by 15% from 1500 to 1700 W in cutting mild steel [56]. These results reported in the literature were performed at varying laser beam velocities, unlike in the present case where the experiments were at constant velocity. Hence, the percentage increase observed in the literature is higher than it is in the present research. Also, the range of laser beam power used was also different in the literature.

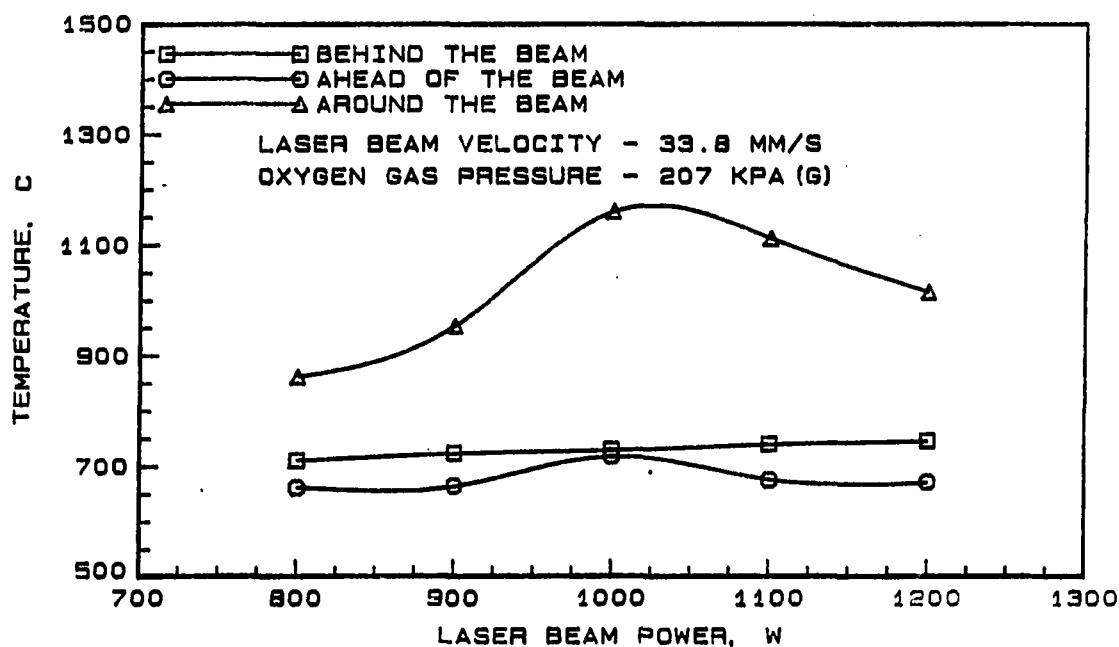


Figure 6.32: Surface temperature dependence on incident laser beam power

Surface temperature

The surface temperature was measured with the infrared sensor spot located ahead and behind the beam, and also surrounding the cutting zone. The average values of the surface temperature recorded by the infrared sensor are shown in Figure 6.32 for the three locations of the sensor spot. The temperature measured ahead of the beam showed only a slight increase with increasing laser power. The values recorded ranged from 661 to 718°C, with the highest temperature occurring at a laser power of 1000 W, which is where the coupling of the laser beam and the sample was the best.

Locating the sensor such that the sensor spot covered the entire cutting zone resulted in similar trends in the surface temperature, except that the temperature values were much higher. Values of recorded temperatures ranged from 861 to 1160°C,

with the highest value at the laser power of 1000 W. When the sensor was located to read at a location behind the cutting zone and the beam, the dissipative effects of the metal result in the temperature increasing with increasing laser power. The surface temperature increased from 710 to 746°C when the laser power increased from 800 to 1200 W. Increasing the laser power has the effect of increasing the energy input to the sample, and the surface temperature measured behind the cutting zone reflects this trend.

As in the sections on the effect of velocity and the gas pressure, the data on the temperature and the kerf is presented in the form of a ratio of the temperature-to-kerf width. Figure 6.33 shows the temperature-to-kerf ratio for the three cases for different values of the laser beam power. The trends in the ratio follow the trends in the surface temperature seen earlier. For the case of locating the sensor ahead the beam, the ratio varied from 1596 to 1979 °C/mm with the maximum value between 900 and 1000 W. When the sensor was located such that it surrounded the cutting zone, the ratio varied from 2300 to 3310 °C/mm, with the maximum at around 1000 W. These results show that when cutting at 33.8 mm/s and an oxygen gas pressure of 207 kPa(gage), the temperature was a maximum and the kerf width a minimum between 900 and 1000 W.

When the sensor was positioned to read behind the cutting zone, this trend in the temperature to kerf ratio was not observed. Instead, the ratio decreased from 2070 to 1869 °C/mm, due to the temperature increasing steadily and the kerf also showing a continuously increasing trend. It can, therefore, be concluded that locating the sensor such that the spot covered the entire cutting zone provides the best results

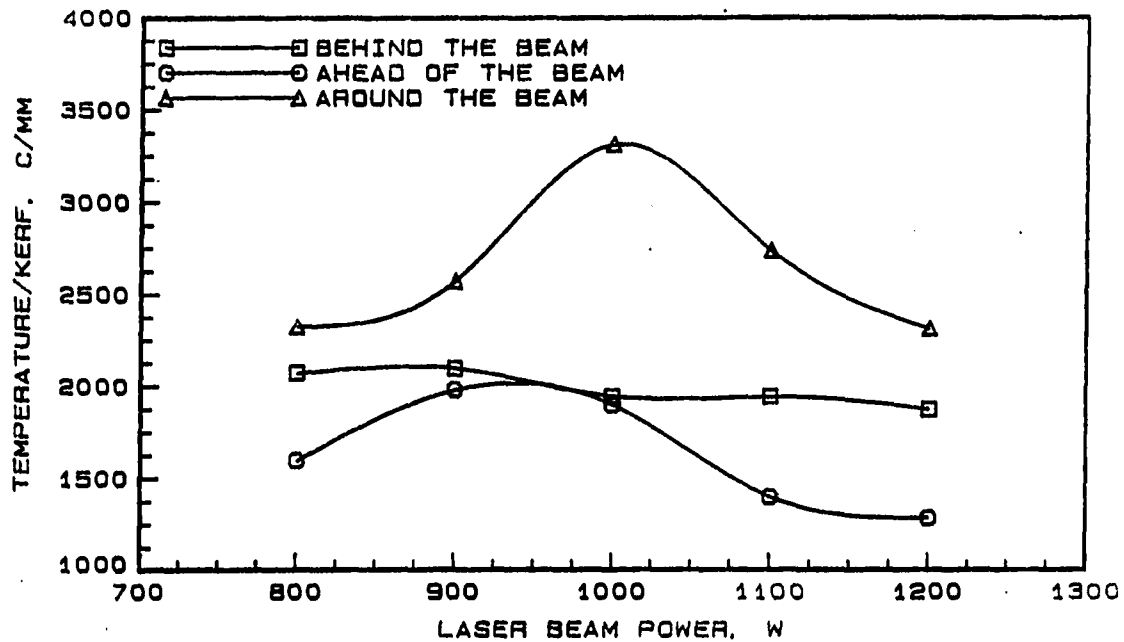


Figure 6.33: Surface temperature to kerf width ratio at different incident laser beam power

in terms of identifying the optimum operating conditions.

The ratio of the temperature and kerf is shown in Figures 6.34 and 6.35 at different surface temperatures. When the sensor spot was located behind the beam, the trend is for the ratio to decrease with increasing surface temperature. This is due to the increase in the kerf being higher than the increase in the surface temperature for increasing values of the laser power. When the sensor spot was located ahead of the beam, the ratio decreases with increasing surface temperature. It reaches a minimum at around 675°C before increasing again. The two trends in the ratio can be compared in Figures 6.16 and 6.17 for the case of varying beam velocity. It is seen that the trends in the ratio with increasing surface temperature are similar, indicating that cutting at a fixed velocity while varying the laser power is equivalent to cutting

at fixed power while varying the velocity of the beam.

Kerf width prediction

The observation that cutting at a fixed velocity while varying the laser power is equivalent to cutting at a fixed laser power while varying the velocity is used in this section to predict the kerf width. The energy input to the metal at any power and laser beam velocity can be calculated from,

$$Energy = \frac{(Power)(Length\ of\ sample)}{Beam\ velocity} \quad (6.28)$$

For example, at a laser beam power of 800 W and velocity of 33.8 mm/s, the energy input to the metal sample of length L mm is,

$$Energy\ Input = \frac{(800\ W)(L\ mm)}{33.8\ mm/s} \quad (6.29)$$

For the laser beam to input the same amount of energy as calculated from Equation 6.29 at a laser beam power of 1000 W, the laser beam should travel at a velocity of,

$$V_{equivalent} = \frac{(1000\ W)(33.8\ mm/s)}{800\ W} \quad (6.30)$$

which can be calculated to be 42.3 mm/s. Once this equivalent beam velocity is known, the kerf width can be found from the experimental data obtained earlier in the velocity experiments. This method was used to predict the kerf width for the power values from 800 to 1200 W, by first calculating the equivalent beam velocity at a power of 1000 W, and then using the kerf width obtained during the velocity experiments.

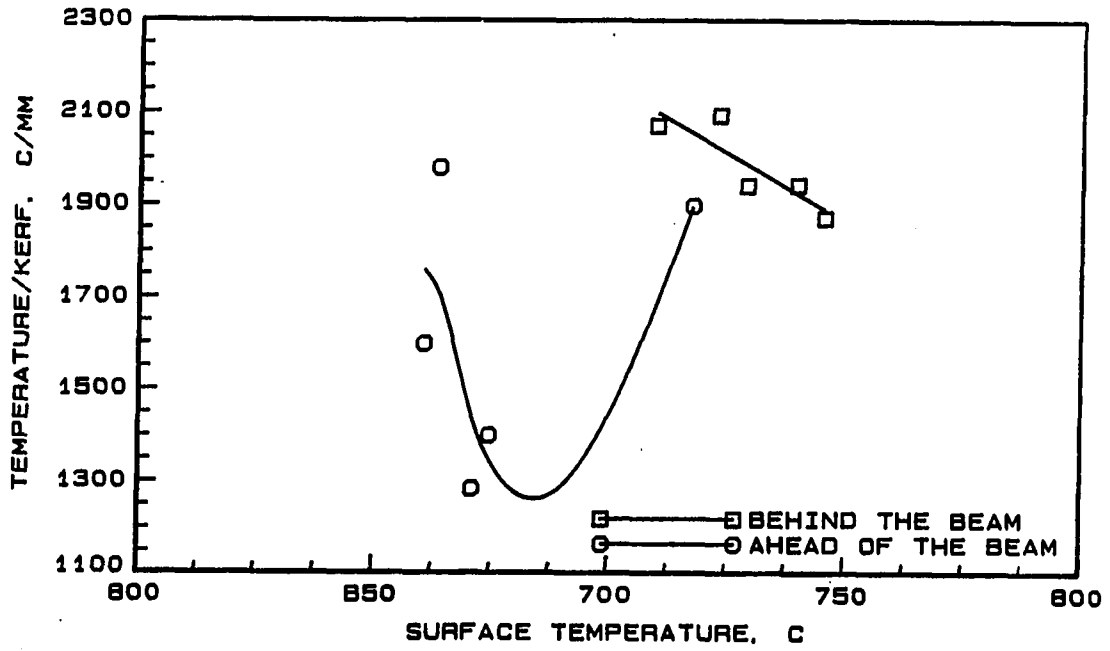


Figure 6.34: Temperature to kerf ratio and surface temperature for the sensor ahead and behind the beam

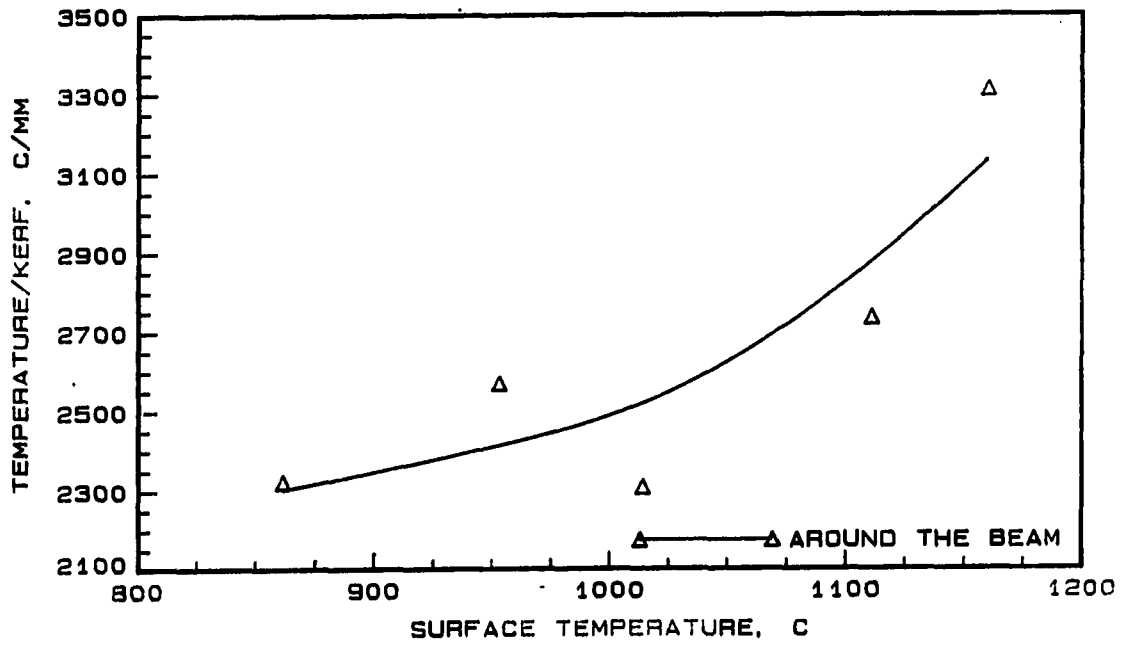


Figure 6.35: Temperature to kerf ratio and surface temperature for the sensor around the beam

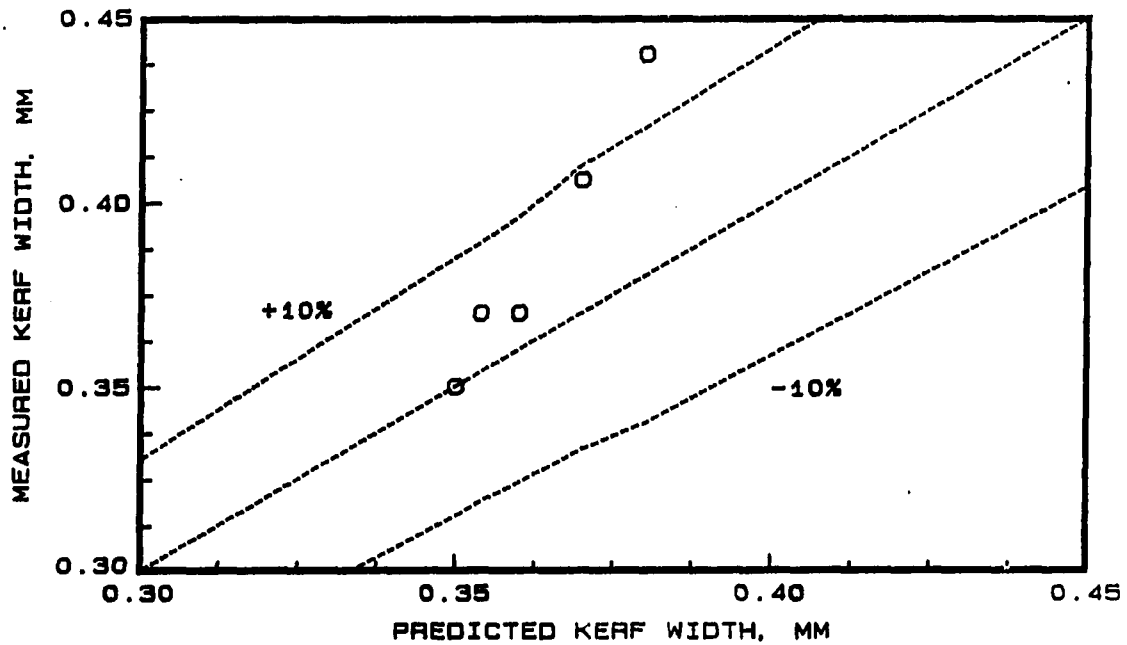


Figure 6.36: Predicted and measured values of kerf width for the case of varying beam power

The predicted and the actual kerf width are compared in Figure 6.36 where it is seen that the predicted results were within 10% of the measured values. The error was higher at the higher kerf width values, which were obtained at the higher laser power values. In fact, the errors increased with increasing difference between the laser power value and the reference value of 1000 W. Specifically, at values of power less than 1000 W, the predicted value was less than the actual, while at values of laser power greater than 1000 W, the predicted values were greater than the actual. This is probably due to the fact that cutting at 1200 W and 33.8 mm/s is not strictly the same as cutting at 1000 W and 28.2 mm/s.

Summary

This section summarizes the results of the effect of the laser process variables on the kerf width and the surface temperature. The conclusions of this chapter are given below.

The kerf width varied over the length of the cut, with the greatest variation at the leading and trailing edges of the workpiece. The kerf width was also not the same for the upper and lower surfaces. Over the bulk of the cut the lower-to-upper surface kerf width ratio was approximately equal to 0.7. No such simple value of the ratio was obtained for the ratio of the lower-to-upper surface kerfs at the leading and trailing edges of the workpiece. However, the ratio of the leading edge-to-center kerf on the upper surface was fairly constant at a value of 0.9. The trailing edge-to-center kerf ratio was also fairly constant with an average value of 1.4. It can be concluded that the kerf at the center of the cut is a fairly good indicator of the kerfs on the lower surface at the center, and on the upper surfaces at the trailing and leading edges of the workpiece. It was not possible to predict the kerf on the lower surfaces at the leading and trailing edges of the sample.

The kerf width on the upper surface at the center of the workpiece was a minimum at an optimum velocity of approximately 34 mm/s. The surface temperature measured with thermocouples mounted away from the cut, showed to be dependent on the kerf. The kerfs for a second set of experiments were predicted with the temperature to kerf correlation from an earlier run, and the results compared to measured values. The predicted and measured kerf widths agreed within $\pm 5\%$ accuracy. Measurements made with the infrared sensor indicated that the temperatures measured

with the sensor spot surrounding the cutting region showed observable dependence on the kerf and the beam velocity. In general, the temperature increased with increasing beam velocity. The temperature-to-kerf ratio also showed a tendency to increase with increasing surface temperature measured.

The oxygen gas acted to produce cooling of the cutting region and the surrounding area, and at the same time, produced energy due to the exothermic oxidation reaction with the metal. Both the cooling effect and the exothermic energy produced increased with increasing gas pressures. The heat removed by the convective action of the jet was approximately a half to one-third of the heat produced by the oxidation process. For a constant laser power input of 1000 W, the convective cooling varied from 10 to 17%, while the heat of oxidation ranged from 30 to 40%, both for gas pressures between 69 and 207 kPa, gage. The kerf width was not a strong function of the gas pressure; in general, however, the kerf tended to decrease with increasing gas pressure. When the temperature was measured around the cutting region with the infrared sensor, the temperature increased with increasing gas pressure. The temperature also depended on the kerf width, and it was possible to predict the kerf from the temperature data to within 5% of the measured values.

The laser beam power had significant effects upon the kerf, an increase in beam power resulting in an increase in the kerf width. The temperature measured with the infrared sensor with the focal spot surrounding the cutting region was a maximum at a laser power of 1000 W. At this power value, the velocity of the beam that was used, 33.8 mm/s, was the maximum optimum velocity. For cases of laser beam power greater than 1000 W, the velocity of 33.8 mm/s used was too slow, resulting

in a lowering of the temperature. Kerf width could be predicted with an alternate method of "equivalent power" to within $\pm 10\%$ accuracy.

CHAPTER 7. RESULTS FOR HEAT-AFFECTED ZONE

The heat-affected zone is the second most important measure of the quality of a laser-cut and is the region in the material that has been thermally affected by the laser energy. The heat-affected zone, in one form or the other, is present in both argon- and oxygen-assisted cutting.

The heat-affected zone usually consists of the visible oxidation region on the surface adjacent to the cut and the heat-treated or hardened region beneath the visible oxide. Figure 7.1 shows a photograph of the visible oxidation region adjacent to the laser-cut, and Figure 7.2 shows the heat-treated region underneath the oxide layer, for the case of oxygen-assisted laser cutting. The heat-treated region was made visible by first polishing and then treating the surface with a 10% Nital solution (a mixture of nitric acid and methanol) as described in Chapter 4.

The basic microstructure of the steel is ferrite, and this is seen as the white regions in Figure 7.2. When heat-treated, the carbon in the steel forms grains of pearlite which are seen as the dark regions in the same figure. Since the procedure to measure this hardened region can be extremely tedious, the standard practice in the literature has been to measure the visible oxidation region and to report this as the heat-affected zone [56].

The visible oxidation region, which is present only in the case of oxygen-assisted



Figure 7.1: The visible oxidation heat-affected zone adjacent to the cut

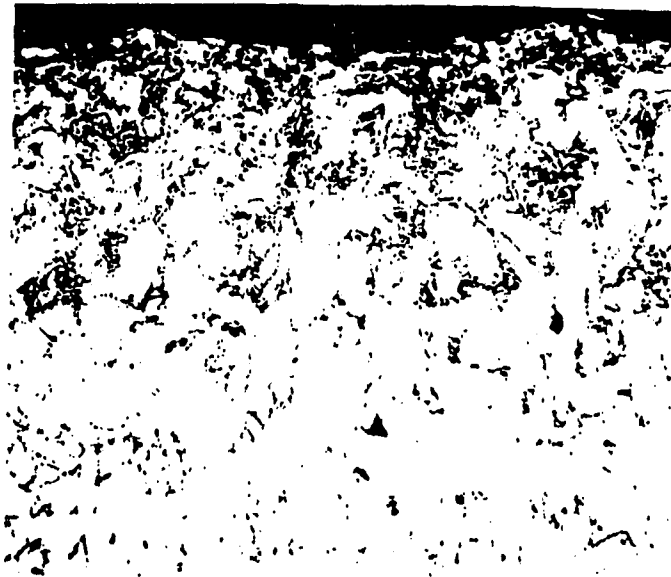


Figure 7.2: The heat-treated metal beneath the visible oxidation region

laser cutting, can be easily removed by any simple surface treatment procedure. It does not, therefore, qualify as permanent damage caused to the material by the cutting process. The heat-treated region, on the other hand, is permanent in nature and cannot be removed. Hence, it is important to understand the relationship between the heat-treated region, which is the actual heat-affected zone, and the oxidation region which is oftentimes used as the measure of the heat-affected zone.

A review of the literature did not yield any study that compared measurements of the heat-affected region and the oxidation region. As part of this research, therefore, a study was conducted to compare measurements of these two regions. The emphasis of the study was to test the hypothesis that the oxidation heat-affected region was a good indicator of the heat-treated region. The results and the conclusions of this study are presented in the section below.

Oxidation and Heat-Treated Regions

The procedures for measuring the visible oxidation region and the heat-treated region were described in detail in Chapter 4. The results of a micro-hardness test on a sample is shown in Figure 7.3. Indentations resulting from the micro-hardness test quite visible. Hardness profiles on samples of 3.2 mm thick, AISI 1018 steel cut at different laser beam velocities are shown in Figure 7.4 for the upper surface and Figure 7.5 for the lower surface. All of the samples were cut at a laser power level of 1000 W and at an oxygen gas pressure of 207 kPa, gage. It is seen from the figures that the typical hardness value of the unaffected material ranged from a Diamond Point Hardness (DPH) number value of 240 to 220. Since the standard error in the

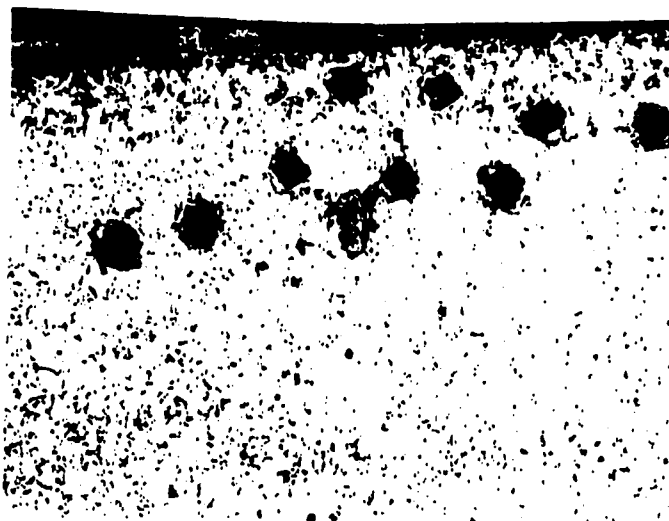


Figure 7.3: Photograph of the hardened region with the diamond-point indentation marks of the hardness testing process

estimation of the hardness number was $\pm 5\%$, the hardness number for the unaffected material was taken to be 230 ± 10 DPH. This was also the cut-off value of the hardness number for the determination of the heat-treated region, as explained below.

Figures 7.4 and 7.5 show all the characteristics of a typical hardness curve for a heat-treated object. Close to the edge of the cut, the hardness value is extremely high (>400 DPH) which then drops rapidly to a value of about 210 DPH, a value lower than the hardness number of the unaffected material. This is the "softened" region that separates the hardened and the unaffected regions. For the upper surface this occurs at distances of 0.1–0.2 mm from the edge, while for the lower surface, it occurs at 0.2–0.4 mm from the cut-edge. Beyond the softened region, the hardness value increases gradually to the value of 230 DPH.

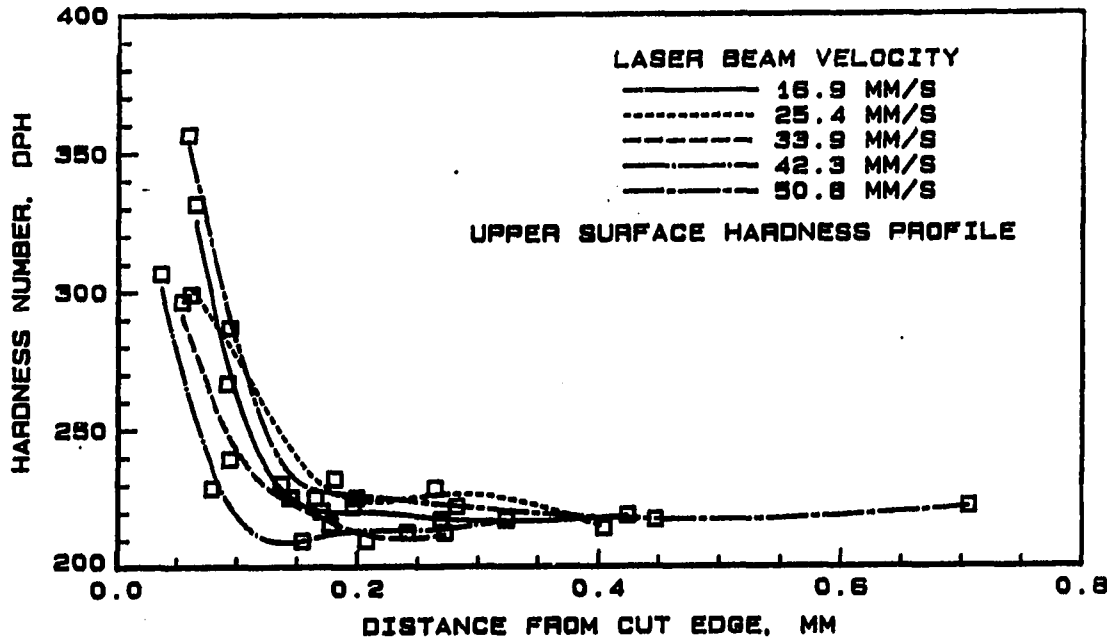


Figure 7.4: Hardness profile for the upper surface perpendicular to the edge of the cut

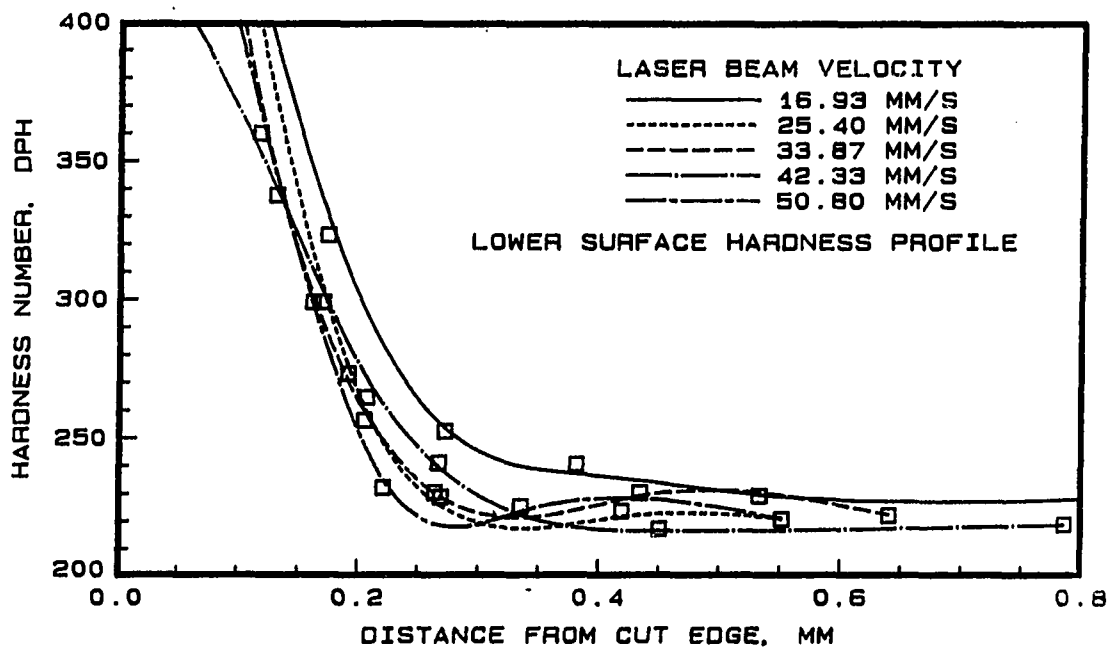


Figure 7.5: Hardness profile for the lower surface perpendicular to the edge of the cut

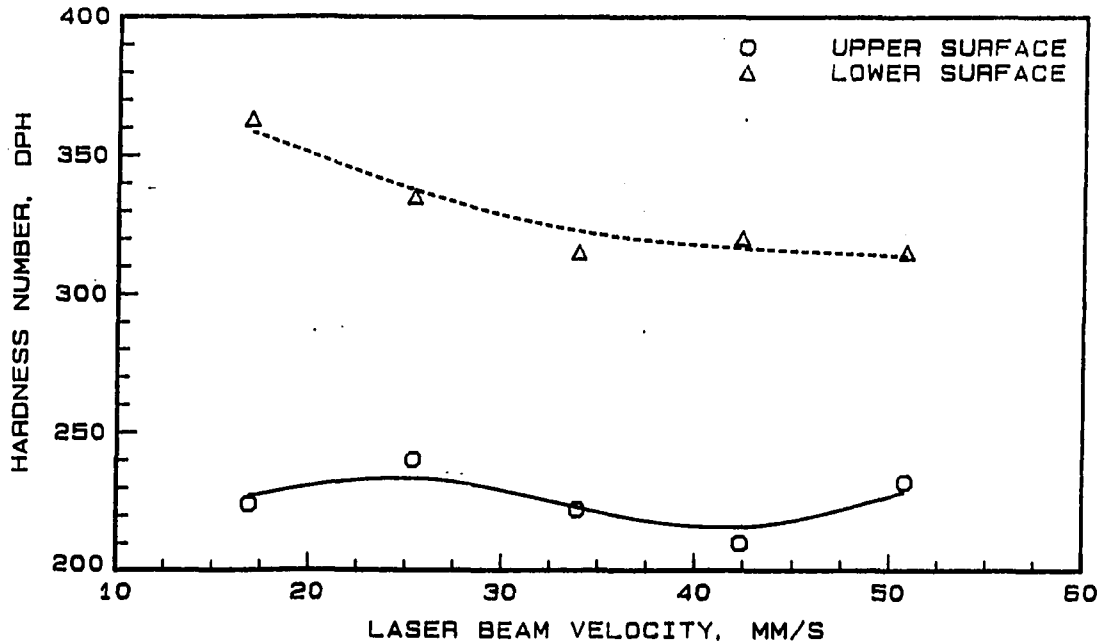


Figure 7.6: DPH hardness values at a distance of 0.15 mm from the edge of the cut

Figure 7.6 shows the hardness values at a fixed distance from the cut edge, as a function of the laser beam velocity. The hardness decreases with increasing laser beam velocity for both surfaces. However, the hardness of the lower surface is much higher than that for the upper surface. This can be attributed to the increased energy available at the lower surface as discussed earlier in Chapter 6.

The heat-treated distances at different velocities for the two surfaces are shown in Figure 7.7. The lower surface is heat-treated to about twice the distance compared to the upper surface. The results also show that the heat-treated distance decreases with increasing velocity; for the upper surface the decrease was about 5% and for the lower surface, about 15%.

The results of the heat-treated HAZ can now be compared with the oxidation HAZ shown in Figure 7.8. Similar to the heat-treated HAZ, the oxidation HAZ on

the lower surface is twice that on the upper surface. Unlike the heat-treated HAZ, however, the oxidation region shows a greater dependence on the velocity of the beam. In addition, the percentage decrease in the heat-affected region was greater on the upper surface in the case of oxidation HAZ, which is exactly opposite of the heat-treated HAZ. For the upper surface, the oxidation region decreases by 40% when the velocity increases from 16.93 to 50.8 mm/s. This decrease is only about 20% for the lower surface over the same range of beam velocity.

To test the hypothesis that the oxidation HAZ predicts the heat-treated HAZ, the two measures of the heat-affected zone are compared in Figure 7.9. It can be seen from the figure that the oxidation HAZ is equivalent to the heat-treated HAZ within a error of $\pm 25\%$ for the lower surface; the error is slightly larger for the upper surface. The error decreases with increasing values of the oxidation HAZ. Especially for the lower surface, the oxidation HAZ is a good indicator of the heat-treated HAZ since this surface is characterized by high values of oxidation HAZ.

To study the variation of the heat-treated HAZ with depth in the sample, the sample was sectioned and the hardness profile obtained at the center of the sample section. Figures 7.10 and 7.11 compare the heat-treated hardness profile at the upper and lower surfaces to that at the center of the sample, i.e., at a depth of 1.6 mm from the top surface, for two velocities of the laser beam. As seen earlier, the hardness at the lower surface is much higher than that at the upper surface. However, the hardness is seen to go through a minimum midway between the upper and lower surfaces. The figures also show that the hardness values at all sections of the cut metal are higher at the higher velocity. As in the earlier cases that were discussed,

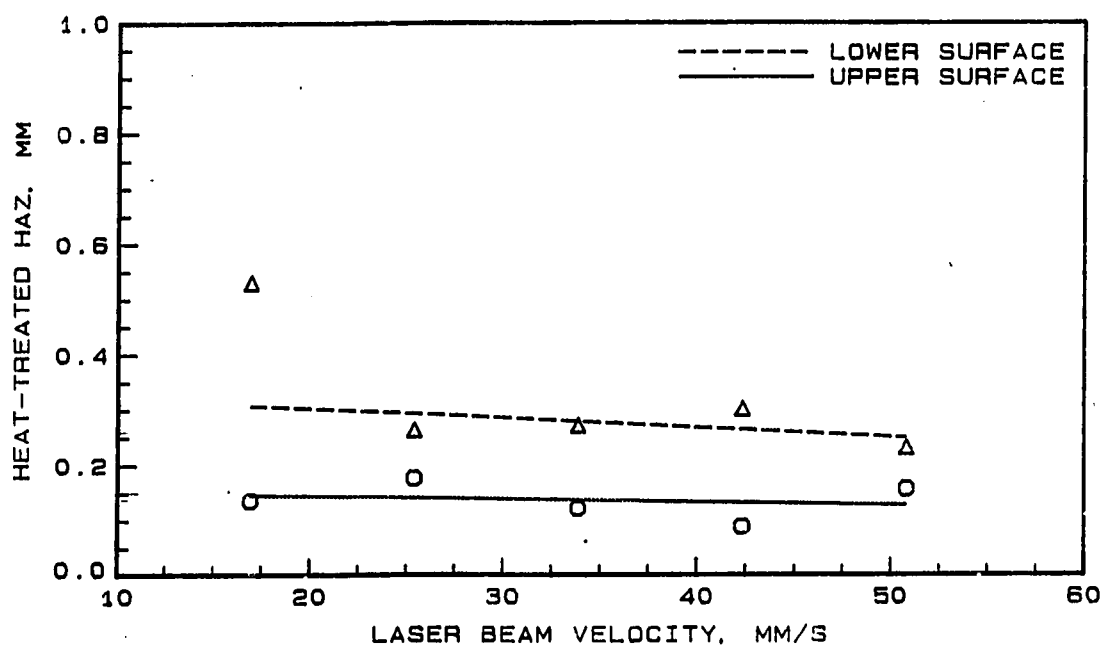


Figure 7.7: Heat-treated HAZ for the upper and lower surfaces at different beam velocities

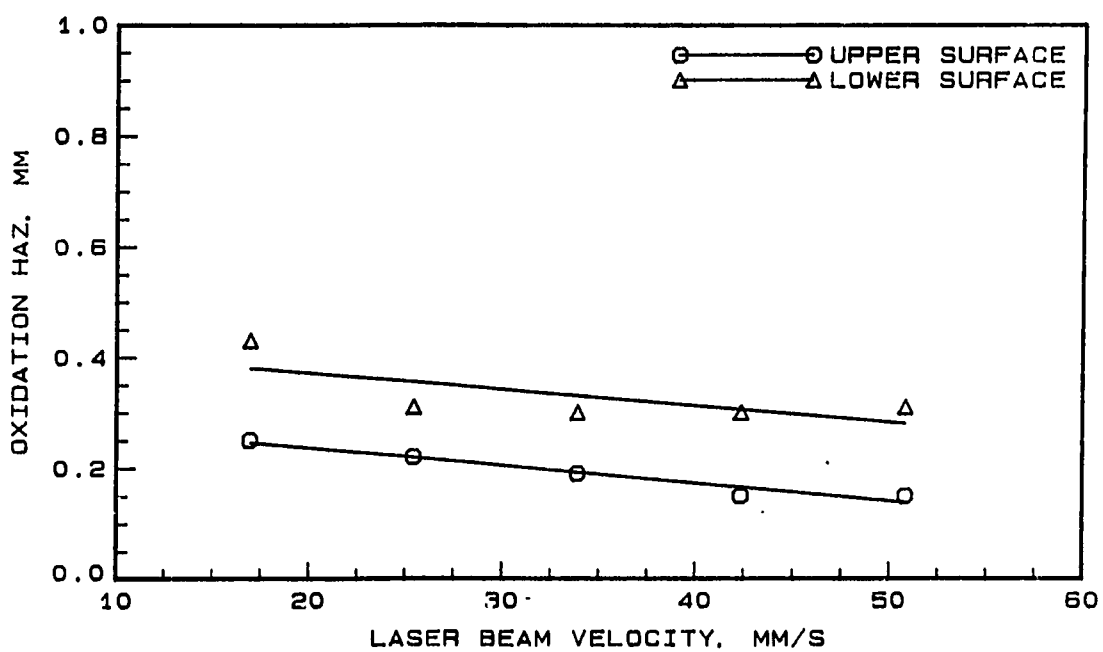


Figure 7.8: Oxidation HAZ for the upper and lower surfaces at different beam velocities

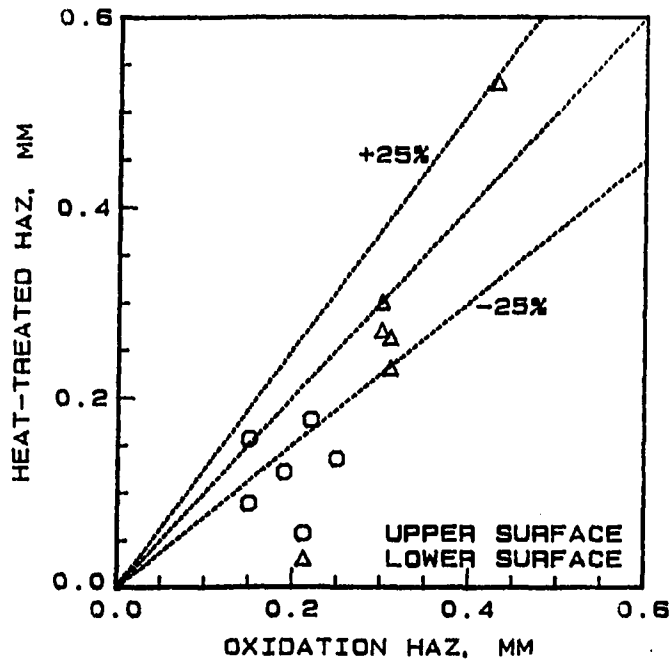


Figure 7.9: Comparison of oxidation and heat-treated HAZ for the two surfaces

the hardness values decrease gradually to the value for the unaffected material, after first going through the softened region minima.

The heat-treated depth at the different sections are compared in Figure 7.12. It can be observed from the figure that the heat-treated distance is a maximum at the lower surface for both the beam velocities shown. The heat-treated region is a minimum between the upper and lower surfaces. It is also seen that the HAZ decreases only slightly with increasing beam velocity, which is in agreement with our earlier observations.

HAZ Variation with Position

Kerf width and the heat-affected zone vary with position along the cut as shown in Figure 7.13 which shows the results for one set of experimental conditions. The

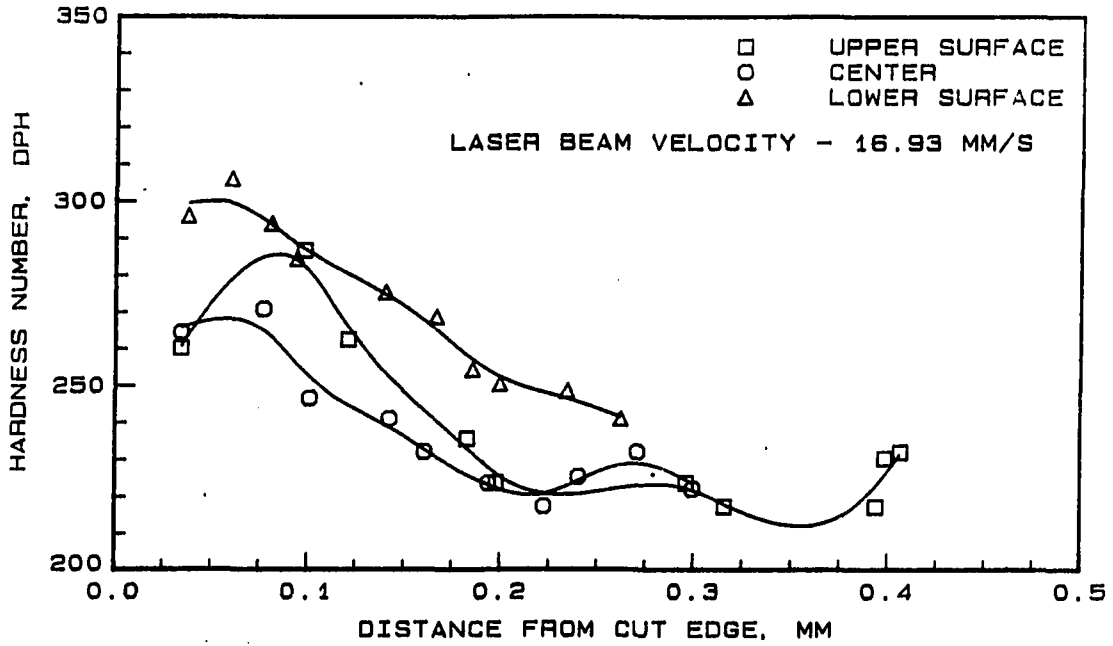


Figure 7.10: Hardness profile at different sections of the cut sample for a beam velocity of 16.93 mm/s

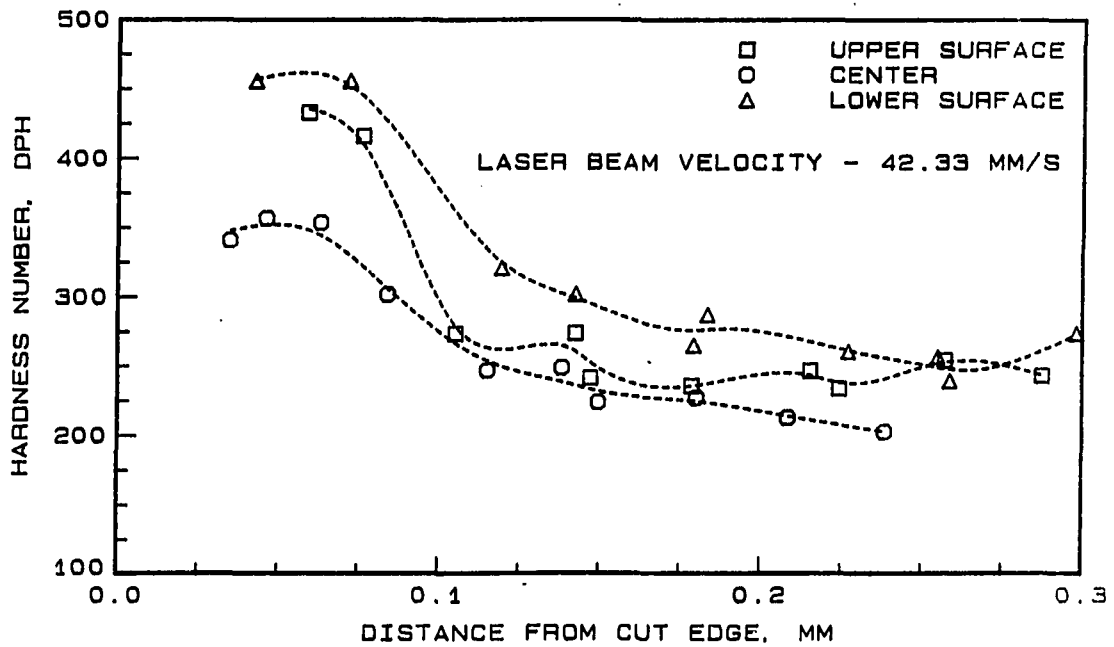


Figure 7.11: Hardness profile at different sections of the cut sample for a beam velocity of 42.33 mm/s

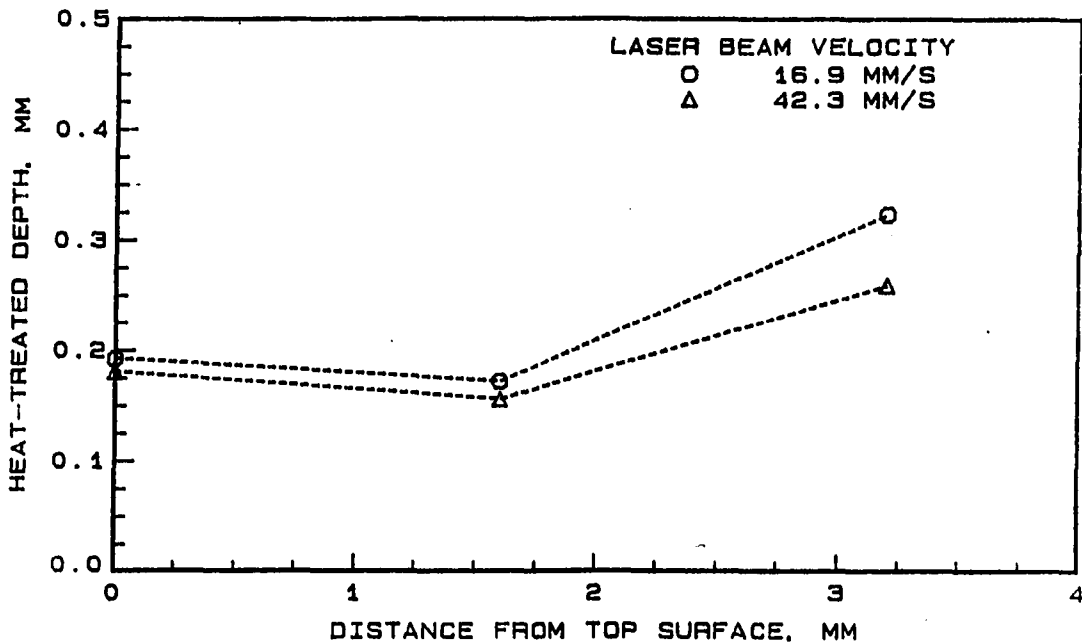


Figure 7.12: Heat-treated depth at different sections of the cut sample for two different beam velocities

figure shows the variations only from the start of the cut for a total length of 60 mm, not including the trailing edge of the cut. Both the kerf width and the heat-affected zone vary significantly at the start of the cut. Unlike the kerf width, the HAZ is seen to be fairly constant over the bulk of the cut. It will be shown later that the heat-affected zone varies significantly at the trailing edge also. In this section of the chapter, the variation of the HAZ between the upper and lower surfaces, and the variation with position along the cut are discussed. It is shown that the HAZ on the upper surface at the center of the cut is a fairly good indicator of the HAZ at the other locations of the cut.

The HAZ on the upper surface at the center of the sample is compared with that on the lower surface in Figure 7.14. The figure shows the ratio of the HAZ on the

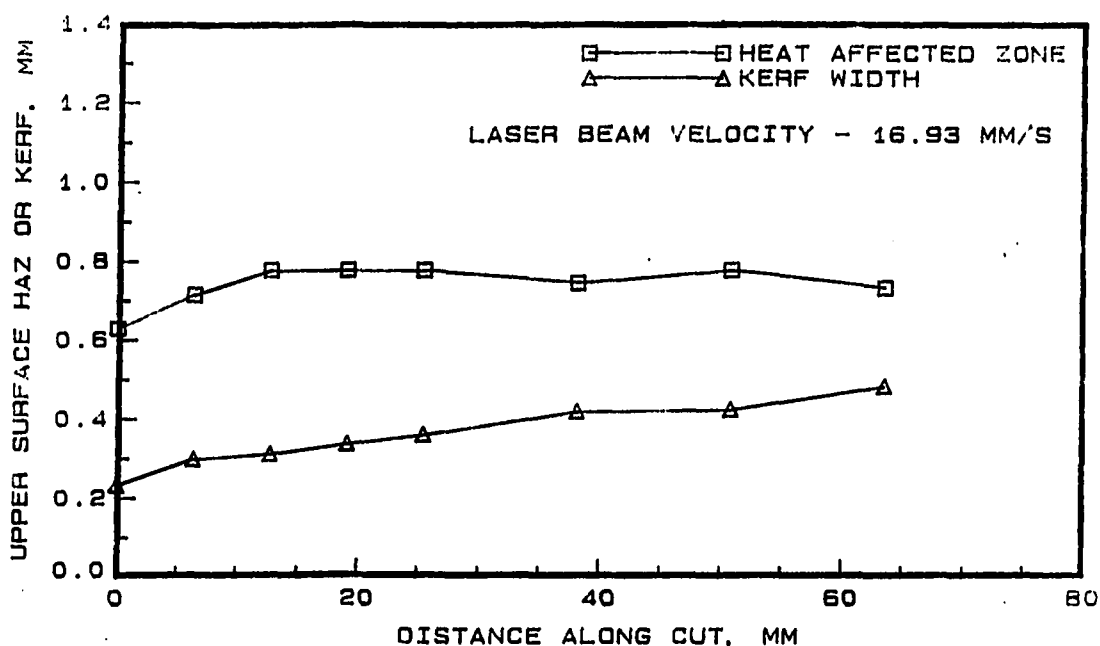


Figure 7.13: HAZ and kerf width variation with position along the cut

lower surface to the HAZ on the upper surface as a function of the HAZ on the upper surface. It is seen that the lower surface HAZ is, on an average, twice that on the upper surface. The figure also shows that nearly all of the data fall within a band of $\pm 25\%$.

One possible reason for the higher HAZ on the lower surface could be the absence of the cooling effect of the gas-jet. It was seen earlier in Chapter 6 that the kerf width was narrower on the lower surface. It was suggested that this could be due to a decrease in the peak intensity of the beam at the plane of the lower surface. Since only the peak intensity of the beam is reduced at the lower surface, a decrease in kerf width, will therefore, result in more energy being available for heating the uncut sample. Hence the oxidation reaction can spread farther on the lower surface, thus producing a wider HAZ.

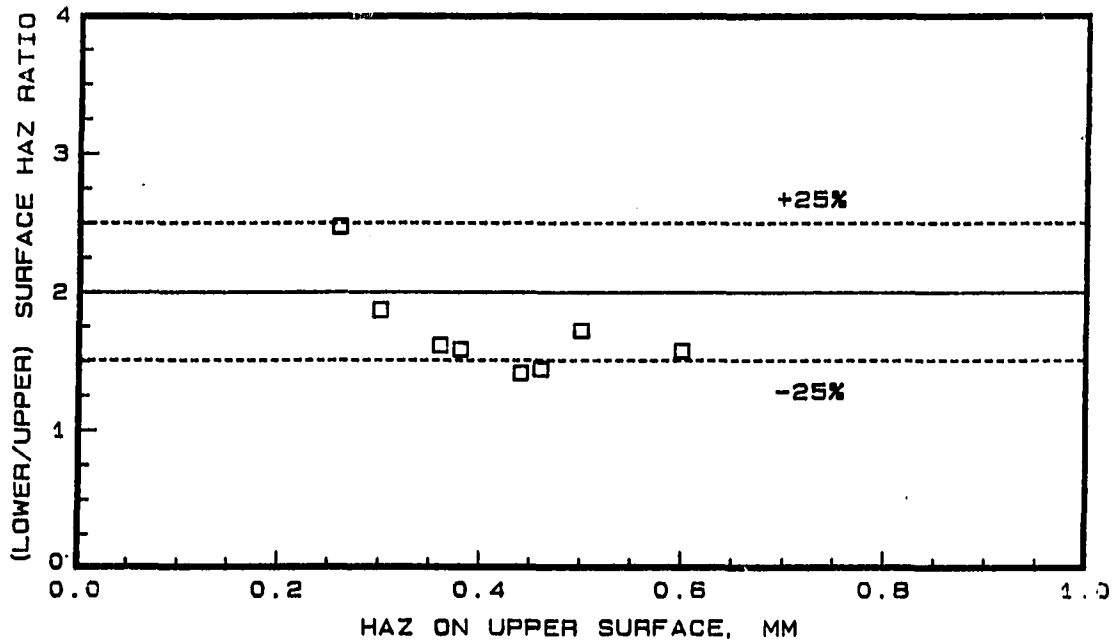


Figure 7.14: Lower to upper surface HAZ ratio variation with upper surface HAZ at the sample center

This behavior was also observed in cutting samples of different thickness. Figure 7.15 shows the lower to upper surface HAZ ratio for three different sample thickness. It is seen that the ratio increases with increasing sample thickness. However, the increase in the ratio was within a band of $\pm 25\%$. At the higher thickness values, the cut quality was not as good as at the lower thickness of 3.2 mm. Also, the peak intensity of the beam was reduced even further (than the value 33% for the 3.2 mm thickness sample, estimated in Chapter 6), thus leading to a smaller kerf and, therefore, a wider HAZ at the lower surface. For samples of all thicknesses at the center of the cut, the oxidation HAZ on the upper and lower surfaces can be approximated by,

$$\frac{\text{Lower surface center HAZ}}{\text{Upper surface center HAZ}} \approx 2 \quad (7.1)$$

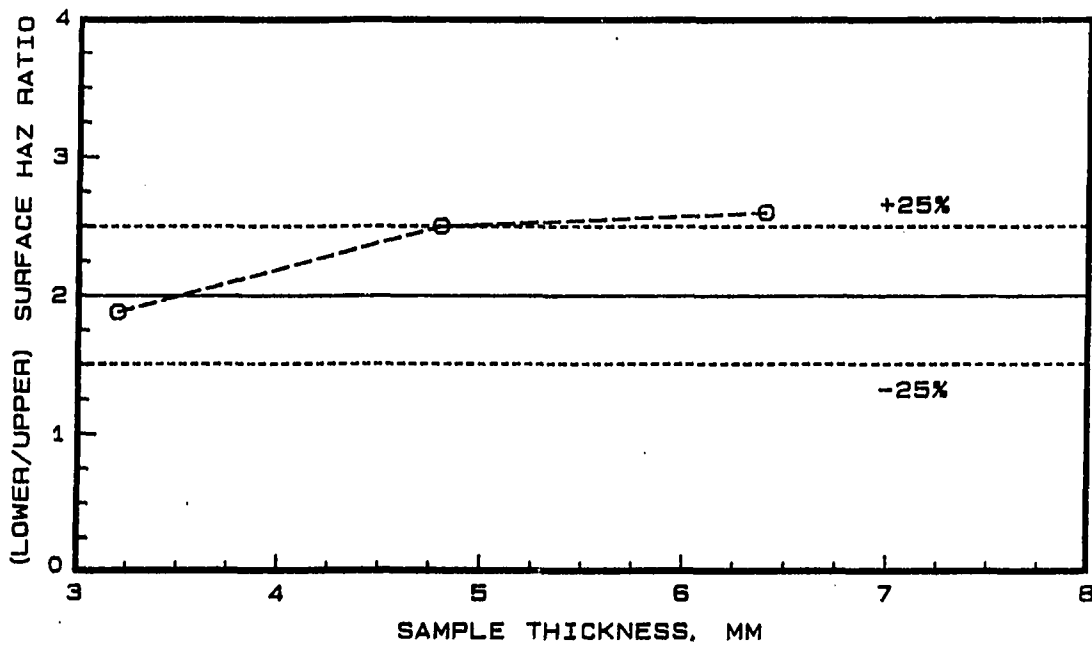


Figure 7.15: Lower to upper surface HAZ ratio variation with sample thickness

Similar behavior was also observed at the leading and trailing edges of the cut. Figure 7.16 shows the ratio of the lower to upper surface HAZ at the leading and trailing edges of the cut. The ratio is close to two particularly at the leading edge at high values of the HAZ, which is obtained at low laser beam velocities. A good cut, defined as a cut that produce no dross attachment at the leading edge, is initiated only at low beam velocities which leads to a HAZ ratio of two. This value at the leading edge is the same as the value at the center of the cut. At high beam velocities, the upper surface HAZ is low; however, a good is not initiated at the leading edge, resulting in a higher than usual HAZ at the lower surface of that edge. The HAZ ratio, therefore, is higher at low HAZ values, which corresponds to high beam velocities. The same argument can be made for the HAZ behavior at the trailing edge of the

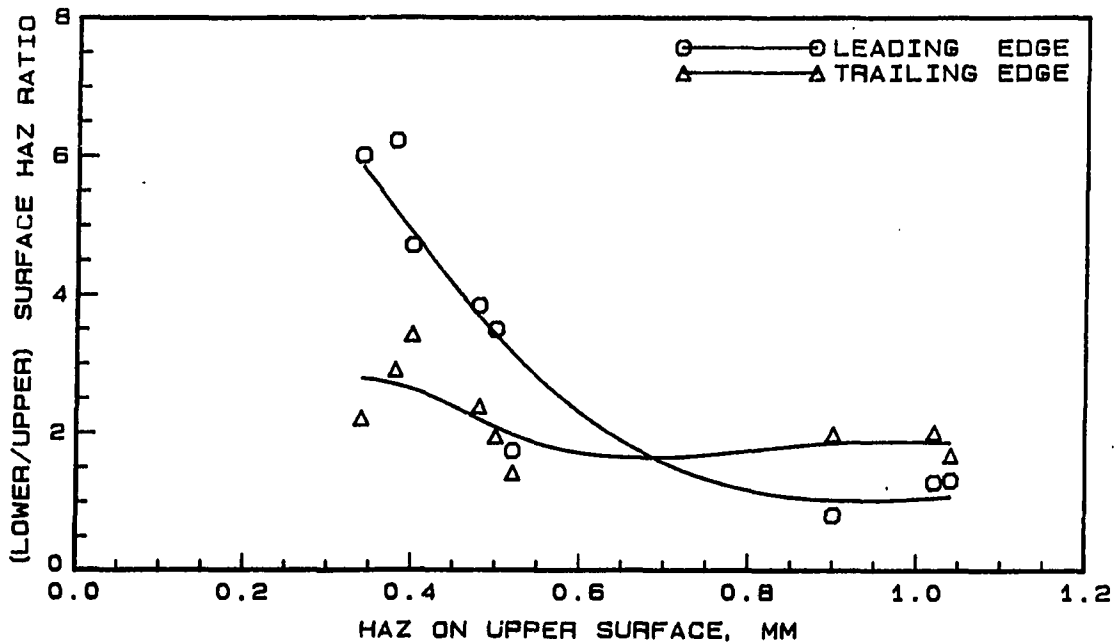


Figure 7.16: Lower to upper surface HAZ ratio variation with upper surface HAZ at the sample edges

cut. For samples of all thicknesses, at the edges of the cut, the oxidation HAZ on the upper and lower surfaces can again be approximated by,

$$\frac{\text{Lower surface edge HAZ}}{\text{Upper surface edge HAZ}} \simeq 2 \quad (7.2)$$

Figure 7.17 shows the ratio of the HAZ at the center of the sample to that at the edges, for the upper surface alone. The ratio is a little over one at both the edges for most of the cases. As in the previous discussions, it is at high velocities of the beam that there is greater uncertainty of obtaining a good cut at the leading edge. This, in turn, leads to HAZ values that are unpredictable. For most of the cases, however,

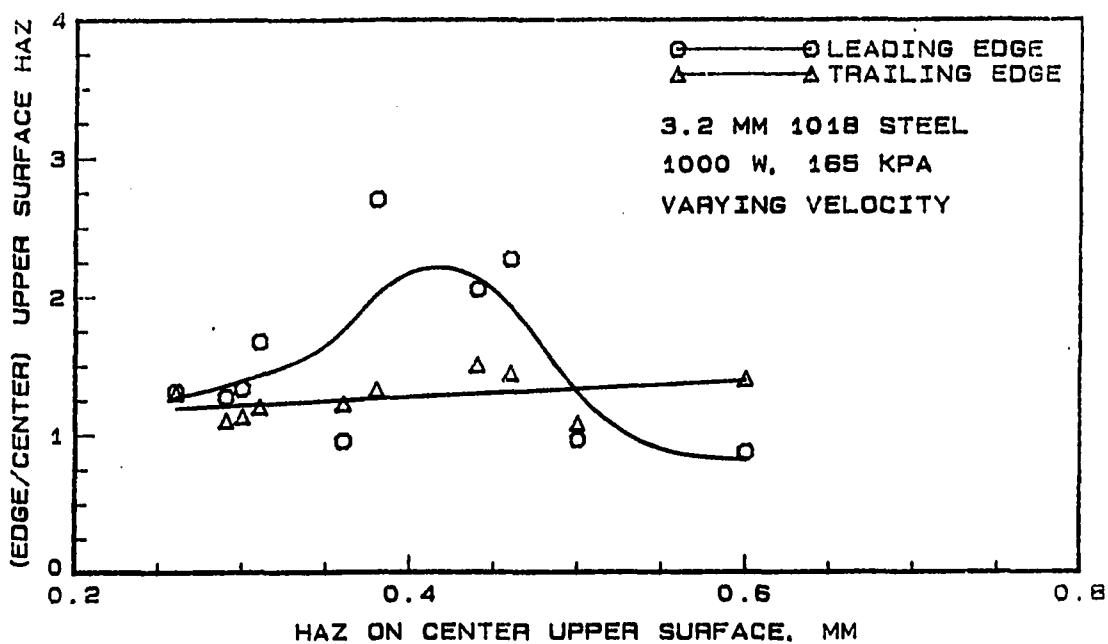


Figure 7.17: Center to edge HAZ ratio variation for the upper surface

the HAZ at the upper surface at the edges can be approximated by,

$$\frac{\text{Leading Edge HAZ}}{\text{Center HAZ}} \simeq 1.2 \quad (7.3)$$

$$\frac{\text{Trailing Edge HAZ}}{\text{Center HAZ}} \simeq 1.2 \quad (7.4)$$

In conclusion, the HAZ at the center of the cut on the upper surface is a fairly good indicator of the HAZ at all other locations along the cut. On the upper surface, the HAZ is fairly constant over the bulk of the length of the cut. For the upper surface, at the leading and trailing edges the HAZ can be approximated by the Equations 7.3 and 7.4. At all locations along the cut the HAZ on the lower surface was twice that on the upper surface when a good cut was obtained. Henceforth, in all discussions of HAZ, only the HAZ at the center of the cut on the upper surface will

be considered, with the understanding that if HAZ at any other location is desired the aforementioned approximations would be used.

Effect of Laser Beam Velocity

In this section the effect of laser beam velocity on the HAZ is discussed. This is followed by a discussion on the results of the effect of the beam velocity on the surface temperature. The results on surface temperature include the measurements made by both thermocouples and the infrared sensor.

Heat affected zone

As seen earlier in Chapter 6, the amount of energy absorbed by the sample is a strong function of the laser beam velocity. Since HAZ is directly dependent upon the amount of energy available, it can be expected that the beam velocity strongly influences the width of the HAZ.

The dependence of HAZ on the velocity is shown in Figure 7.18 where the upper surface HAZ at the center of the cut is plotted against velocity of the laser beam. The HAZ decreases from 0.74 mm at 16.93 mm/s to 0.36 mm at 50.8 mm/s, which is a decrease of 50% in the HAZ value for an increase of 200% in the laser beam velocity. These results are in good agreement with those reported by Steen and Kamalu [56] except that their results were not clear as to whether they are for the upper or lower surface, or both. The results of Steen show that the HAZ initially decreases with increasing beam velocity, but beyond a certain optimum maximum velocity, the HAZ begins to increase again. This type of behavior was detected in our experiments only

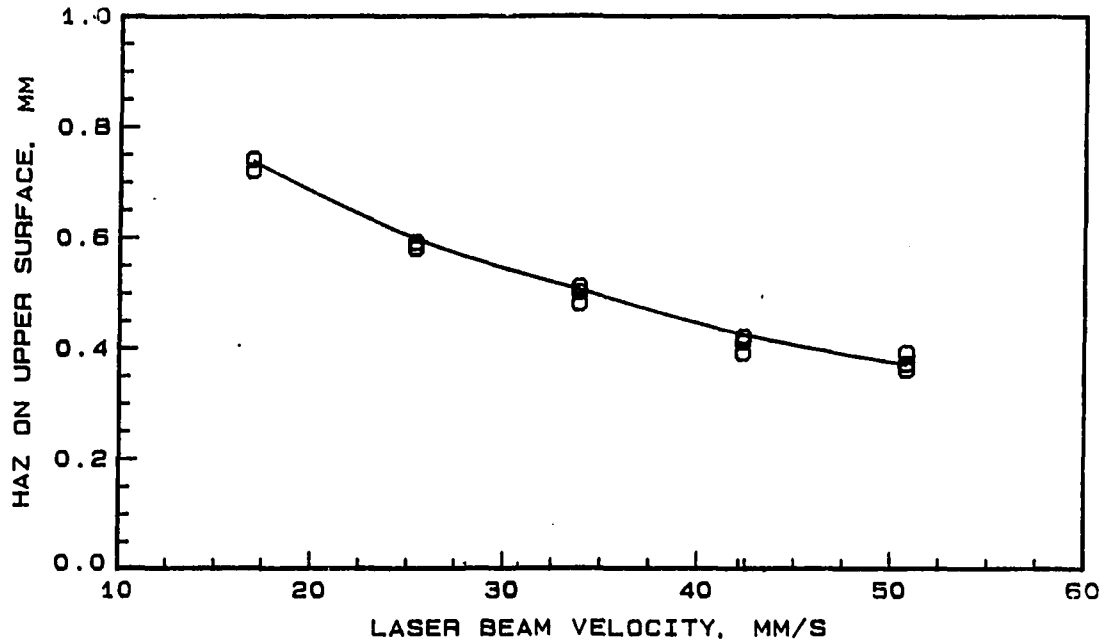


Figure 7.18: Effect of laser beam velocity on the HAZ at the center of the cut for the upper surface

on the lower surface and not for the upper surface. Even at the lower surface, the increase detected after the minima was not as high as those reported by Steen and Kamalu. This could be due to several reasons with the chief among those reasons being that in this study the experiments were conducted by increasing velocity only up to the point where a fairly good cut could be obtained. A fairly good cut was taken to be one where there was little dross attachment on the lower surface. The results presented by Steen are for cases where excessive dross attachment was observed on the lower surface, and, therefore higher HAZ was reported.

Surface temperature

Surface temperatures were measured with thermocouples and infrared sensors. The thermocouple measurements were made at a distance of 4.8 mm from the line of cut, while the infrared sensor recorded temperatures at the line of cut itself. The temperatures measured with the infrared sensor are shown to be a function of the location with respect to the beam, i.e., the cutting front. Three different locations of the sensor were chosen, namely, ahead of the beam, behind the beam, and, at the beam and metal interaction point. The relative merits of each of these locations of the infrared sensor, and the differences in the results obtained with the sensor and the thermocouples are also discussed. This section also discusses a radiation analysis which leads to a possible method of predicting the HAZ at the center of the cut from the infrared sensor temperature measurement. In all discussions of the HAZ, only the HAZ at the center of the cut on the upper surface is used. If HAZ at any other location is required, then the relationships presented in the previous section could be used.

Thermocouple measurements As discussed in Chapter 6, the energy input to the metal decreases with increasing beam velocity. It has also been shown in earlier sections that the oxidation HAZ and the kerf width varied with the beam velocity. This implies that the amount of energy that is available for heating the uncut metal also depends upon the velocity of the beam. Surface temperature measurements made on the uncut sample should show a dependence on the oxidation HAZ.

The surface temperature rise above room temperature and the HAZ variation are

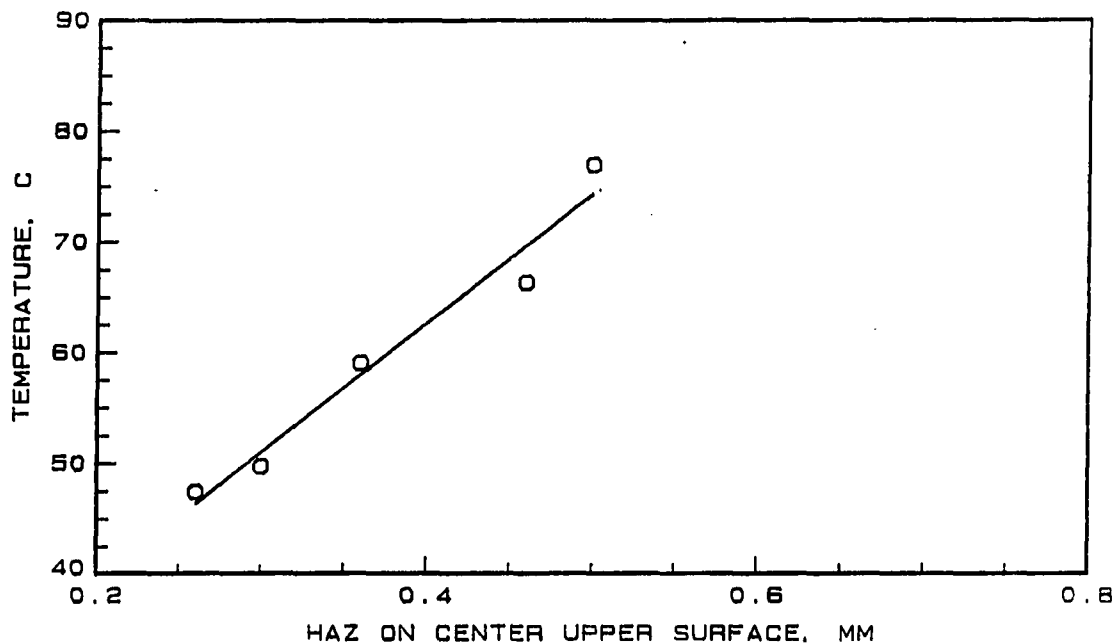


Figure 7.19: HAZ and surface temperature variation at the center of the cut for the upper surface

shown in Figure 7.19. The surface temperature increases with increasing oxidation HAZ. The oxidation HAZ represents the extent to which the surface temperature was high enough to sustain a rapid oxidation of the steel. Since the thermocouples were located 4.8 mm from the cut, as the HAZ increases, the surface temperature also shows an increase and this is seen to be the case in Figure 7.19. For the surface temperature to show a greater dependence on the HAZ, the thermocouples should have been located closer to the line of cut. However, locating the thermocouples closer than 4.8 mm was not possible to due to the fact that the temperature transients at these locations is too fast for the response time of the thermocouples. As it is, the temperatures recorded at the distance of 4.8 mm are more likely to be indicative of the HAZ over a wider portion of the length of the cut.

Figure 7.20 shows the dependence of the ratio of the surface temperature and the HAZ upon the velocity of the laser beam. Since oxidation HAZ and temperature decrease with increasing beam velocity, one could expect their ratio to decrease with increasing beam velocity. However, as beam velocity increases, the energy coupling mechanism between the beam and the metal improves. Therefore, the surface temperature does not decrease as much as it should for a prescribed increase in beam velocity. Hence, the net effect is that the ratio of surface temperature to HAZ increases with increasing beam velocity.

Figure 7.20 was used to predict the oxidation HAZ in a second set of experiments from the surface temperature data at 4.8 mm from the cut. The ratio of the predicted and measured HAZ are shown in Figure 7.21. Over the range of velocities tested in this set of experiments, from 16.9 mm/s to 50.8 mm/s, the predicted and measured HAZ agreed to within $\pm 25\%$. These results show that the surface temperature can indeed be used as an indicator of the HAZ in a cutting process.

Infrared sensor measurements The measurements made with the infrared sensor are a function of the location and size of the sensor spot, the emissivity of the oxidized and unaffected material surface, and the temperature of the surface. The sensor was kept inclined at a constant 15° angle to the horizontal. Two different spot shapes were used in the experiments- one was line-shaped and the second was ellipse-shaped. These were discussed in detail in Chapter 2. Once the spot shape and the angle of inclination was fixed, the spot area was also fixed.

Three different locations of the spot with reference to the beam were chosen, also discussed in Chapter 2. These locations were, ahead and behind the beam and at

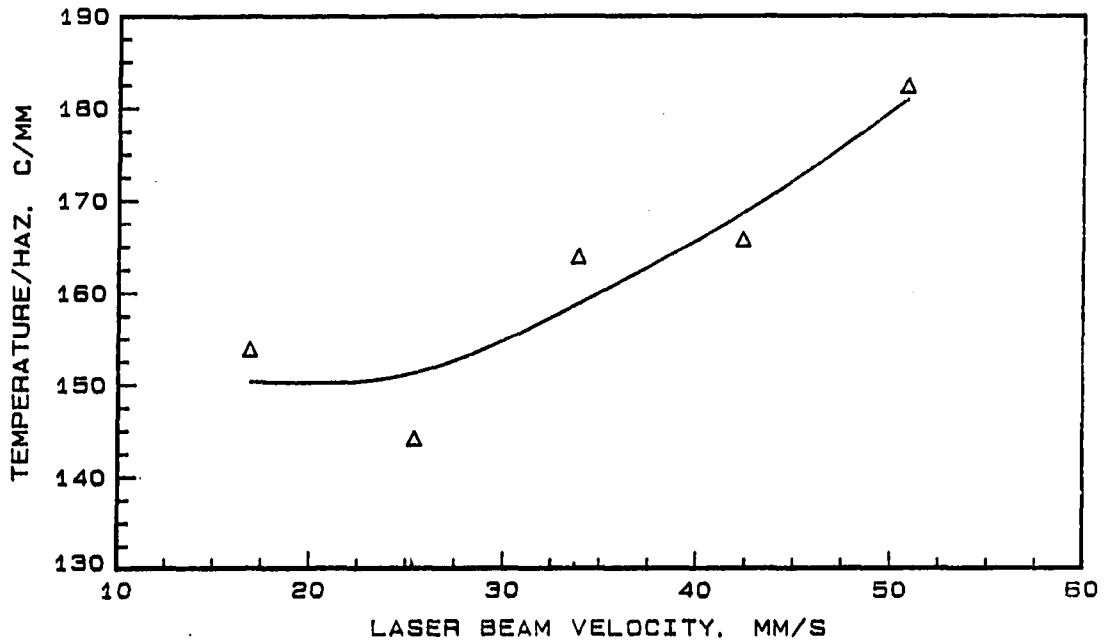


Figure 7.20: Ratio of the surface temperature and HAZ at center of the cut for the upper surface

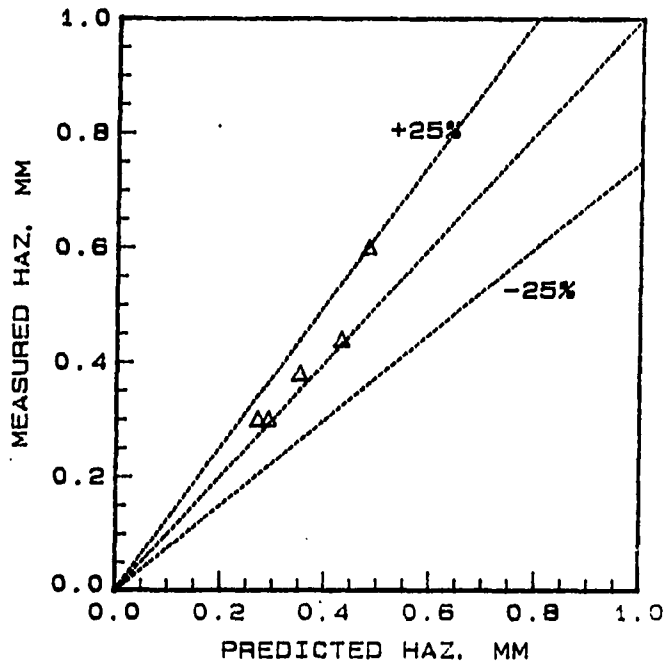


Figure 7.21: Ratio of predicted to measured HAZ at the center of the cut for the upper surface

the cutting point. In the following sections the surface temperature as recorded by the sensor at the three different locations are discussed. The predictive capability of the temperature measurements are also discussed and the relative merits of the three locations are presented.

The data for the infrared sensor measurements are presented in the form of the ratio of the temperature output of the sensor to the measured heat affected zone. The reasoning for such a presentation could be made along the lines similar to that for the kerf width. The output of the sensor T_s is proportional to the radiation energy received in the wavelength band to which the sensor is sensitive, i.e., 1.8 to 3 μm . Figure 7.22 shows a schematic of the sensor's focussing lens and the focal spot around the heat affected zone. Approximating the areas as differential areas, the rate at which radiation is intercepted by the focussing lens is,

$$q_{1-2} \simeq I(A_1 C \cos \theta) \omega_{2-1} \quad (7.5)$$

where, I is the intensity of radiation in the bandwidth of the sensor, θ is the angle of inclination of the sensor and, A_1 is the area of the heat affected zone within the focal spot of the sensor. Only the HAZ area is assumed to radiate energy to the sensor as it is likely to have a higher emissivity than the unaffected material. ω_{2-1} is the solid angle subtended by the lens at the surface of the sample.

The radiation intercepted by the sensor can also be written as,

$$q_{1-2} \simeq I h (l C \cos \theta \omega_{2-1}) \quad (7.6)$$

where all the terms in the parentheses are constant. The intensity of radiation, I is a function of the actual temperature, T_a of the HAZ and is given by the Planck's

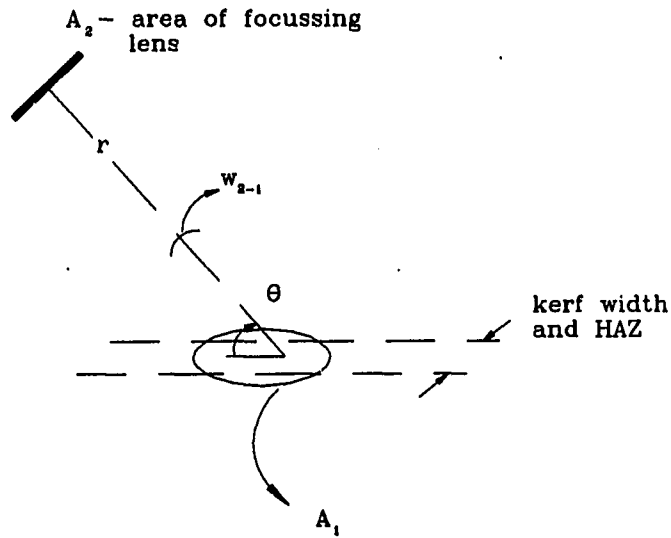


Figure 7.22: Schematic of the relative areas of the sensor and the HAZ for purposes of radiant energy calculations

distribution of radiation; I increases with increasing temperature, T_a . Hence the output of the sensor, T_s , is proportional to the actual temperature, T_a , and the width of the HAZ, h .

$$T_s \propto T_a h \quad (7.7)$$

and,

$$\frac{T_s}{h} \propto T_a \quad (7.8)$$

Since the actual temperature of the heat affected zone is a function of the velocity of the laser beam, a plot of the ratio of the temperature sensed by the infrared sensor to the heat affected zone should show dependence on the laser beam velocity. Figure 7.23 shows T_s/h for three different locations of the sensor at different laser beam velocities. In all the cases the ratio increases with increasing beam velocity,

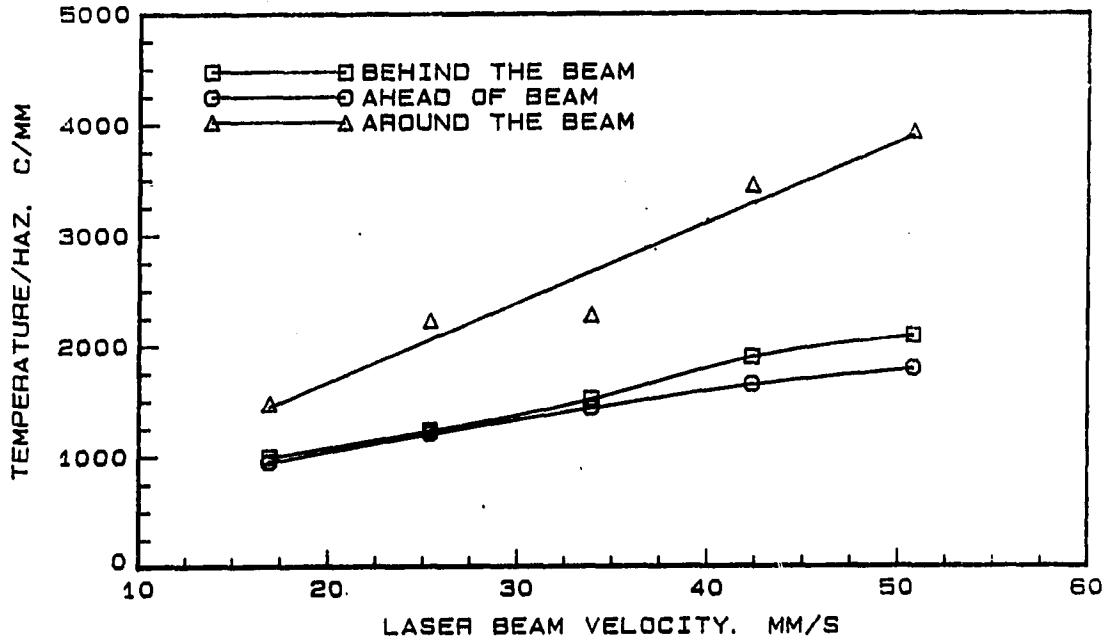


Figure 7.23: Ratio of the infrared sensor temperature to the HAZ for three different locations at different beam velocities

however, the increase is much larger in the case of the sensor spot around the beam. When the sensor was located ahead or behind the beam, the focal spot of the sensor was in the slit as discussed earlier. The distance between the focal spot and the beam location was 0.8 mm (1/32") in both cases. For these two cases the increase in the ratio was $\approx 100\%$ for an increase of beam velocity from 16.9 to 50.8 mm/s. When the sensor spot covered the entire area around the laser beam spot, the increase was $\approx 150\%$ for the same increase in the laser beam velocity. This indicates that locating the sensor such that its focal area covered the entire laser beam spot is preferable to locating it either ahead or behind the beam.

It can also be seen that the actual temperature of the HAZ decreases with increasing laser beam velocity since the amount of energy input decreases. However,

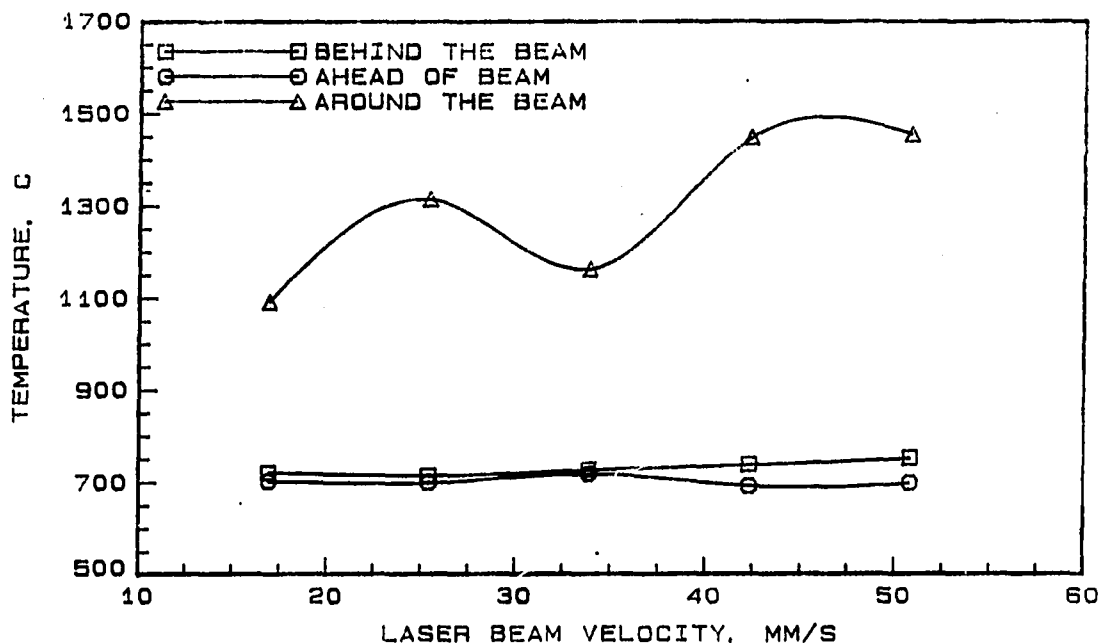


Figure 7.24: Temperature output of the infrared sensor for three different locations at different beam velocities

as seen in Figure 7.24, the infrared sensor temperature does not show this behavior. As discussed in Chapter 6, the cutting front play a very important role in the temperature sensed by the sensor. It was seen that the angle that the cutting front made with the vertical, increased with increasing velocity, thus allowing the sensor to receive radiant energy from a larger area. This, in turn, increases the temperature sensed by the sensor. Hence, the effect of the HAZ upon the sensor temperature cannot be decoupled from the effect of the kerf width.

Figure 7.24 shows that the greatest fluctuations in the sensed temperature was for the case of the sensor spot located ahead of the beam. This location is also seen as undesirable with reference to Figures 7.25 and 7.26 which show the ratio of temperature sensed to the HAZ and the temperature output of the sensor. In the

case of the sensor around the beam and behind the beam, the general tendency was an increase in the ratio with increasing temperature. But this is not the case for the sensor located ahead of the beam which does not show any consistent behavior with increasing temperature.

Effect of Oxygen Gas Pressure

The effect of the oxygen gas pressure upon the heat affected zone and the surface temperature are discussed in the following sections. The oxygen gas pressure was varied from a gage pressure of 69 kPa to a gage pressure of 207 kPa. The gas pressure was measured at the exit of the supply and no losses in the lines were considered. As described in Chapter 4, the nozzle design and the distance between the nozzle and the plate were kept constant.

The role of oxygen gas was discussed in Chapters 4 and 6. In the literature, the exothermic oxidation process is estimated to contribute about 60% of the energy required for the cutting process [56]. However, in Chapter 6 this contribution of the oxidation process was seen to be only between 30 and 40%. In this section the effect of the gas pressure upon the surface heat affected zone and the surface temperature are presented. An attempt is also made to predict the HAZ based the surface temperature measurements.

Heat affected zone

It was seen in an earlier section that the laser beam velocity had a significant effect upon the surface heat affected zone. A 200% increase in the laser beam velocity

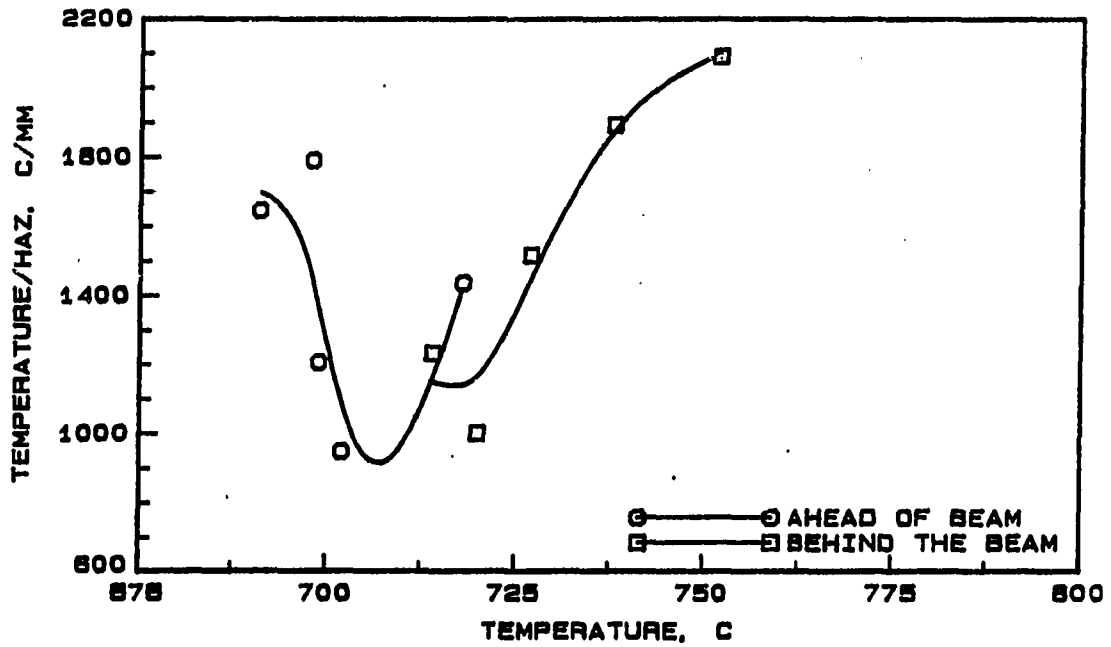


Figure 7.25: Infrared temperature to HAZ ratio for different infrared sensor temperature output ahead and behind the beam

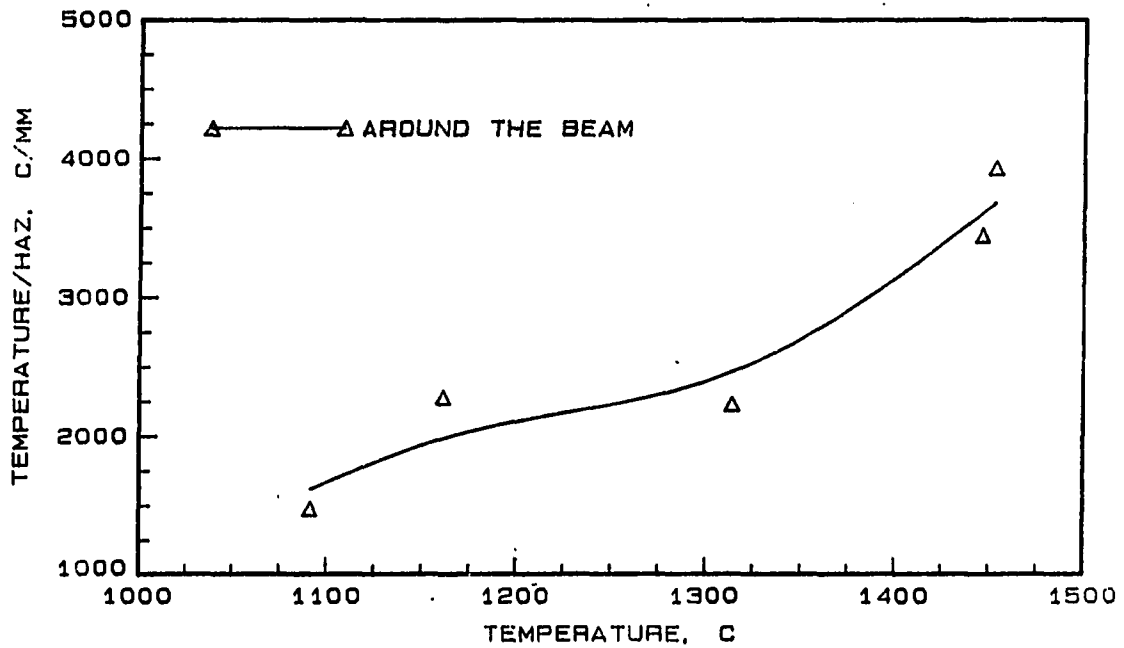


Figure 7.26: Infrared temperature to HAZ ratio for different infrared sensor temperature output around the beam

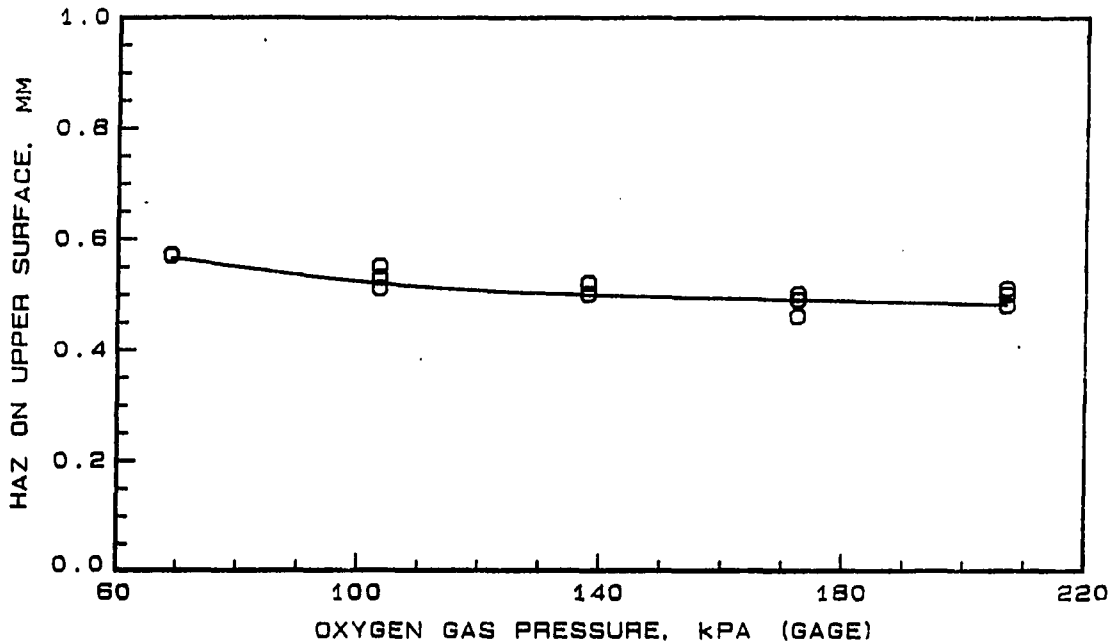


Figure 7.27: Heat affected zone at different oxygen gas pressures

produced a 50% decrease in the heat affected zone. However, for an increase of oxygen gas pressure from 69 kPa to 207 kPa, an increase of 200%, the heat affected zone decreased by only about 15%. Figure 7.27 shows the decrease in heat affected zone with increasing oxygen gas pressure. For an increase of oxygen pressure from 69 kPa to 138 kPa, an increase of 100%, the heat affected zone decreased from 0.57 mm to 0.52 mm, a decrease of only 9%. These results agree well with those reported in the literature, where for a 100% increase in gas pressure, the heat affected zone decreased by 7% [56].

Surface temperature

Surface temperature measurements were made with the infrared sensor only, and not with thermocouples. As in the case of varying laser beam velocity, three different

locations for the infrared sensor were tested. These were a thin line-shaped focal spot, one ahead and one behind the beam, and an ellipse-shaped spot around the beam. The dimensions and a schematic of these focal spots were given in Chapter 4.

It was seen in the earlier section in the discussion of the effect of beam velocity, that the ratio of the surface temperature to the heat affected zone at the center of the cut was a function of the actual temperature at the focal area of the sensor. In the earlier case, the actual temperature was a function of beam velocity and the ratio T_{sensor}/HAZ was seen to be dependent upon the beam velocity. Similarly, since the actual temperature also depends upon the oxygen gas pressure, the ratio T_{sensor}/HAZ and the oxygen gas pressure are shown plotted in Figure 7.28. It is seen that the the ratio is fairly constant at about $1400\text{ }^{\circ}\text{C}/\text{mm}$ for the two cases of the sensor spot ahead and behind the beam. It is only in the case of the sensor spot surrounding the beam spot that the increase in the ratio is significant. This result is similar to that in the case of varying beam velocity. However, the increase in the ratio, T_{sensor}/HAZ , is only 25% for an increase of 200% in the oxygen gas pressure. This can now be contrasted with the increase in the ratio while varying the laser beam velocity. When the beam velocity increased by 200%, the ratio increased by more than 150%. It is therefore apparent that the oxygen gas pressure does not have as much of an effect upon the surface temperature and the heat affected zone to the extent that the laser beam velocity has.

The ratio of the surface temperature to the heat affected zone at different values of the surface temperature are shown for the three spot location cases in Figures 7.29 and 7.30. Locating the sensor spot ahead of the beam results in an initial increase

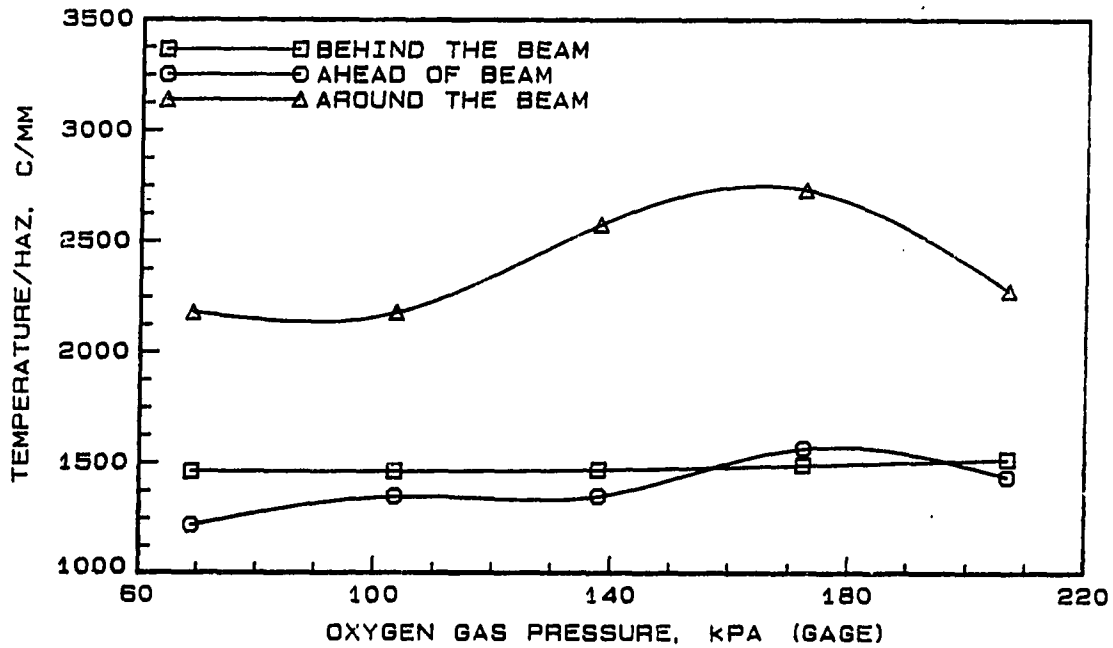


Figure 7.28: Ratio of the surface temperature to heat affected zone at different oxygen gas pressures

in the ratio T_{sensor}/HAZ . After peaking at a temperature close to 725°C , the ratio decreases with increasing temperature. This decrease in the ratio is due to a small increase in the heat affected zone. Since the surface temperature continued to decrease, the net effect was that the ratio of the temperature to the heat affected zone also decreased. However, since the small increase in the heat affected zone was within the error of the experiment, it can be concluded that the ratio T_{sensor}/HAZ increases with increasing surface temperature, T_{sensor} .

When the beam is located behind the beam, the general tendency for the surface temperature was to decrease with increasing gas pressure. When combined with the relative change in the heat affected zone, the net result is that the ratio shows a slight decrease with increasing surface temperature. For a surface temperature

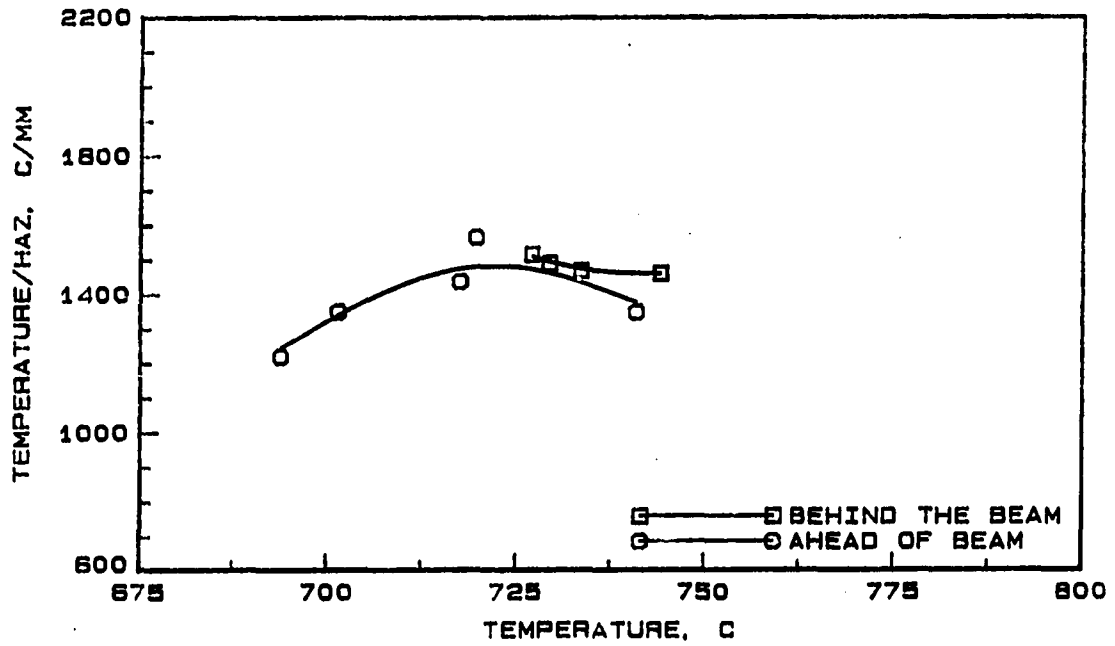


Figure 7.29: T_{sensor}/HAZ at different surface temperatures for the sensor located ahead and behind the beam

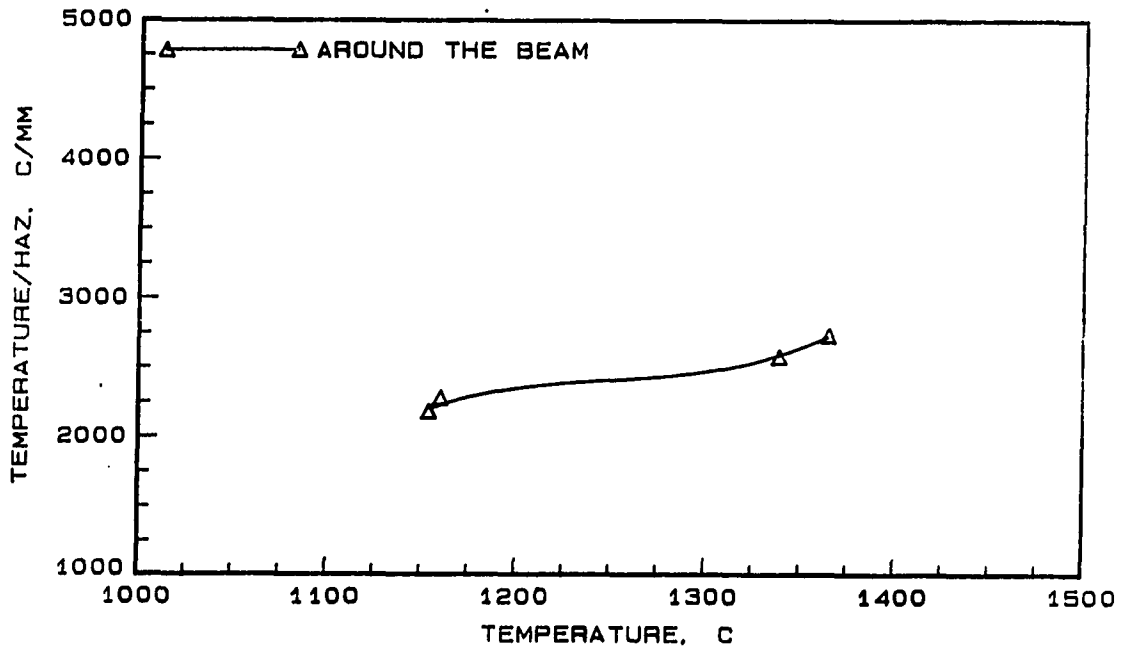


Figure 7.30: T_{sensor}/HAZ at different surface temperatures for the sensor located around the beam

increase from 727 to 744°C, the ratio of temperature to HAZ decreased from 1515 to 1459 °C/mm. Locating the sensor spot around the beam provides better results in terms of relative changes in surface temperature and the heat affected zone. When the surface temperature increased from 1154 to 1365°C, the ratio also increased from 2177 to 2730 °C/mm.

Since the oxygen gas pressure did not have a significant effect upon the surface temperature and the heat affected zone, the validity of using the results from varying the laser beam velocity to predict the HAZ was investigated. Specifically, the results shown in Figure 7.26 were used with the surface temperature measurements made while varying the oxygen gas pressure. From the value of T_{sensor}/HAZ obtained from Figure 7.26, the heat affected zone is predicted. The results of the predicted heat affected zone and the actual measured values are shown in Figure 7.31. The $\pm 25\%$ error tolerance band is also shown in the figure and it is seen that the predicted values compare quite favorably with the measured values. Figure 7.32 shows the error in the predicted values at different values of the heat affected zone. In all the cases, the error was less than 10%, indicating that this method of prediction is valid.

An alternate procedure of heat affected zone prediction is to obtain the value of T_{sensor}/HAZ at the velocity of cutting and to use this value for the calculation of the heat affected zone from the surface temperature measured. The experiments on oxygen gas pressure variation were all performed at a fixed laser beam velocity of 33.8 mm/s. From Figure 7.23, corresponding to this laser beam velocity, the ratio T_{sensor}/HAZ is approximately 2625 °C/mm. The heat affected zone calculated with this value of the ratio at different surface temperature values is shown in Figure 7.33.

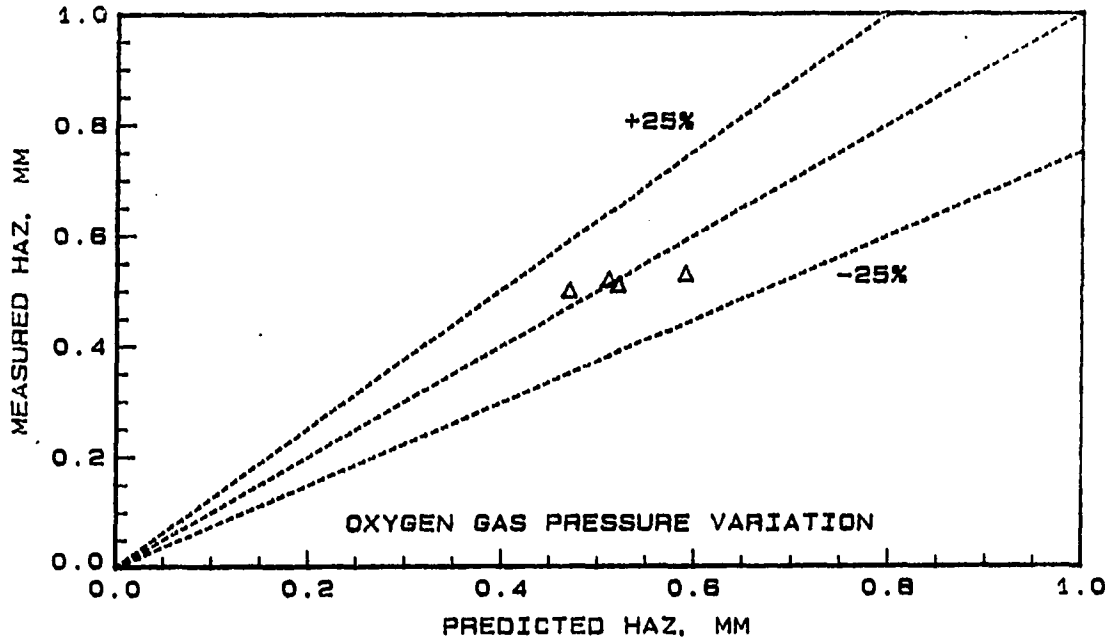


Figure 7.31: Comparison of predicted and measured heat affected zones predicted from the data in velocity experiments

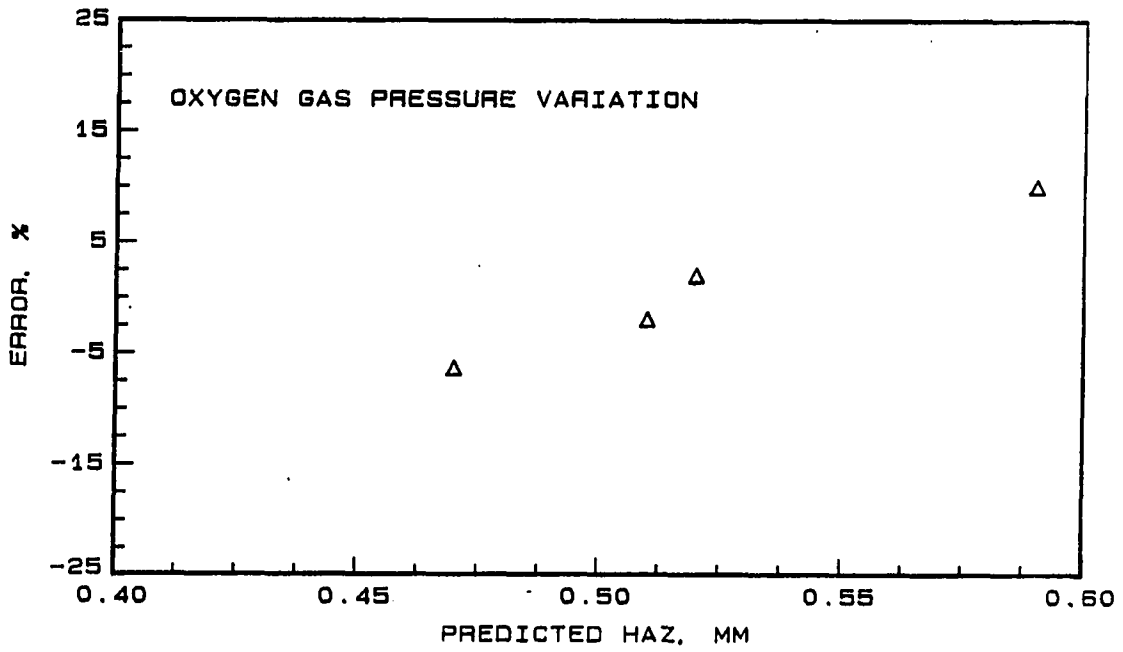


Figure 7.32: Error in predicting heat affected zone from the data in velocity experiments

Again, it is seen that all the predicted values fall within the 25% of the measured values. Figure 7.34 shows the error in the predicted value of the heat affected zone. In this case the error did not exceed 15% for all the tested values. Since the oxygen gas pressure did not as significant an effect as the laser beam velocity, it was possible to predict the heat affected zone from the data from the experiments on varying the beam velocity.

Effect of Laser Power

The effect of the laser power upon the surface temperature and the heat affected zone are discussed in the following sections. At fixed values of the laser beam velocity and the oxygen gas pressure, increasing the laser power increases the energy input to the metal being cut. This, in turn, will produce changes in the heat affected zone and the surface temperature measured. The laser beam power was varied from 800 to 1200 W in steps of 100 W. In all the cases the laser beam velocity and the oxygen gas pressure were kept constant at 33.8 mm/s and 207 kPa, respectively.

Heat affected zone

At constant velocity of the beam, increasing the laser power results in an increase in the energy input to the sample being cut. Hence, there should be greater energy available for heat treating the sample at the higher values of the laser power. This is seen to be the case in Figure 7.35 which shows the variation of the heat affected zone with the laser power. An increase of 50% in the laser power from 800 to 1200 W produced an increase of 20% in the heat affected zone from 0.44 to 0.53 mm.

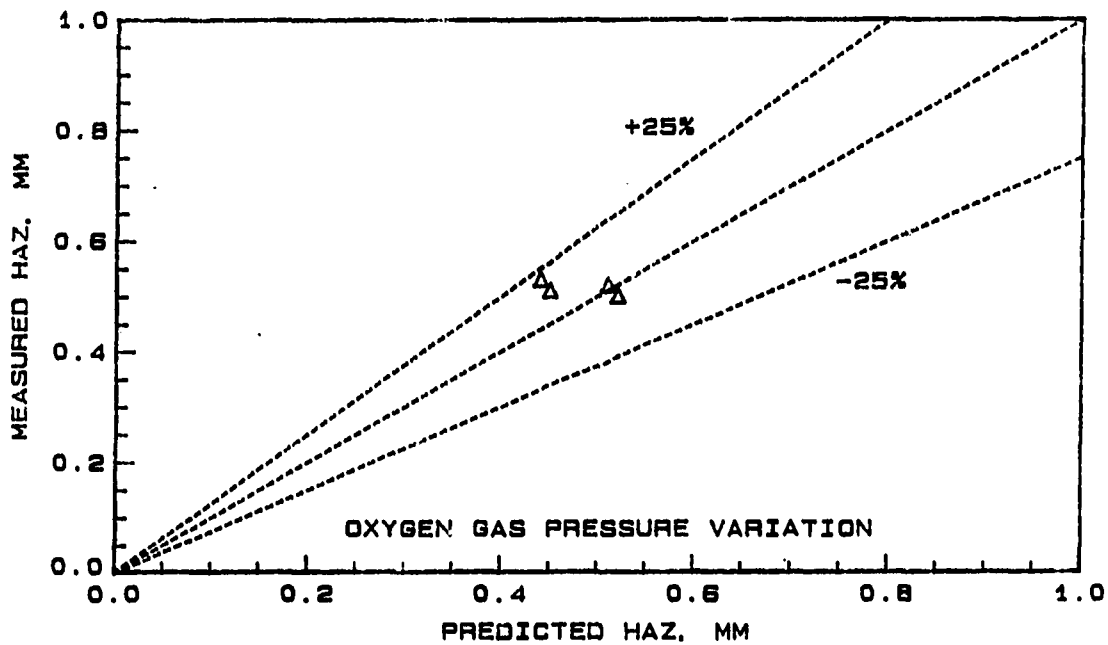


Figure 7.33: Comparison of predicted and measured heat affected zones predicted by the second method

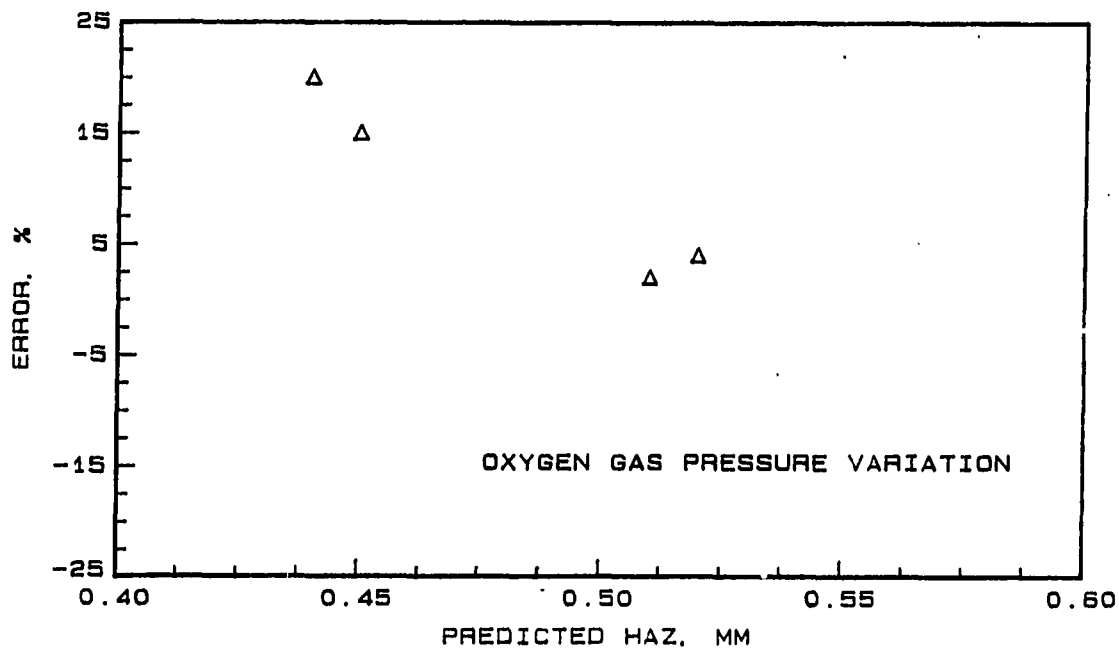


Figure 7.34: Error in predicting heat affected zone by the second method

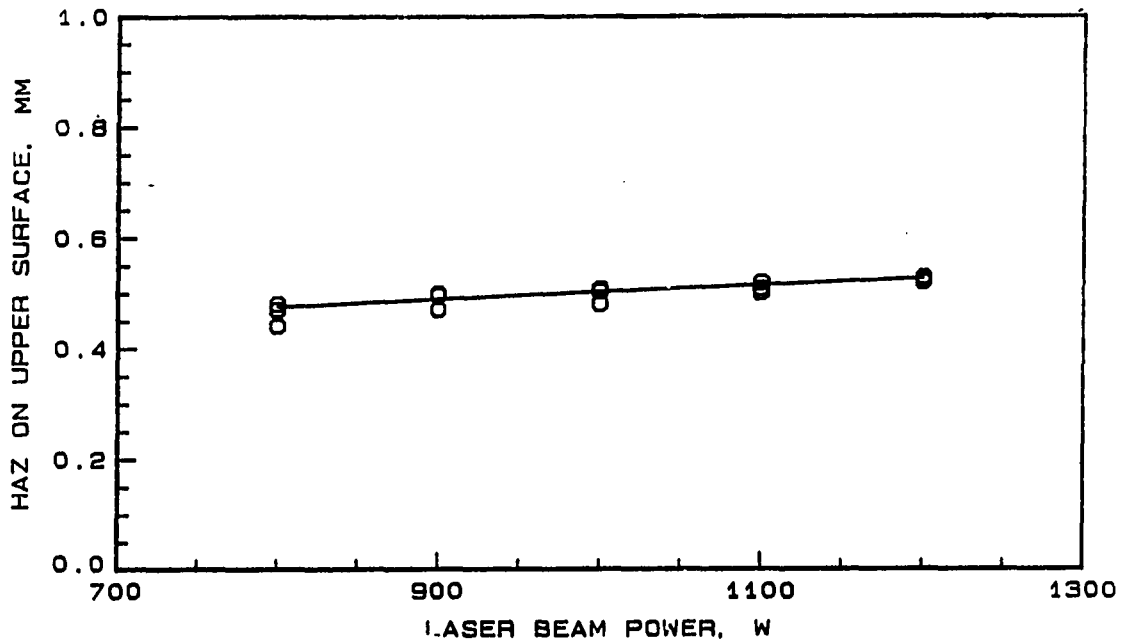


Figure 7.35: Heat affected zone at different values of laser beam power

Surface temperature

The effect of the laser power on the surface temperature depends on the coupling efficiency between the laser beam and the metal sample. The emissivity of AISI 1018 steel to laser radiation was discussed in an earlier chapter. It was also seen that once the kerf had been initiated, all of the incident radiation would be absorbed in the kerf due to the kerf acting as a "black hole" [56]. However, even in this case, only the radiation incident on the material would be absorbed and not the portion of the beam that passes through the kerf without striking any material. This argument was successfully used in an early model of the laser cutting process [25]. In their model, Gonsalves and Duley showed that the portion of the laser beam striking the material increased with increasing beam velocity.

It is known through extensive experimental evidence that there exists an max-

imum possible cutting velocity at any value of the laser power [56, 38]. This can be seen from observing that at low velocities of the beam, a greater portion of the beam is likely to pass through the kerf without striking the metal. As the beam velocity increases, the fraction of the beam striking the surface also increases. However, continued increase of the beam velocity will result in values of the velocity being too high for the beam to complete the cutting process. Hence there is a maximum velocity of the beam at which the laser beam is absorbed most efficiently by the metal in the kerf. This maximum beam velocity has been shown to increase with increasing laser beam power [56].

As in the previous sections, the ratio of the surface temperature as measured by the infrared sensor to the heat affected zone, T_{sensor}/HAZ is presented below. Again, three different locations and spot focal areas were tested. It was seen in Chapter 6 that the kerf width was a minimum at a laser beam power of 1000 W for a beam velocity of 33.8 mm/s and an oxygen gas pressure of 207 kPa, gage. Figure 7.36 shows the change in surface temperature with increasing laser power and Figure 7.37 shows the ratio T_{sensor}/HAZ as a function of the laser beam power. For the case of the measurement made behind the beam, the ratio decreases with increasing beam power from a value of 1613 to 1434 °/mm, a decrease of 10%. The surface temperature recorded increased from 710 to 746°C, but the heat affected zone increased over this range of laser power. The net result was a decrease in the ratio with increasing laser power.

As seen in Figure 7.36, the surface temperature measured ahead of the laser beam showed a general tendency to decrease with increasing laser power, except at

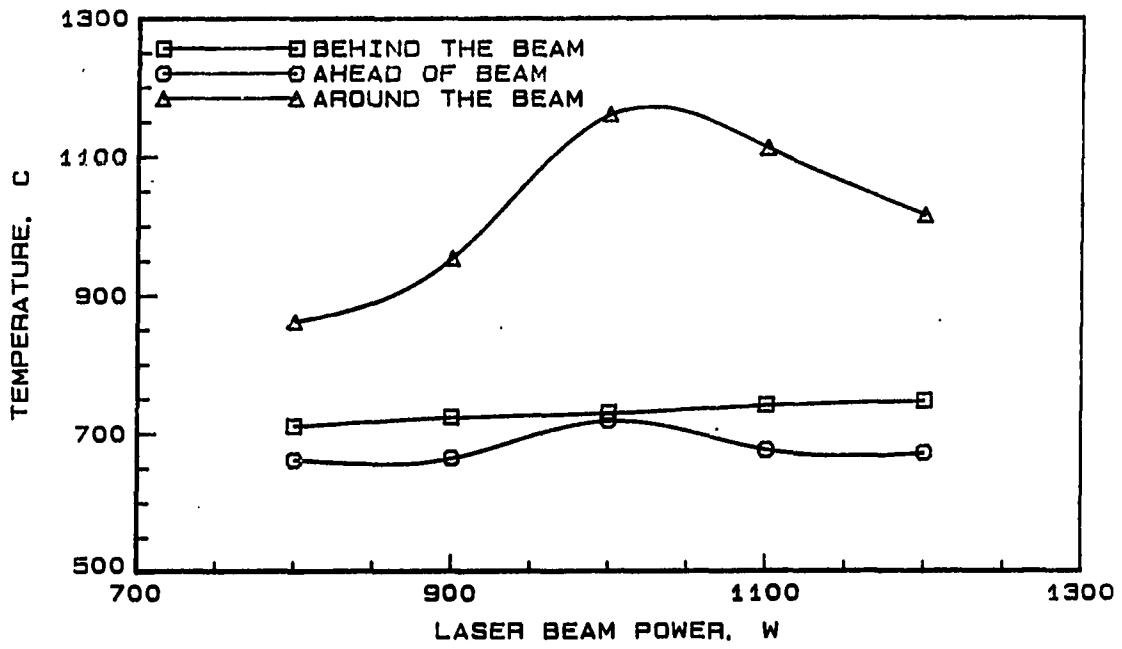


Figure 7.36: Surface temperature at different values of laser beam power

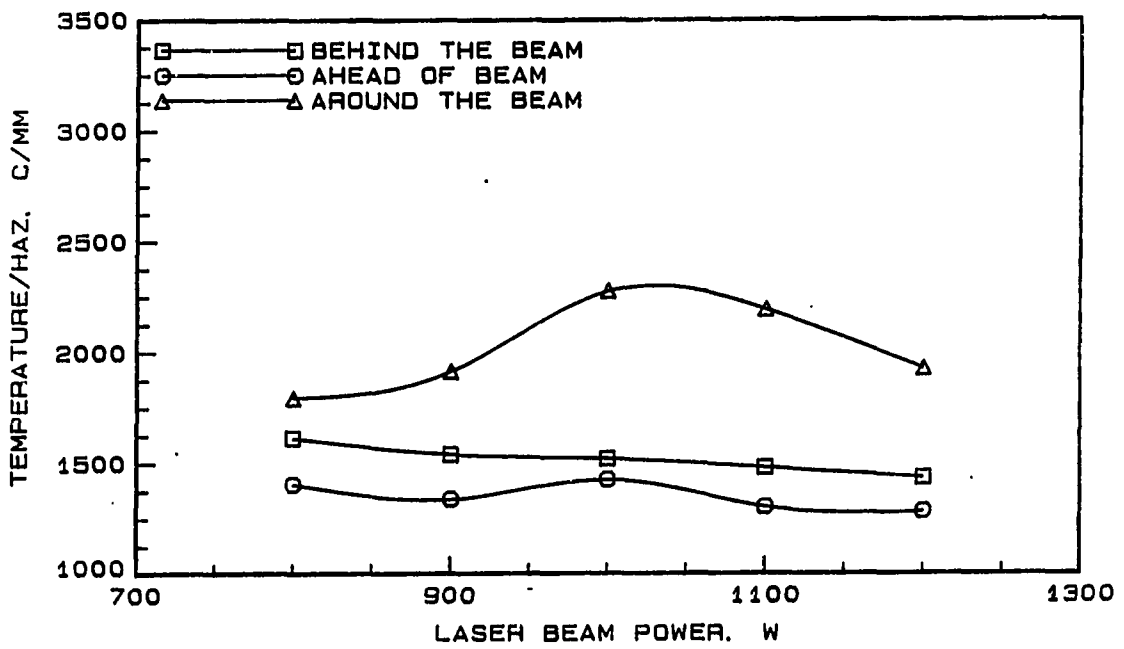


Figure 7.37: Temperature-HAZ ratio at different values of laser beam power

a value of 1000 W, which is the optimum laser power for a velocity of 33.8 mm/s. In Figure 7.37, the ratio is seen to decrease from 1406 to 1283 °/mm when the temperature increased from 661 to 671°C and the heat affected zone increased from 0.47 to 0.53 mm. At the laser power value of 1000 W, the coupling of the laser beam with the sample is at its most efficient, and the kerf is at its minimum. Hence the surface temperature detected is a maximum at this value, though the heat affected zone does not show a minima at this value of laser power.

Similar observations can also be made for the case of the sensor focal area surrounding the beam. In this case, the ratio T_{sensor}/HAZ increases steadily from a value of 1795 °/mm at 800 W to a maximum of 2275 °/mm at a power value of 1000 W. Further increase in the laser power at the same velocity of 33.8 mm/s results in the beam velocity being too slow for the laser power. Hence the surface temperature shows a decrease resulting in a decrease in the temperature-HAZ ratio.

In performing laser cutting operations, it is always desirable to operate at optimum values of laser power and beam velocity. The previous Figures 7.37 and 7.36 would be useful in evaluating such an optimum operating point. At the optimum values of the laser power and the beam velocity, the surface temperature as measured around the beam shows a maximum value as does the temperature-HAZ ratio.

The temperature-HAZ ratio for different values of the surface temperature are shown in Figures 7.38 and 7.39 for the cases of locating the sensor at the three different locations. Locating the sensor ahead of the beam is seen to produce inconsistency in the relative changes in the temperature-HAZ ratio and the temperature. This type of inconsistency was also seen to exist in the earlier results obtained by varying the

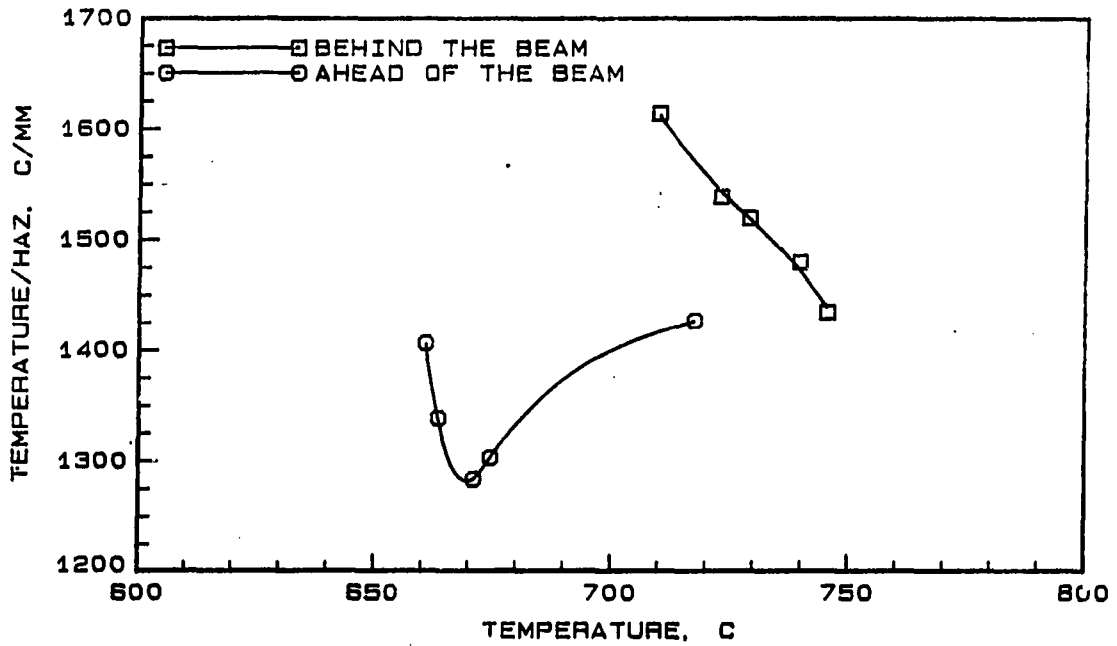


Figure 7.38: Temperature-HAZ ratio and surface temperature variation for the cases of the sensor spot ahead and behind the beam

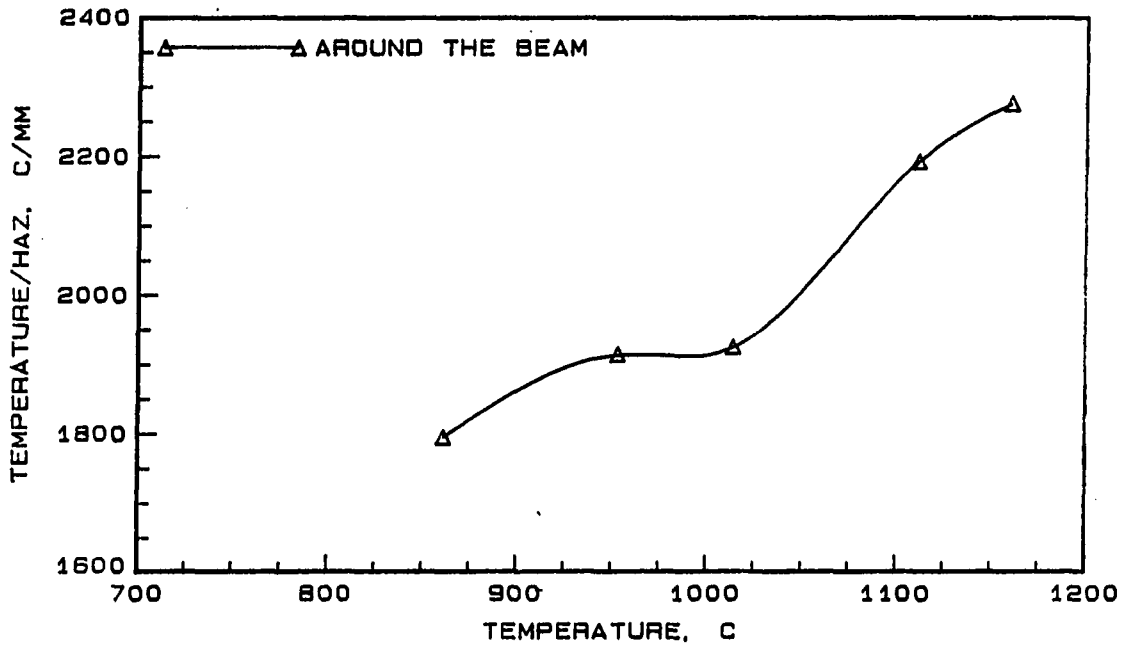


Figure 7.39: Temperature-HAZ ratio and surface temperature variation for the case of the sensor spot around the beam

laser beam velocity and the oxygen gas pressure. It can, therefore, be concluded that locating the sensor ahead of the beam is not desirable in terms of being able to predict the laser cutting process.

Locating the sensor behind the beam results in a decrease in the temperature-HAZ ratio when the temperature increases. This is due to the fact the temperature increased with increase in the laser power, but the decrease in the heat affected zone was greater. The effect of increasing laser power upon the surface temperature behind the beam was not pronounced enough to cause a larger increase in the surface temperature. This could be due to the heat having dissipated away from the area on which the sensor was focussed. When the sensor is located closer to the point at which the cutting is being performed (i.e., when the sensor spot surrounds the beam) then the increase in surface temperature was significant enough to overcome the increase in the heat affected zone. In Figure 7.39 it is seen that the temperature-HAZ ratio increases with increasing surface temperature. This behavior is similar to that observed earlier in the cases of increasing beam velocity and oxygen gas pressure.

In the previous section, it was seen that the heat affected zone did not show a significant change when the gas pressure was changed. It was, therefore, possible to use the results of temperature measured in the velocity experiments to predict the heat affected zone. This is not possible in the present case as the heat affected zone varies significantly with the laser power. Also, the laser power affects the surface temperature value differently as seen in Figure 7.36. Therefore, use of the surface temperature data from the velocity experiments to predict the heat affected zone produces large errors in the predicted values.

Instead, an alternate method of estimating the heat affected zone is presented which yields fairly good results. The energy input to the metal at any power and laser beam velocity can be calculated from,

$$Energy = \frac{(Power)(Length\ of\ sample)}{Beam\ velocity} \quad (7.9)$$

For example, at a laser beam power of 800 W and velocity of 33.8 mm/s, the energy input to the metal sample of length L mm is,

$$Energy\ Input = \frac{(800\ W)(L\ mm)}{33.8\ mm/s} \quad (7.10)$$

For the laser beam to input the same amount of energy as calculated from Equation 7.10 at a laser beam power of 1000 W, the laser beam should travel at a velocity of,

$$V_{equivalent} = \frac{(1000\ W)(33.8\ mm/s)}{800\ W} \quad (7.11)$$

which can be calculated to be 42.3 mm/s. Once this equivalent beam velocity is known, the heat affected zone can be found from the experimental data obtained earlier in the velocity experiments. This method of first calculating the equivalent beam velocity at a power of 1000 W, and then using Figure 7.18 to predict the heat affected zone was used to predict the heat affected zone for the power values from 800 to 1200 W. The predicted and the actual heat affected zone are compared in Figure 7.40 where it is seen that the predicted results fell within the $\pm 25\%$ tolerance. The error between the predicted and the actual heat affected zone values at various power values are shown in Figure 7.41. The maximum error was less than 11% at a laser power value of 800 W.

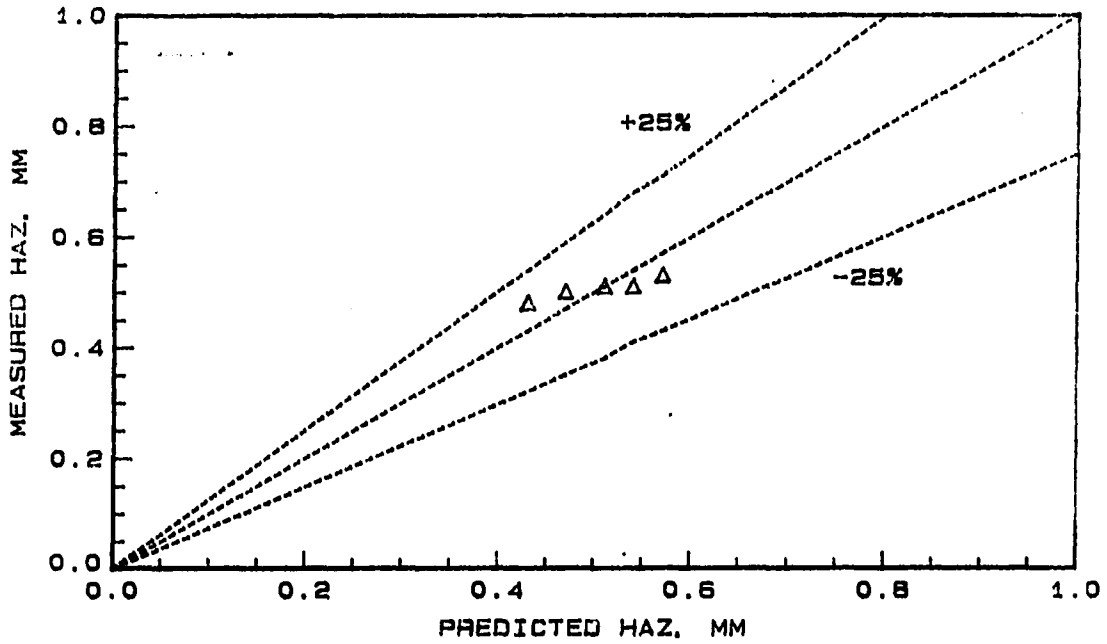


Figure 7.40: Predicted and measured values of heat affected zone for the case of varying beam power

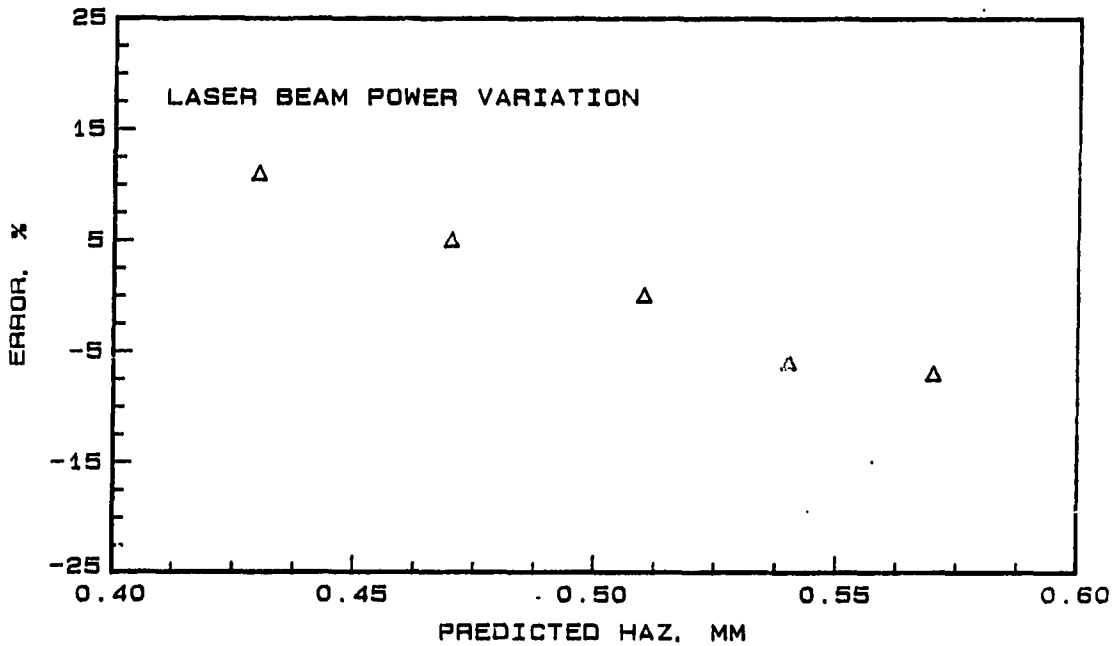


Figure 7.41: Error between the predicted and measured heat affected zone at different values of laser beam power

In fact the errors increased with increasing difference between the laser power value and the reference value of 1000 W. At values of power less than 1000 W, the predicted value was less than the actual, while at values of laser power greater than 1000 W, the predicted values were greater than the actual.

Summary

The experimental results presented in this chapter on the heat affected zone are presented in this section, below.

The oxidation HAZ can predict the heat-treated HAZ to a little over 25% accuracy. The error in the prediction is smaller at the larger values of the heat-affected zones. The oxidation HAZ was higher at lower beam velocities and on the lower surface. While the oxidation HAZ showed dependence on the laser beam velocity, the heat-treated HAZ was fairly independent of the beam velocity. At any point along the cut, a cross-sectional study of the heat-treated HAZ showed that heat-treatment of the material was a minimum at the center of the sample thickness.

Heat affected zone was strongly influenced by the laser beam velocity. The HAZ decreased with increasing velocity for the upper surface. Surface temperature, as measured by an infrared sensor and thermocouple was also affected by the beam velocity. The ratio of the observed temperature to the heat affected zone increased with increasing laser beam velocity. This provided a method of evaluating the HAZ once the beam velocity and the temperature were known. The HAZ could not be predicted to less than 25% accuracy when the thermocouple data were used for prediction. The infrared sensor with the focal spot surrounding the laser beam spot (i.e., the focal

spot covers the entire cutting region) was found to be the best since it provided the highest resolution.

The oxygen gas pressure did not have a significant effect upon the surface temperature and the heat affected zone. An increase of 200% increase in the oxygen gas pressure produced only a small decrease of 15% in the heat affected zone. The change in surface temperature was approximately 20% in the case of the sensor spot around the beam. The method of locating the sensor spot around the laser beam was found to provide the most resolution in terms of the surface temperature. Due to the reduced dependence of the temperature and HAZ upon the oxygen gas pressure, it was possible to predict the heat affected zone from the data obtained by varying the laser beam velocity. Two methods of predicting the heat affected zone were presented and in both case the maximum error was less than 15%.

The laser beam power had significant effect upon the heat affected zone. An increase in the beam power resulted in an increase in the heat affected zone values. The surface temperatures measured around the beam showed a maximum at the value of the power that was optimum for the velocity used in the experiments. Since in laser cutting it is always desirable to operate at the maximum possible optimum value of the beam power and velocity combination, surface temperature could be used to indicate this optimum setting. The heat affected zone could not be predicted from the surface temperature data, but, an alternate method of predicting the heat affected zone from the velocity experiments was successful. The error in the predicted HAZ value was less than $\pm 15\%$.

CHAPTER 8. MODELS OF THE LASER CUTTING PROCESS

Theoretical models of the cutting process are useful in providing an estimate of the amount of material removed (i.e., kerf width) and of the heat affected zone while cutting with the laser. Both analytical and computational models of the cutting process are presented with the objective of not only predicting the kerf width, but also for studying the relative effects of the process variables. Therefore, in addition to providing an estimate of laser cut quality, the models presented in this chapter also provide insight into the cutting process.

Two different models are presented and discussed. The first model is a simple thermodynamic model of the cutting process which accounts for the mass and energy balance in the cutting zone. Several simplifying assumptions are made, and the results of the model are compared to available experimental data. The second model is a two-dimensional finite-element model of the cutting process which is solved using a commercial software package. The results of this second study are also presented and compared with experimental data.

One aim of developing these models is to present useful and simple means of predicting the outcome of the cutting process. Another aim is to show the complexities involved in the cutting process and the several simplifying assumptions that have to be made in developing even the simplest model. In each section below, the develop-

ment of the model, the simplifying assumptions made, and the results of the model are discussed.

Thermodynamic Model

A thermodynamic analysis of a sample undergoing a cutting process is developed in this section. The analysis considers the mass balance and the energy balance of a control volume around the cutting region. Several assumptions are made to obtain a final expression for the amount of material in the cutting process. The model is then used to predict the kerf width in both thin and thick metal cutting and the results are compared with available experimental data.

Mass and energy balance

Figure 8.1 shows a schematic of the sample being cut by a laser beam and the control volume around the cutting region. The cutting region control volume is also shown where metal is assumed to enter the control volume at section (2) with mass flow rate and properties are as shown in the figure. When the metal leaves the control volume at section (4) with different values for its properties, there is a decrease in the mass flow rate. This decrease is due to the mass evaporated, shown leaving at section (6), and the mass melted to form a liquid, shown leaving at section (5). Each of these mass flows leave the control volume at the properties shown in the figure. The energy for the evaporation and the melting comes from the incident laser power, and also from the exothermic oxidation reaction. The oxygen for the oxidation is also shown entering and leaving the control volume at sections (1) and (2), respectively. The

oxygen helps to blow away the molten metal, and also provides convective cooling.

The mass balances for the metal and the oxygen gas can be written as,

$$\frac{dM_{cv}}{dt} = \dot{m}_3 - \dot{m}_5 - \dot{m}_6 - \dot{m}_4 \quad (8.1)$$

and,

$$\frac{dM_{o2}}{dt} = \dot{m}_1 - \dot{m}_2 - \dot{m}_g \quad (8.2)$$

respectively. The mass flow rates identified with numeral subscripts correspond to the mass flow rates at the different sections shown in Figure 8.1. The mass rate of oxygen consumed in the exothermic oxidation process is represented by the term, \dot{m}_g .

The mass rate of evaporated metal is assumed to be negligible compared with the metal melted. Similarly, the mass rate of oxygen gas consumed in the oxidation process is also assumed to be negligible compared with the total oxygen gas flow rate. Assuming also that steady-state conditions exist, the above equations can be written as,

$$\dot{m}_3 = \dot{m}_5 + \dot{m}_4 \quad (8.3)$$

for the metal, and,

$$\dot{m}_1 = \dot{m}_2 \quad (8.4)$$

for the oxygen gas.

The energy balance for the control volume shown in Figure 8.1 can be written as,

$$\begin{aligned} \frac{dE_{cv}}{dt} = & \dot{Q}_{cv} - \dot{W}_{cv} + \dot{m}_1 \left(h_1 + \frac{V_1^2}{2} \right) - \dot{m}_2 \left(h_2 + \frac{V_2^2}{2} \right) \\ & + \dot{m}_3 \left(h_3 + \frac{V_3^2}{2} \right) - \dot{m}_4 \left(h_4 + \frac{V_4^2}{2} \right) - \dot{m}_5 \left(h_5 + \frac{V_5^2}{2} \right) \end{aligned} \quad (8.5)$$

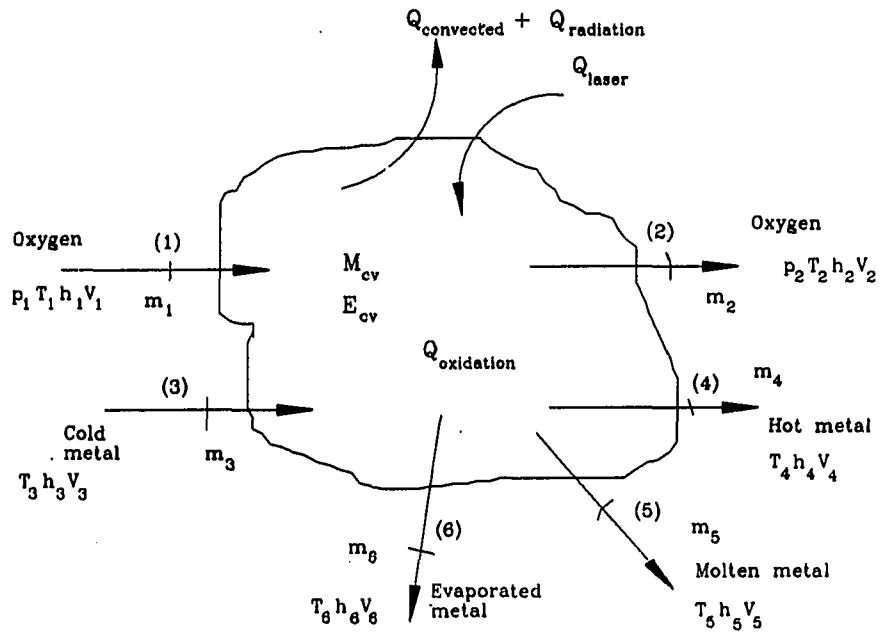
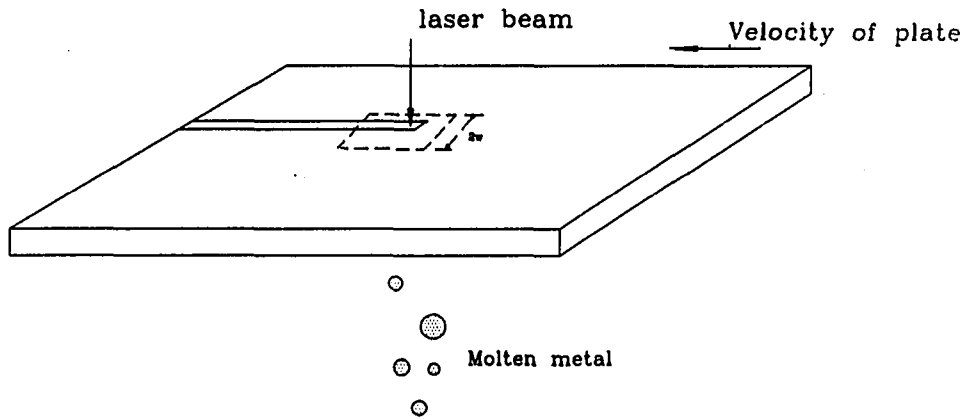


Figure 8.1: Schematic of the metal being cut by the laser beam and the control volume showing the inlet and exit for the oxygen and metal

when all the potential energy effects are considered negligible compared to the other energy terms. In the above equation,

$$\dot{Q}_{cv} = \dot{Q}_{laser} + \dot{Q}_{oxidation} - \dot{Q}_{rad} \quad (8.6)$$

Equation 8.5 can be simplified by assuming steady-state conditions, and equal velocities for the metal entering and leaving the control volume, i.e., $V_3 = V_4$. The simplified energy balance equation can then be solved for the mass flow rate of metal leaving the control volume as a liquid, to yield,

$$\dot{m}_5 = \frac{-[\dot{Q}_{cv} - \dot{Q}_{conv} - \dot{Q}_{rad} + \dot{m}_3(h_3 - h_4)]}{h_4 - h_5 + \frac{V_3^2 - V_5^2}{2}} \quad (8.7)$$

In the above equation, the convective heat transfer rate is,

$$\dot{Q}_{conv} = \dot{m}_1(h_2 - h_1 + \frac{V_2^2 - V_1^2}{2}) \quad (8.8)$$

The calculation of the radiation heat loss, \dot{Q}_{rad} , is discussed later in this section.

In Equation 8.7, assuming constant specific heat, the enthalpy terms in the numerator can be rewritten as,

$$h_3 - h_4 = C_p(T_3 - T_4) \quad (8.9)$$

where C_p is the specific heat of the metal. The enthalpy terms in the denominator include the enthalpy of melting for the metal, and can be written as,

$$h_4 - h_5 = C_p(T_4 - T_5) - i_{sl} \quad (8.10)$$

where, i_{sl} is the enthalpy of melting of the metal. Since kinetic energy contribution is usually very small compared with the other energy terms, the velocity terms in the

denominator of Equation 8.7 can be assumed to cancel each other out of the equation.

Equation 8.7 can finally be written as,

$$\dot{m}_5 = \frac{-[\dot{Q}_{cv} - \dot{Q}_{conv} - \dot{Q}_{rad} + \dot{m}_3 C_p (T_3 - T_4)]}{C_p (T_4 - T_5) - i_{sl}} \quad (8.11)$$

Simplification of the model

The mass flow rate terms in the Equation 8.11 can be written in terms of the velocity and density as follows,

$$\dot{m}_3 = 2wt\rho V_3 \quad (8.12)$$

where, $2w$ is the width of the control volume, t is the thickness of the metal sample, and ρ is the density of the metal which is assumed constant.

The mass rate of metal removed can also be written as,

$$\dot{m}_5 = kt\rho V_3 \quad (8.13)$$

where, k is the kerf width to be determined, t is the thickness of the metal sample, and ρ is the density of the liquid metal assumed to be the same as the value for the solid.

Several assumptions were made in order to solve Equation 8.11. The first assumption concerns the width of the control volume. This distance has been shown in computational models to be usually less than 40 diameters of the beam [48, 38]. In addition, in the experiments conducted during the course of this research, at a distance of approximately 5 mm from the line of cut, the temperature was less than 75°C, when cutting steel that melts at 1535°C with a beam of diameter 0.2 mm.

Therefore, the width of the control volume is assumed to be that distance perpendicular to the line of travel of the beam where the temperature is 5% of the melt temperature, T_m .

The results of the model depend to a large extent on the proper evaluation of the heat transfer terms in Equation 8.11. These terms, $\dot{Q}_{oxidation}$ and \dot{Q}_{conv} , along with their estimation were presented earlier in Chapter 6, and therefore, are not discussed here. However, the estimation of the energy input to the metal by the laser beam, \dot{Q}_{laser} , and the radiation heat loss, \dot{Q}_{rad} , are discussed below.

In the steady cutting of metals a portion of the beam incident upon the sample will actually strike the surface of the sample. That part of the beam that strikes the kerf will pass through the kerf without being absorbed by the metal. This is shown schematically in Figure 8.2, where a beam of diameter d is used to cut the sample. Gonsalves and Duley [25] used the assumption that the portion of the beam striking within the melt isotherm will not strike the metal since the material there has been removed, to estimate the energy input to a sample of stainless steel cut by a laser. They evaluated the fraction of energy striking the surface of a thin metal, f , from an analysis based on the solution to a point source moving on a thin sheet [14]. The fraction f was a function of the incident energy, the emissivity of the surface, and the thermal properties of the material. It was also a function of the velocity of the beam, and it increased with increasing beam velocity.

The rate of energy input to the control volume by the laser beam, \dot{Q}_{laser} , is calculated from the equation below,

$$\dot{Q}_{laser} = \epsilon f P \quad (8.14)$$

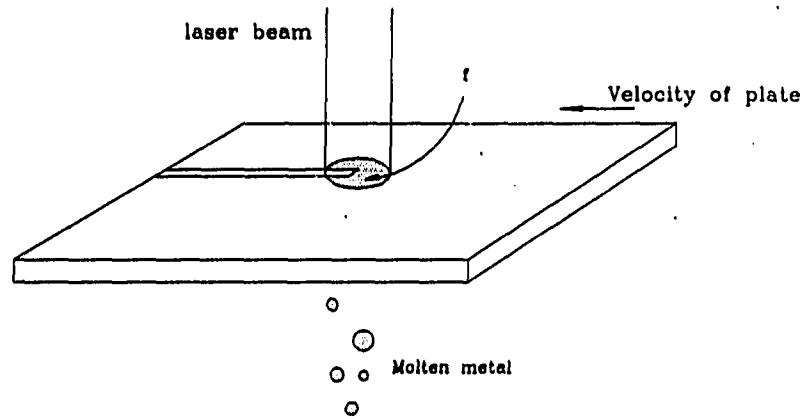


Figure 8.2: Schematic of the cutting front for the case of metal cutting showing the fraction of beam incident on the metal

where f is estimated from the results of Gonsalves and Duley [25], and P is the incident laser beam power. The emissivity of the surface, ϵ , can be calculated from an equation similar to that discussed in Chapter 2, or else found from experiments. For the case of type 302 stainless steel, Gonsalves and Duley [25] experimentally found a value of 0.16 for ϵ .

Calculating the rate of energy input by the laser for the case of thick-metal cutting, such as was performed in the experiments in this research, is based on a approach similar to that described above for thin-metal cutting. The rate of energy input is now given by,

$$\dot{Q}_{laser} = fP \quad (8.15)$$

where f is calculated as before from the results of Gonsalves and Duley [25]. The

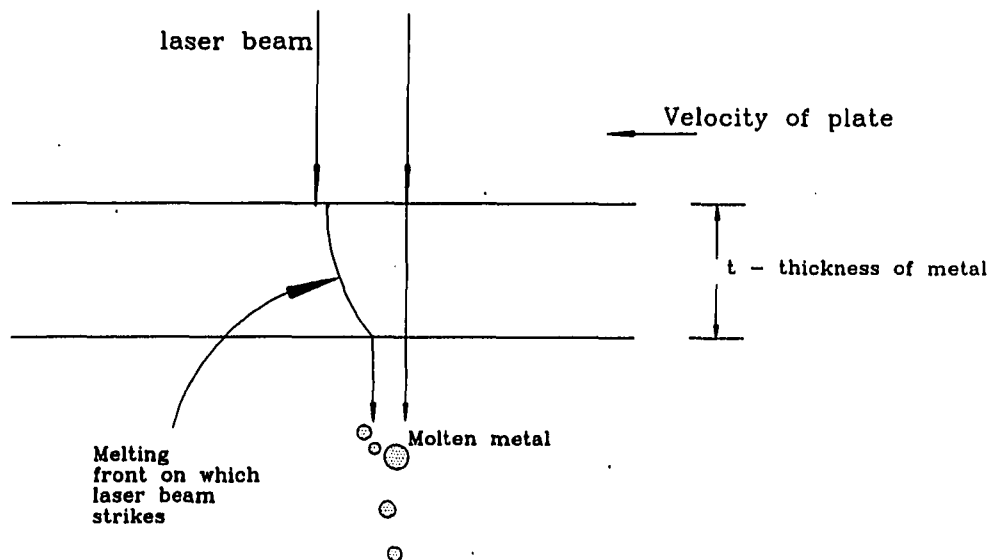


Figure 8.3: Schematic of the cutting front for the case of thick-metal cutting showing the fraction of beam incident on the cutting front

emissivity of the surface is assumed to be unity and the reason is discussed below.

It was mentioned earlier that once the cut is initiated on a thick-metal, the kerf acts as a blackbody and absorbs all of the radiation incident upon it [56]. This seems plausible due to the narrow width of the kerf and the presence of the molten metal within the kerf, whose emissivity is close to unity. High-speed filming of the cutting zone by Arata et al. [5] showed that the beam was actually incident on the cutting front which was inclined at an angle to the vertical. Figure 8.3 shows a typical case where the beam is incident upon the inclined cutting front. It has also been shown that this cutting angle increased with increasing beam velocity [5, 56].

Just as in the case of the cutting of thin-metals, the part of the beam that does not strike the inclined cutting front has to pass through the kerf unaffected. As the

velocity increases, the cutting front angle of inclination increases, thus allowing more of the incident beam to strike the cutting front. The portion of the beam that strikes the cutting front is the fraction f in Equation 8.15. Since this part of the beam strikes the melting metal, the assumption of unity for the emissivity seems reasonable.

In Equation 8.11, the temperature of the uncut metal leaving the control volume at section (4) is another term that needs special attention. In reality, the temperature of the metal leaving the control volume decreases from a value equal to the melt temperature at the cutting zone to less than 5% of this value at a distance of 20 diameters on either side of the cutting line. This was also discussed earlier when the width of the control volume was estimated. A computer program was written to calculate the average temperature of the metal metal and the width of the control volume that was discussed earlier in this section. An average temperature of the metal leaving the control volume can be found once the temperature profile itself is estimated. This is done by using the two-dimensional solution for the case of a point source moving on a sheet [14]. The program calculates the maximum width of the melt isotherm. The temperatures from the point of the maximum width of the melt isotherm up to the point where the temperature is 5% of the melt temperature is then calculated. The width of the control volume is output as the location where the temperature is 5% of the melt temperature, as discussed earlier. An average value for the temperature of the metal leaving the control volume is then calculated from the temperature profile. The errors associated with the above approach increase in magnitude with increasing thickness of the sample due to the deviation from a two-dimensional assumption.

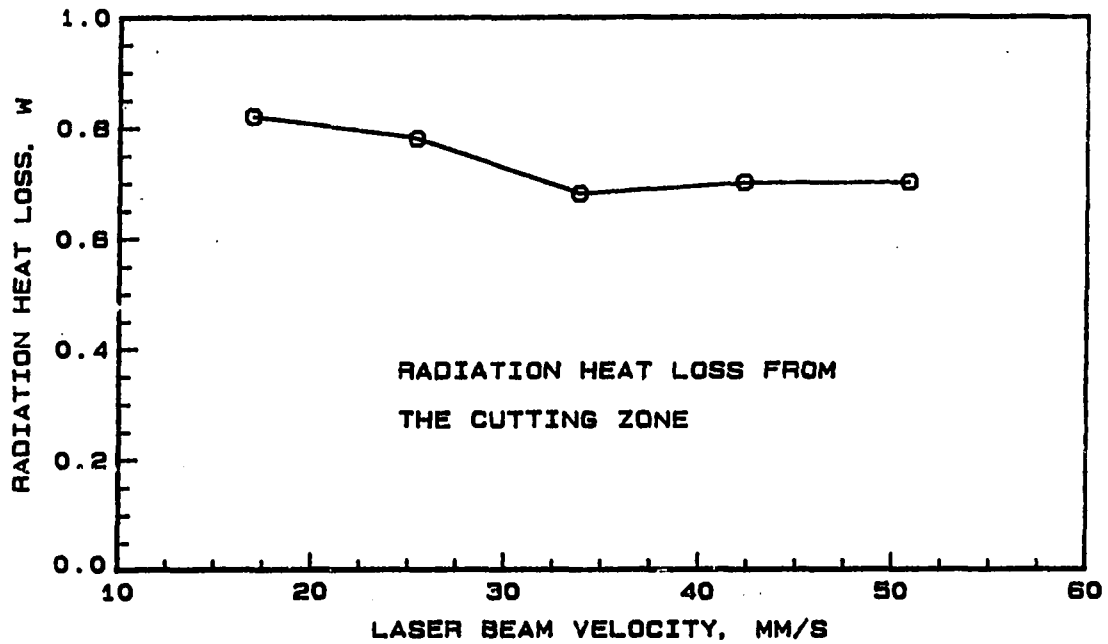


Figure 8.4: The calculated radiation heat loss at different laser beam velocities for the case of AISI 1018 steel

The radiation heat loss from the cutting region is calculated from the equation.

$$\dot{Q}_{rad} = \varepsilon \sigma A T_5^4 \quad (8.16)$$

where, σ is the Stefan-Boltzmann constant, and A is the cutting front area obtained by the product of the kerf width and the thickness of the metal. The emissivity of the cutting zone is assumed to be unity for the reasons discussed earlier in this section. The results of the radiation heat loss calculated from the above equation are shown in Figure 8.4. It is seen that the radiation heat loss ranges from 0.7 to 0.8 W, which is extremely small compared to the convective heat loss. Therefore, the radiation heat loss effects are assumed negligible in the analysis.

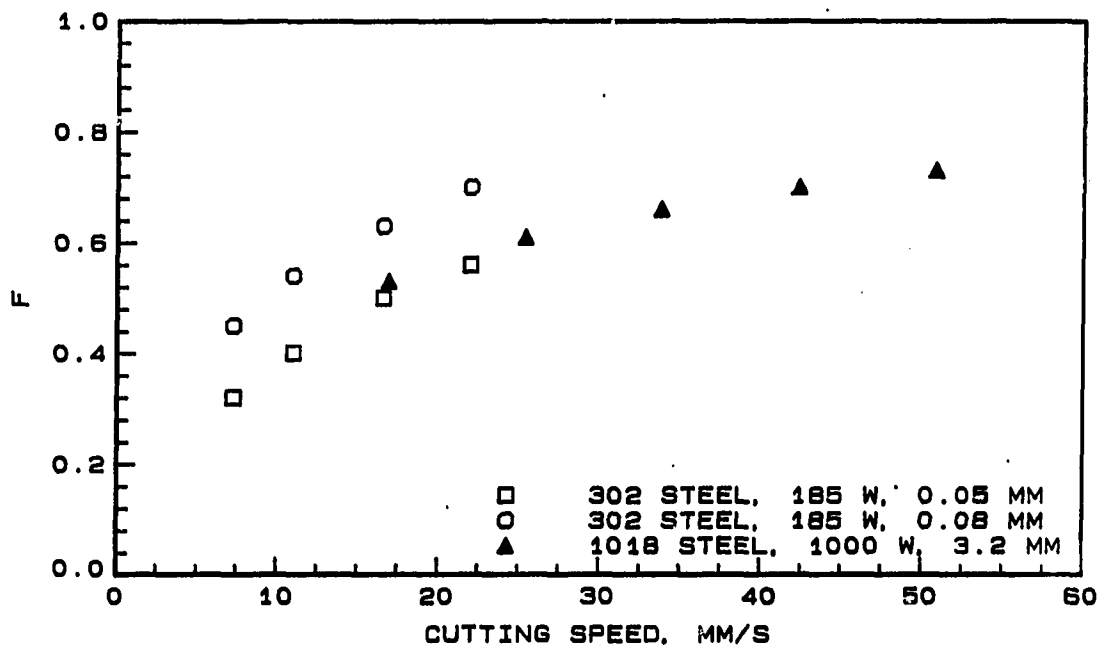


Figure 8.5: Fraction of the laser beam actually striking the surface for the case of 302 stainless steel and 1018 steel used in the model verification

Results of the thermodynamic model

The thermodynamic model that was developed was verified for the case of cutting type 302 stainless steel of two different thicknesses (0.0508 and 0.08 mm), and the cutting of 3.2 mm thick AISI 1018 steel. The data for the type 302 stainless steel were taken from the results of Gonsalves and Duley [25].

Figure 8.5 shows the values of the fraction of the beam incident on the metal calculated by the method of Gonsalves and Duley [25]. The fraction of the beam that is incident increases with increasing beam velocity and material thickness. Since the fraction is also a function of the material properties and the laser beam diameter and power, for the same velocity, there is a greater fraction of the beam incident on the 0.08 mm thick 302 stainless steel than the 3.2 mm thick 1018 steel.

The average temperature of the metal leaving the control volume, T_4 , was calculated by using the computer program in Appendix A which was described earlier. Equation 8.11 can now be solved by substituting the appropriate thermal properties for the materials [26, 39]. In using the model to verify the results for type 302 stainless steel, two additional assumptions were made. The thickness of the stainless steel is such that only a very low pressure argon gas was used as the cover gas [25]. Hence, $\dot{Q}_{oxidation}$ and \dot{Q}_{conv} are both assumed to be zero. This simplifies Equation 8.11 to,

$$\dot{m}_5 = \frac{-[\dot{Q}_{laser} + \dot{m}_3 C_p (T_3 - T_4)]}{C_p (T_4 - T_5) - i_{sl}} \quad (8.17)$$

Sample calculation Equations 8.17, 8.12, and 8.13 are used to calculate the kerf width for the type 302 stainless steel and the 1018 steel. A sample calculation is presented to show the method of estimating the kerf width.

The following are the input data available or calculated for type 302 stainless steel:

$$\begin{aligned} \dot{Q}_{laser} &= \varepsilon f P \\ &= (0.16 \times 0.56 \times 185) \text{ W} \\ V_3 &= 22 \text{ mm/s} \\ t &= 0.05 \text{ mm} \\ w &= 1.9 \text{ mm (calculated by computer program in Appendix A.)} \\ T_3 &= 25^\circ\text{C} \\ T_4 &= 453^\circ\text{C (calculated by computer program in Appendix A.)} \\ T_5 &= 1400^\circ\text{C} \end{aligned}$$

$$\rho = 8 \times 10^{-6} \text{ kg/mm}^3$$

$$C_p = 544 \text{ J/kg-K}$$

$$i_{sl} = 279.2 \text{ kJ/kg}$$

Using the above data, the mass flow rate of metal out of the control volume can be calculated from Equation 8.12 to be, $\dot{m}_3 = 33.5 \times 10^{-6} \text{ kg/s}$. The mass flow rate of metal removed by melting can now be calculated from Equation 8.17 as, $\dot{m}_5 = 11.0 \times 10^{-6} \text{ kg/s}$. Now using Equation 8.13, the kerf width can be found as, $k = 1.3 \text{ mm}$.

The results of the verification of the thermodynamic model are shown in Figure 8.6 for the type 302 stainless steel. The model predicted higher values, with the maximum overprediction being 25% for both sample thickness and for all beam velocities. This error could be due to several reasons, the chief among them being the estimation of the fraction, f , and the temperature of the metal leaving the control volume. Additional errors could also be due to the assumptions of constant thermal properties and negligible cooling of the argon gas jet.

The results of the model for the 3.2 mm thick AISI 1018 steel used in the present study are shown in Figure 8.7. Two sets of predicted values are shown, the case of negligible heat of oxidation and heat loss by convection, and the case when these effects are taken into consideration. The experimental data used in the comparison are taken from the results presented in Chapter 6. The results show that when the oxygen effect is neglected, the predicted kerf width is less than the measured value. However, when the oxygen effect is included in the analysis, the kerf width is over-predicted,

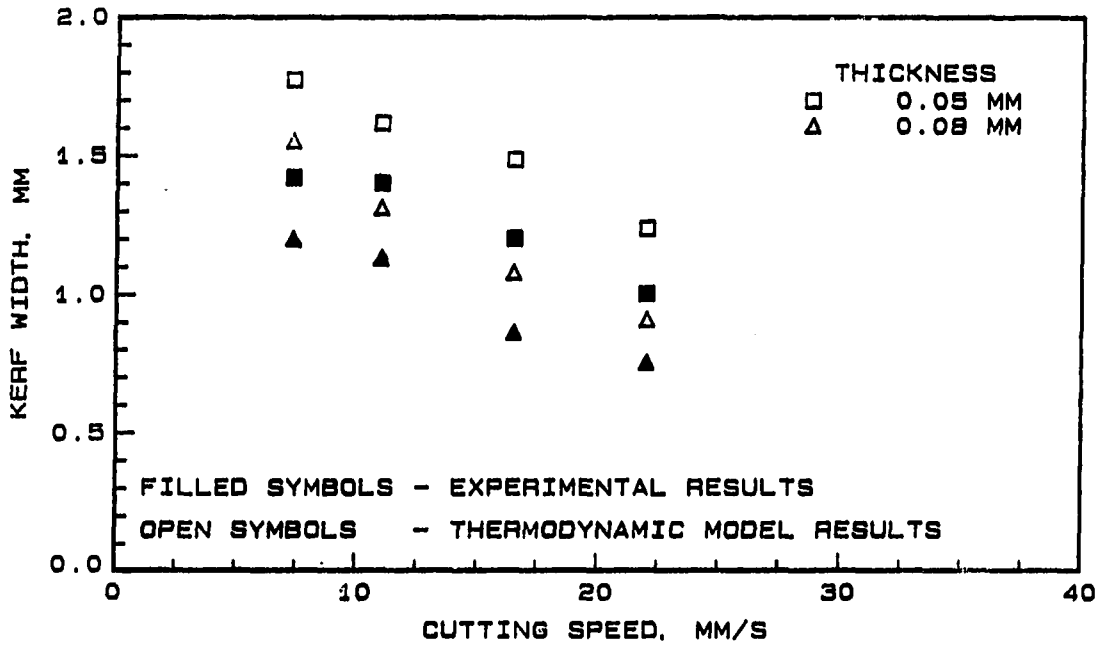


Figure 8.6: Kerf width predicted by the thermodynamic model and the experimental measured values for type 302 stainless steel

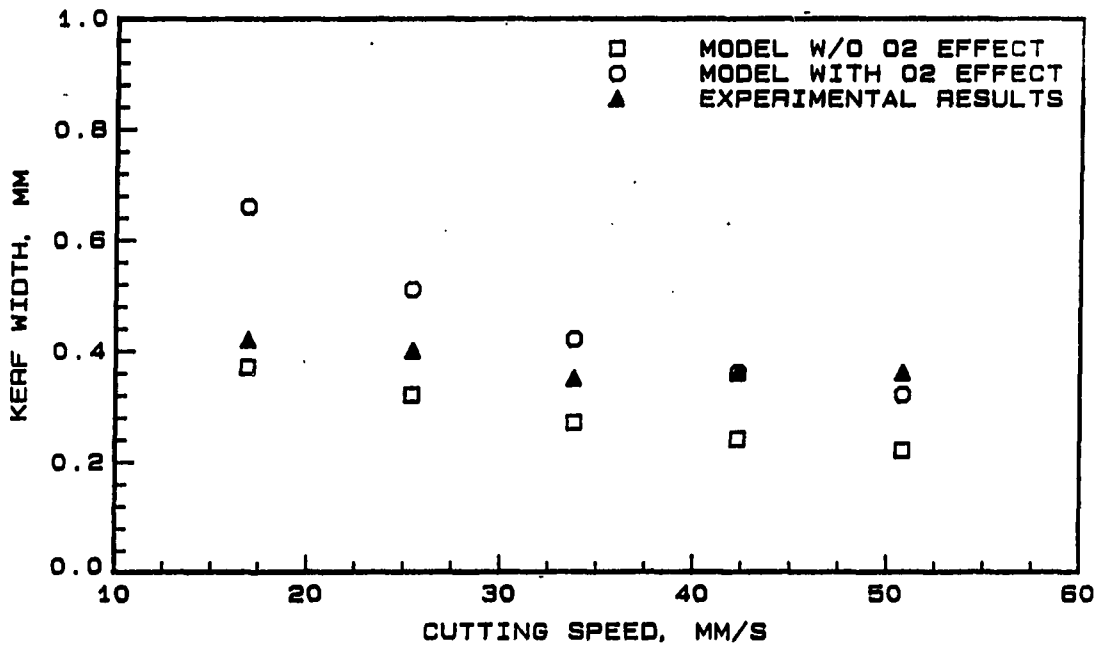


Figure 8.7: Kerf width predicted by the thermodynamic model and the experimental measured values for AISI 1018 steel

especially at the lower beam velocities. The maximum error in the predicted values when the oxygen effect is neglected is as much as 38% at the higher beam velocities. The maximum error when the oxygen effect is included varies from 0% at the higher velocities to 57% at the low beam velocities.

These large errors in the predicted and actual values are due to several reasons, not the least of which is the assumption that the thermal behavior of the thick-metal is the same as a thin-metal. Additional errors are due to the assumption of constant thermal properties, the calculation of the fraction f and the temperature of the metal leaving the control volume.

In spite of these large errors between the predicted and the measured values of the kerf width, the model is useful in predicting the trends in the kerf width when the laser beam power and the velocity are varied. In addition, the model could also be used to test the effect of the material properties on the kerf width. Finally, the model is also useful in highlighting the important processes in the cutting of a sample with the laser.

Finite Element Model

The time-dependent problem of a heat source moving on a flat plate, including phase change, was solved by the finite element method for the temperature distribution on thin plate. The finite element method was chosen due to the availability of packaged computer programs used to solve the conduction problem. In this section, the description of the conduction problem, the finite element mesh, the solution procedure used, and the results of the model are discussed. The kerf width predicted

by the model is compared with experimental data and the usefulness of the model is discussed.

Problem formulation

The problem of the laser-cutting of a plate is treated as that of a heat source moving on a flat plate. The time-dependent, two-dimensional classical heat conduction equation is solved, including the effect of phase change. In addition, the cutting process involves the removal of metal once it has melted to a liquid. The actual cutting process also involves temperature ranges over which the properties of the metal do not remain constant. Even though the results presented in this section are assuming constant thermal properties, the finite element model has the capability to include temperature dependent properties. Heat loss from the metal was also assumed to be negligible.

A metal sample 126.8×20 mm was modelled; due to the symmetry condition of the problem, only one half of the sample had to be analyzed. Assuming that heat source moves along the shorter of the two lengths, the actual space modelled was 63.4×20 mm. This size of the sample was chosen so that a quasi-steady heating of the sample could be achieved after a time, without the front and side edges of the sample influencing the heat transfer process. The solution, however, was carried through until the heat source had travelled the entire distance along the sample.

Finite element mesh

The two-dimensional finite element mesh used to discretize the flat plate is shown in Figure 8.8. Rectangular elements with four to eight nodes were used. The number of elements decreased from 100 close to the line of cut where the steepest gradients are to be found, to 25 in regions far from the heat source. The element size was chosen in conjunction with the time step used both from accuracy and stability considerations. The actual size of the elements used varied with the element location, and is indicated in Figure 8.8. The boundary conditions for the problem are also shown in the same figure. The method of implementing the time dependent flux boundary condition along one edge of the sample is discussed in the section below.

Solution procedure

The finite element problem was solved by using a commercial software package called ADINAT /citeadina on the HDS AS/9180 computer. The software ADINAT requires that data for the problem be input in the card format in the sequence of the statements used to read the data by the program. A typical input data file is included in the Appendix A.

The input data consisted of the nodal coordinates, the element connectivity information, and the physical and thermal properties of the problem. A typical input data file is included in Appendix A. ADINAT had the capability of calculating the temperature profile due to a time-dependent point heat source at a node. This capability of the program was used to simulate the moving heat source by subjecting the nodes along a line to point a heat source for a finite time, Δt . By successively

$$Q = 0$$

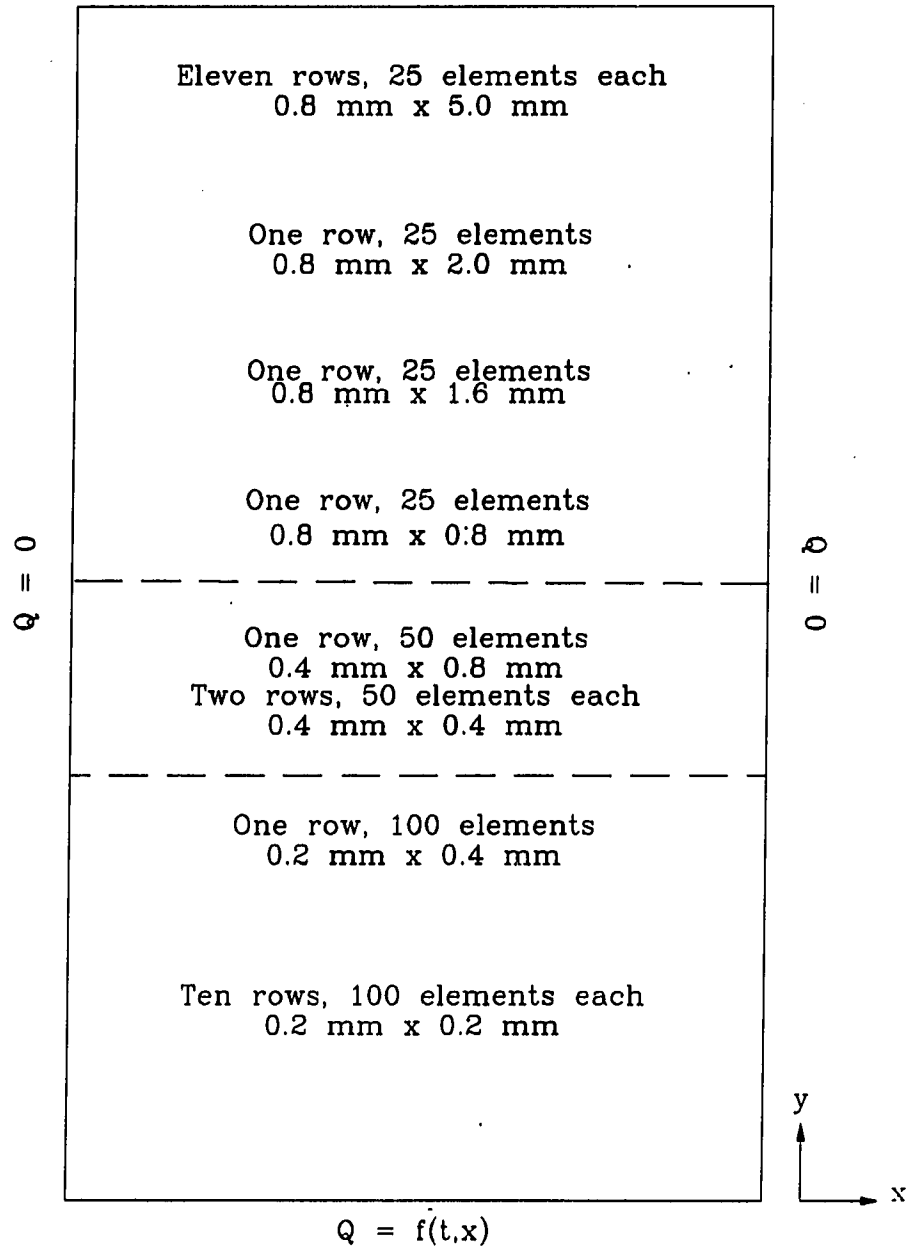


Figure 8.8: Finite element discretization of the flat plate

varying the time at which this heat source is activated on each node, the effect of a moving heat source on the plate was simulated. The heat input to the plate was calculated by the procedure described in Chapter 6 to account for the fraction of the energy that fails to strike any metal and passes through the kerf. The Euler backward integration, which is unconditionally stable [8], was used for the integration in the time domain. The time step for the problem was chosen by first choosing a value and then successively halving it until the results of two consecutive cases agreed with each other. The choice of the time step for the solution process also depends on the velocity of the heat flux that is being simulated. Information for the phase change could be included if needed.

The output of the program ADINAT was temperature at different times, which was stored in a data file that was continuously updated as the solution process continued. This data file is not in a format that can be easily read, and computer programs were written to read this data and write to data files as needed. The data were then plotted and information on the kerf width was extracted. Several test cases were run and the results of these are presented in the section that follows.

Results

The results of the finite element solution are compared with the exact solution in Figure 8.9. The exact solution is calculated from [14],

$$\exp(ux/2\alpha) = \frac{2\pi ktT}{\dot{Q}K_0(ru/2\alpha)} \quad (8.18)$$

for the case of a point source moving on a thin plate at constant velocity. The solution of Equation 8.18 gives the steady temperature profile around the moving heat source.

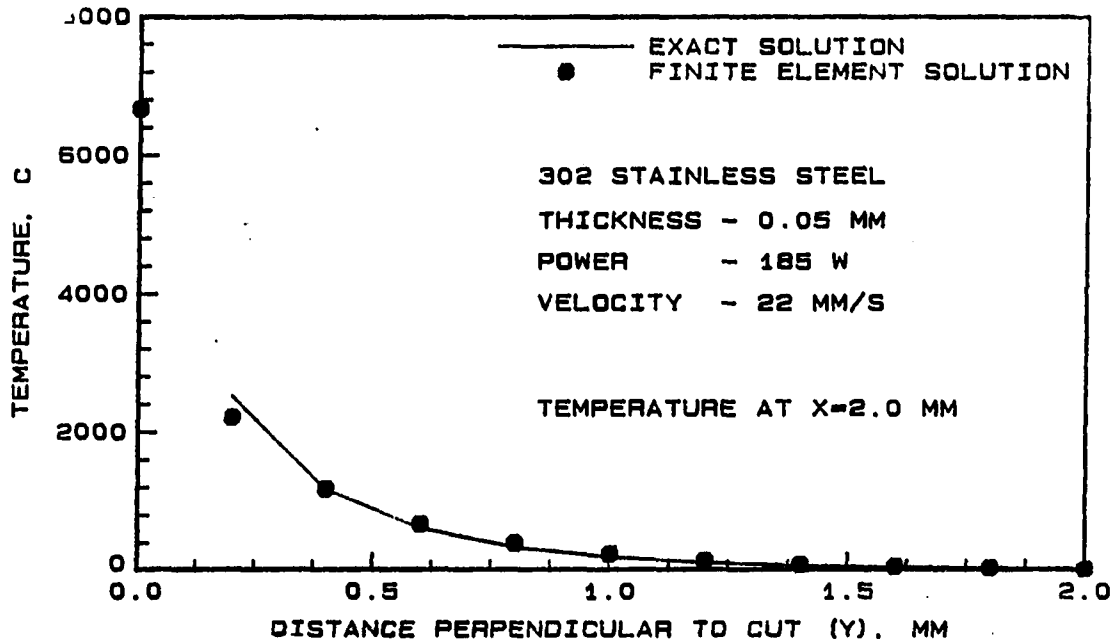


Figure 8.9: Temperature calculated by the finite element model compared with the exact solution

In Equation 8.18, r is the radial distance of a point from the heat source, t is the thickness of the metal sample, α is the thermal diffusivity of the metal, \dot{Q} is the energy input to the metal, u is the velocity of the heat source, and K_0 is the Bessel function of the second kind of order zero.

An initial test case was run to compare the results obtained with and without accounting for the phase change effects. Including the phase change effects in the problem increased the computer time by a factor of five. Figure 8.10 shows the maximum temperature along the line of cut (i.e., line of the heat source). It is seen that the maximum temperature decreased only slightly when the enthalpy of melting is accounted in the problem analysis. This decrease was less than 10% at all the locations along the cut. It was, therefore, concluded that the results obtained by

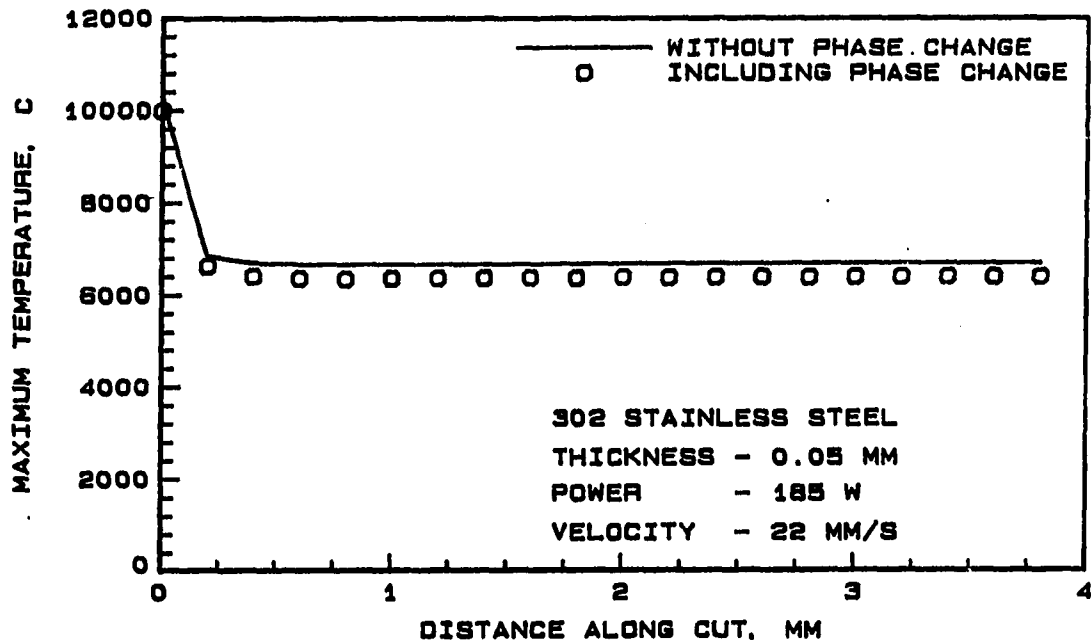


Figure 8.10: Maximum temperature at locations along the line of cut with and without phase change effects

solving the problem without including phase change was the same as the solution obtained by considering phase change. Since the solution of the problem without phase change meant considerable savings in computation time, it was decided to neglect phase change effects.

The maximum temperature along the line of cut varied with position along the line. Figure 8.11 shows the maximum temperature at different locations along the line of cut. The temperatures shown are those calculated for the case of a heat source of power of 185 W moving at a velocity of 22 mm/s on a flat plate of type 302 stainless steel that is 0.05 mm thick. The maximum temperature decreased from a value of about 10,000°C at the leading edge to a value of ~6500°C at a location of ~1.0 mm. The temperature remained fairly steady after that until very close to

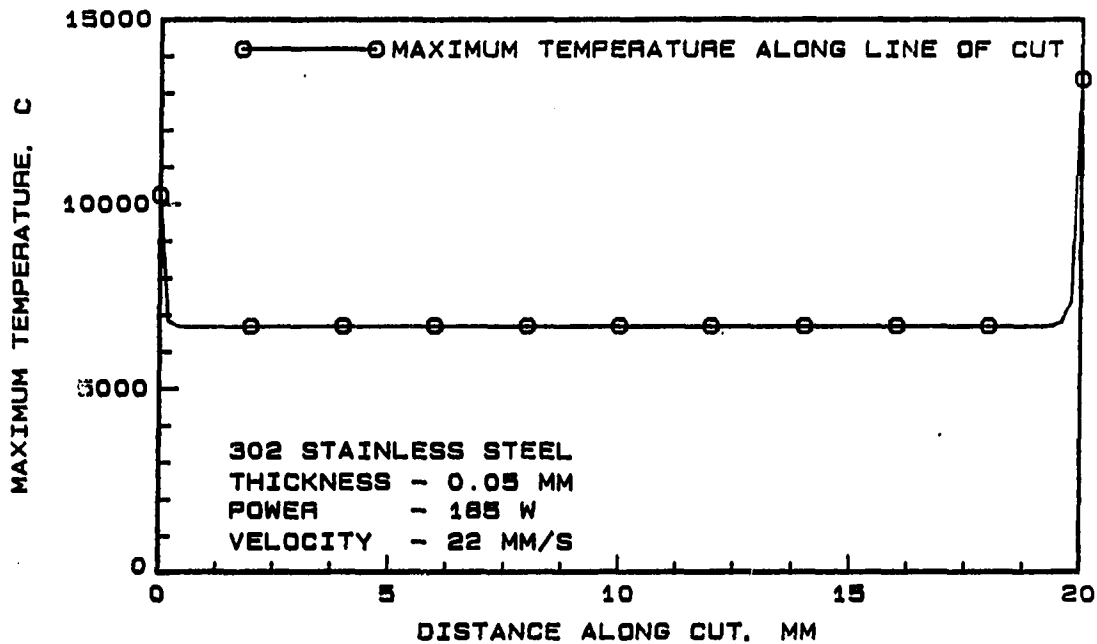


Figure 8.11: Maximum temperature at locations along the line of cut from the leading to the trailing edge of the piece

the trailing edge of the plate. At a distance of ~ 1.5 mm, the maximum temperature starts rising rapidly again, until at the trailing edge itself, the maximum temperature was nearly $14,000^{\circ}\text{C}$. Due to the fact that the maximum temperature was invariant beyond 1.0 mm from the leading edge, for the purposes of evaluating the kerf width from the temperature data, the temperature profile perpendicular to the line of cut at the location of 2.0 mm from the leading edge was chosen.

The temperature profile perpendicular to the line of cut at a distance of 2.0 mm along the line of cut is shown in Figure 8.12. The temperatures at different instances as the heat source approaches and as the heat source moves away from the location of 2.0 mm shows the extent to which the thermal effect has advanced in the direction perpendicular to the line of travel of the heat source. This is also shown in Figure 8.13

where the temperature at different instances in time after the heat source crosses the location of 2.0 mm is plotted. The time when the heat source crosses $x=2.0$ mm is taken to be 0.0. It is seen that the temperature at distances away from the line of cut, peaks after the heat source crosses $x=2.0$ mm. The time at which this peak occurs also increases with increasing distance from the line of cut. These results are consistent with those expected for a heat source moving on a flat plate.

The kerf width is calculated as the maximum width of the melt isotherm, 1400°C for the type 302 stainless steel, and 1535°C for the AISI 1018 steel. The finite element model was tested for the type 302 stainless steel and for the AISI 1018 steel by using the same data as used in the thermodynamic model. The results of the kerf width obtained by using the finite element model are compared with the experimental data [25] in Figure 8.14 for the type 302 stainless steel. The finite element model compares well with the experimental data which validates the thin-plate assumption and the method of Gonsalves and Duley [25] for the calculation of f , the fraction of the laser beam striking the metal.

The finite element model was also tested for the AISI 1018 steel plate of 3.2 mm thickness. The results of the model for two cases are compared with the experimental data in Figure 8.15. The first case is that of the assumption of negligible oxygen effects, while in the second case the effect of the oxygen gas is included. The values used for the heat of oxidation and the cooling effect of the gas the same values used in the thermodynamic model and are taken from the results in Chapter 6.

The minimum and maximum errors in the predicted kerf when the effect of the oxygen gas is included are 3 and 36%, respectively. However, when the effect

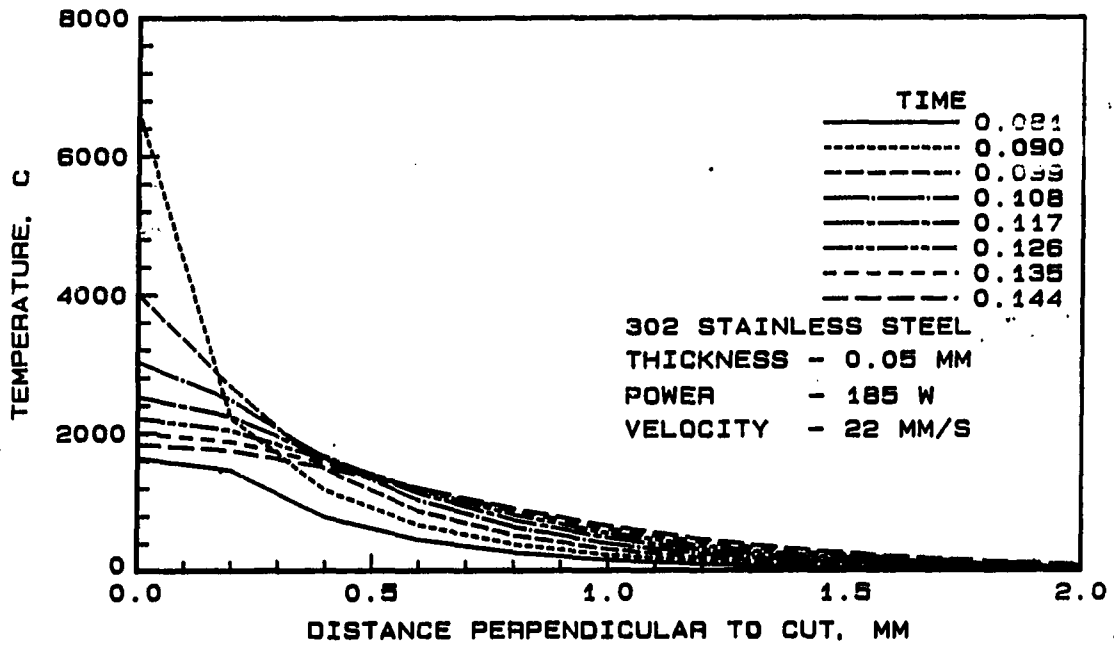


Figure 8.12: Temperature at locations perpendicular to the line of cut at $x=2.0$ mm from the leading edge

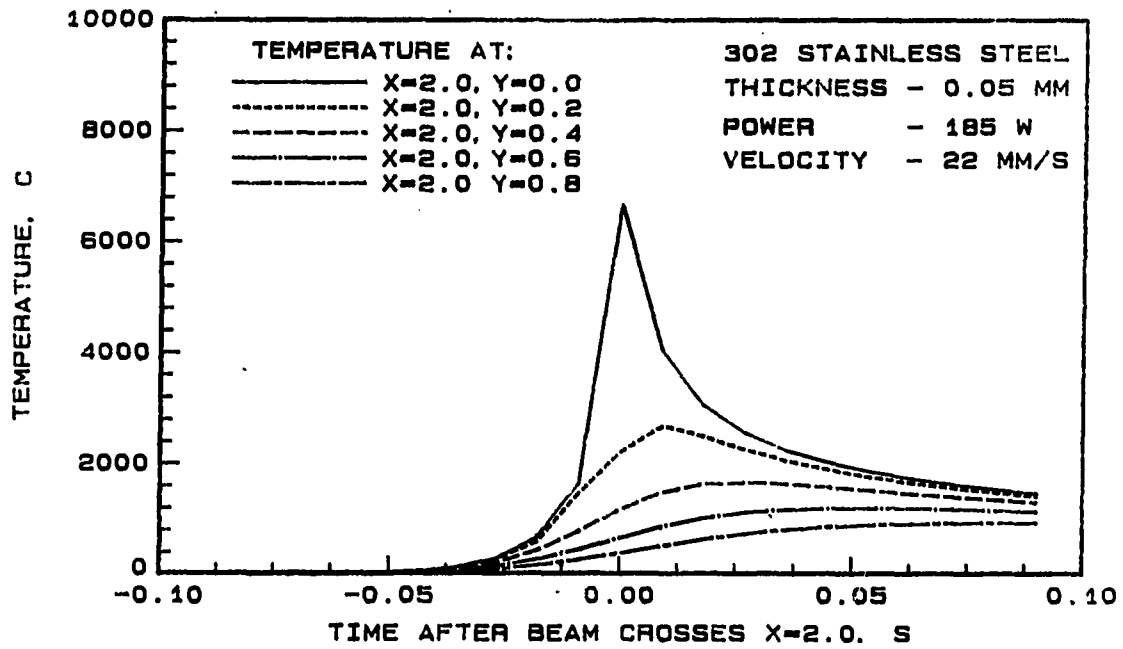


Figure 8.13: Temperature at different y and $x=2.0$ mm with time taken as zero when the source crosses $x=2.0$ mm

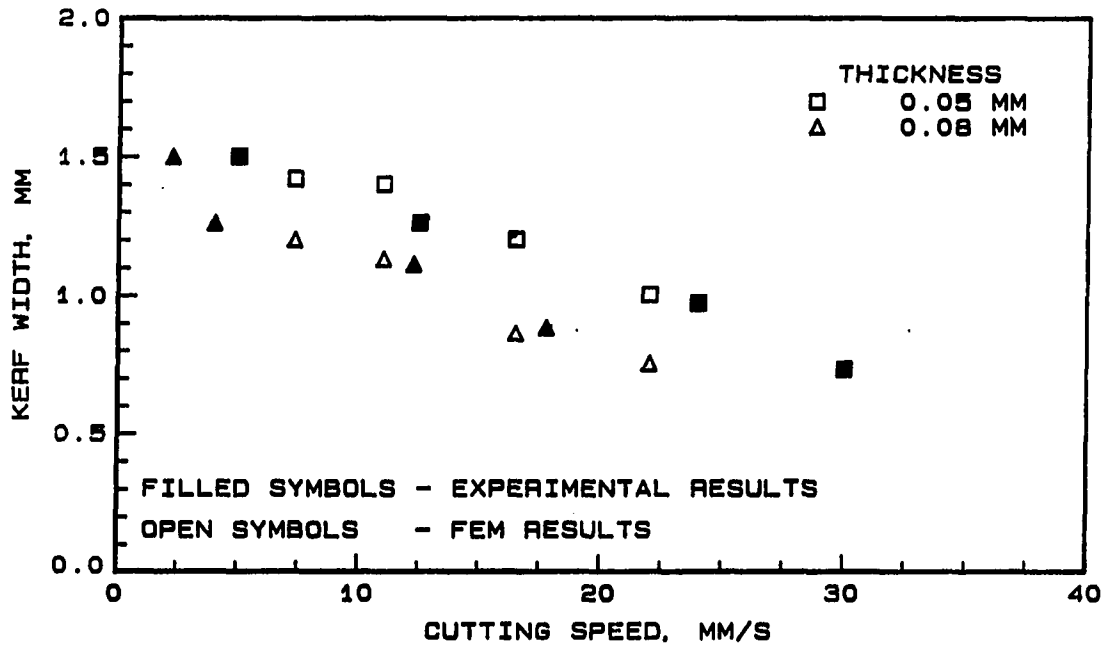


Figure 8.14: Comparison of kerf width calculated by the finite element model and the experimental values for 0.05 mm thick type 302 stainless steel

of the gas is not considered, these errors were 37 and 66%, respectively. The results indicate that the kerf width predicted by including the effect of oxygen is closer to the experimental values than the value obtained by neglecting the gas effects. However, the model predicts a decreasing trend in the kerf width with increasing velocity, which is not very pronounced in the experimental result. This was also seen to be the case in the thermodynamic model discussed earlier. The error could be in the calculation of the actual energy input to the metal and in the estimation of the effects of the oxygen gas jet. In addition, the finite element model could also be in error due to the assumption that a 3.2 mm thick plate behaved as a thin plate.

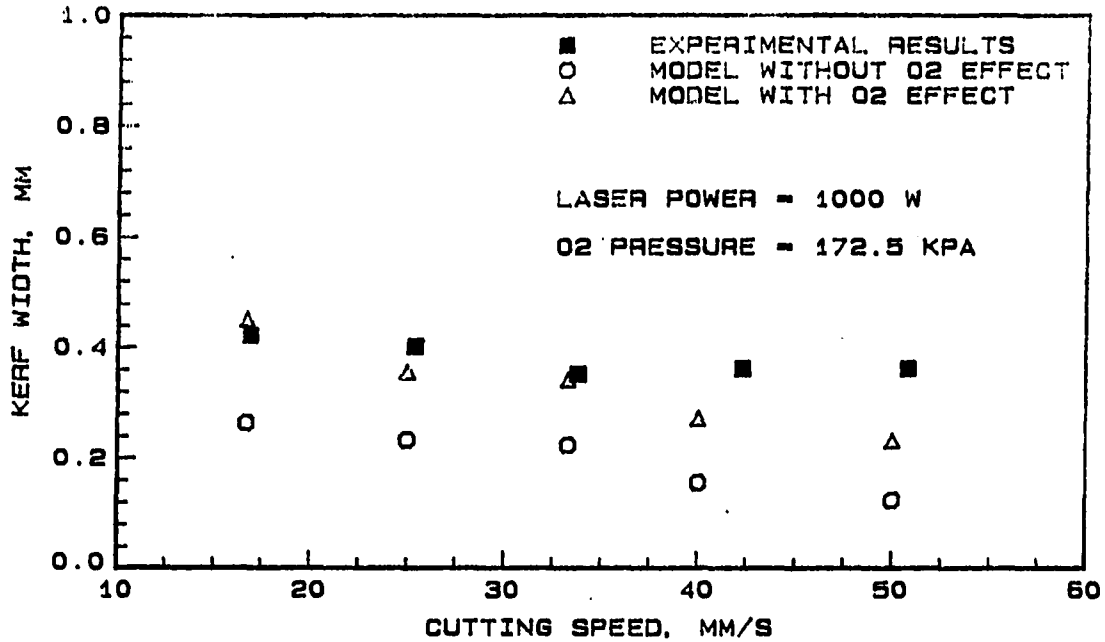


Figure 8.15: Comparison of kerf width calculated by the finite element model and the experimental values for 3.2 mm thick AISI 1018 steel

Summary

Two models of the laser cutting process were presented in this chapter. The first was a simple thermodynamic model of the process. The results of the model for type 302 stainless steel compared fairly well with the experimental data with the maximum error ranging from 0 to 57% depending on the velocity and whether the effects of oxygen gas were included or not. The model was used to predict the kerf width for the AISI 1018 steel; the results obtained by neglecting the oxygen gas effects were within 25% of the experimental values. When the model included the oxygen gas effect, the model over-predicted the kerf width by more than 50%.

The second model was a two-dimensional finite element model of the process. The accuracy of the model was tested against an exact result for the temperature

distribution around a moving heat source. Initial tests of the model indicated that the heat of melting did not have a significant effect upon the temperature predicted. Phase change effects, therefore, were neglected to save computation time. The kerf width predicted by the model was also compared to the experimental data. The model predicted the kerf within 3 to 36% when the effects of oxygen were included, but it was in error by as much as 66% when they were not.

CHAPTER 9. CONCLUSIONS AND RECOMMENDATIONS

Conclusions

This study was undertaken to study the heat transfer effects in cutting samples of metal with a laser. The results of this study indicate that small samples cut with the laser do not have uniform cut quality along the entire length of the cut. This can have detrimental effects, especially when two laser-cut edges have to be joined together along the cut-edge. A possible method of avoiding this could be to cut at continuously varying velocities along the entire length of the cut.

A goal of this study was also to show feasibility that surface temperature could be used to monitor the quality of the cut. This feasibility was demonstrated, however, the location of the temperature measurement played a big role in determining the accuracy of the quality prediction. This study also compared the contribution of the oxygen gas jet to the convective cooling of the cutting region and to the energy input to the metal through the exothermic oxidation reaction. More specific conclusions are presented later in this section.

Two models that could be used to show the relative importance of the different variables in the cutting process were developed as part of this research. One conclusion of the models is that accurate determination of the fraction of the laser beam incident

on the metal (and not passing through the kerf) is essential for the model to predict the cut quality with adequate accuracy.

Specific conclusions related to the kerf width, heat affected zone, and the process models are described below.

Kerf width

For the bulk of the cut, kerfs measured on the upper surface differed from those on the lower surface by as much as a factor of two. However, at the leading and trailing edges, there was considerable variation in ratio of the upper-to-lower surface kerf. This could be attributed to the presence of the adiabatic edges and to the fact that the oxygen gas jet does not act adequately enough to blow away molten metal at the edges. It is also important to note that the sides of the kerf also act to channel the gas flow thus resulting in additional "nozzle" effects.

Kerf width was also found to depend on the velocity of the beam. For the samples used in the experiments, the kerf on the upper surface was found to be minimum at around a velocity of 34 mm/s. The oxygen gas pressure, however, did not have a significant effect on the kerf width. For the range of pressures used in the experiments, 69 to 207 kPa (gage), the convective cooling effect of the jet varies from 10 to 17% of the input laser power, assuming an input power of 1000 W. Over the same range of pressures, and for the same input power, the exothermic heat of reaction was calculated to vary from 30 to 40% of the input power. The laser power also had effect upon the kerf width. For an increase of laser power from 800 to 1200 W, the average kerf value increased by 20%.

Temperatures measured with thermocouples and the infrared sensor showed dependence on the kerf width. From the thermocouple measurements it was possible to predict the kerf width to within $\pm 5\%$ accuracy. The location where the infrared sensor provided the highest resolution of the process was when the sensor's focal area covered the entire cutting region. In this configuration, the angle that the cutting front made with the vertical affected the sensor output especially since the sensor was receiving radiant energy from the cutting front. This cutting front angle increased with increasing beam velocity, with the result that the sensor received radiation from a larger area leading to higher temperatures with increasing beam velocity. The temperature output of the infrared sensor was affected by several factors, thus making it difficult to predict the kerf width from temperature data. It was only in the case of varying oxygen gas pressure that a prediction accuracy of $\pm 5\%$ could be obtained. In the case of varying laser power, kerf predictions were made without using the temperature data to within $\pm 10\%$ accuracy.

Heat affected zone (HAZ)

An important result of this study was the comparison of the oxidation heat affected zone and the heat-treated heat affected zone. Oxidation HAZ is usually reported as the heat affected zone since it is the easier of the two to measure. However, the heat-treated HAZ is permanent in nature, and therefore, more important. It was found that the oxidation HAZ was usually within 25% of the heat-treated HAZ. The two measures of the heat affected zone were more likely to equal each other at higher HAZ values. The oxidation HAZ showed strong dependence on the laser beam

velocity. For example, when the beam velocity increased from 16.9 to 50.8 mm/s, the oxidation HAZ on the upper surface decreased by 40%. At the same time, the heat-treated HAZ on the upper surface showed a decrease of less than 5%. Hence, in reporting oxidation HAZ as the heat affected zone, the heat-treated depth can be estimated to not less than 25% accuracy.

The oxidation HAZ was also influenced slightly by the oxygen gas pressure. An increase of 200% in the oxygen gas pressure, from 69 to 207 kPa (gage), produced only a 15% decrease in the oxidation HAZ. As in the case of kerf width, the laser beam power had a significant effect upon the oxidation HAZ. An increase of laser beam power from 800 to 1200 W produced an increase of 20% in the oxidation HAZ.

The surface temperatures measured with thermocouples and the infrared sensor showed dependence on the heat affected zone. However, the heat affected zone did not influence the temperatures to the same extent that the kerf width did. The result was that in no case was it possible to predict the HAZ to an accuracy better than $\pm 15\%$. As in the case of the kerf width, the infrared sensor provided the best resolution when the sensor spot enveloped the entire cutting region.

Process Models

In the development of the thermodynamic model, several simplifying assumptions had to be made owing to the complexity of the process. A model for estimating the size of the control volume around the cutting region and the average temperature of the metal leaving the control volume was also developed. The thermodynamic model was able to predict the kerf width to accuracies ranging from 0 to 57% in the case

of cutting AISI 1018 steel. The smallest errors were encountered at the higher beam velocities when the oxygen effect was included.

The transient heat flow in a thin sheet of metal was modelled by a finite element model in two dimensions. When used to predict the kerf width of thin sheets of type 302 stainless steel, the model produced results that agreed well with experimental data. However, when the same model was used to predict the kerf for 3.2 mm thick AISI 1018 steel, the errors were larger. When the effects of oxygen gas were ignored, the errors varied from 37 to 66% over the velocity range of 16 to 50 mm/s. However, when the effects of the oxygen gas were included, the error was considerably less, ranging from 3 to 36% over the same range of velocities. The errors in the case of the 3.2 mm thick steel could be due to the assumption of two dimensional heat transfer.

Both the thermodynamic and the finite element model were extremely sensitive to the estimation of the fraction of the laser beam that is actually incident on the metal. Proper evaluation of the fraction is essential before a model can be successfully used for cut quality prediction.

Recommendations for Future Research

The research reported here can be extended into followup studies in the future. Several suggestions of followup topics along with ways of improving these topics are made below.

1. An infrared sensor with a focal spot area smaller than the one used in this research should be used to record temperatures in the vicinity of the cut. A smaller focal area would result in the sensor being more sensitive to changes in

the temperature, and therefore, changes in the cut quality.

2. A fixture should be designed and fabricated that would allow more accurate positioning of the infrared sensor than the one used in the experiments. This would permit greater accuracy in positioning the sensor spot relative to the laser beam.
3. An exhaustive study needs to be performed to determine the optimum location for the infrared sensor. The optimum location is defined as that location of the sensor spot at which the temperatures recorded reflect the cut quality with the highest resolution.
4. A detailed study of temperature measurements for different types of materials of different thicknesses needs to be performed to obtain a complete set of data that could be used to both predict and control the cutting process. This study should also include the effects of other process variables such as surface treatment and the nozzle design and position.
5. Other measures of cut quality, such as the striations and dross attachment, should also be studied. In particular, since dross attachment is extremely undesirable in cutting operations in the industry, the dependence of temperature on the dross attachment would be useful.
6. High-speed filming techniques could be used in conjunction with the temperature measurements to better understand the laser cutting process. This could also be extremely valuable in determining proper locations for the infrared sensor.

7. There is no model available to adequately predict the effects of the process variables on the cut quality. A three-dimensional computational model needs to be developed to predict the temperature transients in processing samples where either the edges or preheating of the sample could be expected to influence the heat transfer. This requires that a prior study be performed to develop a method of predicting the fraction of the laser beam that is intercepted by the sample.
8. Two possible applications of temperature measurement, namely, cut quality prediction (i.e., process monitoring) and process control need to be investigated further. In addition to surface temperature other methods of process monitoring could also be investigated.
9. The method of using surface temperature as a predictive tool is not limited to laser cutting alone. The application of this method in other laser processes such as, laser heat-treating, laser-cladding, laser-welding, and laser chemical vapor deposition, could also be investigated.

BIBLIOGRAPHY

- [1] *ADINAT A finite Element Program for Automatic Dynamic Incremental Non-linear Analysis of Temperatures*. ADINA Engineering, Inc. (Watertown, MA) Report AE 81-2, 1981.
- [2] Y. Arata, and I. Miyamoto. "Some Fundamental Properties of High Power Laser Beam as a Heat Source (Report 1) - Beam Focussing Characteristics of CO₂ Laser." *Transactions of Japan Welding Research Institute* 3, No. 1 (1972): 143-151.
- [3] Y. Arata, and I. Miyamoto. "Some Fundamental Properties of High Power Laser Beam as a Heat Source (Report 2) - CO₂ Laser Absorption Characteristics." *Transactions of Japan Welding Research Institute* 3, No. 1 (1972): 152-162.
- [4] Y. Arata, and I. Miyamoto. "Some Fundamental Properties of High Power Laser Beam as a Heat Source (Report 3) - Metal Heating By Laser Beam." *Transactions of Japan Welding Research Institute* 3, No. 1 (1972): 163-180.
- [5] Y. Arata, H. Maruo, I. Miyamoto, and S. Takeuchi. "Dynamic Behavior in Laser Gas Cutting of Mild Steel." *Transactions of Japan Welding Research Institute* 8, No. 2 (1979): 175-186.
- [6] D. Auric, E. Kerrand, J. de Miscault, and J. Cornillault. "Thermal Imaging System for Material Processing." In *High Power Lasers: Proceedings of SPIE - The International Society of Optics and Engineering*, 801 (1987): 354-359.
- [7] V. P. Babenko and V. P. Tychinskii. "Gas-Jet Laser Cutting (Review)." *Soviet Journal of Quantum Electronics* 2, No. 5 (1973): 399-410.
- [8] K. Bathe. *Finite Element Procedures in Engineering Analysis*. Englewood Cliffs: Prentice-Hall, Inc., 1982.
- [9] N. A. Bekeshko. "Certain Pressing Questions of the Development of Methods and Means of Thermal Nondestructive Methods." *The Soviet Journal of Nondestructive Testing* 22, No. 12 (1986): 838-844.

- [10] D. A. Belforte. "Industrial Lasers: the Trend is Upward." *Laser Focus World*. Tulsa: Pennwell, December, 1989.
- [11] D. A. Belforte and M. Levitt. "Laser Material Processing Data Guidelines." In SPIE Vol. 629 *The Industrial Laser Annual Handbook*, edited by D. A. Belforte and M. Levitt, 1-13. Tulsa: Pennwell Books, 1986.
- [12] R. P. Benedict. *Fundamentals of Temperature, Pressure, and Flow Measurements*. 2nd Edition. New York: John Wiley & Sons, 1977.
- [13] M. R. Bramson. *Infrared Radiation: A Handbook for Application*. New York: Plenum, 1968.
- [14] H. S. Carslaw and J. C. Jaeger. *Conduction of Heat in Solids*. 2nd edition. Oxford: Oxford University Press, 1976.
- [15] S. Ciarcia. "Electromagnetic Interference." *BYTE* 6, No. 1 (1981): 48-68.
- [16] H. E. Cline and T. R. Anthony. "Heat Transfer and Melting Material with a Scanning Laser or Electron Beam." *Journal of Applied Physics* 48, No. 9 (1977): 3895-3901.
- [17] G. Daurelio, M. Dell'Erba, and L. Cento. "Cutting Copper Sheets by CO₂ Laser." *Lasers & Applications* 5, No. 3 (1986): 59-64.
- [18] A. Dillio, G. Dionoro, F. M. C. Minutolo, and V. Tagliaferri. "Laser Cutting of Al 707 Sheets." In *Proceedings of the 2nd International Conference on Lasers in Manufacturing Held in Birmingham 26-28 March 1985*, edited by M. F. Kimmitt, 57-62. New York: IFS Publications Ltd., 1985.
- [19] L. D. Favro, P. K. Kuo, and R. L. Thomas. "Thermal Wave Techniques for Imaging and Characterization of Materials." In Vol. 6 *Review of Progress in Quantitative NDE*, edited by D.O.Thompson and D.E.Chimenti, 293-299. New York: Plenum Press, 1987.
- [20] J. T. Gabzdyl, W. M. Steen, and M. Cantello. "Nozzle-Beam Alignment for Laser Cutting." In *Laser Materials Processing: Proceedings of the 6th International Congress on Applications of Lasers and Electrooptics ICALEO '87 Held in San Diego 8-12 November 1987*, edited by S. L. Ream, 143-148. New York: IFS Publications Ltd., 1987.
- [21] S. C. Gates. "Laboratory Data Collection with an IBM PC." *BYTE* 9, No. 5 (1984): 366-378.

- [22] J. M. Glass, H. P. Groger, R. J. Churchill, J. W. Lindau, and T. T. Diller. "Heat Transfer in Metallic Glasses During Laser Cutting." In HTD-Vol. 113 *Heat Transfer in Manufacturing and Materials Processing: Papers presented at The 1989 National Heat Transfer Conference held in Philadelphia 6-9 August 1989*, edited by R. K. Shah, 31-38. New York: American Society of Mechanical Engineers, 1989.
- [23] D. S. Gnanamuthu and V. S. Shankar. "Laser Heat Treatment of Iron-Base Alloys." *Applications of High Power Lasers: Proceedings of SPIE - The International Society for Optical Engineering* 527 (1985): 56-72.
- [24] R. J. Goldstein, A. I. Behbahani, and K. K. Heppelmann. "Streamwise Distribution of the Recovery Factor and the Local Heat Transfer Coefficient to an Impinging Circular Air Jet." *International Journal of Heat and Mass Transfer* 29, No. 8 (1986): 1227-1235.
- [25] J. N. Gonsalves and W. W. Duley. "Cutting Thin Metal Sheets with the CW CO₂ Laser." *Journal of Applied Physics* 43, No. 11 (1972): 4684-4687.
- [26] *Handbook of Chemistry and Physics*. 63rd Edition. Boca Raton: CRC Press, 1983.
- [27] P. L. Harrison and A. D. Yoffe. "The Burning of Metals." *Proceedings of the Royal Society of London, Series A*, 261 (1961): 357-370.
- [28] K. Hauffe. *Oxidation of Metals*. New York: Plenum, 1965.
- [29] R. C. Heckman. "Intrinsic Thermocouples in Thermal Diffusivity Measurements." In *Proc. 7th Symposium on Thermophysical Properties*, 155-159. New York: American Society of Mechanical Engineers, 1977.
- [30] C. D. Henning and R. Parker. "Transient Response of an Intrinsic Thermocouple." *Journal of Heat Transfer, Transactions of the ASME* 39 (1967): 146-154.
- [31] F. P. Incropera and D. P. DeWitt. *Fundamentals of Heat and Mass Transfer*. 2nd Edition. New York: John Wiley & Sons, 1985.
- [32] L. Kirschfeld. "Die Brennbarkeit von Metallen in Sauerstoff." *Angewandte Chemie* 71 (1959): 663-667.
- [33] P. Kosftad. *High-temperature Oxidation of Metals*. New York: John Wiley & Sons, 1966.

- [34] O. Kubaschewski and B. E. Hopkins. *Oxidation of Metals and Alloys*. 2nd Edition. New York: Academic Press Inc., 1962.
- [35] L. Li, W. M. Steen, R. H. Hibberd and V. M. Weerasinghe. "Real-Time Expert Systems for Supervisory Control of Laser Cladding." In *Laser Materials Processing: Proceedings of the 6th International Congress on Applications of Lasers and Electrooptics ICALEO '87 Held in San Diego 8-12 November 1987*, edited by S. L. Ream, 9-16. New York: IFS Publications Ltd., 1987.
- [36] *Manual on the Use of Thermocouples in Temperature Measurement*. ASTM Special Technical Publications 470B. Philadelphia: American Society for Testing and Materials, 1983.
- [37] J. Mazumder. "The State-of-the-Art of Laser Materials Processing." In *Interdisciplinary Issues in Materials Processing and Manufacturing: The Winter Annual Meeting of the American Society of Mechanical Engineers Held in Boston 13-18 December 1987*, edited by S. K. Samantha, R. Komanduri, R. McMeeking, M. M. Chen, and A. Tseng, 599-630. New York: American Society of Mechanical Engineers, 1987.
- [38] J. Mazumder and W. M. Steen. "Heat Transfer Model for CW Laser Material Processing." *Journal of Applied Physics* 51, No. 2 (1980): 941-947.
- [39] *Metals Handbook: Properties and Selection of Irons and Steels*. Vol. 1. Metals Park: American Society for Metals, 1978.
- [40] M. F. Modest and H. Abakians. "Evaporative Cutting of a Semi-Infinite Body with a Moving CW Laser." *Journal of Heat Transfer, Transactions of the ASME* 108 (1986): 602-607.
- [41] M. Moriyasu, S. Hiramoto and W. Shimada. "CO₂ Laser Cutting of Fiber Reinforced Plastics." *Paper Presented at the 7th International Congress on Applications of Lasers and Electrooptics ICALEO '88 Held in Santa Clara 30 October - 4 November 1988*.
- [42] S. J. Na, Y. S. Yang, H. M. Koo, and T. K. Kim. "Effect of Shielding Gas Pressure in Laser Cutting of Sheet Metals." *Journal of Engineering Materials and Technology, Transactions of the ASME* 111 (1989): 314-318.
- [43] *Omega 1987 Complete Temperature Measurement Handbook and Encyclopedia*. Stamford: Omega Engineering, Inc., 1987.

- [44] W. O'Neill and W. M. Steen. "Infrared Absorption by Metallic Surfaces as a Result of Powerful UV Laser Pulses." In *Laser Materials Processing: Proceedings of the 7th International Congress on Applications of Lasers and Electrooptics ICALEO '88 Held in Santa Clara 30 October - 4 November 1988*, edited by G. Bruck, 90-97. New York: IFS Publications Ltd., 1988.
- [45] J. Paidassi. "Sur l'Oxydation du Protoxyde de Fer dans l'Air dans l'Intervalle 600-1350°C." *Acta Metallurgica* 6 (1958): 219-221.
- [46] T. C. Peng and J. Mazumder. "Comparison of Heat-Transfer Modelling for Laser Melting of Ti-Alloys." In *Laser processing of Materials: Proceedings of a Symposium Sponsored by the Physical Metallurgy and Solidification Committees of The Metallurgical Society of AIME Held at the 119th Annual Meeting in Los Angeles 26 February - 1 March 1984*, edited by K. Mukherjee and J. Mazumder, 51-59. Warrendale: The Metallurgical Society of American Institute of Mining, Metallurgical and Petroleum Engineers, 1985.
- [47] J. Powell, T. G. King, and I. A. Menzies. "Cut Edge Quality Improvement by Laser Pulsing." In *Proceedings of the 2nd International Conference on Lasers in Manufacturing Held in Birmingham 26-28 March 1985*, edited by M. F. Kimmitt, 37-45. New York: IFS Publications Ltd., 1985.
- [48] S. Rajaram and R. J. Coyle. "Numerical Modelling of Laser Material Processing." In Vol. 38 *Laser Materials Processing: Proceedings of the 6th International Congress on Applications of Lasers and Electrooptics ICALEO '83*, 216-223. New York: IFS Publications Ltd., 1983.
- [49] J. F. Ready. *Industrial Applications of Lasers*. New York: Academic Press, 1978.
- [50] O. Renius. "Laser Illumination for Infrared Nondestructive Testing." *Materials Evaluation* 31, No. 5 (1973): 80-84.
- [51] D. M. Roessler. "An Introduction to the Laser Processing of Materials." In *The Industrial Laser Annual Handbook*, edited by D. A. Belforte and M. Levitt, 16-37. Tulsa: Pennwell Books, 1986.
- [52] O. A. Sandven. "A Three-Dimensional Heat Flow Model for Prediction of Case Depth in Laser Surface Transformation Hardening." In Vol. 38 *Laser Materials Processing: Proceedings of the 6th International Congress on Applications of Lasers and Electrooptics ICALEO '83*, 208-215. New York: IFS Publications Ltd., 1983.

- [53] D. Schuocker. "Laser Cutting." In SPIE Vol. 629 *The Industrial Laser Annual Handbook*, edited by D. A. Belforte and M. Levitt, 87-107. Tulsa: Pennwell Books, 1986.
- [54] G. Sepold and R. Rothe. "Laser Beam Cutting of Thick Steel." In Vol. 38 *Laser Materials Processing: Proceedings of the 6th International Congress on Applications of Lasers and Electrooptics ICALEO '83*, 156-159. New York: IFS Publications Ltd., 1983.
- [55] C. M. Sharp. "CO₂ Laser Cutting of Highly Reflective Materials." In *Laser Materials Processing: Proceedings of the 6th International Congress on Applications of Lasers and Electrooptics ICALEO '87 Held in San Diego 8-12 November 1987*, edited by S. L. Ream, 149-155. New York: IFS Publications Ltd., 1987.
- [56] W. M. Steen and J. N. Kamalu. "Laser Cutting." In *Laser Materials Processing*, edited by M. Bass, 15-112. Amsterdam: North-Holland, 1983.
- [57] A. B. J. Sullivan and P. T. Houldcroft. "Gas-jet Laser Cutting". *British Welding Journal* 14 (1967): 443-445.
- [58] V. Tagliaferri, A. Dillio, and I. C. Visconti. "Laser Cutting of Fiber-Reinforced Polysters." *Composites* 16, No. 4 (1985): 317-325.
- [59] Y. Tal and E. Lenz. "Temperature Controlled Laser Cutting." In Vol. 31 *Laser Materials Processing: Proceedings of the 6th International Congress on Applications of Lasers and Electrooptics ICALEO '82*, 149-161. New York: IFS Publications Ltd., 1982.
- [60] *Thermocouple Reference Tables*, NBS Monograph 125. Washington D.C.: National Bureau of Standards, 1979.
- [61] G. J. Van Wylen and R. E. Sonntag. *Fundamentals of Classical Thermodynamics*. 3rd Edition. New York: John Wiley & Sons, 1986.
- [62] Vanzetti Systems. "Fiberoptic Thermal Monitoring and Control Systems." *Product Literature*. Vanzetti Systems, Stoughton, MA. 1988.
- [63] T. Webber. "Real-Time Laser Welding Quality Control System." In *Laser Materials Processing: Proceedings of the 6th International Congress on Applications of Lasers and Electrooptics ICALEO '87 Held in San Diego 8-12 November 1987*, edited by S. L. Ream, 25-36. New York: IFS Publications Ltd., 1987.

APPENDIX A: COMPUTER PROGRAMS

This appendix provides a listing of the computer programs and input data file as mentioned in Chapters 2 and 8. The first listing is the computer program used to acquire data with the MC-MIO16 A/D board. This is followed by the program that was written to calculate the average temperature of the metal leaving the control volume described in the thermodynamic model in Chapter 8. The listing following this is a typical input data file used in the finite element model using the software ADINAT.

Data Acquisition Program

```
'THIS PROGRAM IS THE MODIFIED VERSION OF THE EXAMPLE PROGRAM
'WRITTEN BY NI. THE MODIFICATIONS ARE SUITABLE FOR THE VANZETTI
'INFRARED SENSOR. THE PROGRAM CREATES TWO FILES: A BINARY FILE THAT
'CONTAINS THE DATA COLLECTED BY THE BOARD AND A DOCUMENT FILE THAT
'CONTAINS THE EXPERIMENT INFORMATION. READ THE NATIONAL
'INSTRUMENTS MANUAL AND FAMILIARIZE YOURSELF WITH THE DATA
'ACQUISITION BOARD BEFORE USING THIS PROGRAM.
'THIS PROGRAM CALLS DOS LABDRIVER FUNCTIONS FOR PROGRAMMING DOUBLE
'BUFFERED A/D CONVERSIONS ON SINGLE INPUT CHANNEL OF THE NI'S
'MIO-16 BOARD.
'
'THE INPUT CHANNEL IS SELECTED BY THE USER. THE ARRAY IN WHICH
'DATA IS CYCLICALLY STORED IS CALLED 'FULL.BUF'. 'FULL.BUF' MAY
'BE THOUGHT OF AS AN ARRAY WITH TWO HALVES. EACH HALF OF THE DATA
'IS ALTERNATELY ACQUIRED INTO AN ARRAY CALLED 'HALF.BUF'. THE
```

'DATA FROM 'HALF.BUF' IS STORED IN A BINARY FILE OF INTEGERS, AND
'THEN 'HALF.BUF' IS FILLED WITH NEW DATA TO BE STORED INTO THE
'BINARY FILE.

'DATA CAN BE ACQUIRED IN TWO DOUBLE BUFFERED MODES, WHICH ARE:
'FIXED MODE

'IN THIS MODE THE USER SPECIFIES THE NUMBER OF TIMES
'HALF.BUF' IS TO BE FILLED AND THEN STORED IN A FILE.
'THE ACQUISITION STOPS AFTER 'HALF.BUF' HAS BEEN FILLED
'AND STORED THE DESIRED NUMBER OF TIMES. THE TOTAL NUMBER
'OF POINTS TRANSFERRED TO THE FILE IS DISPLAYED.

'CONTINUOUS MODE.

'IN THIS MODE THE STOP-TRIGGER FEATURE OF THE BOARD IS USED TO
'CONTINUOUSLY ACQUIRE DATA IN 'HALF.BUF' AND STORE IN A FILE. THE
'ACQUISITION STOPS BY APPLYING A LOW-TO-HIGH EDGE AT THE STOP-TRIGGER
'PIN OF THE BOARD. IN THIS CASE THE USER SPECIFIES THE NUMBER OF
'SAMPLES TO ACQUIRE AFTER THE STOP-TRIGGER. SINCE THE ACQUISITION
'COULD HAVE STOPPED ANYWHERE IN THE BUFFER, THE LAST TIME 'HALF.BUF'
'IS NOT NECESSARILY COMPLETELY FILLED WITH NEW DATA. SO, WE PRINT
'THE TOTAL NUMBER OF POINTS TRANSFERRED TO FILE AND THE NUMBER OF
'POINTS TRANSFERRED TO 'HALF.BUF' THE LAST TIME.

'THE FOLLOWING ANALOG INPUT DEFAULTS ARE ASSUMED:

' INPUT MODE: DIFFERENTIAL (8 DOUBLE ENDED INPUT CHANNELS)
' INPUT RANGE: 10 VOLTS
' POLARITY: UNIPOLAR (0 TO +10 VOLTS)
' IF BIPOLAR, CHECK IF -5 TO +5, OR, -10 TO +10 VOLTS
' GAIN = 1
' NO EXTERNAL CONVERSION PULSES OR TRIGGERING

DECLARE SUB ERR.EXIT (PROCNAME\$, ERR.NUM%)
REM \$INCLUDE: 'C:\DOSLBDRV\DOSLBDRV.INC'
DECLARE SUB PLOT (PLOT.BUF%(), START.BUF%, PTS.TO.PLOT%, DAQU.RATE#)

GAIN% = 1
POLARITY% = 1 ' IF POLARITY IS BIPOLAR, WRITE 0
 ' IF POLARITY IS UNIPOLAR, WRITE 1
INPUT.RANGE% = 10 ' 10 OR 5 IN VOLTS
INPUT.MODE% = 0 ' 0 FOR DIFFERENTIAL, 1 FOR SINGLE-ENDED
BRD% = 3 ' NUMBER OF THE SLOT CONTAINING THE BOARD

```

'RESET ANALOG INPUT CONFIGURATION TABLE
ERR.NUM% = AI.CONFIG(BRD%, INPUT.MODE%, INPUT.RANGE%, POLARITY%)
ERR.EXIT "AI.CONFIG", ERR.NUM%

INPUT "ENTER THE CHANNEL (0-7) TO BE READ: ", CHANNEL%

INPUT "ENTER THE ACQUISITION RATE IN POINTS PER SECOND: ", DAQU.RATE#

INPUT "ENTER HIGH OR LOW TEMPERATURE LENS (HI/LO): ", LENS$

' CONVERT THE ACQUISITION RATE TO A TIMEBASE AND SAMPLE INTERVAL
ERR.NUM% = DAQ.RATE(DAQU.RATE#, 0, TIMEBASE%, SAMP.INT%)
ERR.EXIT "DAQ.RATE", ERR.NUM%

' GET THE NUMBER OF DATA POINTS TO BE ACQUIRED
' DETERMINE THE SIZE OF THE CIRCULAR BUFFER. IT IS ROUGHLY
' PROPORTIONAL TO THE ACQUISITION RATE.
IF DAQU.RATE# < 200! THEN
    NUM.SAMPLES% = 200
ELSEIF DAQU.RATE# > 25000 THEN
    NUM.SAMPLES% = 32766
ELSE
    NUM.SAMPLES% = DAQU.RATE#
    IF NUM.SAMPLES% MOD 2 THEN NUM.SAMPLES% = NUM.SAMPLES% + 1
END IF

DIM SHARED FULL.BUF%(NUM.SAMPLES% - 1)
DIM SHARED HALF.BUF AS STRING
DIM PLOT.BUF%(99)      '100 ELEMENT INTEGER ARRAY FOR PLOTTING

' SET THE SIZE OF HALF.BUF%() TO HOLD ONE HALF THE NUMBER OF
' SAMPLES THAT FULL.BUF%() CAN HOLD. SINCE EACH SAMPLE IS 2 BYTES
' IN SIZE, THE NUMBER OF BYTES NEEDED TO HOLD NUM.SAMPLES% / 2
' EQUALS NUM.SAMPLES%

HALF.BUF = STRING$(NUM.SAMPLES%, " ")

INPUT "ENTER 'Y' OR 'Y' TO ACQUIRE DATA IN THE CONTINUOUS MODE: ",
    CH$
IF (CH$ = "Y" OR CH$ = "Y") THEN
    STOPT.DAQ% = 1
    INPUT "ENTER NUMBER OF SAMPLES AFTER STOP TRIGGER: ",

```

```

        STOPT.SAMPLES%
    ERR.NUM% = DAQ.TRIGGER.CONFIG(BRD%, 1, STOPT.SAMPLES%)
    ERR.EXIT "DAQ.TRIGGER.CONFIG", ERR.NUM%
ELSE
    STOPT.DAQ% = 0
    PRINT "EACH HALF BUFFER WILL HOLD "; NUM.SAMPLES% / 2; "SAMPLES."
    INPUT "ENTER NUMBER OF TIMES TO FILL AND STORE HALF BUFFERS.",
        NUM.HBUFS%
END IF

' CONFIGURE FOR DOUBLE BUFFERED ACQUISITION
    ERR.NUM% = DAQ.DB.CONFIG(BRD%, 1)
    ERR.EXIT "DAQ_DB_CONFIG", ERR.NUM%

INPUT "ENTER FILENAME FOR STORING DATA: ", FILE$

' BINARY DATA FILE IS NAMED WITH EXTENSION
FILENAME$ = FILE$ + ".BIN"

' OPEN FILE, CLOSE IT AND DELETE IT TO MAKE SURE THAT FILE IS EMPTY
OPEN FILENAME$ FOR BINARY ACCESS WRITE AS #1
CLOSE #1
KILL FILENAME$
OPEN FILENAME$ FOR BINARY ACCESS WRITE AS #1

IF STOPT.DAQ% = 1 THEN
    PRINT "YOU HAVE SELECTED THE PRETRIGGER MODE. THE ACQUISITION
        WILL ACQUIRE"
    PRINT "DATA UNTIL A PULSE IS APPLIED TO THE STOP TRIG PIN
        (PIN 39) OR UNTIL"
    PRINT "THE DISK IS FULL. ONE WAY TO APPLY THE TRIGGER PULSE IS
        TO CONNECT A"
    PRINT "WIRE TO PIN 33 AND, WHEN THE TRIGGER IS DESIRED, TOUCH
        THE OTHER END"
    PRINT "OF THE WIRE TO PIN 39."
END IF

INPUT "HIT RETURN TO START ACQUISITION ", CH$

' START ACQUIRING DATA

IF STOPT.DAQ% = 1 THEN

```

```

' THE PRETRIGGER MODE HAS BEEN SELECTED
' INITIALIZE THE NUMBER OF HALF BUFFERS ACQUIRED TO 0
  NUM.HBUFS% = 0
' ENABLE ERROR CHECKING
  ON ERROR GOTO PRETRIG.HANDLER

  ERR.NUM% = DAQ.START(BRD%, CHANNEL%, GAIN%, FULL.BUF%(),
    NUM.SAMPLES%, TIMEBASE%, SAMP.INT%)
  ERR.EXIT "DAQ.START", ERR.NUM%

DO
  ERR.NUM% = DAQ.DB.STRTRANSFER(BRD%, HALF.BUF, PTS.TFR%,
    STATUS%)
  IF (ERR.NUM% OR STATUS%) THEN
  EXIT DO
  ELSE
  PUT #1, , HALF.BUF
  NUM.HBUFS% = NUM.HBUFS% + 1
  END IF
LOOP WHILE 1 'ALWAYS TRUE, THE TEST CONDITION IS INSIDE
  'THE DO LOOP

END.OF.PRETRIG.DAQ:

' DISABLE ERROR CHECKING
  ON ERROR GOTO 0

  ERR.EXIT "DAQ.DB.STRTRANSFER", ERR.NUM%

  IF STATUS% = 1 AND ERR.NUM% = 0 THEN
  PRINT "ACQUISITION HAS STOPPED. WRITING THE LAST
    BIT OF DATA TO DISK."
  FOR I% = 1 TO PTS.TFR% * 2 STEP 2
  SAMPLE$ = MID$(HALF.BUF, I%, 2)
  PUT #1, , SAMPLE$
  NEXT I%
  END IF

  TOT.SAMPLES& = NUM.HBUFS%
  TOT.SAMPLES& = TOT.SAMPLES& * (NUM.SAMPLES% / 2)
  IF STATUS% = 1 THEN
  TOT.SAMPLES& = TOT.SAMPLES& + PTS.TFR%

```

```
END IF

ELSE
' THE FIXED MODE HAS BEEN SELECTED
  I% = NUM.HBUFS%          ' TO COUNT NUMBER OF HALF BUFFERS
                          ' TRANSFERRED

  ON ERROR GOTO FIXED.HANDLER

  ERR.NUM% = DAQ.START(BRD%, CHANNEL%, GAIN%, FULL.BUF%(),
                      NUM.SAMPLES%, TIMEBASE%, SAMP.INT%)
  ERR.EXIT "DAQ.START", ERR.NUM%

  DO
    ERR.NUM% = DAQ.DB.STRTRANSFER(BRD%, HALF.BUF,
                                  PTS.TFR%, STATUS%)
    IF ERR.NUM% THEN
      EXIT DO
    ELSE
      PUT #1, , HALF.BUF
      I% = I% - 1
    END IF
  LOOP UNTIL I% = 0

END.OF.FIXED.DAQ:
  ON ERROR GOTO 0

  ERR.EXIT "DAQ_DB_STRTRANSFER", ERR.NUM%
  ERR.NUM% = DAQ.CLEAR(BRD%)
  ERR.EXIT "DAQ.CLEAR", ERR.NUM%
  TOT.SAMPLES& = NUM.HBUFS% - I%
  TOT.SAMPLES& = TOT.SAMPLES& * NUM.SAMPLES% / 2

END IF

CLOSE #1          'CLOSE THE BINARY DATA FILE

PRINT
IF STOPT.DAQ% = 1 AND STATUS% = 1 THEN
  PRINT "THE LAST HALF BUFFER HAD"; PTS.TFR%; "DATA POINTS."
END IF
```

```
PRINT "THE FILE "; FILENAME$; " HAS A TOTAL OF"; TOT.SAMPLES&;
"INTEGER DATA POINTS ACQUIRED"
```

```
'CONVERSION FACTOR FOR BITS TO VOLTS
```

```
IF POLARITY% = 0 THEN
  V = INPUT.RANGE%: BIT = 2048
ELSE
  V = INPUT.RANGE%: BIT = 4096
END IF
```

```
SCALE# = V / (GAIN% * BIT)
```

```
'CONVERSION TO VOLTAGE AND TEMPERATURE
```

```
OPEN FILE$ + ".DOC" FOR OUTPUT AS #2 'DOCUMENT FILE
```

```
PRINT #2, "LENS TYPE:"; LENS$
PRINT #2, "DATA ACQUISITION RATE (HZ): "; DAQU.RATE#
PRINT #2, "TOTAL NO OF READINGS      : "; TOT.SAMPLES&
PRINT #2, "BIT TO VOLT CONVERSION (V/BIT): "; SCALE#
PRINT #2, "NO OF READINGS AFTER STOP TRIGGER: "; STOPT.SAMPLES%
```

```
CLOSE #2
```

```
PRINT "TYPE 'Y' OR 'Y' TO SEE A PLOT OF PARTS OF DATA FROM FILE"
```

```
INPUT " ENTER ANY OTHER KEY TO QUIT: ", CH$
```

```
IF CH$ = "Y" OR CH$ = "Y" THEN
```

```
  IF (TOT.SAMPLES& <= 100) THEN
```

```
    SAMPS.TO.USE% = TOT.SAMPLES&
```

```
    OPEN FILE$ FOR BINARY ACCESS READ AS #1
```

```
    FOR I% = 1 TO SAMPS.TO.USE%
```

```
      GET #1, 2 * I% - 1, PLOT.BUF%(I% - 1)
```

```
    NEXT I%
```

```
    PRINT "HIT RETURN TO SEE A PLOT OF"; SAMPS.TO.USE%;
```

```
      "DATA POINTS IN FILE"
```

```
    INPUT CH$
```

```
    CALL PLOT(PLOT.BUF%(), 0, SAMPS.TO.USE%, DAQU.RATE#)
```

```
  ELSE
```

```
    PRINT
```

```
    PRINT "YOU WILL PLOT 100 POINTS OF DATA FROM THE DATA FILE"
```

```
    PRINT "THE FIRST DATA POINT IS AT INDEX 1"
```

```

INPUT "ENTER INDEX OF FIRST DATA POINT TO TAKE FROM FILE
      (<= 0 TO QUIT): ", INDEX&
WHILE INDEX& > 0
SAMPS.TO.USE% = 100
IF INDEX& + 99& > TOT.SAMPLES& THEN
  PRINT : PRINT "ERROR : TRIED TO READ PAST END OF FILE": PRINT
ELSE
  OPEN FILE$ FOR BINARY ACCESS READ AS #1
  FOR I& = 1 TO (INDEX& - 1)
    GET #1, 2& * I& - 1, AJUNK%
  NEXT I&
  FOR I& = INDEX& TO (INDEX& + 99&)
    GET #1, 2& * I& - 1, PLOT.BUF%(I& - INDEX&)
  NEXT I&
  CLOSE #1
  CALL PLOT(PLOT.BUF%(), INDEX&, SAMPS.TO.USE%, DAQU.RATE#)
END IF
PRINT "YOU WILL PLCT 100 POINTS OF DATA FROM THE DATA FILE"
PRINT "THE FIRST DATA POINT IS AT INDEX 1"
INPUT "ENTER INDEX OF FIRST DATA TO TAKE FROM FILE (<= 0 TO END): "
, INDEX&
  WEND
END IF
CLOSE #1
END IF
ERASE FULL.BUF%

PRINT "GOODBYE!"

END

PRETRIG.HANDLER:
  SELECT CASE ERR
    CASE 61
      PRINT
      PRINT "DISK IS FULL. ACQUISITION HALTED."
      PRINT
      RR% = DAQ.CLEAR(BRD%)
      RESUME END.OF.PRETRIG.DAQ
    CASE ELSE
      PRINT
      PRINT "FILE I/O ERROR. ACQUISITION HALTED."

```

```

PRINT
RR% = DAQ.CLEAR(BRD%)
RESUME END.OF.PRETRIG.DAQ
END SELECT

```

```

FIXED.HANDLER:

```

```

SELECT CASE ERR
CASE 61
PRINT
PRINT "DISK IS FULL. ACQUISITION HALTED."
RESUME END.OF.FIXED.DAQ
CASE ELSE
PRINT
PRINT "FILE I/O ERROR. ACQUISITION HALTED."
RESUME END.OF.FIXED.DAQ
END SELECT

```

```

*****

```

```

SUB ERR.EXIT (PROCNAME$, ERR.NUM%)

```

```

' THIS SUB-ROUTINE PRINTS THE ERROR, IF ANY, FROM A DOS LABDRIVER
' FUNCTION.
' IN CASE OF AN ERROR MEMORY ALLOCATED FOR BUFFER IS FREED AND THE
' PROGRAM IS ENDED.

```

```

IF ERR.NUM% <> 0 THEN
PRINT "ERROR IN "; PROCNAME$; " IS "; ERR.NUM%
ERASE FULL.BUF%
INPUT "PRESS ENTER", CH$
STOP
END IF
END SUB

```

```

SUB PLOT (Y.BUFFER%(), BUF.START&, PTS.TO.PLOT%, DAQU.RATE#)

```

```

INPUT "TYPE OF PLOT, LINE OR DOT (1 OR 0)?", DOT

```

```

' THIS SECTION IS WHERE THE STARTING GRAPH COORDINATES AND SCREEN
' SCALE RATIO IS SET. OX,OY = STARTING POINT OF GRAPH.
' QX,QY = SCREEN SCALE X:Y.

```

```

CLS : OX = 70: OY = 0: QX = 1.8: QY = .9000001

```

```

      YLB$ = "TEMP (C)"
      XLB$ = "TIME (S)"
,
'THIS LOOP SCANS THE DATA AND SETS THE X,Y MAX/MIN VALUES
,
      DT# = 1! / DAQU.RATE#
      X1 = (BUF.START& - 1) * DT#
      X2 = (BUF.START& + 99&) * DT#
      Y1 = 0
      Y2 = 0
      FOR I = 0 TO (PTS.TO.PLOT% - 1)
        IF Y.BUFFER%(I) < Y1 THEN Y1 = Y.BUFFER%(I)
        IF Y.BUFFER%(I) > Y2 THEN Y2 = Y.BUFFER%(I)
      NEXT I
,
'THIS SECTION ESTABLISHES THE ACTUAL SCALE FACTORS USED TO PLOT THE
'DATA AS THE FILES ARE READ. THESE VALUES ARE ALSO THE SAME
'VALUES SAVED ON THE DISK WHEN A SAVE COMMAND IS EXECUTED.
,
      SCREEN 2
      DX = ABS(CINT((X2 - X1) / 25 + .5))
      DY = ABS(CINT((Y2 - Y1) / 25) + .5))
      SX = 260 / (X2 - X1)
      SY = 140 / (Y2 - Y1)
,
'THIS SECTION LOCATES THE AXIS X,Y AND PLOTS THEM OUT WITH THE SMALL
'TICK MARKS IDENTIFYING THE SCALE. THE AXIS LABELS ARE ALSO PRINTED.
,
      IF Y2 <= 0 THEN YA = 10: GOTO PLOT1
      IF Y1 >= 0 THEN YA = 150: GOTO PLOT1
      YA = 10 + SY * Y2
,
PLOT1:
'SET THE RANGE LIMITS
,
      IF X2 <= 0 THEN XA = 270: GOTO PLOT2
      IF X1 >= 0 THEN XA = 10: GOTO PLOT2
      XA = 10 - SX * X1
PLOT2: FOR YLBL = 1 TO 16
      LOCATE 2 + YLBL, 6: PRINT MID$(YLB$, YLBL, 1);

```

```

NEXT YLBL
LOCATE 1, 1: PRINT USING "#.##^0000"; Y2;
LOCATE 19, 1: PRINT USING "#.##^0000"; Y1;
LOCATE 20, 10: PRINT USING "#.##^0000"; X1;
LOCATE 20, 68: PRINT USING "#.##^0000"; X2;
PSET (QX * 0 + OX, QY * 0 + OY)
LINE -(QX * 279 + OX, QY * 0 + OY)
LINE -(QX * 279 + OX, QY * 159 + OY)
LINE -(QX * 0 + OX, QY * 159 + OY)
LINE -(QX * 0 + OX, QY * 0 + OY)
LINE (QX * XA + OX, QY * 10 + OY)-(QX * XA + OX, QY * 150 + OY)
LINE (QX * 10 + OX, QY * YA + OY)-(QX * 270 + OX, QY * YA + OY)
,
'MARK THE X AXIS TICKS
,
K = 0
B = YA - 2
C = YA + 2
PLOT3:
K = K + 1
A = DX * K
AA = XA + SX * A
IF AA > 271 THEN GOTO PLOT4
LINE (QX * AA + OX, QY * B + OY)-(QX * AA + OX, QY * C + OY)
GOTO PLOT3
PLOT4: K = 0
PLOT5: K = K + 1
A = DX * K
AA = XA - SX * A
IF AA < 9 THEN GOTO PLOT6
LINE (QX * AA + OX, QY * B + OY)-(QX * AA + OX, QY * C + OY)
GOTO PLOT5
,
'MARK THE Y AXIS TICKS
,
PLOT6: K = 0
A = XA - 2
C = XA + 2
PLOT7: K = K + 1
B = DY * K
BB = YA - SY * B
IF BB < 9 THEN GOTO PLOT8

```

```

LINE (QX * A + OX, QY * BB + OY)-(QX * C + OX, QY * BB + OY)
GOTO PLOT7
PLOT8: K = 0
PLOT9: K = K + 1
B = DY * K
BB = YA + SY * B
IF BB > 151 THEN GOTO PLOT10
LINE (QX * A + OX, QY * BB + OY)-(QX * C + OX, QY * BB + OY)
GOTO PLOT9
PLOT10: LOCATE 22, 1
PRINT "          X SPACING= "; INT(DX); "          Y SPACING="; INT(DY)
LOCATE 20, 32: PRINT XLB$; : LOCATE 22, 1
,
'THIS SECTION RECALLS THE DATA AND PLOTS.
FOR I = 0 TO (PTS.TO.PLOT% - 1)
X = (BUF.START% - 1 + I) * DT#
Y = Y.BUFFER%(I)
IF I = 0 THEN XTMP = X: YTMP = Y
PS = 0
AA = XA + SX * (X - X1)
AT = XA + SX * XTMP
BB = YA - SY * Y
BT = YA - SY * YTMP
IF AA < 9 OR BB < 9 THEN PS = 1
IF AA > 271 OR BB > 151 THEN PS = 1
IF PS THEN GOTO PLOT12
IF INT(DOT + .5) = 2 THEN GOTO PLOT12 'NO PLOT
IF INT(DOT + .5) = 0 THEN GOTO PLOT11 'DOT PLOT
LINE (QX * AT + OX, QY * BT + OY)-(QX * AA + OX, QY * BB + OY)
GOTO PLOT12
PLOT11: PSET (QX * AA + OX, QY * BB + OY)
PLOT12: XTMP = X: YTMP = Y
NEXT I
,
'----- PROGRAM PLOT COMPLETED -----
,
'THIS IS THE CONVERSATIONAL PART OF THE PROGRAM WHERE THE USER MAY
'SAVE THE PLOT/GRAPH OR ADD MORE DATA OR PRINT PLOT/GRAPH.
,
,
PLOT13: LOCATE 24, 1: INPUT "ENTER E TO EXIT: "; OPTX$
IF OPTX$ = "E" OR OPTX$ = "E" THEN GOTO PLOT14

```

```

LOCATE 24, 1: PRINT SPC(79); : LOCATE 24, 1: GOTO PLOT13
PLOT14: CLS : SCREEN 0, 0, 0
END SUB
'*****
,
' THIS PROGRAM WILL SORT THROUGH A BINARY FILE AND CREATE ANOTHER
' FILE BY SKIPPING DATA POINTS, IF NEEDED.
,
FIRST:
INPUT "INPUT FILENAME WITHOUT .BIN EXTENSION:", FILE$
OPEN FILE$ + ".BIN" FOR BINARY ACCESS READ AS #1

INPUT "TOTAL NO OF READINGS:", NMAX
INPUT "NO OF READINGS TO SKIP:", NSKP
NSKP = NSKP + 1

OPEN FILE$ + ".TMP" FOR OUTPUT AS #2

FOR I& = N1 TO NMAX STEP NSKP
  GET #1, 2 * I& - 1, T%
  PRINT #2, I&, T%
NEXT I&

CLOSE #2
CLOSE #1
INPUT "WORK ON ANOTHER FILE?:", RESP$
IF (RESP$ = "Y") OR (RESP$ = "Y") GOTO FIRST
END
'*****

```

Program Used in Thermodynamic Model

```

C *****
C *                               TAVRG                               *
C *****
C
C THIS PROGRAM WILL CALCULATE AN AVERAGE TEMPERATURE FOR THE METAL
C LEAVING THE CONTROL VOLUME IN THE THERMODYNAMIC MODEL OF THE
C CUTTING PROCESS.
C THE EQUATION USED IS FROM CARSLAW AND JAEGER

```

```
C (ALSO IN DULEY).
C
C LINK WITH IMSL/LIB
C
IMPLICIT DOUBLE PRECISION (A-H,O-Z)
CHARACTER*10 REPLY
DIMENSION T(100),Y(100)
REAL*8 K
EXTERNAL BSKO
PI=CONST('PI')
C
PRINT*, 'INPUT VALUE OF FLUX Q:'
READ*, Q
PRINT*, 'INPUT VALUE OF THERMAL CONDUCTIVITY:'
READ*, K
PRINT*, 'INPUT VALUE OF THERMAL DIFFUSIVITY:'
READ*, ALPHA
PRINT*, 'INPUT VELOCITY OF HEAT SOURCE:'
READ*, V
PRINT*, 'INPUT THICKNESS OF METAL:'
READ*, D
PRINT*, 'INPUT MELT TEMPERATURE (C):'
READ*, TM
C
PRINT*, 'INPUT DXN'
READ*, DXN
XN=0.0

IN=0
C
  155 XN=XN+DXN
CON=2.*PI*K*D*TM/(Q*DEXP(XN*V/(2.*ALPHA)))

C ITERATE FOR THE R VALUE AT WHICH THIS MELT TEMP OCCURS
R=0.1
STP=0.01
  DUMB=0

  111 IF (R.LE.0.0) THEN
    R=R+STP
    STP=STP/10.0
    R=R-STP
```

```

ELSE
ENDIF
C PRINT*,R,STP
      CONT=BSKO(R*V/(2.*ALPHA))
C PRINT*, 'CONT',CONT, 'CON',CON

      ERROR=CON-CONT          ! CHECK ITERATION CONVERGENCE
IF (DABS(ERROR).LT.1.0D-4) GOTO 222
IF ((ERROR.GT.0).AND.(DUMB.EQ.-1)) THEN
      STP=STP-.5*STP
      R=R-STP
      DUMB=1
      GOTO 111
ENDIF
IF ((ERROR.LT.0).AND.(DUMB.EQ.1)) THEN
      STP=STP-0.5*STP
      R=R+STP
      DUMB=-1
      GOTO 111
ENDIF
IF (ERROR.GT.0) THEN
      R=R-STP
      DUMB=1
ENDIF
IF (ERROR.LT.0) THEN
      R=R+STP
      DUMB=-1
ENDIF
GOTO 111

222  RMAX=R      ! MAXIMUM VALUE OF X
C      PRINT*, 'RMELT=',RMAX

C END ITERATION
C
C FIND YN
YNEW=DSQRT(R**2.-XN**2.)
C PRINT*,YNEW,XN
IF (YOLD.LE.YNEW) THEN
      YOLD=YNEW
GOTO 155

```

```

ELSE
  XN=XN-DXN
  YN=YOLD
ENDIF
C
C PRINT*,CONT,CON
C PRINT*, 'YMAX=', YN, 'XLOC=', XN

C ONCE THE LOCATION OF X AND YMAX ARE KNOWN, AVERAGE FOR
C A DISTANCE WHERE THE TEMPERATURE IS 5% OF TMELT
C
TMIN=0.05*TM
X=XN
DY=0.1
Y(1)=YN+DY/2.0
I=0

E=DEXP(V*X/(2.*ALPHA))
A=Q*E/(2.*PI*K*D)

300   I=I+1
      R=SQRT(X**2.+Y(I)**2.)
T(I)=A*BSKO(R*V/(2.*ALPHA))

C PRINT*, TMIN, Y(I), T(I)
IF(T(I).GT.TMIN) THEN
  Y(I+1)=Y(I)+DY
  ITOT=I+1
  GOTO 300
ELSE
ENDIF

C CALCULATE THE AVERAGE TEMPERATURE

SUM=0.0
DO I=1, ITOT
  SUM=SUM+T(I)
ENDDO
TAVRG=SUM/ITOT
PRINT*, 'T AVERAGE =', TAVRG, 'YMAX = ', Y(ITOT)

STOP

```

END

C*****

ADINAT Input Data File

```

//RAJAN JOB N1$NXR,RAJ,MSGLEVEL=1
//*JOBPARM LINES=10
//*JOBPROC DSN=PROG.ADINA.PROCLIB
//A EXEC ADINAT,REGION=4096K,TIME=(6,30)
//STEPLIB DD DSN=N1$NXR.ADINAT.LOADLIB,DISP=SHR
//ADINAT.FT03F001 DD UNIT=SCRATCH,DISP=(NEW,DELETE),
// SPACE=(TRK,(10,10)),DCB=(RECFM=VBS,LRECL=1014,BLKSIZE=1018)
//ADINAT.FT04F001 DD UNIT=SCRATCH,DISP=(NEW,DELETE),
// SPACE=(TRK,(10,10)),DCB=(RECFM=VBS,LRECL=1014,BLKSIZE=1018)
//ADINAT.FT07F001 DD UNIT=SCRATCH,DISP=(NEW,DELETE),
// SPACE=(TRK,(10,10)),DCB=(RECFM=VBS,LRECL=1014,BLKSIZE=1018)
//ADINAT.FT12F001 DD UNIT=SCRATCH,DISP=(NEW,DELETE),
// SPACE=(TRK,(10,10)),DCB=(RECFM=VBS,LRECL=1014,BLKSIZE=1018)
//FT56F001 DD UNIT=DISK,DSN=N1$NXR.TEMP1M,DISP=(NEW,CATLG),
// SPACE=(6233,(60,30),RLSE)
//FT57F001 DD UNIT=DISK,DSN=N1$NXR.HEAT1M,DISP=(NEW,CATLG),
// SPACE=(6233,(60,30),RLSE)
//SYSIN DD *
MOVING SOURCE ON 2-D BODY, INCLUDES MELTING
1729 1 0 1 1 0.00 1 1
1 0 1
0
0 0 0 1.E-03
1 1.00
1 0
1 101
5
0.0090
1 0 0.00 0.00 0.00 1
101 0 0.00 20.0 0.00 1
102 0 0.00 0.00 0.20 1
202 0 0.00 20.0 0.20 1
203 0 0.00 0.00 0.40 1
303 0 0.00 20.0 0.40 1
304 0 0.00 0.00 0.60 1

```

404	0	0.00	20.0	0.60	1
405	0	0.00	0.00	0.80	1
505	0	0.00	20.0	0.80	1
506	0	0.00	20.0	1.00	1
607	0	0.00	0.00	1.20	1
707	0	0.00	20.0	1.20	1
708	0	0.00	0.00	1.40	1
808	0	0.00	20.0	1.40	1
809	0	0.00	0.00	1.60	1
909	0	0.00	20.0	1.60	1
910	0	0.00	0.00	1.80	1
1010	0	0.00	20.0	1.80	1
1011	0	0.00	0.00	2.00	1
1111	0	0.00	20.0	2.00	1
1112	0	0.00	0.00	2.40	1
1212	0	0.00	20.0	2.40	1
1213	0	0.00	0.00	2.80	1
1263	0	0.00	20.0	2.80	1
1264	0	0.00	0.00	3.20	1
1314	0	0.00	20.0	3.20	1
1315	0	0.00	0.00	4.00	1
1365	0	0.00	20.0	4.00	1
1366	0	0.00	0.00	4.80	1
1391	0	0.00	20.0	4.80	1
1392	0	0.00	0.00	6.40	1
1417	0	0.00	20.0	6.40	1
1418	0	0.00	0.00	8.40	1
1443	0	0.00	20.0	8.40	1
1444	0	0.00	0.00	13.4	1
1469	0	0.00	20.0	13.4	1
1470	0	0.00	0.00	18.4	1
1495	0	0.00	20.0	18.4	1
1496	0	0.00	0.00	23.4	1
1521	0	0.00	20.0	23.4	1
1522	0	0.00	0.00	28.4	1
1547	0	0.00	20.0	28.4	1
1548	0	0.00	0.00	-33.4	1
1573	0	0.00	20.0	33.4	1
1574	0	0.00	0.00	38.4	1
1599	0	0.00	20.0	38.4	1
1600	0	0.00	0.00	43.4	1

505	504	403	404	0	0	0	0		
401	4	0	1	1		1	0.05		0
507	506	405	406	0	0	0	0		
500	4	0	1	1		1	0.05		0
606	605	504	505	0	0	0	0		
501	4	0	1	1		1	0.05		0
608	607	506	507	0	0	0	0		
600	4	0	1	1		1	0.05		0
707	706	605	606	0	0	0	0		
601	4	0	1	1		1	0.05		0
709	708	607	608	0	0	0	0		
700	4	0	1	1		1	0.05		0
808	807	706	707	0	0	0	0		
701	4	0	1	1		1	0.05		0
810	809	708	709	0	0	0	0		
800	4	0	1	1		1	0.05		0
909	908	807	808	0	0	0	0		
801	4	0	1	1		1	0.05		0
911	910	809	810	0	0	0	0		
900	4	0	1	1		1	0.05		0
1010	1009	908	909	0	0	0	0		
901	4	0	1	1		1	0.05		0
1012	1011	910	911	0	0	0	0		
1000	4	0	1	1		1	0.05		0
1111	1110	1009	1010	0	0	0	0		
1001	4	0	1	1		1	0.05		0
1113	1112	1011	1012	0	0	0	0		
1100	4	0	1	1		1	0.05		0
1212	1211	1110	1111	0	0	0	0		
1101	5	0	1	0		1	0.05		0
1214	1213	1112	1114	0	0	1113	0		
1102	5	0	1	0		1	0.05		0
1215	1214	1114	1116	0	0	1115	0		
1103	5	0	1	0		1	0.05		0
1216	1215	1116	1118	0	0	1117	0		
1104	5	0	1	0		1	0.05		0
1217	1216	1118	1120	0	0	1119	0		
1105	5	0	1	0		1	0.05		0
1218	1217	1120	1122	0	0	1121	0		
1106	5	0	1	0		1	0.05		0
1219	1218	1122	1124	0	0	1123	0		
1107	5	0	1	0		1	0.05		0

1220	1219	1124	1126	0	0	1125	0		
1108	5	0	1	0		1	0.05		0
1221	1220	1126	1128	0	0	1127	0		
1109	5	0	1	0		1	0.05		0
1222	1221	1128	1130	0	0	1129	0		
1110	5	0	1	0		1	0.05		0
1223	1222	1130	1132	0	0	1131	0		
1111	5	0	1	0		1	0.05		0
1224	1223	1132	1134	0	0	1133	0		
1112	5	0	1	0		1	0.05		0
1225	1224	1134	1136	0	0	1135	0		
1113	5	0	1	0		1	0.05		0
1226	1225	1136	1138	0	0	1137	0		
1114	5	0	1	0		1	0.05		0
1227	1226	1138	1140	0	0	1139	0		
1115	5	0	1	0		1	0.05		0
1228	1227	1140	1142	0	0	1141	0		
1116	5	0	1	0		1	0.05		0
1229	1228	1142	1144	0	0	1143	0		
1117	5	0	1	0		1	0.05		0
1230	1229	1144	1146	0	0	1145	0		
1118	5	0	1	0		1	0.05		0
1231	1230	1146	1148	0	0	1147	0		
1119	5	0	1	0		1	0.05		0
1232	1231	1148	1150	0	0	1149	0		
1120	5	0	1	0		1	0.05		0
1233	1232	1150	1152	0	0	1151	0		
1121	5	0	1	0		1	0.05		0
1234	1233	1152	1154	0	0	1153	0		
1122	5	0	1	0		1	0.05		0
1235	1234	1154	1156	0	0	1155	0		
1123	5	0	1	0		1	0.05		0
1236	1235	1156	1158	0	0	1157	0		
1124	5	0	1	0		1	0.05		0
1237	1236	1158	1160	0	0	1159	0		
1125	5	0	1	0		1	0.05		0
1238	1237	1160	1162	0	0	1161	0		
1126	5	0	1	0		1	0.05		0
1239	1238	1162	1164	0	0	1163	0		
1127	5	0	1	0		1	0.05		0
1240	1239	1164	1166	0	0	1165	0		
1128	5	0	1	0		1	0.05		0

1241	1240	1166	1168	0	0	1167	0	
1129	5	0	1	0		1	0.05	0
1242	1241	1168	1170	0	0	1169	0	
1130	5	0	1	0		1	0.05	0
1243	1242	1170	1172	0	0	1171	0	
1131	5	0	1	0		1	0.05	0
1244	1243	1172	1174	0	0	1173	0	
1132	5	0	1	0		1	0.05	0
1245	1244	1174	1176	0	0	1175	0	
1133	5	0	1	0		1	0.05	0
1246	1245	1176	1178	0	0	1177	0	
1134	5	0	1	0		1	0.05	0
1247	1246	1178	1180	0	0	1179	0	
1135	5	0	1	0		1	0.05	0
1248	1247	1180	1182	0	0	1181	0	
1136	5	0	1	0		1	0.05	0
1249	1248	1182	1184	0	0	1183	0	
1137	5	0	1	0		1	0.05	0
1250	1249	1184	1186	0	0	1185	0	
1138	5	0	1	0		1	0.05	0
1251	1250	1186	1188	0	0	1187	0	
1139	5	0	1	0		1	0.05	0
1252	1251	1188	1190	0	0	1189	0	
1140	5	0	1	0		1	0.05	0
1253	1252	1190	1192	0	0	1191	0	
1141	5	0	1	0		1	0.05	0
1254	1253	1192	1194	0	0	1193	0	
1142	5	0	1	0		1	0.05	0
1255	1254	1194	1196	0	0	1195	0	
1143	5	0	1	0		1	0.05	0
1256	1255	1196	1198	0	0	1197	0	
1144	5	0	1	0		1	0.05	0
1257	1256	1198	1200	0	0	1199	0	
1145	5	0	1	0		1	0.05	0
1258	1257	1200	1202	0	0	1201	0	
1146	5	0	1	0		1	0.05	0
1259	1258	1202	1204	0	0	1203	0	
1147	5	0	1	0		1	0.05	0
1260	1259	1204	1206	0	0	1205	0	
1148	5	0	1	0		1	0.05	0
1261	1260	1206	1208	0	0	1207	0	
1149	5	0	1	0		1	0.05	0

1262	1261	1208	1210	0	0	1209	0		
1150	5	0	1	0		1	0.05	0	
1263	1262	1210	1212	0	0	1211	0		
1151	4	0	1	1		1	0.05	0	
1265	1264	1213	1214	0	0	0	0		
1200	4	0	1	1		1	0.05	0	
1314	1313	1262	1263	0	0	0	0		
1201	4	0	1	1		1	0.05	0	
1316	1315	1264	1265	0	0	0	0		
1250	4	0	1	1		1	0.05	0	
1365	1364	1313	1314	0	0	0	0		
1251	5	0	1	1		1	0.05	0	
1367	1366	1315	1317	0	0	1316	0		
1252	5	0	1	1		1	0.05	0	
1368	1367	1317	1319	0	0	1318	0		
1253	5	0	1	1		1	0.05	0	
1369	1368	1319	1321	0	0	1320	0		
1254	5	0	1	1		1	0.05	0	
1370	1369	1321	1323	0	0	1322	0		
1255	5	0	1	1		1	0.05	0	
1371	1370	1323	1325	0	0	1324	0		
1256	5	0	1	1		1	0.05	0	
1372	1371	1325	1327	0	0	1326	0		
1257	5	0	1	1		1	0.05	0	
1373	1372	1327	1329	0	0	1328	0		
1258	5	0	1	1		1	0.05	0	
1374	1373	1329	1331	0	0	1330	0		
1259	5	0	1	1		1	0.05	0	
1375	1374	1331	1333	0	0	1332	0		
1260	5	0	1	1		1	0.05	0	
1376	1375	1333	1335	0	0	1334	0		
1261	5	0	1	1		1	0.05	0	
1377	1376	1335	1337	0	0	1336	0		
1262	5	0	1	1		1	0.05	0	
1378	1377	1337	1339	0	0	1338	0		
1263	5	0	1	1		1	0.05	0	
1379	1378	1339	1341	0	0	1340	0		
1264	5	0	1	1		1	0.05	0	
1380	1379	1341	1343	0	0	1342	0		
1265	5	0	1	1		1	0.05	0	
1381	1380	1343	1345	0	0	1344	0		
1266	5	0	1	1		1	0.05	0	

1382	1381	1345	1347	0	0	1346	0		
1267	5	0	1	1		1	0.05		0
1383	1382	1347	1349	0	0	1348	0		
1268	5	0	1	1		1	0.05		0
1384	1383	1349	1351	0	0	1350	0		
1269	5	0	1	1		1	0.05		0
1385	1384	1351	1353	0	0	1352	0		
1270	5	0	1	1		1	0.05		0
1386	1385	1353	1355	0	0	1354	0		
1271	5	0	1	1		1	0.05		0
1387	1386	1355	1357	0	0	1356	0		
1272	5	0	1	1		1	0.05		0
1388	1387	1357	1359	0	0	1358	0		
1273	5	0	1	1		1	0.05		0
1389	1388	1359	1361	0	0	1360	0		
1274	5	0	1	1		1	0.05		0
1390	1389	1361	1363	0	0	1362	0		
1275	5	0	1	1		1	0.05		0
1391	1390	1363	1365	0	0	1364	0		
1276	4	0	1	1		1	0.05		0
1393	1392	1266	1367	0	0	0	0		
1300	4	0	1	1		1	0.05		0
1417	1416	1390	1391	0	0	0	0		
1301	4	0	1	1		1	0.05		0
1419	1418	1392	1393	0	0	0	0		
1325	4	0	1	1		1	0.05		0
1443	1442	1416	1417	0	0	0	0		
1326	4	0	1	1		1	0.05		0
1445	1444	1418	1419	0	0	0	0		
1350	4	0	1	1		1	0.05		0
1469	1468	1442	1443	0	0	0	0		
1351	4	0	1	1		1	0.05		0
1471	1470	1444	1445	0	0	0	0		
1375	4	0	1	1		1	0.05		0
1495	1494	1468	1469	0	0	0	0		
1376	4	0	1	1		1	0.05		0
1497	1496	1470	1471	0	0	0	0		
1400	4	0	1	1		1	0.05		0
1521	1520	1494	1495	0	0	0	0		
1401	4	0	1	1		1	0.05		0
1523	1522	1496	1497	0	0	0	0		
1425	4	0	1	1		1	0.05		0

1547	1546	1520	1521	0	0	0	0		
1426	4	0	1	1		1	0.05		0
1549	1548	1522	1523	0	0	0	0		
1450	4	0	1	1		1	0.05		0
1573	1572	1546	1547	0	0	0	0		
1451	4	0	1	1		1	0.05		0
1575	1574	1548	1549	0	0	0	0		
1475	4	0	1	1		1	0.05		0
1599	1598	1572	1573	0	0	0	0		
1476	4	0	1	1		1	0.05		0
1601	1600	1574	1575	0	0	0	0		
1500	4	0	1	1		1	0.05		0
1625	1624	1598	1599	0	0	0	0		
1501	4	0	1	1		1	0.05		0
1627	1626	1600	1601	0	0	0	0		
1525	4	0	1	1		1	0.05		0
1651	1650	1624	1625	0	0	0	0		
1526	4	0	1	1		1	0.05		0
1653	1652	1626	1627	0	0	0	0		
1550	4	0	1	1		1	0.05		0
1677	1676	1650	1651	0	0	0	0		
1551	4	0	1	1		1	0.05		0
1679	1678	1652	1653	0	0	0	0		
1575	4	0	1	1		1	0.05		0
1703	1702	1676	1677	0	0	0	0		
1576	4	0	1	1		1	0.05		0
1705	1704	1678	1679	0	0	0	0		
1600	4	0	1	1		1	0.05		0
1729	1728	1702	1703	0	0	0	0		

STOP

//

C*****

APPENDIX B: SUBSURFACE FLAW DETECTION

Thermal methods in nondestructive testing utilize the fact that the thermal properties of a defect differ from those of the host material so that temperature distortions result when the material is heated. If the temperature distortions are measured (e.g., by an infrared camera), the data can be analyzed to possibly locate and/or size the defect. Heating materials having defects has been accomplished in the past by using heat sources such as halogen lamps, hot air, or pulsed lasers.

The thermal methods described above tend to fall into two categories. One category is the use of pulsed lasers, which provides a rapid thermal transient by local heating of a sample surface. This method has been used successfully to measure flaw location and flaw size [19, 50, 9]. The disadvantage of this method is that in its present form it can only be used to measure flaws very near the surface (e.g., submicron to a few mm) of a material. In the second category of thermal methods the temperature of a large volume of the sample is raised above ambient by using heat sources such as halogen lamps or hot air, thus producing a less severe thermal transient [50]. Unlike the laser pulse method, this second method can be used to detect flaws well below the surface of a sample; however, it is less successful at providing flaw size information.

A feasibility study was performed for using remotely measured surface temperature as an indicator of the presence of defects located well below the heated surface.

A high power industrial laser was used to heat a sample moving continuously past the stationary laser beam. The temperature transients were then measured with thermocouples mounted near flaws in the metal being heated by the moving laser beam. The results of the experiments conducted with different flaw sizes, and different laser beam velocities, are discussed with reference to applications in nondestructive testing, especially in testing the quality of a laser-weld.

Test Conditions

Samples of AISI 1018 steel, 102x64x3.2 mm, were uniformly ground to obtain the same surface finish. A flaw was located in each sample in the form of a hole 4.8 mm in diameter. The depth of the hole in each sample was 1.1 mm, 1.6 mm, 2.2 mm, and 2.7 mm, respectively. This resulted in flaw depths below the upper surface ranging from 2.1 mm to 0.5 mm.

The upper surfaces of the samples were heated by a moving laser beam of constant power of 210 ± 5 W, with an estimated 10% of the incident power being absorbed. The beam was focused to a point in a plane 13 mm above the upper surface of the sample to avoid damage to the sample surface. The laser beam was traversed along four different lines of travel, on the edge of the hole and at distances of 1.6 mm, 3.2 mm, and 4.8 mm from the edge of the hole. For each beam location, the beam velocity was varied as 25.4 mm/s, 21.2 mm/s, 16.9 mm/s, 12.7 mm/s, and 8.5 mm/s. Type-K, chromel-alumel 30-gage thermocouples were used to record the temperatures. Six thermocouples were mounted intrinsically on the upper surface. One thermocouple was located on either side of the flaw and one directly over it. The other three

thermocouples were located 9.6 mm away to give the temperatures at corresponding locations that did not experience the effect of the flaw. A schematic of the test sample with the location of the thermocouples is shown in Figure B.1. A seventh thermocouple was located on the sample surface as a reference for the beam position.

Experiments were performed on each sample by varying the velocity of the beam at each location of the line of travel of the beam. The temperature transients and the maximum temperature rise above the ambient value recorded for the various tests are presented in the following section.

Results

Typical temperature transients recorded in the vicinity of the flaw are presented, followed by the effects of the flaw location below the upper surface and the heat source velocity on the temperature transients. Finally, the effect of the distance of the heat source from the flaw edge on the temperature is presented.

Temperature profile near flaw: The temperature transient near the flaw for a fixed set of test conditions is shown in Figure B.2. The figure shows the temperature rise on either side of the flaw and directly over the flaw. The presence of the flaw decreases the thermal mass in the region over the flaw giving rise to higher temperatures. This is also seen in Figure B.3, which shows the temperature rise transients over the flaw (as recorded by thermocouple 2) and at a corresponding location in a region without a flaw (as recorded by thermocouple 5) for the same heat source distance. The temperature over the flaw was always higher than the values on either side, and the trailing edge always recorded the lowest temperature.

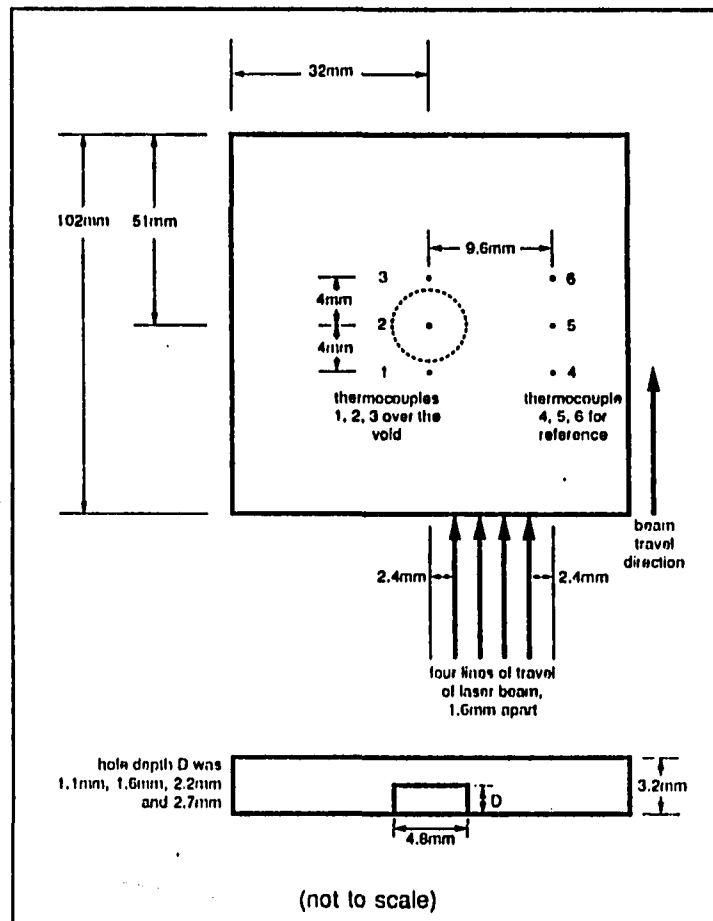


Figure B.1: Schematic of the test sample with location of thermocouples

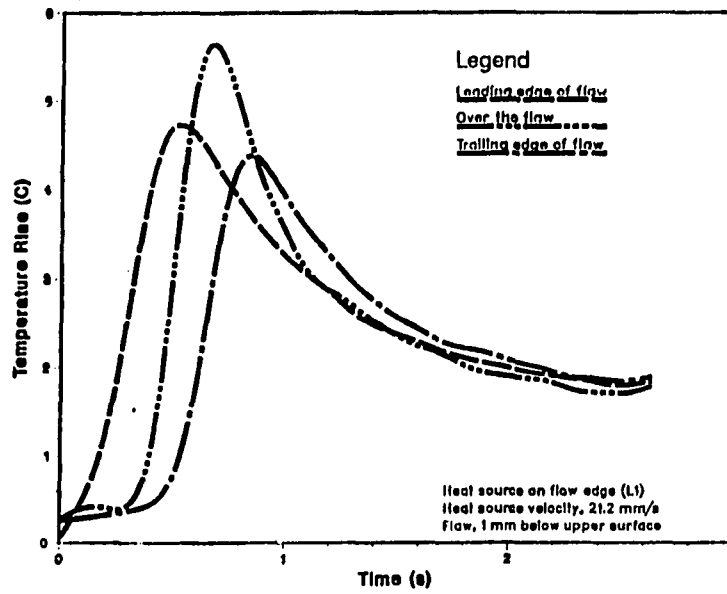


Figure B.2: Typical temperature record in the vicinity of a flaw

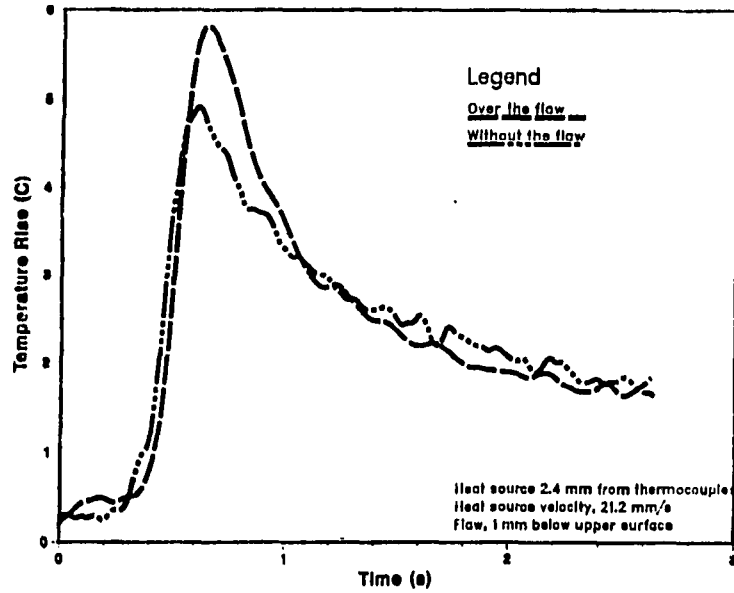


Figure B.3: Typical temperature record in regions with and without a flaw

Flaw depth: In all the tests, only the depth of the drilled hole was varied. This had the effect of varying the size of the flaw and the location, or flaw depth, below the upper surface.

The temperature transients over the flaw for different flaw depths are shown in Figure B.4. With decreasing flaw depth, the peak temperature increases. However, the flaw depth does not have a noticeable effect upon the rate of change of temperature. The maximum temperatures at two locations 2.4 mm from the heat source are shown in Figure B.5. The higher temperature was recorded over the flaw (thermocouple 2) and the lower temperature was recorded over a region without a flaw (thermocouple 5). The effect of the flaw upon the temperature is insignificant beyond 2.0 mm for the range of beam velocities and the power level used in the experiments. The important conclusion from these figures is that in addition to detecting the presence of the flaw there exists a potential to quantify its location from surface temperature data.

Velocity of heat source: The heat source velocity determines the amount of energy input to the sample, and, therefore, the magnitude of the temperatures recorded for a given flaw size. The heat source velocity also determines the maximum rate at which a sample can be scanned.

The temperature rise transient directly over the flaw for different velocities of the heat source is shown in Figure B.6. Decreasing the velocity increases the total energy input to the sample, thus increasing the peak temperature values for a particular flaw size. The effect of the heat source velocity on the maximum temperatures recorded at two locations 2.4 mm from the heat source, with one location directly above a flaw,

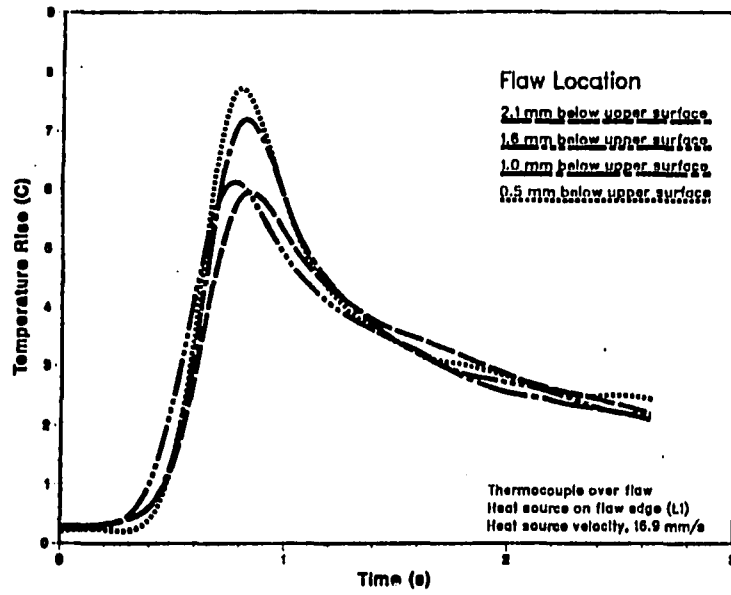


Figure B.4: Surface temperature record for different flaw depths

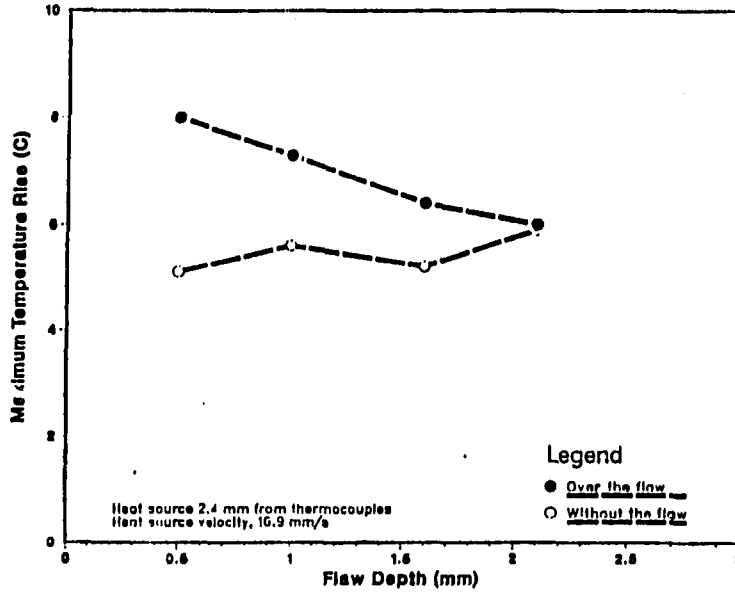


Figure B.5: Peak surface temperature near regions with and without a flaw

is shown in Figure B.7. The heat source velocity, together with the resolution of the temperature measuring device will, therefore, determine the minimum flaw size that can be detected.

Distance of heat source: The heat source distance from a flaw affects the temperature in the region around the flaw, and therefore, the detectability of the flaw. Figure B.8 shows the effect of increasing the heat source distance on the transient temperature over a flaw. With increasing distance from the flaw, the peak temperature and therefore the detectability of the flaw, decreases. The resolution of the temperature measuring device and the minimum size of the flaw to be detected will determine the maximum heat source distance from a flaw.

This, in turn, will determine the maximum area that can be scanned on either side of the beam, and hence, the total rate of scanning. The effect of the heat source distance is also seen in Figure B.9, which shows the maximum temperature for various heat source distances for the cases with a flaw and without a flaw.

Summary

The results of the preliminary tests indicate that the presence of flaws can be detected by temperature measurements made when the sample is heated by a moving heat source. For a given resolution of the temperature measuring device, the minimum flaw size that can be detected depends upon the beam power level and velocity. The maximum depth at which a flaw can be detected also depends on the beam velocity and power level.

The heat source has to pass on the edge of the flaw or over the flaw for best results.

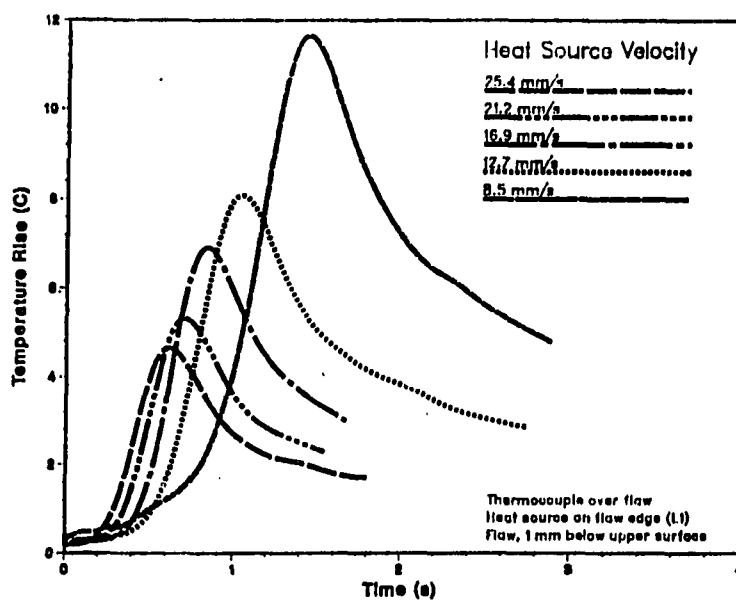


Figure B.6: Surface temperature variation over the flaw for different beam velocities

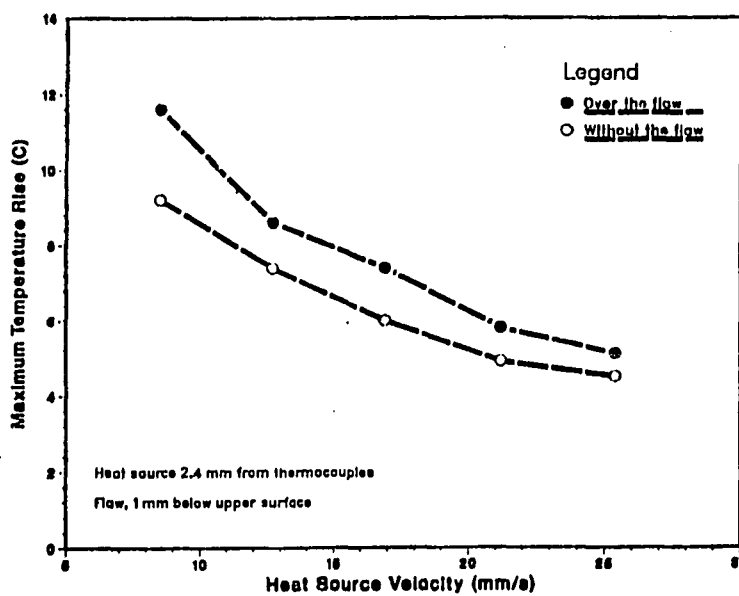


Figure B.7: Peak surface temperature variation over the flaw for different beam velocities

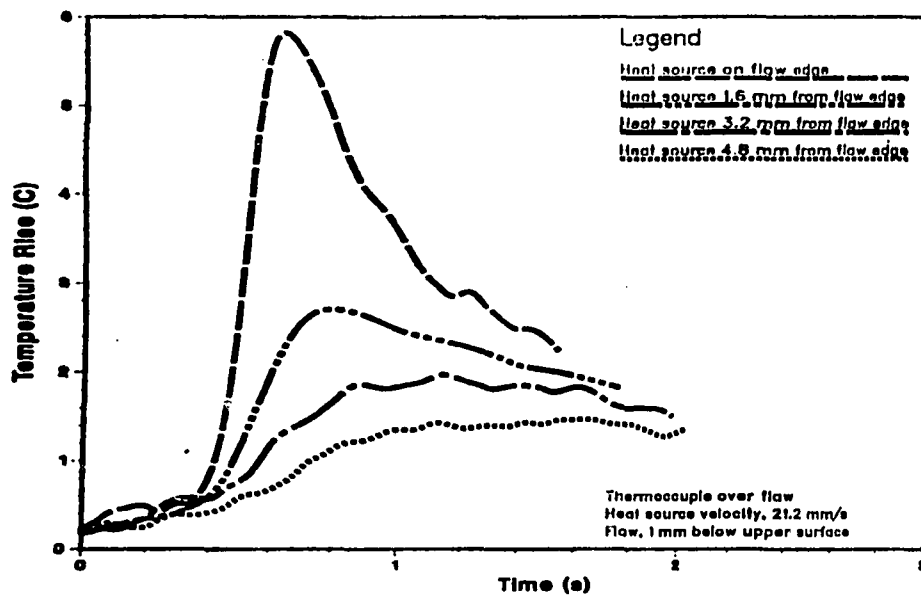


Figure B.8: Surface temperature variation with increasing heat source distance

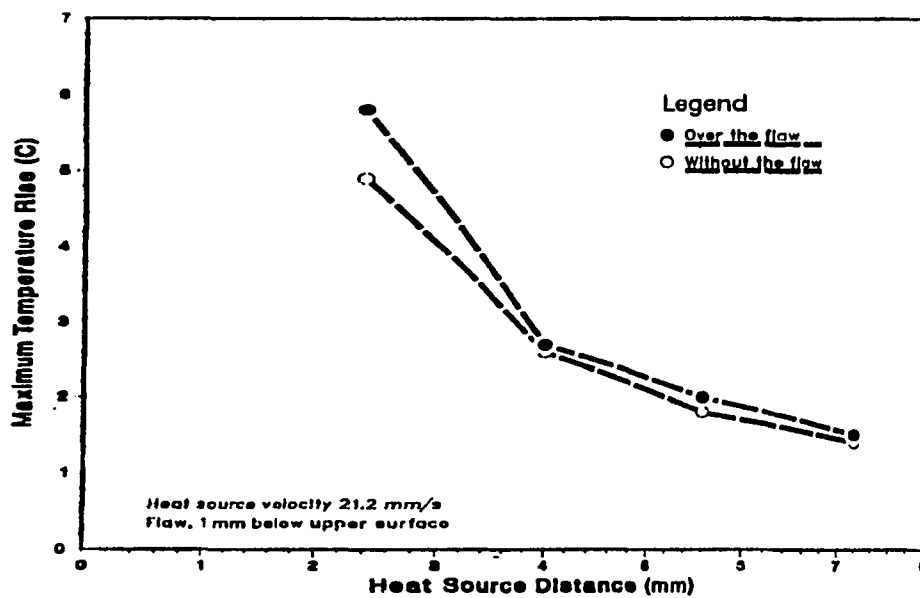


Figure B.9: Peak surface temperature variation with increasing heat source distance

This limits the scanning area on either side of the beam and decreases the overall scanning rate. The detectability of flaws can be improved by decreasing the heat source velocity or increasing the heat source power. The technique will prove useful in detecting flaws in manufactured materials in general and also in laser materials processing such as welding, heat treating, and cladding.